The Pennsylvania State University
The Graduate School

SUBGRID MODELING USING TRANSPORT EQUATIONS: LARGE-EDDY SIMULATION OF THE ATMOSPHERIC BOUNDARY LAYER

A Dissertation in
Meteorology
by
Sanjiv Ramachandran

Submitted in Partial Fulfillment
of the Requirements
for the Degree of

Doctor of Philosophy

August 2010

The dissertation of Sanjiv Ramachandran was reviewed and approved* by the following:

John C. Wyngaard
Professor of Meteorology
Dissertation Advisor, Chair of Committee

Yvette Richardson
Associate Professor of Meteorology

James G. Brasseur
Professor of Mechanical Engineering, Bioengineering and Mathematics

Joel Peltier
Adjunct Professor of Mechanical Engineering

Marcelo Chamecki
Assistant Professor of Meteorology

William H. Brune
Professor of Meteorology
Head of the Department of Meteorology

*Signatures are on file in the Graduate School.

Abstract

In large-eddy simulation (LES), the modeling of subfilter-scale motions when the filter width ($\sim \Delta$) is comparable to the size of the energy-carrying eddies ($\sim l$), is a challenging task. Under such conditions, the SFS model is required to parameterize the SFS eddies realistically in addition to extracting energy from the resolved, large eddies.

In this dissertation, we analyze an SFS model that solves for the SFS fluxes prognostically using a truncated version of the SFS conservation equations. We evaluate the model's performance in LES of the moderately convective, stable and neutral atmospheric boundary layer (ABL). We supplement our LES studies of the convective and stable ABL with analysis of the SFS conservation equations using data from the Horizontal Array Turbulence Study (HATS) experiments conducted in 2003. In LES of the convective ABL, we find that the transport-equation-based SFS model predicts the mean values and fluctuation levels of the SFS fluxes better than does an eddy-viscosity closure, when compared to HATS data. The modeled SFS conservation equations reproduce reasonably well the dominant trends in the real conservation equations. The scaled, dominant production terms in the modeled SFS stress budgets exhibit asymptotes at low l/Δ, some of which agree well with theoretically derived values in the limit $l/\Delta \to 0$.

The HATS analysis for the stable ABL shows that terms typically ignored in eddy-viscosity closures contribute significantly to both the mean values and fluctuation levels of the SFS fluxes at low l/Δ. We perform LES of a moderately stable ABL with the modeled SFS conservation equations, using physical conditions identical to those used in a previous LES-intercomparison study. The predictions of bulk parameters and equilibrium profiles of important statistics are robust to changes in resolution but the "locally" scaled effective eddy-viscosities of heat and momentum are overpredicted compared to observations.

We perform LES of the neutral ABL in order to test whether a recently developed framework — known as the "high accuracy zone" (HAZ) — to improve LES predictions in the surface layer is applicable to non-eddy-viscosity closures. We find that the modeled SFS conservation equations fail to eliminate the overshoot in the profile of the nondimensional mean-gradient of velocity without following the algorithm prescribed by the HAZ framework. This result provides further evidence for the generality of the HAZ framework.

Table of Contents

List of Figures

List of Tables

Acknowledgments

I am immensely fortunate to have wonderful parents who have always lent me their constant support and encouragement in all my undertakings. Never have they tried talking me into pursuing a career in the Indian equivalent of "plastics": software engineering. For that alone, I cannot thank them enough. Thanks also to my two brothers back home whose best wishes and kind words have helped in no small measure.

I am grateful to my advisor John Wyngaard for his guidance, instincts and insights. I truly admire his ability to interpret a complex equation and convey its essence in plain English. It is a skill I hope to cultivate someday. As someone who used to have a fetish for fancy math, I owe it to Dr. Wyngaard that I now look askance at anything that claims to be "A Theory of...", especially in the field of turbulence (though it would still be cool if somebody could prove the existence and uniqueness of solutions to the 3D Navier-Stokes equations). One particular insight of his that I never intend to forget is this: "In particular, beware jargon and sophisticated-sounding names. An uncalibrated model by any other name is still an uncalibrated model." I wish him well as he eases into his new role as Professor Emeritus.

I am grateful to my co-advisor Yvette Richardson for helping me significantly in the early stages of the project when I was wading through mesoscale codes. Her patience with a student who constantly asked her ridiculously naive questions, is most appreciated.

I am grateful to James Brasseur for having invested large amounts of his time in discussions with me and Tie Wei, which eventually led to interesting results. I am astonished by the depth of his knowledge. His passion for the subject and meticulous style of work are a reminder of the reasons why some of us chose research as a career.

I thank committee members Joel Peltier and Marcelo Chamecki for their useful advice and suggestions within the scope of our interactions.

I am indebted to Chin-Hoh Moeng and Peter Sullivan for their help in more ways than one. I am most impressed by their total inability to offer anything but perfectly sound and practical advice. I thank Dr. Moeng for graciously hosting my stay at NCAR, Boulder and for agreeing to read my preprints. I thank Dr. Sullivan for helping me with the HATS post-processing and for freely sharing with me many of his valuable insights into turbulence. He belongs to a rare breed by virtue of his being an expert in both turbulence and the art of extracting the most out of your codes.

I thank my former office mate Mark Kelly for being the ideal co-worker: quiet, knowledgeable and immensely helpful. I am also grateful for some good brainstorming sessions that I had with him. I thank Tie Wei for many stimulating discussions on turbulence. It was fun collaborating and exchanging ideas with him. I acknowledge help from Martin Otte early on when I was familiarizing myself with the pseudospectral code.

Life so far away from home would have been a lot harder without friends. I thank them all.

I acknowledge full financial support by the National Science Foundation (NSF) for the entire duration of my Ph.D. I am also grateful to the American taxpayer who funds institutions like the NSF.

Finally, I thank the National Center for Atmospheric Research and the Penn State High Performance Computing Group for providing excellent computer support. It would have been impossible to run my codes without using their supercomputers and linux clusters. I also thank Chuck Pavloski and Chad Bahrmann in the Department of Meteorology for providing local computer support.

Chapter 1

Introduction and literature review

Large-eddy simulation (LES) has gained widespread acceptance as a reliable technique for simulating the high Reynolds-number (Re) atmospheric boundary layer (ABL). In LES, we filter spatially the Navier-Stokes equations to obtain the resolved (or filtered) scales of motion and parameterize the effect of the unresolved (or subfilter) scales on the resolved scales using a subfilter-scale (SFS) model. When the filter scale is much smaller than the energy-producing scales, the primary role of the SFS model is to drain energy from the large, resolved eddies at the correct rate, which can be achieved by simple eddy diffusivity models such as the Smagorinsky model, as outlined by Lilly (1967). If, however, the filter scale is comparable to the energy-containing scales, as in the near-wall region, the SFS model is required not only to extract energy from the large eddies but also to represent the SFS stresses and fluxes.

In conditions of under-resolved turbulence, constant-eddy-diffusivity closures can fare poorly (Khanna and Brasseur, 1997) in their predictions of low-order flow statistics. Zhou et al. (2001) have shown that in the near-wall region, contributions from the SFS motions to the evolution of the resolved scales are of the same order as those from the resolved scales themselves. Consequently, the evolution of the flow in the near-wall region is highly sensitive to the SFS model. Using LES of the moderately convective ABL, Khanna and Brasseur (1998) found errors incurred in the near-wall region affected flow structure in the entire ABL.

In spite of its deficiencies, the Smagorinsky closure is used widely owing to its simplicity and ease of implementation. There are numerous SFS closures for the

ABL that overcome some of the shortcomings of the Smagorinsky closure. We mention briefly a few such attempts. The standard dynamic Smagorinsky model (Germano et al., 1991) and its subsequent variants (Basu and Porté-Agel, 2006; Porté-Agel, 2004; Porté-Agel et al., 2000) improve upon the original Smagorinsky closure by computing the model parameter in real time from the resolved scales. For instance, in the neutral ABL, the scale-dependent dynamic model (Porté-Agel et al., 2000) yields better profiles of ϕ_m (stability function for velocity) than the traditional Smagorinsky closure. Following Schumann (1975), Sullivan et al. (1994) developed a two-part eddy-viscosity model whose predictions of ϕ_m and ϕ_h (stability function for potential temperature) were significantly better than those of the Smagorinsky closure in both neutral and unstable ABLs. Mason and Thomson (Mason and Thomson, 1992) incorporated a stochastic term which enabled backscatter, a feature absent in the Smagorinsky closure. They also used a modified length scale that allowed the energy-containing eddies to scale with z in the inertial surface layer. Their SFS model resulted in good improvements in the predictions of the mean velocity profile and streamwise variances. Kosović (1997) developed an SFS stress model based on the nonlinear constitutive relationship suggested by Speziale (1991). Results obtained using Kosovic's SFS model for a moderately convective ABL showed considerable improvement over those obtained using the Smagorinsky closure (Chen et al., 2009).

While the closures discussed above model the SFS stress directly, there are SFS models that parameterize the unresolved velocity components from which the SFS stress is then reconstructed. We now describe briefly two such attempts in the latter category: the Resolvable-Subfilter-Scale (RSFS) model (Zhou et al., 2001) and a model developed by Chow et al. (2005). In LES, we have two cutoff filters: (i) the grid cutoff filter, which is imposed explicitly by the grid; and (ii) the LES cutoff filter, which is imposed either explicitly in a dealiasing step (in a pseudospectral code) or implicitly (in a physical-space code), in order to maintain numerical stability. By definition, the LES cutoff filter is coarser than the grid cutoff filter. Zhou et al. (2001) decomposed the SFS velocity field into two components: (i) resolvable-subfilter-scale (RSFS); and (ii) subgrid-scale (SGS). The RSFS component corresponds to scales that reside between the LES filter cutoff and the grid filter cutoff, i.e., the scales that are resolvable on the grid but are discarded due to the effect of the LES filter. The SGS component, on the other hand, corresponds to scales smaller than the grid filter cutoff and hence, is unresolvable. Evidently, the resolved scales feel the direct impact of the RSFS component more than that of the SGS component. The RSFS model solves for the RSFS component prognostically and uses it as a surrogate for the unresolved velocity field, which, in reality, also includes the SGS component. Zhou et al. (2001) found that under conditions where the turbulence is under-resolved, the RSFS model represents both the energy transfer from the resolved to the RSFS scales, and the SFS terms in the momentum equation better than do eddy-viscosity closures. Chow et al. (2005) combined multiple modeling strategies, such as, dynamic eddy viscosity (Wong and Lilly, 1994), reconstruction from RSFS motions and a "canopy" model (Brown et al., 2001), and observed improvements in the prediction of ϕ_m for a neutral ABL.

To study the general features in an SFS model that lead to better resolved-scale statistics, Chen and Tong (2006) devised an approach based on the joint probability density function (jpdf) of the resolved-scale velocity field. They derived the evolution equation of the one-time, one-point joint pdf of the resolved-scale velocity components, isolating the two terms on its right hand side that involved SFS contributions: (i) conditional mean of SFS stress; and (ii) conditional mean of SFS production rate. Subsequently, they performed *a priori* (Chen and Tong, 2006) and *a posteriori* (Chen et al., 2009) tests for the convective ABL comparing results using different SFS models with those from HATS data, their evaluation criteria being the correct prediction of the conditional means of the SFS stresses and the SFS production rate. Their LES results showed that SFS models which yielded poor predictions of the conditional means of SFS stress and SFS production rate fared poorly in the near-wall region. From the trends in the conditional means of the SFS stress and SFS production rate, Chen and Tong argued that errors in the predictions of low-order statistics in the near-wall region were related to under-prediction of SFS anisotropy and lack of SFS buoyant production. Previous work by Juneja and Brasseur (1999) has found the Smagorinsky closure to severely underpredict the level of anisotropy at the subfilter scales in the near-wall region. Chen and Tong (2009; 2006) observed that SFS models capable of exhibiting higher anisotropy, such as the nonlinear model of Kosović (1997), resulted in better LES predictions of low-order velocity moments.

1.1 SFS conservation equations

A natural way to begin to address some of the deficiencies in eddy-diffusivity closures is to consider the parent equations from which they are derived, namely, the conservation equation for the SFS stresses and SFS fluxes. A scalar eddy-diffusivity closure can be derived (Lilly, 1967) from the SFS conservation equations by retaining only the isotropic production term and the pressure-strain covariance, the latter being modeled using the Rotta model (Rotta, 1951).

Deardorff (1973), seeking "a more sophisticated treatment of the subgrid Reynolds stresses and fluxes" was the first to implement a version of the SFS conservation equations themselves as a subgrid model in his LES study of the convective ABL. His SFS model consisted of a set of ten conservation equations for all the second-order moments: (i) the six SFS stresses, τ_{ij} ; (ii) three SFS scalar (potential temperature, θ) fluxes, f_i ; and (iii) the SFS variance of θ. The conservation equations were then 'closed' by modeling the following: (i) third-order transport terms; (ii) pressure-strain covariances; and (iii) the scalar dissipation rate. We list below the two main conclusions of his study, followed by a brief discussion:

1. The SFS conservation equations are capable of removing energy from the resolved scales at the correct rate provided that numerical errors due to truncation can be controlled.

2. The use of conservation equations for SFS stresses yields increased SFS anisotropy near the wall.

Since the Smagorinsky closure is capable of draining energy from the large scales, it is reasonable to expect the parent SFS transport equation to be capable of the same, as confirmed by Deardorff's findings. The truncation errors he encountered were a source of instability in his simulations and he imposed artificial bounds on all second-order modeled SFS quantities in order to ensure the stability of his system of equations.

The cause of the observed increase in SFS anisotropy is the presence of production mechanisms in the SFS conservation equations that are ignored in eddy-diffusivity closures. These mechanisms (mentioned earlier) include: (i) nonlinear generation of SFS stresses due to SFS anisotropy; and (ii) buoyant generation

(Wyngaard, 2004) of SFS stresses by SFS scalar fluxes.

Deardorff's study demonstrated successfully the use of the SFS conservation equations as an SFS model in LES. In spite of obtaining encouraging results, however, he abandoned the conservation-equation-based approach and reverted to eddy-diffusivity closures in his later works (Deardorff, 1980) due to computational constraints at that time. While the notion of modeling the turbulent stresses and fluxes through their conservation equations has been embraced in ensemble-averaged modeling (Canuto et al., 1993; Cheng et al., 2001; Mellor and Yamada, 1974), three-dimensional mesoscale modeling still relies primarily on eddy-viscosity closures, as evidenced in state-of-the-art mesoscale codes like Advanced Regional Prediction System (Xue et al., 2000) and, Weather Research and Forecasting (Skamarock and Klemp, 2008).

Wyngaard (2004) has argued for revisiting the SFS conservation equations as a basis for SFS modeling, especially in the so-called "Terra Incognita" regime where the energy-containing length scales are of the same order as the grid resolution. Such a situation is encountered in both coarse-mesh LES and in fine-mesh mesocale simulations. He showed that the simplest SFS model consistent across the entire range of grid resolutions involves additional SFS production terms that are present in the governing SFS conservation equations but ignored in eddy-diffusivity closures.

Building upon the study by Wyngaard (2004), Hatlee and Wyngaard (2007) analyzed unstable cases from the HATS data set, and tested two SFS closures: (i) a truncated version of the SFS conservation equations; and (ii) an eddy-diffusivity closure with a constant model parameter. The SFS conservation equations yielded better predictions of both the diagonal (normal) and the off-diagonal (shear) components of the SFS stress tensor. The SFS conservation equations also outperformed the eddy-diffusivity closure in its predictions of SFS scalar fluxes and the scalar variance transfer rate. For instance, the difference in the predictions of the horizontal SFS scalar flux, in particular, by the two SFS models was dramatic. The conservation equations have an explicit flux-tilting term (discussed in more detail later) which tilts the vertical SFS flux into the horizontal direction in regions of high vertical shear of the horizontal velocity, e.g., near the surface. An eddy-diffusivity closure, on the other hand, can produce a horizontal SFS flux only in the presence of a horizontal scalar gradient. As a result, the SFS conservation equations predict a non-zero value for the SFS horizontal scalar flux, in good agreement with observations, whereas the eddy-diffusivity closure predict a near-zero value.

1.2 Motivation

SFS models have evolved considerably since Smagorinsky's original formulation (Smagorinsky, 1963). They have become more nuanced and sophisticated (Kosović, 1997; Mason and Thomson, 1992; Sullivan et al., 1994; Zhou et al., 2001) in their attempts to address better both their functions: (i) to drain energy from the large scales at the correct rate; and (ii) to parameterize correctly the SFS stresses and fluxes. In conditions where the turbulence is poorly resolved, the SFS model needs to perform both the above functions satisfactorily. For these reasons, it is desirable to develop SFS parameterizations that are not overly simplistic in their representation of the SFS stresses and fluxes.

The SFS conservation equations, in principle, enable the description of SFS stresses and fluxes according to their governing equations. As a result, important SFS physics such as anisotropy, backscatter and buoyant production are built into the equations and don't need to be modeled explicitly. While the third-order terms in the SFS conservation equations still need to be modeled, the principal SFS production mechanisms (Wyngaard, 2004) can be described in their exact analytical form. An additional advantage of the SFS conservation equations is their generality, which enables them to describe flows across a wide range of stabilities.

Deardorff's study (1973) was seminal yet limited in its scope as its main objective was to "realistically simulate the transfer of larger scale variance to subgrid scales" using the SFS conservation equations, which he achieved successfully. The studies by Wyngaard (2004) and Hatlee and Wyngaard (2007) show the potential of the conservation equations to overcome some of the major deficiencies that plague eddy-diffusivity closures. If the SFS conservation equations show promise, they are also complicated and merit further study. Hence, in this dissertation, we revisit the notion of SFS modeling based on the conservation equations for the SFS stresses and fluxes. The SFS model we use in our study is identical to that used by Hatlee and Wyngaard (2007). The use of additional prognostic equations necessarily implies higher computational expense. Deardorff (1973) using a 1 MHz processor which was considered state-of-the-art at the time, concluded that "the results were worth the price." Today, it is routine to run high-resolution LES simulations on huge parallel clusters of 2 GHz processors. This tremendous surge in computing power mitigates partially the concerns regarding the computational expense incurred in using the SFS conservation equations.

1.2.1 SFS model versus other factors

In the previous sections, we discussed the potential benefits of using an SFS model that wasn't too restrictive in its assumptions. Within the context of an LES, however, the SFS model is only one of many factors affecting the resolved-scale statistics. The evolution of the resolved scales depends in a complex way on a host of factors: (i) the SFS model; (ii) the numerical scheme employed (finite-difference versus pseudospectral); (iii) grid size; (iv) aliasing error; (v) discretization error; and (vi) the boundary conditions. All these factors affect non-trivially the time-evolution of the discretized Navier-Stokes (N-S) equations and in general, it is not easy to untangle their individual influences.

Recent studies of the neutral ABL by Brasseur and Wei (2010) have unearthed some crucial insights into the interplay between some of the factors cited above. In their studies, they focused on the requirements for obtaining law-of-the-wall scaling in the inertial surface layer. They found that the familiar overshoot in the non-dimensional mean velocity gradient ϕ_m was caused by a spurious manifestation of numerical "friction." In order to eliminate the overshoot and recover law-of-the-wall scaling, they have proposed a so-called 'High Accuracy Zone' (HAZ) framework (discussed in Ch. (4). They have validated it using LES of the shear-driven neutral ABL. Presently, the HAZ framework is yet to be extended to the convective and the stable ABLs.

As Brasseur and Wei (2010) demonstrated the validity of the HAZ framework using the Smagorinsky closure, it is of interest to examine its applicability to other non-eddy-viscosity closures, such as the SFS conservation equations.

1.3 Outline

In the next chapter, we discuss the implementation and performance of an SFS closure that uses conservation equations, in LES of the moderately convective ABL. We perform coarse-mesh LES to gain insight into various terms in the SFS conservation equations. We then use high-resolution LES and compare select SFS statistics with observations from the Horizontal Array Turbulence Study (HATS) experiment. We conclude the second chapter by analyzing the conditional means of the SFS stresses and the SFS production rate.

The third chapter contains results obtained from analysis of HATS data and LES for the stable boundary layer. In the first part of the chapter, we use HATS data to assess the relative importance of various production terms in the SFS budgets and their impact on the magnitudes of SFS stresses and fluxes. The second part of the chapter is devoted to LES studies of a moderately stable boundary layer.

In the fourth chapter, we perform LES of the shear-driven neutral ABL using the conservation-equation-based SFS model, in order to test the applicability of the HAZ framework to non-eddy-viscosity-closures.

We summarize our conclusions in the fifth chapter and suggest potential topics for future work.

Chapter 2

Large-eddy simulation of the moderately convective atmospheric boundary layer

In the previous chapter, we summarized the potential advantages of an SFS model that uses conservation equations for the SFS stresses and fluxes. In this chapter, we discuss the implementation of such an SFS model (Hatlee and Wyngaard, 2007) and its performance in LES of the moderately convective boundary layer. The outline of the chapter is as follows. Using coarse-mesh LES, we first illustrate the significance of the various terms in the SFS model using simple qualitative arguments. We then compare various subfilter-scale statistics in the surface layer obtained using high-resolution LES, to those obtained from the Horizontal Array Turbulence Study or HATS (Sullivan et al., 2003). Finally, we test the performance of the SFS model using criteria devised by Chen and Tong (2006) that involve studying the trends in the conditional means of the SFS stresses and the SFS production rate.

2.1 Model equations

We begin by obtaining filtered equations for the potential temperature and velocity fields making the following assumptions:(i) the Boussinesq approximation[1] is valid; (ii) the Re of the flow is high enough to ensure either (a) the viscous sublayer is confined to a very thin region near the ground and therefore, unresolved; or (b) the surface is characterized by an effective roughness scale that is also unresolved; and (iii) high Peclet number[2], Pe. The high Re and Pe imply that the viscous terms can be neglected in the filtered equations for velocity and the potential temperature. The potential temperature, θ, is related to temperature, T, as follows (Wyngaard, 2010):

$$\theta = T\left[\frac{p(0)}{p(z)}\right]^{R_d/c_p}, \tag{2.1}$$

where p is the pressure, R_d is the gas constant for dry air and c_p is the specific heat of dry air at constant pressure. From Eq. (2.1), potential temperature of an air parcel is the temperature of that parcel after it is brought adiabatically and reversibly to a reference state, typically assumed to correspond to sea-level conditions. In dry, adiabatic conditions potential temperature is a conserved scalar (Wyngaard, 2010).

2.1.1 Equations for the filtered scalar and velocity fields

The continuity equation for a Boussinesq flow is (Wyngaard, 2010),

$$\frac{\partial u_i}{\partial x_i} = 0 \tag{2.2}$$

Filtering Eq. (2.2) spatially yields,

$$\frac{\partial \bar{u}_i}{\partial x_i} = 0 \tag{2.3}$$

[1]Density differences are dynamically significant only when they are multiplied by the acceleration due to gravity.

[2]The Peclet number is defined as $Pe \equiv UL/\kappa$, where U and L are characteristic velocity and length scales, while κ is the thermal diffusivity. It is the ratio of transport of heat by advection to that by conduction.

The evolution equation for θ is given by

$$\frac{\partial \theta}{\partial t} + u_i \frac{\partial \theta}{\partial x_i} = \gamma \frac{\partial^2 \theta}{\partial x_i \partial x_i}, \tag{2.4}$$

where u_i is the component of velocity in the ith direction and γ is the molecular diffusivity of the scalar. Filtering (2.4) spatially and using the Boussinesq approximation yields

$$\frac{\partial \bar{\theta}}{\partial t} + \bar{u}_i \frac{\partial \bar{\theta}}{\partial x_i} + \frac{\partial f_i}{\partial x_i} = 0, \quad f_i = \overline{\theta u_i} - \bar{\theta}\bar{u}_i, \tag{2.5}$$

where the overbar denotes the filtering operation and f_i denotes the component of the SFS scalar flux in the ith direction. The diffusive terms are absent in Eq. (2.5) due to the assumption of high Pe. The only restriction placed on the filtering operation is that it commute with differentiation, which is true when the filter function is uniform in space. For nonuniform grids the filter width varies in space and consequently, the commutation error is non-zero (Ghosal and Moin, 1995). The linearized, filtered momentum equation written in rotation form for a Boussinesq flow (Moeng, 1984), is

$$\frac{\partial \bar{u}_i}{\partial t} = \epsilon_{ijk}\bar{u}_j\bar{\omega}_k - \frac{1}{\rho_0}\frac{\partial p^*}{\partial x_i} + \frac{g}{\Theta_0}\bar{\theta}\delta_{i3} + \epsilon_{ij3}(2\Omega)\left[\bar{u}_j - U_j^g\right] - \frac{\partial \tau_{ij}^d}{\partial x_j}, \tag{2.6}$$

where $\bar{\omega}_k$ is the kth component of filtered vorticity, p^* is the modified pressure (discussed below), ρ_0 is the reference density, Θ_0 is the reference potential temperature, $\mathbf{U^g} = (U_g, V_g, 0)$ is the geostrophic wind vector, g is the acceleration due to gravity, ϵ_{ijk} is the third-order permutation tensor, Ω is earth's angular velocity and τ_{ij}^d denotes the deviatoric part (the isotropic part is subtracted out) of the SFS momentum stress tensor, defined as

$$\tau_{ij}^d = \tau_{ij} - \frac{2}{3}\delta_{ij}e = (\overline{u_i u_j} - \bar{u}_i\bar{u}_j) - \frac{2}{3}\delta_{ij}e \tag{2.7}$$

where δ_{ij} is the Kronecker-Delta operator and $e = (\overline{u_i u_i} - \bar{u}_i\bar{u}_i)$ is the SFS kinetic energy. The viscous terms are absent in Eq. (2.6) due to the assumption of high Re. All filtered quantities in Eqs. (2.5)–(2.6) represent small deviations from a base state in hydrostatic equilibrium (Wyngaard, 2010). The expression for the buoyant forcing in Eq. (2.6) assumes that the deviations in velocity are much smaller than the speed of sound, a reasonable approximation in the turbulent ABL (Wyngaard, 2010). Following Moeng (1984), the modified pressure p^* is given by

$$p^* = \bar{p} + \rho_0 \left(\frac{2}{3} e + \frac{\overline{\bar{u}_k \bar{u}_k}}{2} \right) \tag{2.8}$$

where $\bar{p}$ is the filtered pressure. Taking the divergence of Eq. (2.6) and invoking the Boussinesq approximation yields the following Poisson equation for p^*:

$$\frac{1}{\rho_0} \frac{\partial^2 p^*}{\partial x_i \partial x_i} = \frac{\partial r_i}{\partial x_i}, \tag{2.9}$$

where r_i denotes the right-hand side of Eq. (2.6) without the pressure-gradient term. Equation (2.9) shows that p^* in a Boussinesq flow is purely a diagnostic field.

To close Eqs. (2.5)–(2.6), we need models for f_i, τ_{ij}^d and e. We refer to the models for f_i and τ_{ij}^d collectively as the 'SFS model.' In the next section, we outline the conservation equations for f_i and τ_{ij}^d which form the basis for our SFS model. Deardorff (1973) derived the SFS conservation equations for the 'total' τ_{ij} variables (deviatoric + isotropic) which introduced the turbulent dissipation rate $\epsilon = (\nu/2)\overline{(u_{i,j} + u_{j,i})(u_{i,j} + u_{j,i})}$ into the equations for the diagonal components, $\tau_{\alpha\alpha}$, $(\alpha = 1, 2, 3)$, where $u_{i,j} \equiv (\partial u_i / \partial x_j)$. To close the conservation equations, he used a model for ϵ. In our analysis, the conservation equations describe only the deviatoric components. Hence, the equations for the normal components, $\tau_{\alpha\alpha}^d$, do not contain ϵ. We, however, still need a model for ϵ as one of the inputs to our SFS models is the SFS kinetic energy, e, whose prognostic equation (discussed later in Sec. 2.1.4) requires the parameterization of ϵ. In Deardorff's SFS model, e is given simply by the trace of τ_{ij}.

2.1.2 Conservation equations for the SFS flux and stress

In this section we discuss the conservation equations for the SFS fluxes and stresses. We only present the final equations without going through their derivation.

2.1.2.1 Conservation equation for f_i

The conservation equation for the SFS flux of potential temperature, f_i, is (Hatlee and Wyngaard, 2007):

$$\begin{aligned}\frac{\partial f_i}{\partial t} + \bar{u}_j \frac{\partial f_i}{\partial x_j} + \frac{\partial}{\partial x_j}(\overline{\theta u_i u_j} - \overline{\theta u_i}\bar{u}_j - \bar{\theta}\overline{u_i u_j} - \bar{u}_i\overline{\theta u_j} - \bar{u}_i\overline{\theta u_j} + 2\bar{\theta}\bar{u}_i\bar{u}_j) \quad = \\ -f_j\frac{\partial \bar{u}_i}{\partial x_j} - \tau^d_{ij}\frac{\partial \bar{\theta}}{\partial x_j}\boxed{-\frac{2}{3}e\frac{\partial \bar{\theta}}{\partial x_i}} + \frac{g}{\Theta_0}\left(\overline{\theta^2} - \bar{\theta}^2\right)\delta_{i3} \\ -2\,e_{mij}\,\Omega_m\,f_j - \frac{1}{\rho_0}\frac{\partial}{\partial x_i}(\overline{p\theta} - \bar{p}\bar{\theta}) + \boxed{\frac{1}{\rho_0}\left(\overline{p\frac{\partial \theta}{\partial x_i}} - \bar{p}\frac{\partial \bar{\theta}}{\partial x_i}\right)}\end{aligned} \tag{2.10}$$

where e_{mik} is the permutation tensor and $\mathbf{\Omega}$ is the angular velocity vector of the coordinate frame. The second and third terms on the left hand side represent advection and turbulent transport, respectively. On the right hand side, the terms represent (in order): flux tilting and stretching, anisotropic and isotropic gradient-production, buoyant production, rotation, pressure transport and pressure scalar-gradient covariance. The last two terms together represent pressure destruction[3]. We refer to the second term on the right hand side as anisotropic production as it would vanish under conditions of isotropy, which would require τ^d_{ij} to be zero. We refer to the third term on the right hand side as isotropic production due to its dependence on e, the isotropic part of the total stress tensor, τ_{ij}. The molecular diffusion terms are absent in Eq. (2.10) due to the assumption of high Re and Pe. The molecular destruction terms are absent due to local isotropy, as confirmed by experiments (Mydlarski, 2003). An eddy-diffusivity closure can be derived from Eq. (2.10) by assuming a balance solely between the boxed terms, i.e., isotropic gradient-production and modeled pressure strain-rate covariance (Wyngaard, 2004) (model discussed in Sec. 2.1.2.4). Pressure destruction is the principal sink term in Eq. (2.10) (Hatlee and Wyngaard, 2007; Wyngaard, 2004).

Given models for f_i, τ^d_{ij} and e, we need to model the buoyant, turbulent-transport and pressure-destruction terms.

[3]Hatlee and Wyngaard (2007) refer to only the pressure scalar-gradient covariance as pressure destruction. While the pressure transport term vanishes upon integrating over a finite volume, it contributes to destruction of SFS scalar fluxes locally. Hence, we include the pressure transport term in our definition of pressure destruction.

2.1.2.2 Conservation equation for τ_{ij}^d

The conservation equation for the deviatoric stress is given by (Hatlee and Wyngaard, 2007),

$$
\begin{aligned}
\frac{\partial \tau_{ij}^d}{\partial t} + \bar{u}_k \frac{\partial \tau_{ij}^d}{\partial x_k} = \frac{\partial}{\partial x_k} \Big[& \overline{u_i u_j u_k} - \bar{u}_i \overline{u_j u_k} - \bar{u}_j \overline{u_i u_k} - \bar{u}_k \overline{u_i u_j} + 2 \bar{u}_i \bar{u}_j \bar{u}_k \\
& - \frac{\delta_{ij}}{3} \left(\overline{u_l^2 u_k} - 2 \bar{u}_l \overline{u_l u_k} - \bar{u}_k \overline{u_l^2} + 2 \bar{u}_l^2 \bar{u}_k \right) \Big] \\
\boxed{-\frac{2}{3} e \left(\frac{\partial \bar{u}_i}{\partial x_j} + \frac{\partial \bar{u}_j}{\partial x_i} \right)} & - \left[\tau_{ik}^d \frac{\partial \bar{u}_j}{\partial x_k} + \tau_{jk}^d \frac{\partial \bar{u}_i}{\partial x_k} - \frac{1}{3} \delta_{ij} \tau_{kl}^d \left(\frac{\partial \bar{u}_k}{\partial x_l} + \frac{\partial \bar{u}_l}{\partial x_k} \right) \right] \\
& + \frac{g}{\Theta_0} \left[\delta_{j3} f_i + \delta_{i3} f_j - \left(\frac{2}{3} \right) \delta_{ij} f_3 \right] \\
& - 2\, \Omega_k \left[e_{ikl}\, \tau_{jl}^d + e_{jkl}\, \tau_{il}^d - \left(\frac{2}{3} \right) e_{mkl}\, \tau_{ml}^d \right] \\
& + \boxed{\frac{1}{\rho_0} \left[\overline{p \left(\frac{\partial u_i}{\partial x_j} + \frac{\partial u_j}{\partial x_i} \right)} - \bar{p} \left(\frac{\partial \bar{u}_i}{\partial x_j} + \frac{\partial \bar{u}_j}{\partial x_i} \right) \right]} \\
- \frac{1}{\rho_0} \frac{\partial}{\partial x_k} & \left[\delta_{ik} (\overline{u_j p} - \bar{u}_j \bar{p}) + \delta_{jk} (\overline{u_i p} - \bar{u}_i \bar{p}) - \frac{2}{3} \delta_{ij} (\overline{u_k p} - \bar{u}_k \bar{p}) \right].
\end{aligned}
\tag{2.11}
$$

The second term on the left side is advection. The terms on the right side are, in order, turbulent transport (split over two lines), isotropic production, anisotropic production, buoyant production, rotational production, pressure strain-rate covariance and pressure transport. The pressure strain-rate covariance has zero trace and represents intercomponent energy transfer. The last two terms in Eq. (2.11) together represent pressure destruction[4]. As in Eq. (2.10), retaining only the boxed terms, i.e., isotropic production and modeled pressure strain-rate covariance (model discussed in Sec. (2.1.2.4)), yields an eddy-viscosity closure. The anisotropic-production term is similar to the flux-tilting term in Eq. (2.10) as it describes generation of τ_{ij}^d through both tilting and stretching of the different τ_{ij}^d components. The pressure destruction term plays the role of the sink, just as in Eq. (2.10). The molecular diffusion terms are negligible outside the thin viscous sublayer due to the assumption of high Re. The molecular destruction terms in the

[4]As in the SFS flux conservation equations, Hatlee and Wyngaard (2007) identify only pressure strain-rate covariance as pressure destruction. Our definition, however, includes the pressure transport term as well.

off-diagonal equations are negligible under the assumption of local isotropy (Wyngaard et al., 1971) and are absent in the $\tau^d_{\alpha\alpha}$ equations as Eq. (2.11) describes the evolution of the deviatoric stresses and not the total stresses (deviatoric + isotropic).

Given models for f_i, τ^d_{ij} and e, we need to model turbulent transport and pressure destruction.

The buoyant terms in Eq. (2.11) are determined explicitly as a function of f_i. In the SFS flux conservation equations, the buoyant terms affect only f_3 and their parameterization requires a model for the SFS variance of θ. We present results later showing that the buoyant terms are small compared to the dominant terms in the f_3 budget.

The Coriolis terms in the SFS conservation equations are expected to play an important role when the SFS Rossby number, $\sqrt{e}/(f\Delta)$ where $f = 2\Omega$ is the Coriolis parameter, is of order unity. Equivalently, the SFS time scale given by $\Delta/\sqrt{e}$ should be comparable to the rotational time scale, $1/f$. In the present study, we use $f = 10^{-4}$. In our LES runs we found the SFS time scale increases monotonically with height (due to decreasing e) and typically assumes a value of 60–90 at the base of the capping inversion, i.e., a value two orders of magnitude smaller than the rotational time scale. It is even smaller in the surface layer, where the SFS motions are most important. For comparison, the time scale for the large eddies in our LES runs is typically an order of magnitude higher than the SFS time scale.

The transport terms vanish upon integrating Eqs. (2.10)–(2.11) over a finite volume and assuming zero velocity on its boundaries. Locally, they can be significant, especially under convectively unstable conditions in the "mesoscale limit" (Wyngaard, 2004), where essentially all the turbulence is parameterized by the SFS model.

We now discuss the Rotta model (Rotta, 1951) for the slow part of the pressure-strain-rate covariance.

2.1.2.3 Rotta's model

We can split the pressure field formally into three parts, $p = p_T + p_S + p_B$ (Hatlee and Wyngaard, 2007; Moeng and Wyngaard, 1986), where p_T and p_S denote contributions to the total pressure field from turbulent-turbulent and mean-turbulent interactions, respectively, while p_B denotes those from buoyancy. The components p_T and p_S are referred to as the "slow" and "rapid" components as p_S responds instantaneously to mean gradients while p_T does not (Mathieu and Scott, 2000). The Rotta model (Rotta, 1951) is applicable to that part of the ensemble-averaged pressure strain-rate covariance arising purely from the slow component, p_T, assuming the absence of factors that induce anisotropy, such as, mean gradients and stratification. Under such conditions, the slow pressure strain-rate covariance drives the SFS stresses towards isotropy. Hence, the Rotta model is also referred to as a return-to-isotropy model. According to the Rotta model,[5]

$$\frac{1}{\rho_0}\left(\overline{p_T\frac{\partial\theta}{\partial x_i}} - \bar{p}_T\frac{\partial\bar{\theta}}{\partial x_i}\right) = -\frac{f_i}{T_\theta} \tag{2.12}$$

$$\frac{1}{\rho_0}\left[\overline{p_T\left(\frac{\partial u_i}{\partial x_j} + \frac{\partial u_j}{\partial x_i}\right)} - \bar{p}_T\left(\frac{\partial\bar{u}_i}{\partial x_j} + \frac{\partial\bar{u}_j}{\partial x_i}\right)\right] = -\frac{\tau^d_{ij}}{T_\tau}, \tag{2.13}$$

where T_θ and T_τ are timescales for the SFS motions, models for which are discussed in the next section.

2.1.2.4 Deriving an eddy-viscosity closure from the SFS conservation equations

We now review the derivation of an eddy-viscosity closure from Eqs. (2.10)–(2.11) (Lilly, 1967; Wyngaard, 2004). The SFS time scales T_θ and T_τ are modeled as proportional to $l_{\mathrm{SFS}}/\sqrt{e}$ where l_{SFS} is the length scale for the SFS eddies. We denote the proportionality constants in the expressions for T_θ and T_τ by c_θ and c_τ, respectively. Retaining isotropic gradient-production and modeling the slow pressure strain-rate covariance using the Rotta model while neglecting the rest of the terms in Eq. (2.10) yields (Wyngaard, 2004),

$$\begin{aligned} -\frac{2}{3}e\left(\frac{\partial\bar{\theta}}{\partial x_i}\right) &= \frac{f_i}{c_\theta\, l_{\mathrm{SFS}}}\sqrt{e} \\ \implies f_i &= -\frac{2}{3}\,c_\theta\, l_{\mathrm{SFS}}\sqrt{e}\left(\frac{\partial\bar{\theta}}{\partial x_i}\right). \end{aligned} \tag{2.14}$$

[5] Moeng and Wyngaard (1986) note that Rotta originally proposed Eq. (2.13) which was then extended to scalars, as in Eq. (2.12), by Zeman (1981).

Defining $K_h \equiv (2/3)\, c_\theta\, l_{\mathrm{SFS}}\, \sqrt{e}$, where K_h is the scalar eddy-viscosity, we recognize Eq. (2.14) as the one-equation eddy-viscosity closure for the SFS scalar flux (Deardorff, 1980). Retaining only isotropic production and the modeled slow pressure strain-rate covariance in Eq. (2.11) yields,

$$\begin{aligned} -\frac{2}{3} e \left(\frac{\partial \bar{u}_i}{\partial x_j} + \frac{\partial \bar{u}_j}{\partial x_i} \right) &= \frac{\tau_{ij}^d}{c_\tau\, l_{\mathrm{SFS}}} \sqrt{e} \\ \Longrightarrow \; \tau_{ij}^d &= -\frac{2}{3}\, c_\tau\, l_{\mathrm{SFS}}\, \sqrt{e} \left(\frac{\partial \bar{u}_i}{\partial x_j} + \frac{\partial \bar{u}_j}{\partial x_i} \right). \end{aligned} \tag{2.15}$$

Equation (2.15) is an eddy-viscosity closure where $K_m \equiv [(2/3)\, c_\tau\, l_{\mathrm{SFS}}\, \sqrt{e}]$ is the eddy-viscosity for momentum. Deardorff's eddy-viscosity closure for τ_{ij}^d prescribes a factor of (4/15) instead of (2/3), as in Eq.(2.15), because his model for the pressure strain-rate covariance in the τ_{ij}^d conservation equations is different from that used in the above derivation. The constants c_τ and c_θ in Eqs. (2.14)–(2.15) can be tuned empirically (Deardorff, 1980) such that the SFS model extracts energy at the correct rate from the resolved scales.

In most eddy-viscosity closures, K_m and K_h are not estimated independently but differ by a factor, the turbulent Prandtl number, which is typically assumed to be constant and equal to 1/3 under unstable conditions (Moeng, 1984) although the basis for this assumption is questionable (Moeng and Wyngaard, 1988). Some eddy-viscosity closures, such as the locally-averaged scale-dependent dynamic model (Basu and Porté-Agel, 2006), estimate K_m and K_h independently, thereby allowing the turbulent Prandtl number to vary.

2.1.3 SFS model

While Eqs. (2.10)–(2.11) represent the conservation equations for f_i and τ_{ij}^d with the entire suite of terms, Hatlee and Wyngaard (2007) modeled them by neglecting the transport and rotational production terms while accounting for only the slow pressure strain-rate covariance through Rotta's model. They retained the buoyant production terms in the conservation equations for the SFS stress but not in those for the SFS flux. After observing inadequate performance of their modeled conservation equations for the SFS deviatoric stress, they also modeled the rapid contribution to the pressure strain-rate terms, which improved the performance of their SFS model.

Our motivation for the present work is similar to that of Hatlee and Wyngaard (2007), namely, to try and improve upon eddy-viscosity closures by including additional SFS production mechanisms in their exact analytical form while modeling select unclosed terms in the simplest way possible. Thus, we use an SFS model similar to that used by Hatlee and Wyngaard (2007), the only difference being that we account only for the slow pressure-destruction terms. We follow Hatlee and Wyngaard (2007) in neglecting the transport and rotational production terms in the modeled SFS conservation equations. For reasons stated earlier, we do not expect the Coriolis terms to play a significant role in the SFS conservation equations. By omitting the transport terms and modeling only the slow pressure strain-rate covariance, we strive to achieve a reasonable balance between retaining sufficient physics in the SFS model and avoiding the use of too many ad hoc models. The final truncated version of the full conservation equations that will serve as the SFS model is shown in Eqs. (2.16)–(2.17) :

$$
\begin{aligned}
\frac{\partial f_i}{\partial t} + \bar{u}_j \frac{\partial f_i}{\partial x_j} &= -f_j \frac{\partial \bar{u}_i}{\partial x_j} - \left(\tau_{ij}^d + \frac{2}{3}\delta_{ij} e \right) \frac{\partial \bar{\theta}}{\partial x_j} - \frac{f_i}{T_\theta}. && (2.16) \\
\frac{\partial \tau_{ij}^d}{\partial t} + \bar{u}_k \frac{\partial \tau_{ij}^d}{\partial x_k} &= -\frac{2}{3} e \left(\frac{\partial \bar{u}_i}{\partial x_j} + \frac{\partial \bar{u}_j}{\partial x_i} \right) \\
&- \left[\tau_{ik}^d \frac{\partial \bar{u}_j}{\partial x_k} + \tau_{jk}^d \frac{\partial \bar{u}_i}{\partial x_k} - \frac{1}{3}\delta_{ij} \tau_{kl}^d \left(\frac{\partial \bar{u}_k}{\partial x_l} + \frac{\partial \bar{u}_l}{\partial x_k} \right) \right] \\
&+ \frac{g}{\Theta_0} \left[\delta_{j3} f_i + \delta_{i3} f_j - \left(\frac{2}{3} \right) \delta_{ij} f_3 \right] - \frac{\tau_{ij}^d}{T_\tau}. && (2.17)
\end{aligned}
$$

The SFS length scale, l_{SFS}, scales on the length scale for the smallest resolved eddies, i.e., the grid cut-off length scale. Thus, in regions of unstable stratification we set $l_{\mathrm{SFS}} = \Delta = (\Delta x \Delta y \Delta z)^{1/3}$ (Deardorff, 1973), where Δx is the resolution in the x-direction and likewise for Δy and Δz. In regions of stable stratification, however, using Δ as the SFS length scale causes the SFS model to blow up. We confirmed that using $l_{\mathrm{SFS}} = \Delta$ in stably-stratified regions leads to insufficient dissipation ($\propto 1/l_{\mathrm{SFS}}$) of SFS fluxes and stresses in Eqs. (2.16)–(2.17), in a plane-averaged sense. A better estimate for l_{SFS} in stably-stratified regions is given by $l_{\mathrm{SFS}} = 0.76\sqrt{e}/N$ where $N = \sqrt{(g/\Theta_0)(\partial\theta/\partial z)}$ is the Brunt-Väisälä frequency

(Deardorff, 1973). This formulation for the SFS length scale accounts explicitly for the effects of stable stratification and reduces l_{SFS} accordingly, thereby preventing Eqs. (2.16)–(2.17) from blowing up. Hence, we use $l_{\text{SFS}} = 0.76\sqrt{e}/N$ in stably-stratified regions.

2.1.4 Conservation equation for the SFS turbulent kinetic energy

The exact conservation equation for the SFS turbulent kinetic energy, e, is:

$$\frac{\partial e}{\partial t} = -\tau_{ij}^{d}\overline{S}_{ij} - \frac{\partial}{\partial x_j}\left(\bar{u}_j e\right) + \frac{g}{\Theta_0} f_3 - \frac{\partial}{\partial x_j}\left(\overline{u_j e} - \bar{u}_j \bar{e} + \frac{1}{\rho_0}(\overline{u_j p} - \bar{u}_j \bar{p})\right) - \epsilon, \quad (2.18)$$

The turbulent and pressure transport terms are modeled together following Moeng (1984):

$$\left(\overline{u_j e} - \bar{u}_j \bar{e} + \frac{1}{\rho_0}(\overline{u_j p} - \bar{u}_j \bar{p})\right) = -\left(2K_m \frac{\partial e}{\partial x_j}\right), \quad (2.19)$$

where K_m is an eddy-diffusivity. It is modeled as $K_m = c_k\sqrt{e}\,\Delta$ (Moeng, 1984), where c_k denotes the SFS model constant. Lilly (1967) derived the value of c_k for homogeneous, isotropic turbulence and found it to be 0.094 while Deardorff (1973) and Moeng (1984) used $c_k = 0.1$ in their LES. We will use $c_k = 0.1$ for our LES runs. Thus, the modeled prognostic equation for e is given by,

$$\frac{\partial e}{\partial t} = -\tau_{ij}^{d}\overline{S}_{ij} - \frac{\partial}{\partial x_j}\left(\bar{u}_j e\right) + \frac{g}{\Theta_0} f_3 + \frac{\partial}{\partial x_j}\left(2K_m \frac{\partial e}{\partial x_j}\right) - \epsilon, \quad (2.20)$$

where $\overline{S}_{ij} = (1/2)(\partial\bar{u}_i/\partial x_j + \partial\bar{u}_j/\partial x_i)$ is the resolved strain-rate tensor, $K_m = c_k\sqrt{e}\,\Delta$ is the eddy-diffusivity (Moeng, 1984) and ϵ is viscous dissipation of e. The terms on the right side of Eq. (2.20) represent (in order): downscale (larger to smaller) energy transfer, advection, buoyant production, modeled turbulent and pressure transport, and viscous dissipation.

We model the viscous dissipation term as $\epsilon = c_\epsilon\, e^{3/2}/\Delta$ (Lilly, 1967). We use $c_\epsilon = 0.93$, a value first derived by Lilly (1967) and commonly used in LES (Moeng, 1984; Moeng and Wyngaard, 1988).

An eddy-diffusivity closure for τ_{ij}^d makes $-\tau_{ij}^d \bar{S}_{ij}$ positive definite everywhere and at all times. In principle, this is too strong a constraint as the cascade of energy from the larger to the smaller scales exists only on average. The flow of energy locally or instantaneously from the smaller to the larger scales, or 'backscatter,' was reported first by Piomelli et al. (1991) through direct numerical simulation (DNS) . It has since been observed in laboratory flows and field measurements (Porté-Agel et al., 1998; Sullivan et al., 2003; Tao et al., 2002). The dynamic model (Germano et al., 1991), the stochastic backscatter model (Mason and Thomson, 1992), the resolvable subfilter scale (RSFS) model (Zhou et al., 2001), Kosović's nonlinear model (Kosović, 1997) and the modeled SFS stress conservation equations, as represented by Eq. (2.17), all exhibit backscatter although in some models, such as the dynamic model, the backscatter is averaged to ensure numerical stability.

In a one-equation eddy-diffusivity closure, the buoyancy term in Eq. (2.20) accounts indirectly for the effects of stratification on the SFS stresses and fluxes as follows. An increase in upward buoyant forcing increases e, which leads to higher magnitudes of eddy-diffusivities ($K_m \propto \sqrt{e}$), thereby increasing turbulent mixing. Equivalently, in such closures buoyancy modulates the deviatoric stresses, τ_{ij}^d, through the isotropic part, e. It follows that this mechanism does not allow for buoyancy to affect τ_{ij}^d differentially but the SFS conservation equations show that the buoyant terms in the τ_{ij}^d equations do not assume identical analytical forms.

2.2 Details of LES code

The LES code used in this study is based on a serial pseudospectral code developed by Sullivan and Moeng (1994) that was later parallelized by Otte and Wyngaard (2001) using the Message Passing Interface (MPI).

The code employs periodic boundary conditions in the horizontal plane (Otte and Wyngaard, 2001) to simulate a horizontally homogeneous flow. The mesh is staggered vertically such that the first plane of u, v and θ is located a distance $\Delta z/2$ above the surface, while that of w and e is located a distance Δz above the surface. The SFS variables f_3, τ_{13}^d and τ_{23}^d are colocated with w while the remaining SFS flux components are colocated with u. A spectral cut-off filter eliminates the top third of the wavenumbers generated by the nonlinear advective term, in order to suppress aliasing errors. We compute horizontal derivatives in Fourier-space and use second order finite-differencing for the vertical derivatives.

In our implementation of Eq. (2.17), we found that the buoyancy term led to instabilities near the capping inversion causing the simulation to blow up. To remove the instability, we reduced the buoyancy term linearly to zero over the top 10% of the ABL such that its magnitude is exactly zero at the inversion height, which we define to be the base of the capping inversion.

2.2.1 Boundary conditions

Due to the staggered nature of the grid, we require boundary conditions for w, e, τ^d_{13}, τ^d_{23} and f_3. At the lower boundary, we set $w = 0$ and $e = e_1$, where e_1 is the value of e at the first grid level (Otte and Wyngaard, 2001). Enforcing the lower boundary conditions for τ^d_{13}, τ^d_{23} and f_3 requires knowledge of the surface friction velocity, u_*, and the Monin-Obukhov (MO) length, L. The square of the friction velocity, u_*^2, is equal to the ensemble-averaged wall stress. The MO length is defined to be the height below which production of turbulent kinetic energy by shear exceeds that by buoyancy, and is given by,

$$L = -\frac{u_*^3}{k(g/\theta_0)Q_0}, \tag{2.21}$$

where Q_0 is the surface heat flux and k approximated as 0.4 is the von Kármán constant. We now discuss an iterative procedure to estimate the values of u_* and L (Khanna, 1995; Otte and Wyngaard, 2001).

The mean surface potential temperature, θ_s, can be evaluated as follows assuming the profile of mean potential temperature is Monin-Obukhov (MO) similar (Paulson, 1970):

$$\langle \overline{\theta}_1 \rangle - \theta_s = 0.74\frac{\theta_*}{k}\left[\ln\left(\frac{z_1}{z_0}\right) - \psi_2\right], \tag{2.22}$$

where $\overline{\theta}_1$ is the potential temperature at the first θ level (angled brackets denote horizontal averaging), $\theta_* = -Q_0/u_*$, $z_1 = \Delta z/2$ is the height of the first θ level, z_0

is the surface roughness height and

$$\psi_2 = 2\ln\left[\frac{1+y^2}{z}\right], \quad y = \left(1 - 9\frac{z_1}{L}\right)^{1/4}. \tag{2.23}$$

The surface roughness height, z_0, represents the height at which the mean wind speed is zero assuming it exhibits a logarithmic profile. The use of Eq. (2.22) requires knowledge of u_* and L. The variable u_* is determined using a procedure similar to that for θ_s (Paulson, 1970):

$$\langle \overline{U}_1 \rangle = \frac{u_*}{k}\left[\ln\left(\frac{z_1}{z_0}\right) - \psi_1\right], \tag{2.24}$$

where $\overline{U}_1$ is the wind speed at the first u grid level and

$$\begin{aligned} \psi_1 &= 2\ln\left[\frac{1+x}{2}\right] + \ln\left[\frac{1+x^2}{2}\right] - 2\tan^{-1}x + \frac{\pi}{2}, \\ x &= \left(1 - 15\frac{z_1}{L}\right)^{1/4}. \end{aligned} \tag{2.25}$$

In the neutral limit, $z/L \to 0$ and consequently, $\psi_1 \to 0$. Equating ψ_1 to zero in Eq. (2.24), we recover the familiar log-law. Thus, we interpret ψ_1 as a factor accounting for the effects of stratification.

In principle, the two unknowns u_* and L can be estimated simultaneously from Eqs. (2.21)–(2.24). In practice it is easier to solve for them iteratively. Thus, we initiate the iterative sequence by assuming a value for u_* which is then used to evaluate L from Eq. (2.21). This value of L is then used to evaluate u_* from Eq. (2.24). The newly obtained value of u_* is substituted back in Eq. (2.21) to reevaluate L. In this way, the iterative procedure is repeated till two successive estimates of L differ by less than 1%.

The surface values of $\tau^d_{\alpha 3}$ ($\alpha = 1, 2$) and f_3 are modeled using the following surface stress model (Moeng, 1984):

$$\tau^d_{\alpha 3} = C_D\left[\overline{U}_1 \langle \bar{u}_{\alpha_1} \rangle + \langle \overline{U}_1 \rangle \left(\bar{u}_{\alpha_1} - \langle \bar{u}_{\alpha_1} \rangle\right)\right], \tag{2.26}$$

$$f_3 = C_\theta\left[\overline{U}_1\left(\langle \overline{\theta}_1 \rangle - \theta_0\right) + \langle \overline{U}_1 \rangle \left(\overline{\theta}_1 - \langle \overline{\theta}_1 \rangle\right)\right] \tag{2.27}$$

where $\bar{u}_{\alpha_1}$ denotes the value of $\bar{u}_\alpha$ at the first u level. The coefficients C_D and C_θ

are defined as

$$C_D = -\frac{u_*^2}{\left\langle \overline{U}_1 \right\rangle^2}, \;\; C_\theta = \frac{Q_0}{\left\langle \overline{U}_1 \right\rangle \left\langle \left\langle \overline{\theta}_1 \right\rangle - \theta_0 \right\rangle} \tag{2.28}$$

The lower boundary condition for pressure is derived by substituting $w = 0$ in the w-momentum equation. The vertical gradients of u, v and θ at the surface are set equal to their computed values at $z_1 = \Delta z$.

We specify a geostrophic wind vector that is constant with height.

At the upper boundary, w and all SFS quantities are set to zero (Moeng, 1984). A radiative boundary condition (Klemp and Durran, 1983) allows gravity waves to pass out of the computational domain without undergoing reflection.

The complete set of prognostic equations describing the evolution of the resolved and the SFS fields are:

- Filtered fields, $\bar{u}_i$ and $\bar{\theta}$: Eqs. (2.5)–(2.6) (**4 equations**)
- SFS stresses, τ_{ij}^d, and fluxes, f_i: Eqs. (2.16)–(2.17) (**9 equations**)
- SFS turbulent kinetic energy, e: Eq. (2.20) (**1 equation**)

Since τ_{ij}^d is symmetric, we only need to solve for six of its nine components. Of these six components, only five are independent as the trace is zero. At every iteration, these 14 nonlinear coupled equations are integrated forward in time using a third-order Runge-Kutta scheme with a time step that is computed dynamically for a fixed CFL number (Sullivan et al., 1996).

Utilizing horizontal homogeneity, we compute all necessary statistics by averaging over horizontal planes.

2.2.2 Realizability

Deardorff (1973), in his implementation of SFS conservation equations, enforced "realizability" conditions on all SFS quantities at every grid point at every time step in order to stabilize the code. In our simulations, we do not impose realizability conditions on the SFS stresses and SFS fluxes. As noted earlier, we prescribe a linear variation of the buoyancy term in Eq. (2.17) such that it reduces to zero over the top 10% of the ABL. In other words, the magnitude of the buoyancy term in Eq. (2.17) at the boundary layer top is precisely zero. The only prognostic variable for which we have an explicit constraint is e. The constraint, which ensures that $e > 0$ at all grid points and at all times, is necessary as the subfilter length scale in stably-stratified regions is parametrized as being proportional to $\sqrt{e}$ (Deardorff, 1980). The need for a realizability constraint on e, however, is a consequence of using the spectral cut-off filter and not of the underlying SFS model. Vreman et al. (1994) have illustrated theoretically and numerically that use of a spectral cut-off filter generates negative values of e.

2.3 Spectra

In this section, we show that the SFS transport equations can be "tuned" to extract energy from the resolved scales at the correct rate. We simulate a a moderately convective ABL with the parameters prescribed in Table 2.1. The prescribed value of the roughness height, z_0, is such that $z_0/z_1 \ll 1$, where z_1 is the height of the first grid level, thereby rendering the roughness height unresolved, as assumed earlier in Sec. (2.1). A list of the important diagnosed parameters is shown in Table 2.2. We begin by showing in Fig. (2.1) the following statistics: (i) velocity variances (resolved + SFS) scaled with w_*^2; (ii) vertical shear stress scaled with u_*^2; (iii) vertical heat flux scaled with Q_0; (iv) mean potential temperature; and (v) mean velocity. The magnitudes of the scaled variances (resolved + SFS) in Fig. (2.1) are typical of moderately convective ABLs (Sullivan and Moeng, 1994). The near-linear profiles of shear stress and vertical heat flux show that the simulation has attained a quasi-steady state. The profiles of mean temperature and mean velocity are representative of a well-mixed moderately convective ABL. In Fig. (2.2), we show the nondimensional mean-gradients of potential temperature and velocity, denoted by ϕ_h and ϕ_m, respectively. Inaccuracies in LES predictions of ϕ_m and ϕ_h have been a long-standing problem (Mason and Thomson, 1992) and have recently been addressed in detail for the case of a neutral ABL by Brasseur and Wei (2010), who have isolated the fundamental reasons that cause LES to overpredict ϕ_m. Brasseur and Wei (2010) also provide a systematic framework for accurate LES predictions of ϕ_m in the inertial surface-layer of the neutral ABL. Later in this dissertation, we perform LES of the neutral ABL to determine the applicability of the findings of Brasseur and Wei (2010) to the modeled SFS conservation equations.

Table 2.1. A list of important prescribed physical parameters. L_x, L_y and L_z are the physical dimensions of the computational domain in the x, y and z directions, respectively. N_x is the number of grid points in the x-direction and similarly for N_y and N_z. Q_0 is the prescribed surface temperature flux, z_0 is the roughness length, U_g and V_g are the geostrophic wind velocity components in the x and y directions, Γ is the lapse rate above the capping inversion and f is the Coriolis parameter.

Prescribed physical parameters of LES	
L_x(m)	6000
L_y(m)	6000
L_z(m)	1600
N_x, N_y	192
N_z	144
Q_0(K m s^{-1})	0.20
z_0(m)	0.05
U_g(m s^{-1})	15
V_g(m s^{-1})	0
Γ(K m^{-1})	0.003
f(s^{-1})	0.0001

Table 2.2. A list of important diagnosed physical parameters. The variable u_* is the friction velocity, w_* is the mixed layer convective velocity scale, L is the Monin-Obukhov length and z_i is the inversion height.

Diagnosed physical parameters of LES	
u_*(m s^{-1})	0.68
w_*(m s^{-1})	1.77
$-L$(m)	119
z_i(m)	857
$-z_i/L$	7.2

The turbulent spectra in the inertial subrange have the following form (Tennekes and Lumley, 1972):

$$E_\theta(\kappa) = 1.4\,\beta\,\epsilon^{-1/3}\chi\,\kappa^{-5/3}. \tag{2.29}$$

$$E_h(\kappa) = 1.64\,\alpha\,\epsilon^{2/3}\kappa^{-5/3}. \tag{2.30}$$

In Eqs. (2.29)–(2.30), $E_\theta(\kappa)$ and $E_h(\kappa)$ are the resolved two-dimensional ring spectra of potential temperature and horizontal turbulent kinetic energy, respectively, while κ is the radial wavenumber (Peltier et al., 1996). The constants α and β are

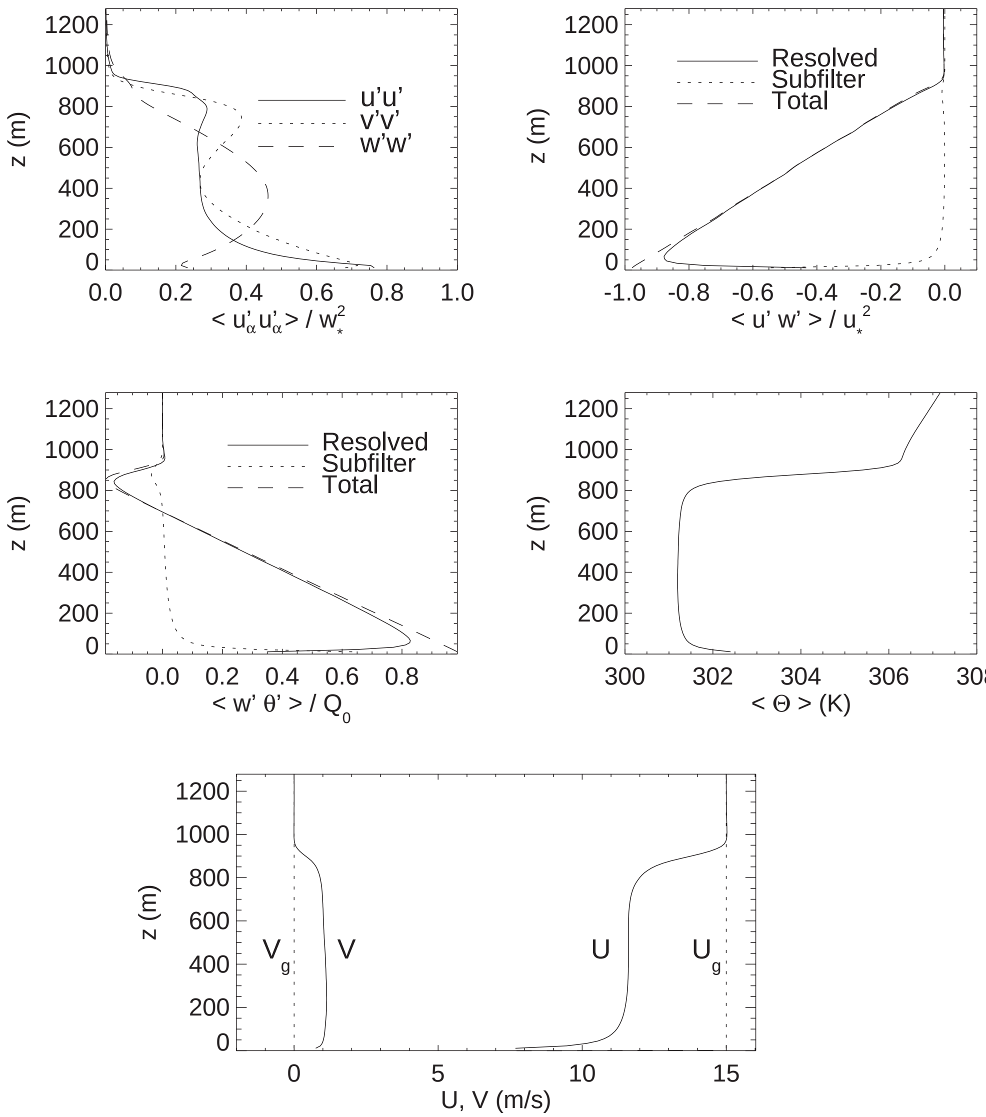

Figure 2.1. (i) Total velocity variances (resolved + SFS) scaled with w_*^2 (ii) The (1,3) stress component scaled with u_*^2 (iii) vertical heat flux scaled with Q_0 (iv) mean potential temperature; and (v) mean velocity components, U and V. The geostrophic velocity components are denoted by U$_g$ and V$_g$.

universal and are known as the Kolmogorov constant and the Corrsin-Obukhov constant, respectively. The variable χ denotes the plane-averaged rate of destruction of θ-variance at the smallest scales while ϵ denotes the plane-averaged dissipation of turbulent kinetic energy at the smallest scales. While Eqs. (2.29)–(2.30)

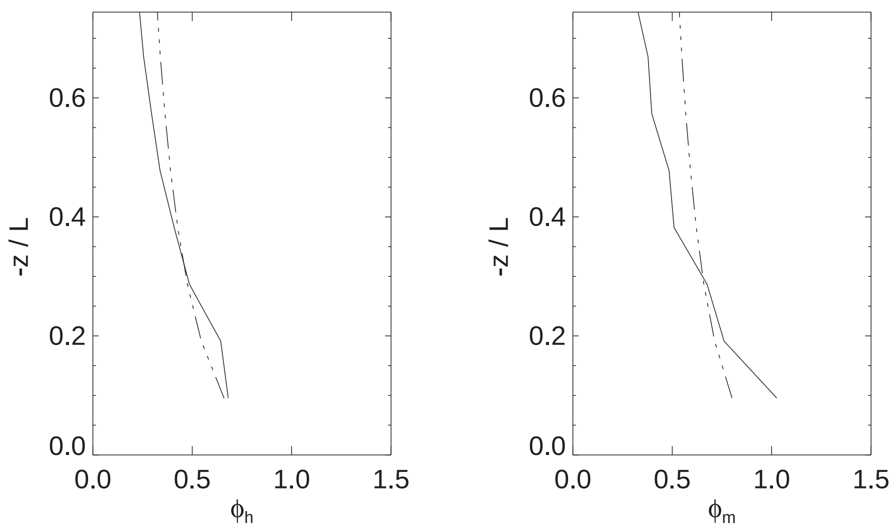

Figure 2.2. Left panel: Nondimensional mean gradient of potential temperature, ϕ_h, versus $-z/L$, where L is the Monin-Obukhov length. Right panel: Nondimensional mean gradient of velocity, ϕ_m, versus $-z/L$. The top of the layer shown corresponds to $z/z_i = 0.1$. Legend – Solid line : modeled SFS conservation equations, dot-dash line : empirical fit (Businger et al., 1971).

describe two-dimensional spectra, α and β have been scaled appropriately to correspond to their values for one-dimensional spectra. This is done to facilitate easy comparison between our results and observations as α and β are obtained typically from measurements of one-dimensional spectra. Sreenivasan (1995; 1996) has done an extensive compilation of the values of these universal spectral constants cited in the literature. He found their consensus values to be $\alpha \approx 0.5$ and $\beta \approx 0.4$ which will also serve as our reference. At equilibrium, χ is equal to the rate of variance transfer from the resolved to the subfilter scales. Hence, we obtain the following expression for χ:

$$\chi = \left\langle -f_j \frac{\partial \bar{\theta}'}{\partial x_j} \right\rangle, \tag{2.31}$$

where the $\langle\rangle$ operator denotes averaging over a plane and $\bar{\theta}' = \bar{\theta} - \langle\bar{\theta}\rangle$. Similarly, we can derive an expression for ϵ at equilibrium:

$$\epsilon = \left\langle -\tau_{ij}^{d} \frac{\partial \bar{u}_i}{\partial x_j} \right\rangle. \tag{2.32}$$

The RHS of Eq. (2.32) is the mean rate of transfer of turbulent kinetic energy from the resolved to the subfilter scales.

In Fig. (2.3a)-(2.3c) we show two-dimensional turbulent spectra of potential temperature, horizontal kinetic energy and vertical kinetic energy, denoted by $E_\theta(\kappa)$, $E_h(\kappa)$ and $E_w(\kappa)$, respectively. The spectra are plotted against $\kappa L/2\pi$, where $L = L_x, L_y$ and $\kappa = \sqrt{\kappa_1^2 + \kappa_2^2}$ is the radial wavenumber. The spectra correspond to mid-ABL levels where we expect the turbulence to be well resolved into a discernible inertial range. In Fig. (2.3a) we plot temperature spectra holding $c_\tau = 0.10$ constant while c_θ assumes the values $(0.17, 0.21, 0.26)$. In Fig. (2.3b)-(2.3c) are shown the horizontal and vertical velocity spectra, respectively, for $c_\theta = 0.21$ and $c_\tau = (0.06, 0.10, 0.15)$. Figure (2.3a) shows that the effects of changing (c_θ, c_τ) are felt most at scales close to the filter cutoff. As c_θ is increased, the spectra droop increasingly downward at the smaller scales implying greater dissipation by the SFS model. From Fig. (2.3b)-(2.3c), increasing c_τ has a similar effect on the resolved-scale spectra of horizontal and vertical kinetic energy. Excessively low values of (c_θ, c_τ) tend to result in a build up of variance close to the filter cut-off. For instance, when $c_\tau = 0.06$, the energy spectra droop upward implying an unphysical build-up of energy close to the filter cutoff due to insufficient dissipation by the SFS model. These observations can be explained crudely in conditions of well-resolved turbulence as follows. Increasing c_θ weakens the sink term in Eq. (2.12) leading to larger SFS fluxes which in turn increase the rate of drain of variance from the resolved scales, based on Eq. (2.31). We are implicitly assuming that the resolved-scale scalar gradient depends only weakly on the SFS model in regions of well-resolved turbulence. Similar arguments can be made accounting for the effect of c_τ on the resolved kinetic energy spectra. Higher c_τ results in larger magnitudes of the SFS stresses which extract more energy from the resolved scales through Eq. (2.32). Again, we are assuming that the resolved-scale velocity gradients depend only weakly on the SFS model in regions where the turbulence is well-resolved.

Hatlee and Wyngaard (2007) found that $(c_\theta, c_\tau) = (0.21, 0.08)$ best optimized the run-averaged modeled SFS stress and flux values, and the rate of variance transfer in comparison with observations. As an illustrative case, we plot in Fig. (2.4) the spectral constants α and β, associated with $(c_\theta, c_\tau) = (0.21, 0.10)$. While the agreement between the consensus and LES values is better for β than for α, it is reasonable to infer from Figs. (2.3)-(2.4) that the modeled SFS conservation equations are able to extract energy from the resolved scales at approximately the correct rate.

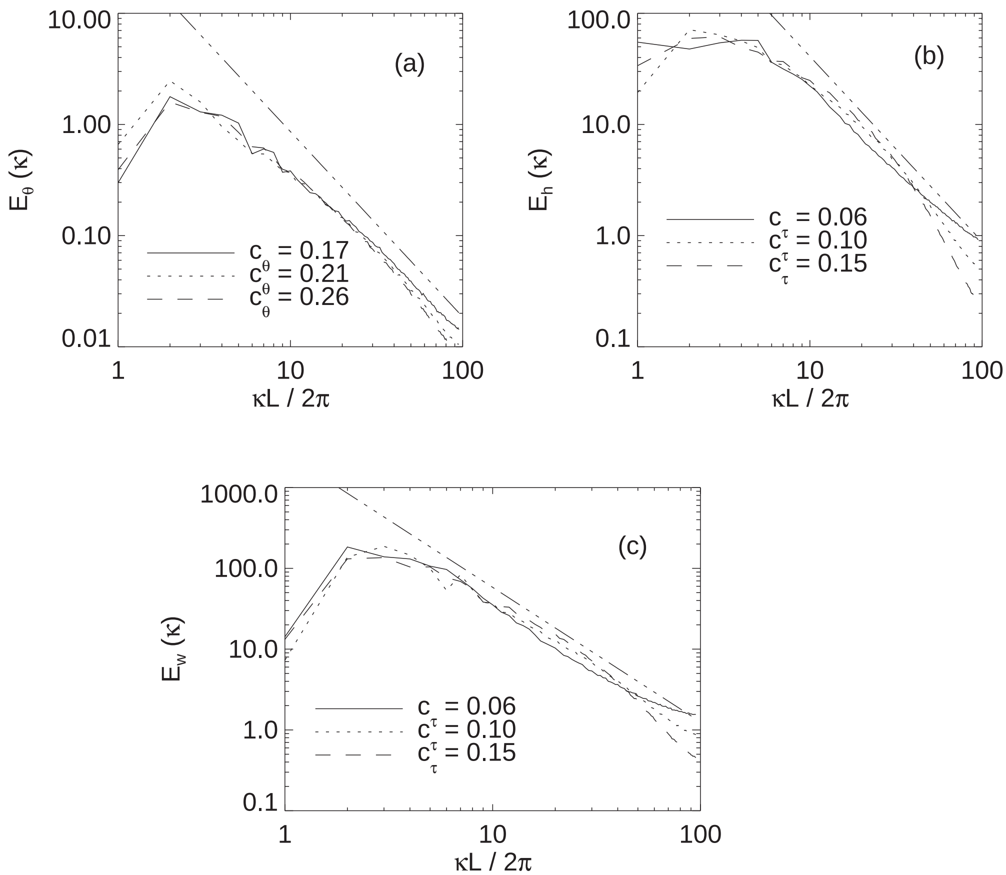

Figure 2.3. Two-dimensional (Wyngaard, 2010) resolved-scale spectra of: (a) potential temperature (b) horizontal kinetic energy (c) vertical kinetic energy, versus nondimensional horizontal wavenumber at mid-ABL. In (a), $c_\tau = 0.10$ while in (b)-(c), $c_\theta = 0.21$. $E_\theta(\kappa)$ has the units K^2m and $E_{h,w}(\kappa)$ has the units m^3s^{-2}. The radial wavenumber, κ, is given by $\kappa = \sqrt{\kappa_1^2 + \kappa_2^2}$ where $\kappa_{1,2}$ are wavenumbers corresponding to the 1,2 directions. The dash-dot line has a slope of (-5/3).

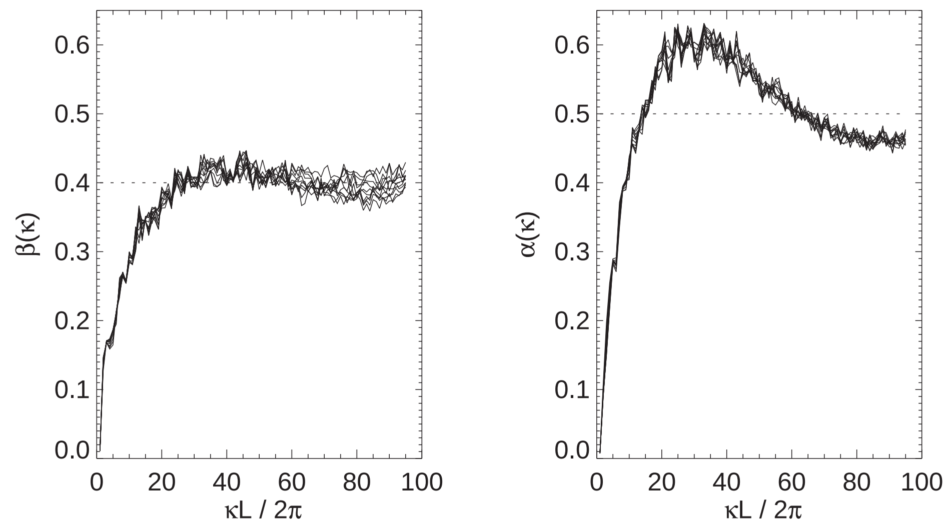

Figure 2.4. The spectral constants β and α. The consensus values are shown using dotted lines.

2.4 SFS budgets

In this section, we study the modeled SFS stress and flux budgets given by Eqs. (2.16)–(2.17). Eddy-diffusivity closures are derived from the SFS conservation equations by retaining solely isotropic gradient-production and modeled slow pressure strain-rate covariance, using the Rotta model for the latter. Hence, it is of interest to explore the relative contributions of different terms in the SFS budgets.

2.4.1 SFS flux budgets

The SFS flux budgets are shown in this section for a 64x64x48 grid mesh. The physical conditions describing the run (apart from the grid size) are identical to those in Table 2.1. In Fig. (2.5) we plot the plane-averaged terms in the f_i budgets versus height for $0 < z < 1.2z_i$. To examine closer the budgets in the lower part of the ABL, we also plot in Fig. (2.6) the SFS flux budgets for $0 < z < 0.3z_i$ where $z_i = 787.5$m is the inversion height.

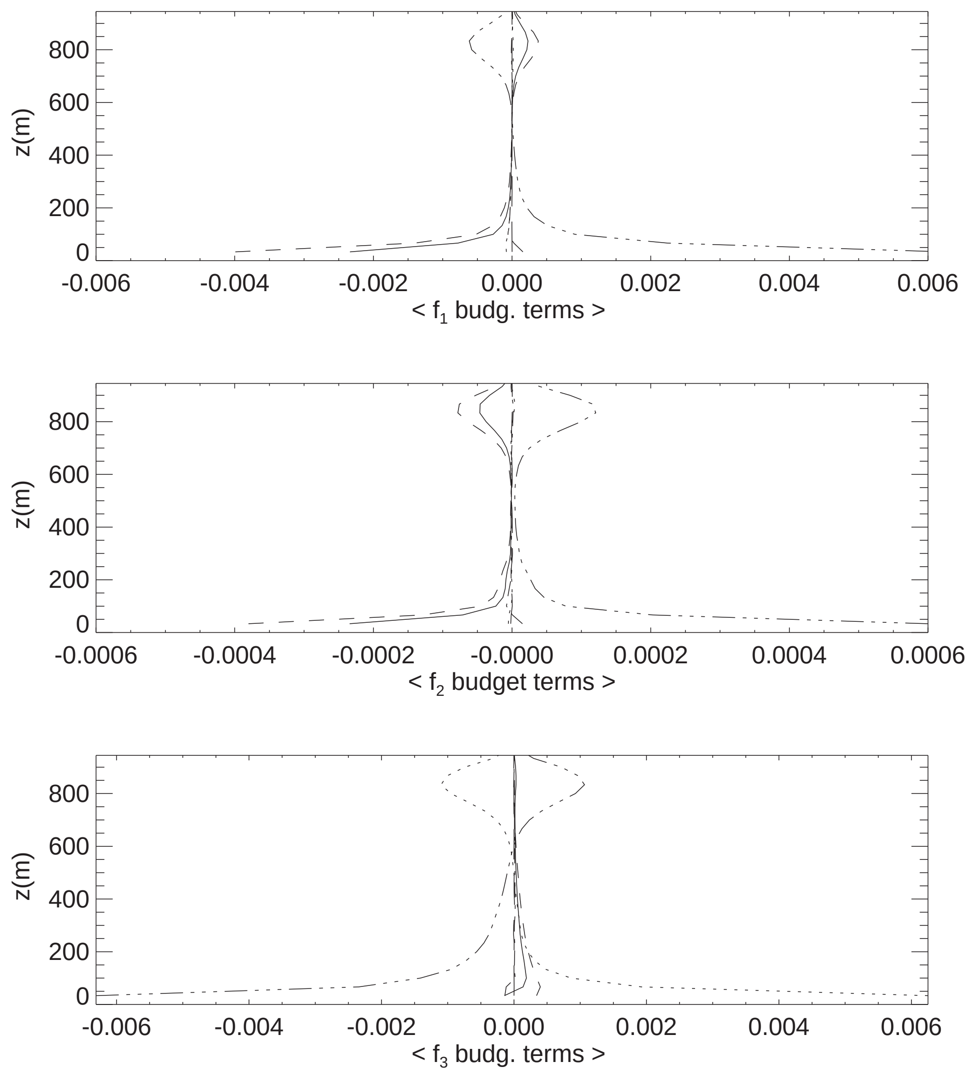

Figure 2.5. Plane-averaged terms in the f_i budgets plotted versus height. The inversion height is 787.5m. The units on all the budget terms is mKs^{-2}. Plot legend : (—) Anisotropic gradient-production, $(\cdots)$ Isotropic gradient-production, (– –) Flux tilting, (– ·) Advection, (– · · · –) Modeled slow pressure strain-rate covariance, (— —) Time tendency

2.4.1.1 f_1 and f_2 budgets

From Fig. (2.6), the dominant terms in the f_1 budget are flux-tilting, anisotropic gradient-production and modeled slow pressure strain-rate covariance. Using HATS data, Sullivan (2010) has studied the partitioning of SFS production in the scalar

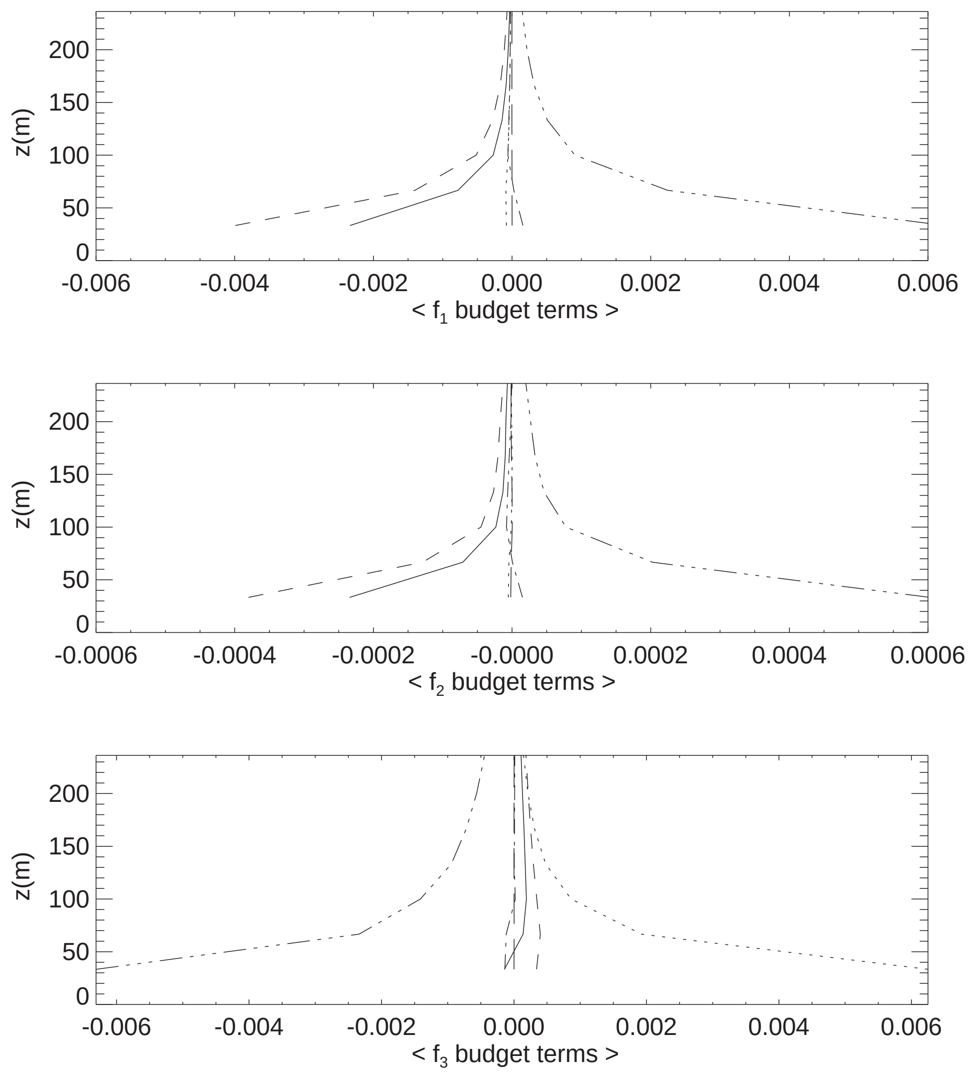

Figure 2.6. Plane-averaged terms in the f_i budgets for $0 < z < 0.3z_i$. The units on all the budget terms is mKs^{-2}. Plot legend : (—) Anisotropic gradient-production, $(\cdots)$ Isotropic gradient-production, (– –) Flux tilting, $(- \cdot)$ Advection, $(- \cdots -)$ Modeled slow pressure strain-rate covariance, (— —) Time tendency

flux budgets into its isotropic and anisotropic components. He found anisotropic production to dominate isotropic production in the f_1 budget and the reverse to hold true of the f_3 budget. Thus, Fig. (2.6) is consistent with his findings but also highlights the importance of the tilting term. The mean flux-tilting term in the f_1 budget, given by $\langle -f_3 \left(\partial \bar{u}_1 / \partial x_3 \right) \rangle$, represents the generation of f_1 by the tilting of f_3 into the 1-direction due to the presence of vertical shear. As the near-wall region in the presence of a mean wind is shear-dominated, the tilting term is most effective there and gradually decreases in magnitude with height in the region below the inversion. Near the inversion, the presence of wind shear causes the flux-tilting term to increase although to a lesser degree than near the surface as the magnitude of f_3 is considerably higher near the surface than at the inversion.

The gradient-production term can be split into: (i) anisotropic gradient production, $\left\langle -\tau^d_{1j}\left(\partial\bar{\theta}/\partial x_j\right)\right\rangle$; and (ii) isotropic gradient production, $\left\langle -(2/3)e\left(\partial\bar{\theta}/\partial x_1\right)\right\rangle$. The anisotropic gradient-production term involves gradients of $\bar{\theta}$ in all three directions while its isotropic counterpart depends solely on the gradient in the 1-direction. In our simulations, the mean temperature gradients in the horizontal directions are insignificant compared to those in the vertical. As a result, the isotropic gradient-production term is ineffective in generating horizontal SFS fluxes. The anisotropic gradient-production term, on the other hand, has significant contributions from $\left\langle -\tau^d_{13}\left(\partial\bar{\theta}/\partial x_3\right)\right\rangle$. Consequently, it is maximum near the surface and decreases monotonically with height in the region below the inversion. As we approach the inversion, the vertical gradients of $\bar{\theta}$ become significant causing the anisotropic gradient-production to increase in magnitude.

The flux tilting and anisotropic gradient-production terms are balanced by modeled slow pressure strain-rate covariance. The horizontal advection terms, $\partial\left\langle f_1\bar{u}_1\right\rangle/\partial x_1$ and $\partial\left\langle f_2\bar{u}_1\right\rangle/\partial x_2$, are zero due to horizontal homogeneity while the vertical advection term is negligible compared to the other terms in the budget.

The f_2 budget over most of the ABL is qualitatively similar to the f_1 budget except near the inversion. The magnitudes of the various terms in the budget, however, are much smaller as $|\partial\bar{u}_2/\partial x_3| \ll |\partial\bar{u}_1/\partial x_3|$ and $|\tau^d_{23}| \ll |\tau^d_{13}|$, on average. Near the inversion, the tilting and anisotropic gradient-production terms in the f_2 budget have signs opposite to those in the f_1 budget. The difference in the sign of the tilting terms can be explained by observing that $\partial\left\langle\bar{u}_1\right\rangle/\partial z > 0$ and $\partial\left\langle\bar{u}_2\right\rangle/\partial z < 0$, near the inversion.

In Fig. (2.7) we plot the horizontal heat fluxes (resolved and SFS) nondimensionalized with the surface heat flux, Q_0, obtained using two SFS models: (i) the modeled SFS conservation equations; and (ii) an eddy-diffusivity closure, wherein $\tau^d_{ij} = -2\,K_m\overline{S}_{ij}$ and $f_i = -K_h\left(\partial\bar{\theta}/\partial x_i\right)$. We defined the eddy-diffusivity for mo-

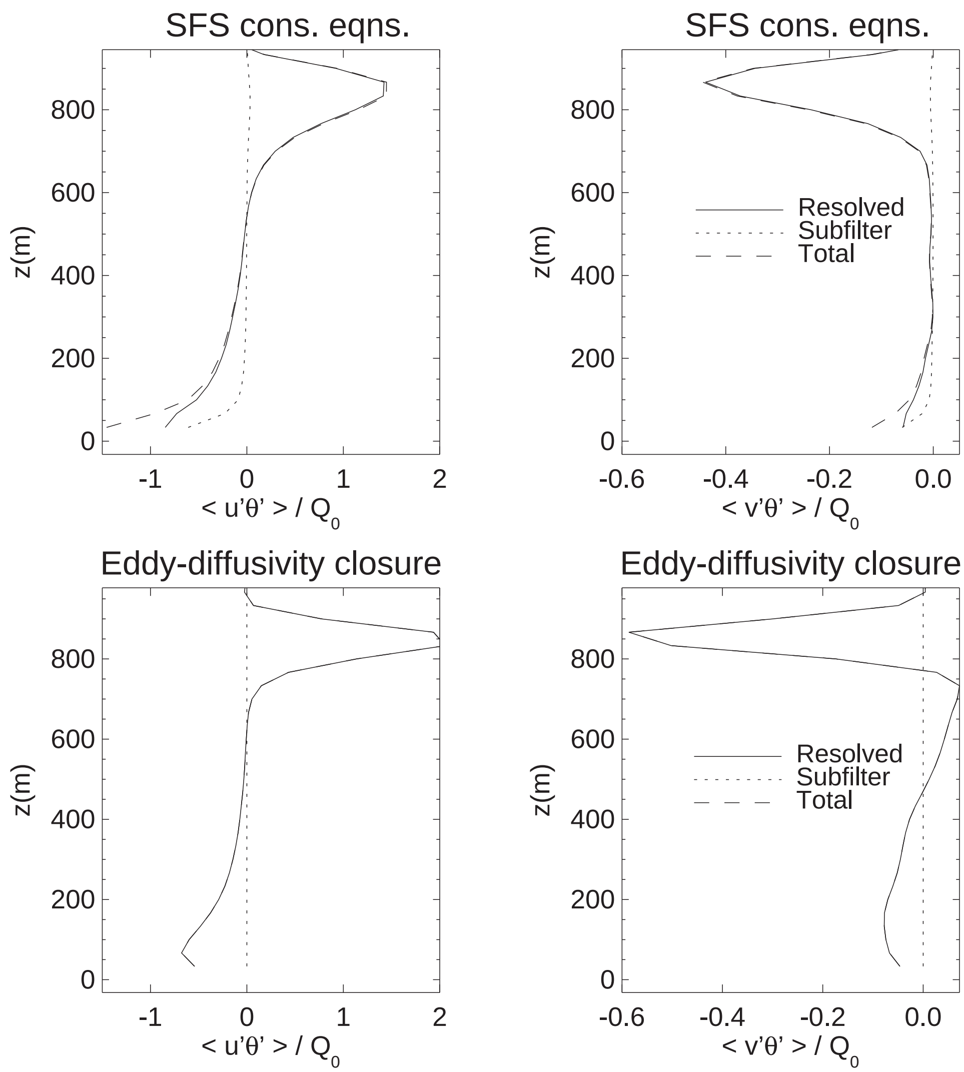

Figure 2.7. Plot showing predicted nondimensional horizontal heat fluxes (resolved and SFS) as functions of height. Top panel: from modeled SFS conservation equations, bottom panel: from eddy-diffusivity closure.

mentum, K_m, earlier in Sec. (2.1.4). The eddy-diffusivity for heat, K_h, is given by $K_h = [1 + 2\, l_{\rm SFS}/\Delta]\, K_m$ (Moeng, 1984), where $l_{\rm SFS}$ is the length scale for the SFS eddies (see Sec. (2.1.2.4)).

The modeled SFS conservation equations (top panel) predict significant SFS horizontal fluxes near the surface due to flux tilting and anisotropic gradient-production. The eddy-diffusivity closure (bottom panel) is unable to produce any horizontal SFS flux due to its dependence solely on isotropic gradient-production.

These findings are in agreement with those of Hatlee and Wyngaard (2007) who found that eddy-diffusivity closures underpredict the SFS horizontal fluxes severely.

2.4.1.2 f_3 budget

The f_3 budget is dominated by isotropic gradient-production and modeled slow pressure-strain covariance. The dominance of isotropic over anisotropic production is consistent with the studies by Sullivan (2010). Near the surface, positive buoyancy causes the nonlinear stretching term, $\langle f_3 \left(\partial \bar{u}_3/\partial x_3\right)\rangle$, to attain positive values, but it plays a small role in the overall budget. Anisotropic gradient-production, given by $\left\langle\left(-\tau_{33}^d \partial\bar{\theta}/\partial x_3\right)\right\rangle$, is insignificant compared to isotropic gradient-production, $\left\langle\left(-(2/3)\ e\ \partial\bar{\theta}/\partial x_3\right)\right\rangle$ as $|\tau_{33}^d| \ll |(2/3)e|$. The dominance of isotropic production in the modeled f_3 budget suggests that f_3 is more suitable to eddy-diffusivity closures than f_1 or f_2.

2.4.1.3 Role of SFS advection in the SFS flux budgets

From the previous section, the mean advection terms play an insignificant role in the modeled SFS flux budgets. This does not imply, however, that the advection terms are insignificant in the instantaneous budgets as well.

Deardorff (1973) found the advective term in the SFS rate equations gave rise to large truncation errors that led to numerical instabilities. Hatlee and Wyngaard (2007) found that the SFS flux equations without the advection terms behave incorrectly when the coordinate system translates at a constant velocity, thereby violating Galilean invariance. We found that excluding the SFS advection terms in the flux conservation equations has no effect on the mean values of the SFS fluxes themselves. It does affect the resolved-scale potential temperature spectrum significantly. In Fig. (2.8a)-(2.8b) we show the resolved-scale potential temperature spectrum at mid-ABL with and without the advection terms in the SFS flux conservation equations. We retain the advection terms in the SFS stress equations. Omitting the advection terms causes the potential temperature spectrum to exhibit a spurious build up of energy at the smaller scales and deviate considerably from a $-(5/3)$ slope (in log-log axes) in the inertial range. Figure (2.8) shows that SFS advection, while negligible in the mean, plays a crucial role in the conservation

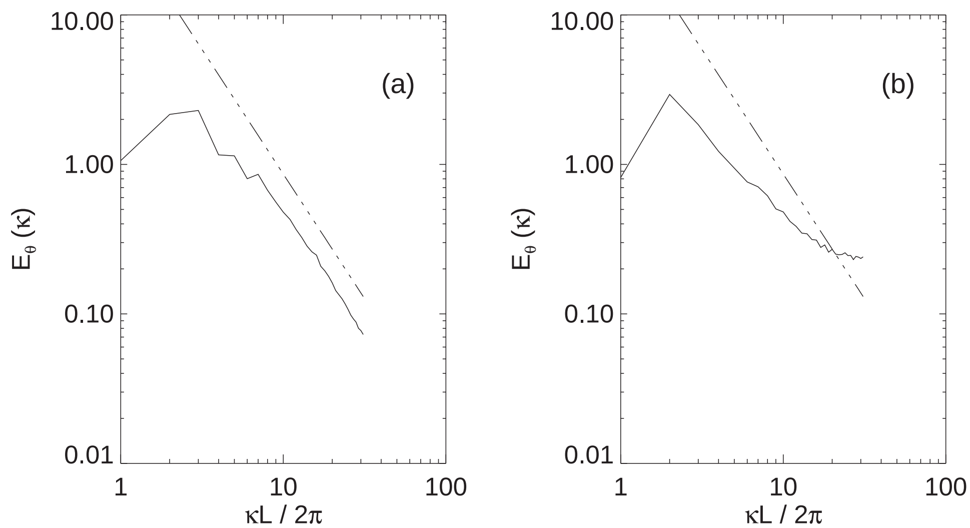

Figure 2.8. Resolved-scale potential temperature spectra at mid-ABL for $(c_\tau, c_\theta) = (0.10, 0.21)$: (a) with advection of SFS fluxes; and (b) without advection of SFS fluxes. The straight line has a slope of $-5/3$.

equations, as without them the SFS model is unable to extract energy adequately from the resolved scales leading to unphysical potential temperature spectra.

2.4.1.4 Summary

We summarize below the main inferences from our discussion of the modeled SFS flux budgets:

- Eddy-diffusivity closures are based on the premise that the SFS flux budgets are in equilibrium between isotropic gradient-production and modeled slow pressure-strain-rate covariance. Our LES results suggest – in agreement with observations (Hatlee and Wyngaard, 2007) – that this assumption is justifiable for f_3 but not for the horizontal SFS fluxes, f_1 and f_2.

- Flux-tilting and anisotropic gradient-production are the two dominant sources of production in the f_1 and f_2 budgets. Flux-tilting rotates vertical SFS fluxes into horizontal directions in regions of high shear. Anisotropic gradient-production produces horizontal scalar SFS fluxes even in the absence of horizontal scalar gradients. The absence of flux tilting and anisotropic gradient-production in eddy-diffusivity closures causes them to underestimate the values of horizontal SFS fluxes (Hatlee and Wyngaard, 2007).

- The advection terms in the SFS flux conservation equations are negligible in the mean but are crucial in enabling the SFS model to extract energy from the resolved scales. Excluding the advection terms yields incorrect potential temperature spectra that lack an inertial range and exhibit spurious build up of energy at the smaller scales.

2.4.2 SFS stress budgets

Using HATS data, Sullivan (2010) found that anisotropic production dominates isotropic production in the $\tau^d_{\alpha\alpha}$ budgets and the reverse to be true of the τ^d_{13} budget. We plot the budgets of the six τ^d_{ij} components in Fig. (2.9). To understand better the budgets in the lower part of the ABL, we plot the SFS stress budgets for $0 < z < 0.3z_i$ in Fig. (2.10).

2.4.2.1 $\tau^d_{\alpha\alpha}$ budgets

(i) $\boldsymbol{\tau^{d}_{11}}$: Fig. (2.10) shows anisotropic production to be positive in the τ^d_{11} budget. This is consistent with strong anisotropy in the shear-dominated surface layer which yields $\langle\tau^d_{11}\rangle > 0$ and $(\langle\tau^d_{22}\rangle, \langle\tau^d_{33}\rangle) < 0$ (Sullivan et al., 2003). Anisotropic production is much larger than isotropic production, which is in agreement with the findings by Sullivan (2010). The buoyant contribution, $\langle -\left(2g/3\Theta_0\right) f_3\rangle$, is negative as $f_3 > 0$, on average. The modeled slow pressure strain-rate term drives τ^d_{ij} towards zero, i.e., towards isotropy. It is negative in sign as it is modeled as being proportional to $\langle -\tau^d_{11}\rangle$. The mean horizontal advection terms, $\partial\left\langle \bar{u}_i \tau^d_{\alpha\alpha}\right\rangle/\partial x_i$ where $i = (1, 2)$, are zero due to homogeneity in the plane while mean vertical advection is negligible.

(ii) $\boldsymbol{\tau^{d}_{22}}$: By definition, the sum of the deviatoric SFS stresses, τ^d_{ii} (summation implied), is identically zero. Hence, the anisotropic production terms in their budgets must also sum to zero. The same is true of other production and destruction terms as well. Consequently, the sign of anisotropic production in the τ^d_{22} budget is opposite that in the τ^d_{11} budget. As in the τ^d_{11} budget, anisotropic production is considerably larger in magnitude than the isotropic production term. The buoyancy term is negative and the isotropic production term positive for reasons similar to those applicable to the τ_{11}^d budget. The modeled slow pressure strain-rate term is positive as $\langle \tau_{22}^d \rangle < 0$. The mean advection terms are negligible.

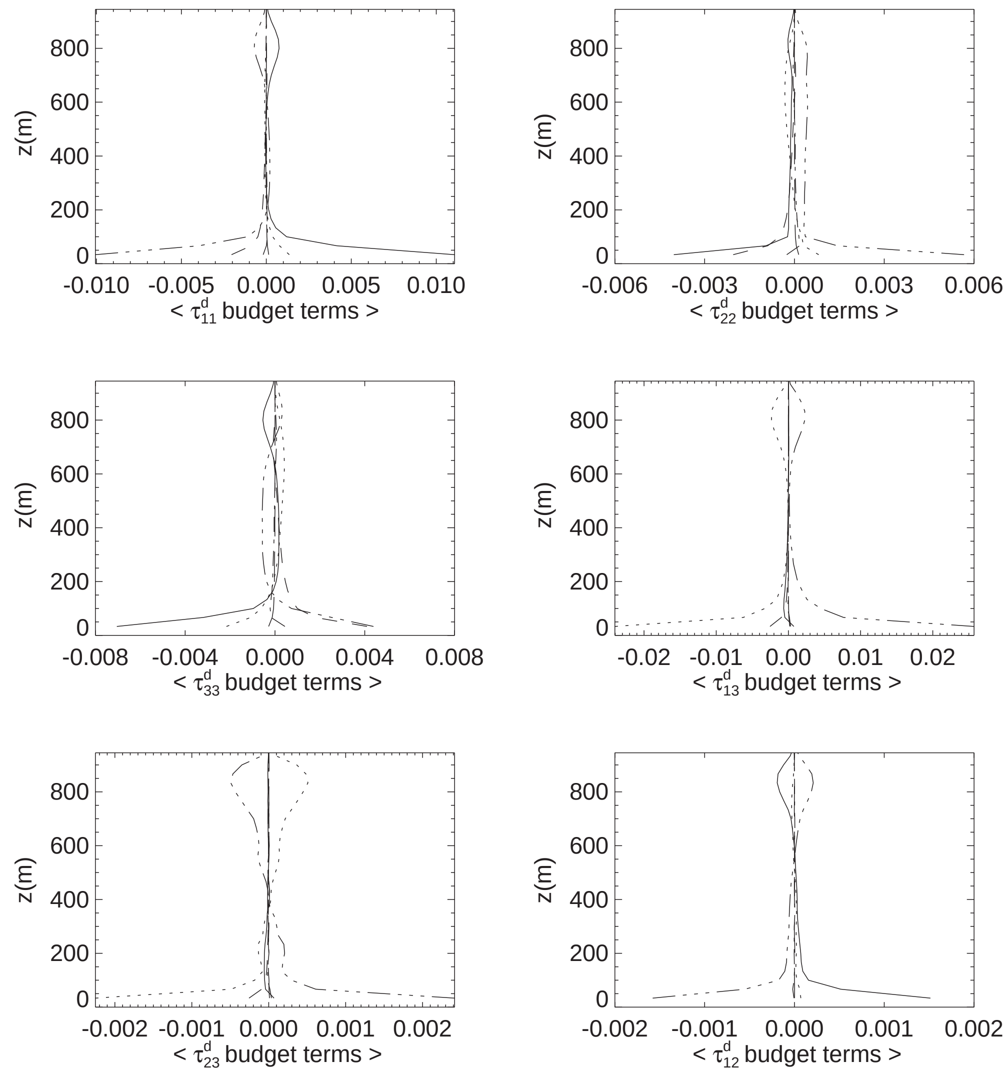

Figure 2.9. Plane-averaged values of terms in the SFS stress budgets plotted versus height. The units on all the budget terms are m^2s^{-3}. The inversion height is 787.5m. Plot legend: (—) Anisotropic production, ($\cdots$) Isotropic production, (– –) Buoyant production, (– ·) Advection, (– $\cdots$ –) Modeled slow pressure strain-rate covariance, (——) Time tendency

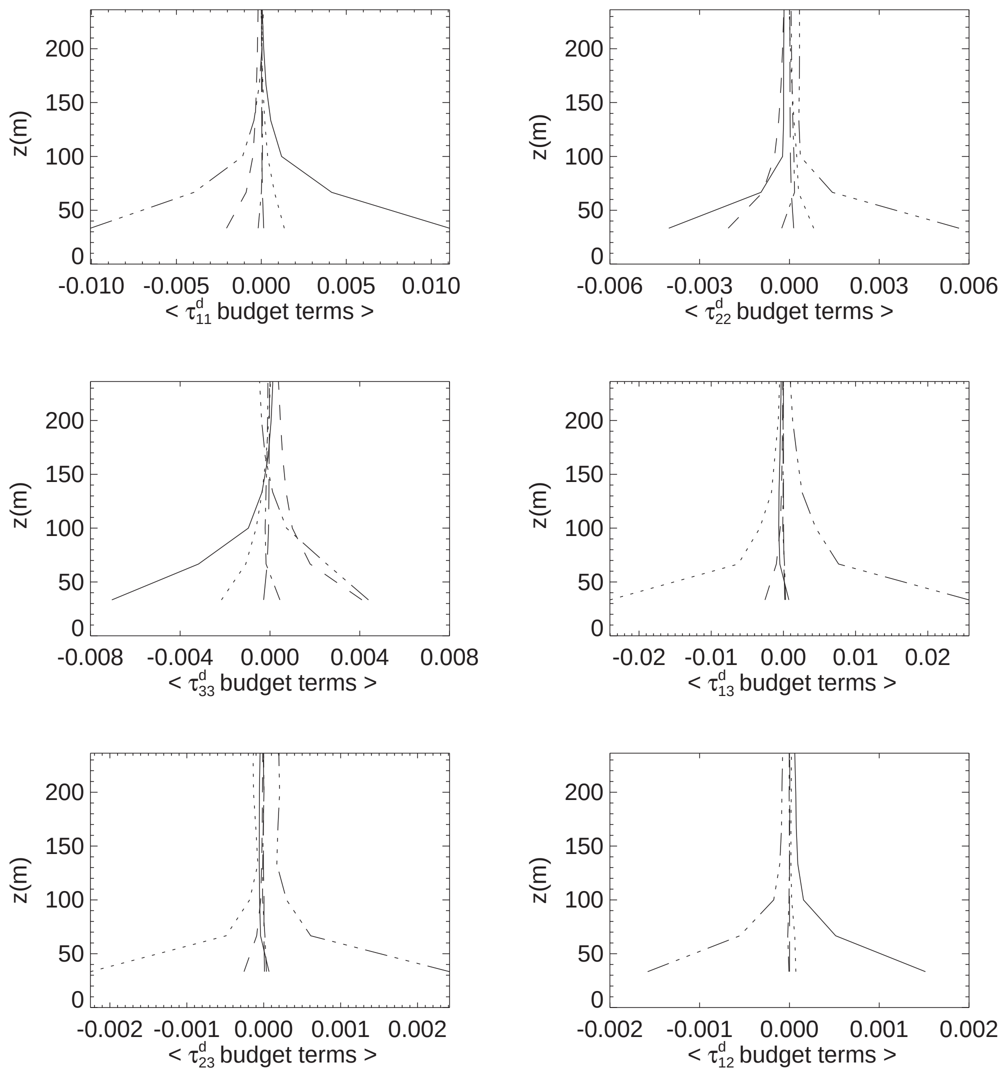

Figure 2.10. Plane-averaged values of terms in the SFS stress budgets for $0 < z < 0.3z_i$. The units on all the budget terms are $\mathrm{m^2 s^{-3}}$. The inversion is 787.5m. Plot legend: (—) Anisotropic production, ($\cdots$) Isotropic production, (– –) Buoyant production, (–$\cdot$) Advection, (– $\cdots$ –) Modeled slow pressure-strain-rate covariance, (— —) Time tendency

(iii) $\tau^{\mathbf{d}}_{\mathbf{33}}$: The buoyancy term, $\langle (4g/3\Theta_0)\, f_3 \rangle$, appears as a production term in the budget. Isotropic production, $\left\langle (-2/3)\, e\bar{S}_{33} \right\rangle$, is negative as $\bar{S}_{33} > 0$, on average, due to positive buoyancy. Anisotropic production is negative owing to its traceless nature. The modeled slow pressure-strain-rate term is positive as

$\left\langle \tau_{33}^d \right\rangle < 0$. Once again, the mean advection terms are insignificant.

2.4.2.2 $\tau_{\alpha\beta}^d$ budgets

Figure (2.10) shows that the τ_{13}^d and τ_{23}^d budgets are in balance mainly between isotropic production and modeled slow pressure-strain-rate covariance. The dominance of isotropic over anisotropic production is consistent with studies by Sullivan (2010). Buoyant effects are unimportant in Fig. (2.10) but might become significant at coarser resolutions (Wyngaard, 2004). Thus, for resolutions comparable to that in Fig. (2.10), eddy-diffusivity closures can be expected to fare reasonably for the components τ_{13}^d and τ_{23}^d.

The τ_{12}^d budget is in equilibrium primarily between anisotropic production and modeled slow pressure-strain-rate covariance. Both the resolved and SFS components of the horizontal shear stress (1-2 plane) are much smaller in magnitude than those of the other stresses.

2.4.2.3 Role of advection in the SFS stress budgets

From our discussion of the SFS flux budgets, the SFS advection terms are necessary to yield realistic potential temperature spectra that do not exhibit a large build up of variance at the smaller scales. We find the advection terms play a similar role in the SFS stress conservation equations. In Fig. (2.11a)-(2.11b) we plot the horizontal kinetic energy spectra at mid-ABL with and without SFS advection, respectively. From Fig. (2.11b), the lack of SFS advection results in a large build up of energy at the smallest resolved scales and the absence of a well-defined inertial range. The spectra of resolved vertical velocity, shown in Fig. (2.12), also displays a build up of energy at the smallest resolved scales when there is no SFS advection, although there is a discernible inertial-range unlike Fig. (2.11b). Hence, we conclude that the SFS advection terms are essential to ensure that the SFS model extracts energy from the resolved scales in a physically meaningful manner.

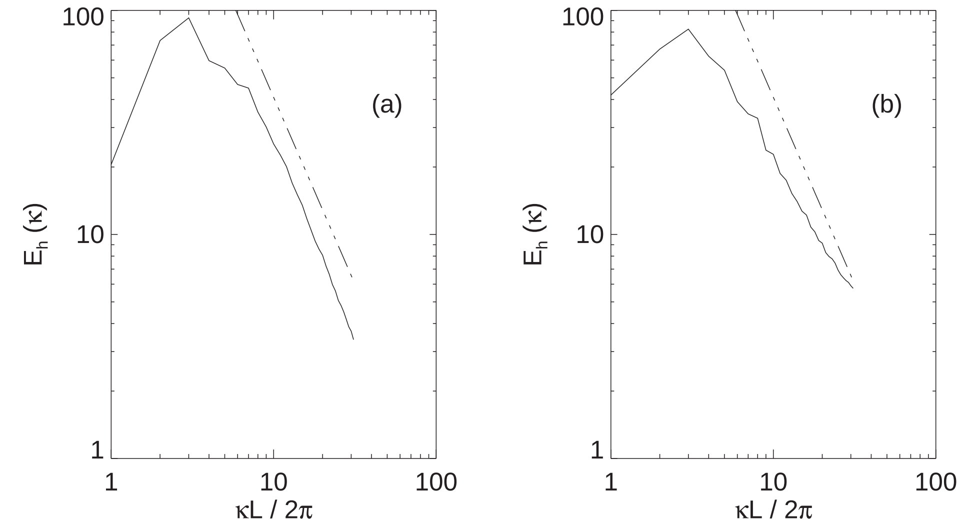

Figure 2.11. Resolved-scale horizontal kinetic energy spectra at mid-ABL for $(c_\tau, c_\theta) = (0.10, 0.21)$: (a) with SFS advection; (b) without SFS advection. The straight line has a slope of $-5/3$.

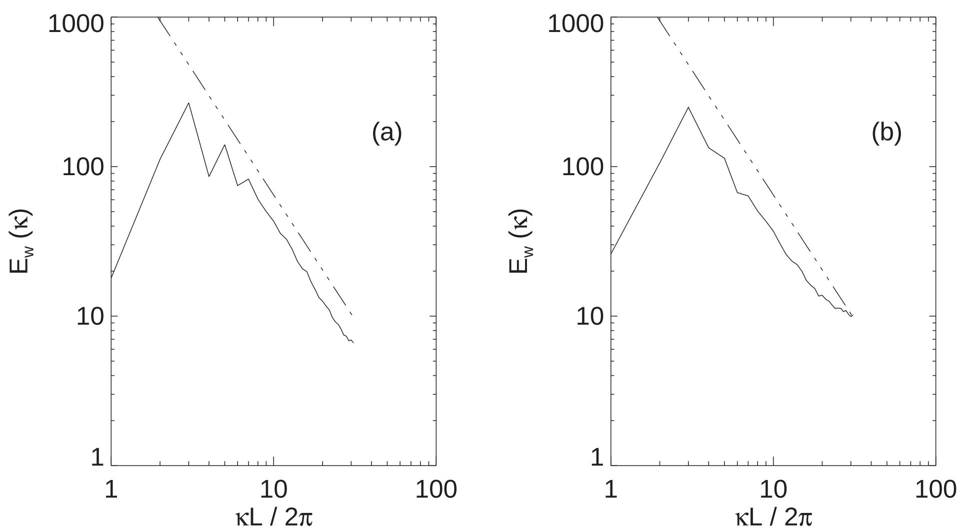

Figure 2.12. Resolved-scale vertical kinetic energy spectra for $(c_\tau, c_\theta) = (0.10, 0.21)$: (a) with SFS advection; (b) without SFS advection. The straight line has a slope of $-5/3$.

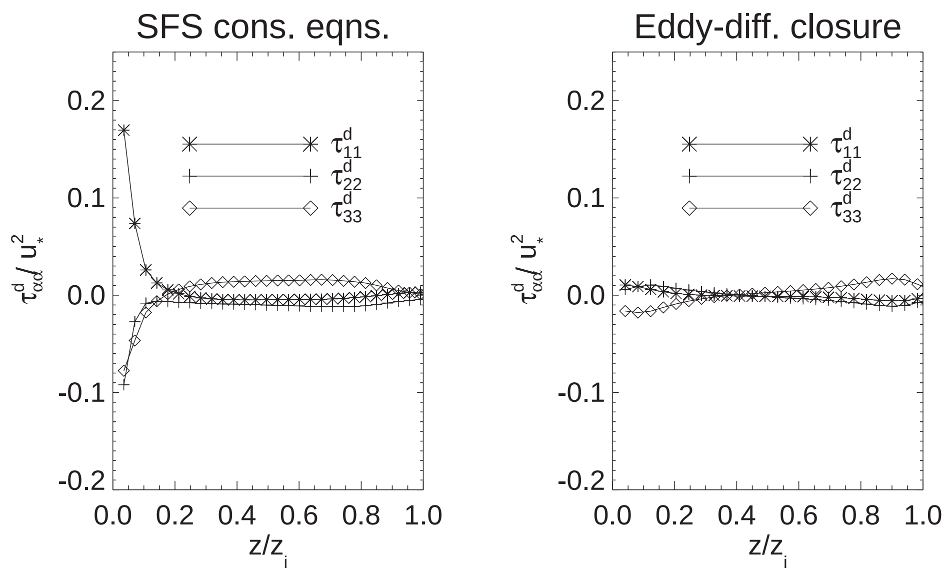

Figure 2.13. Plot showing $\tau^d_{\alpha\alpha}/u^2_*$ versus z/z_i. Left panel: SFS conservation equations, right panel: eddy-diffusivity closure.

2.4.2.4 Effect of anisotropic production on predictions of $\tau^d_{\alpha\alpha}$

In Fig. (2.13) we plot the nondimensional deviatoric stresses, $\tau^d_{\alpha\alpha}/u^2_*$, obtained using two SFS models: (i) the SFS conservation equations; and (ii) an eddy-diffusivity closure which models the SFS stresses as $\tau^d_{ij} = -K_m\overline{D}_{ij}$, where $K_m = c_k\Delta\sqrt{e}$ is the eddy-diffusivity and $\overline{D}_{ij} = 2\ \overline{S}_{ij}$ is the resolved-scale deformation rate. Following Moeng and Wyngaard (1988), we set $c_k = 0.1$. We first discuss the lower part of the ABL corresponding to $0 < z/z_i < 0.2$.

In the convective ABL with a mean wind, both shear and buoyancy are sources of anisotropy at the energy-containing scales (Kaimal et al., 1972). We expect isotropy at scales much smaller than the production scales (Kaimal et al., 1972; Lumley and Panofsky, 1964). Closer the filter cutoff is to the energy-containing range, the more we expect the anisotropy of the production scales to spill over into the subfilter scales. Near the surface, the energy-containing scales vary as z and hence, the subfilter scales are forced to be anisotropic regardless of the grid resolution. Thus, a mean wind in the 1-direction induces strong anisotropy near the surface such that $\langle\tau^d_{11}\rangle > 0$. This shear-induced anisotropy is counteracted in the convective ABL by buoyancy (Katul et al., 1995), which we recall tends

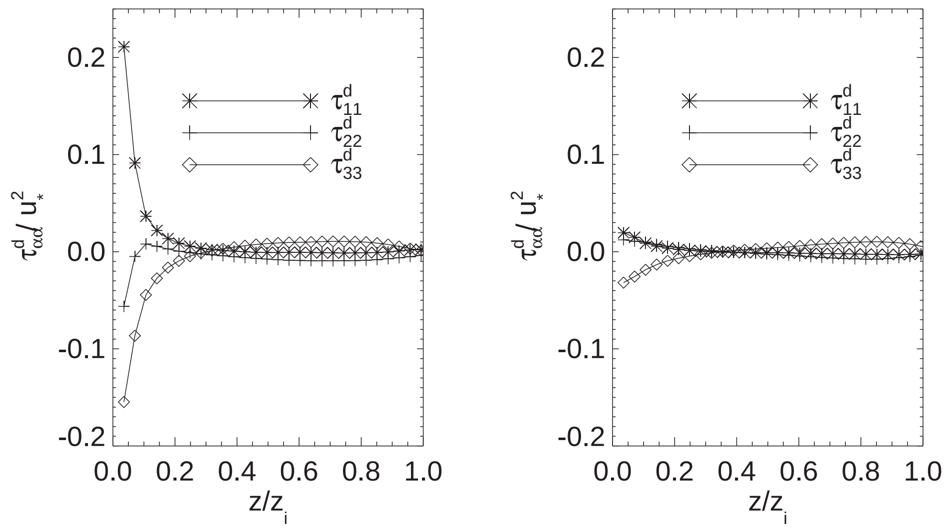

Figure 2.14. Plot showing $\tau^d_{\alpha\alpha}/u_*^2$ versus z/z_i. Left panel: SFS conservation equations without SFS buoyancy production , right panel: SFS conservation equations without SFS anisotropic or buoyant production.

to increase τ^d_{33} and decrease τ^d_{11}. The near-wall region in a moderately convective ABL is shear-dominated and hence, the net effect of shear and buoyancy is to yield $\langle\tau^d_{11}\rangle > 0$ and $\langle\tau^d_{33}\rangle < 0$ (Chen and Tong, 2006).

Figure (2.13) shows that the SFS conservation equations exhibit strong SFS anisotropy near the wall with $\langle\tau^d_{11}\rangle > 0$. The other two normal components are such that $\langle\tau^d_{22}\rangle < 0$ and $\langle\tau^d_{33}\rangle < 0$, due to the traceless nature of $\tau^d_{\alpha\alpha}$. Compared to the SFS conservation equations, the eddy-diffusivity closure yields severely reduced levels of SFS anisotropy near the surface. To examine the source of anisotropy near the surface in the case of the SFS conservation equations, we plot in Fig. (2.14) $\tau^d_{\alpha\alpha}/u_*^2$ obtained: (i) without the buoyancy term (left panel); and (ii) without the anisotropic production or buoyancy terms (right panel). Wyngaard (2004) used scaling arguments to show that the effect of buoyancy on the SFS budgets depends on the grid resolution, becoming more important at coarser resolutions. Comparing the left panel of Fig. (2.14) to that of Fig. (2.13), at the current resolution, buoyancy appears to influence the values of $\langle\tau^d_{\alpha\alpha}\rangle$ only weakly in the mixed layer, where τ^d_{33} attains slightly higher values with the inclusion of the SFS buoyant term than without. Near the surface, the absence of SFS buoyant production results in slightly increased levels of SFS anisotropy due to the lack of competition between shear and buoyancy in the conservation equations. The effects of anisotropic production are more apparent from a comparison of the right panel of Fig. (2.14) and the left panel of Fig. (2.13). Omitting the anisotropic production term causes the SFS conservation equations to predict negligible levels of anisotropy near the surface. Hence, the anisotropic production term is essential for the conservation equations to yield realistic predictions of $\tau^d_{\alpha\alpha}$ in the near-wall region. The eddy-diffusivity closure doesn't account for anisotropic production and subsequently, yields very low SFS anisotropy.

The SFS conservation equations and the eddy-diffusivity closure also differ in their $\tau^d_{\alpha\alpha}$ predictions over the rest of the ABL although to a lesser extent than near the surface. Figure (2.13) shows that the conservation-equation-based closure yields $\langle\tau^d_{33}\rangle > 0$ and $(\langle\tau_{11}\rangle, \langle\tau_{22}\rangle) < 0$ over a wider range of z/z_i in the mixed layer than does the eddy-diffusivity closure. The anisotropy of subfilter scales in the mixed layer is due to buoyancy, as shear-induced anisotropy is negligible in the mixed layer, where the mean gradients are weak. But the direct effects of buoyancy on the SFS budgets are resolution-dependent (Wyngaard, 2004). In Fig. (2.15), we plot the scaled deviatoric stresses, $\tau^d_{\alpha\alpha}/u_*^2$, obtained using the SFS conservation equations but with a finer grid containing 192x192x144 points. A similar plot corresponding to the eddy-diffusivity closure is shown in Fig. (2.16). The physical conditions for the fine-resolution runs are identical to those for the coarser runs.

The SFS conservation equations continue to exhibit significant SFS anisotropy near the surface in the high-resolution run, due to reasons outlined earlier. For $z/z_i > 0.15$, however, $\tau^d_{\alpha\alpha}$ is negligible indicating isotropy at the subfilter scales. This suggests that the anisotropy observed at mid-ABL levels in Fig. (2.13) (left panel), while due to buoyancy, depends also on the coarseness of the grid. In the mixed layer, the energy-containing eddies scale on z_i, the inversion height. Thus, a sufficiently fine grid ensures that the filter cutoff is far removed from the energy-containing scales, yielding isotropy at the subfilter scales.

At the higher resolution, the eddy-diffusivity closure yields near-zero levels of SFS anisotropy (Fig. (2.16)) throughout the ABL, which can be attributed to the absence of the anisotropic production term in such closures.

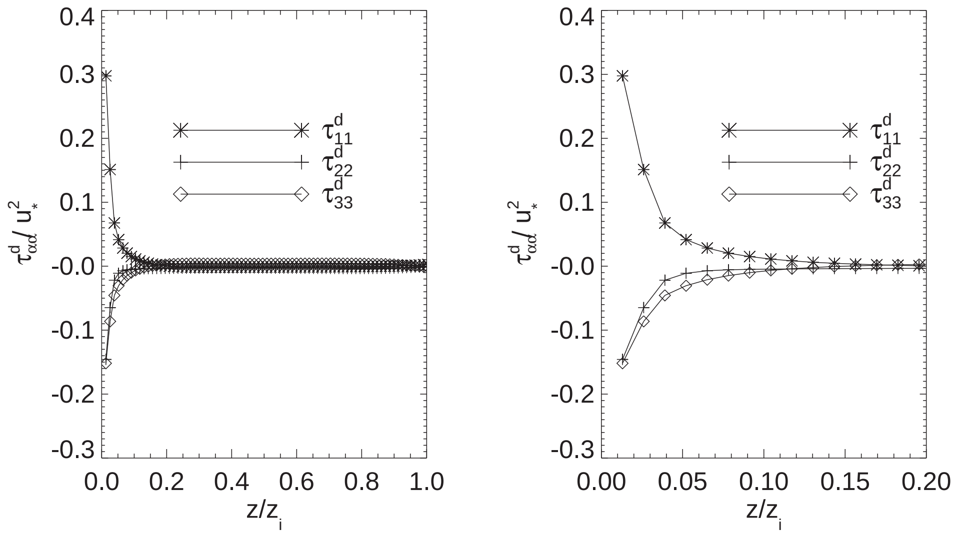

Figure 2.15. $\tau^d_{\alpha\alpha}/u_*^2$ versus z/z_i, obtained using SFS conservation equations in high-resolution LES (192^2x144 grid) . Left panel: $0 < z/z_i < 1.0$, right panel: $0 < z/z_i < 0.2$

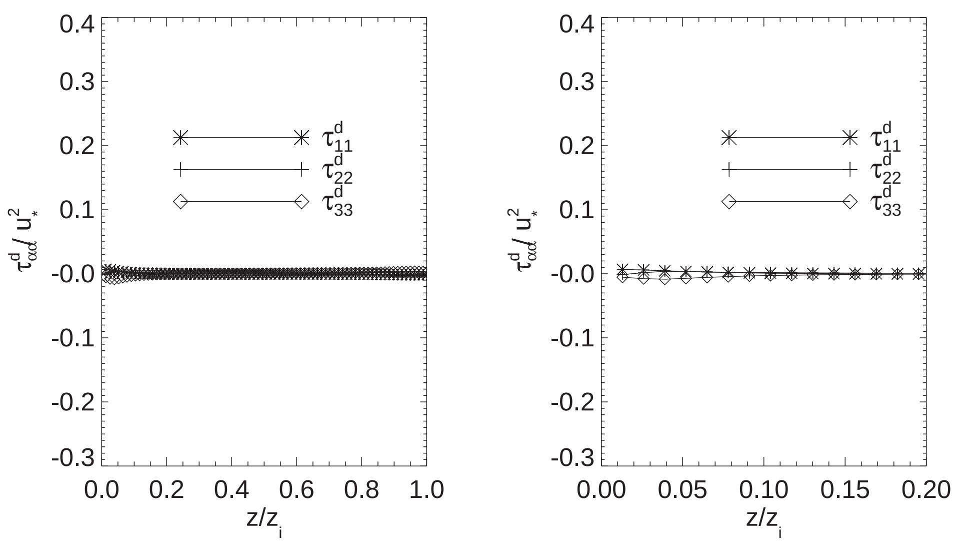

Figure 2.16. $\tau^d_{\alpha\alpha}/u_*^2$ versus z/z_i, obtained using an eddy-diffusivity closure in high-resolution LES (192^2x144 grid) . Left panel: $0 < z/z_i < 1.0$, right panel: $0 < z/z_i < 0.2$

2.4.2.5 Summary

We summarize below our discussion of the SFS stress budgets.

- Eddy-diffusivity closures assume that the budgets of all the SFS stress components are in equilibrium between isotropic production and modeled slow pressure strain-rate covariance. Our LES result suggest that this assumption is too simplistic for the $\tau^d_{\alpha\alpha}$ budgets where anisotropic production dominates isotropic production. It is justifiable for the τ^d_{13} and τ^d_{23} budgets, however, where isotropic production is considerably more significant than anisotropic production.

- The presence of anisotropic production in the SFS budgets is essential for realistic predictions of $\tau^d_{\alpha\alpha}$ near the wall.

- The SFS advection terms are negligible in the mean but are necessary in the instantaneous rate equations for the SFS model to extract energy from the resolved scales in a physically realistic manner. Omitting the advection terms leads to a spurious build up of resolved-scale turbulent kinetic energy at the smaller scales.

2.5 Comparison of statistics from high-resolution LES with HATS data

In the previous sections, we used coarse-mesh LES and qualitative arguments to gain insight the relative contributions of various terms in the modeled SFS budgets. In this section, we further test the performance of the SFS conservation equations by comparing surface-layer statistics obtained using high-resolution LES with those obtained from the HATS experimental campaign (Sullivan et al., 2003).

2.5.1 Description of the HATS study

The HATS study used the array filtering technique which was developed first by Tong et al. (1998) and has since been adopted in numerous experimental studies (Horst et al., 2003; Kleissl et al., 2003; Porté-Agel et al., 2001). A schematic of the experimental configuration is shown in Fig. (2.17). The array comprises two rows of sonic anemometers facing the mean wind, five in the top row and nine in the bottom row. Following Sullivan et al. (2003) we filter the fields in streamwise

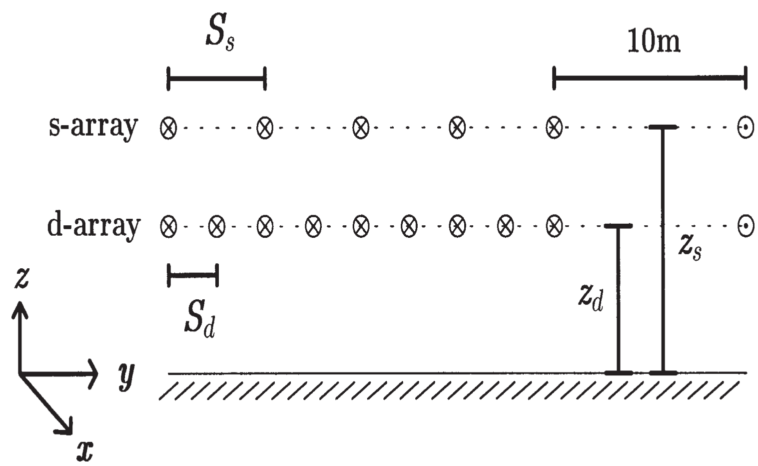

Figure 2.17. Schematic showing the array configuration of sonic anemometers used in the HATS experiment (figure reproduced from (Horst et al., 2003)). The variables S_s and S_d denote the spacings between the sonics in the top and the bottom arrays. The distances of the top and the bottom arrays from the ground are denoted by z_s and z_d, respectively.

and crosswise directions using a Gaussian and top-hat filter, respectively. As the crosswise filter can consist of a maximum of five or nine sonics, it is required to be compact in physical space. This constraint makes the top-hat filter a natural choice for the crosswise filter. In the streamwise direction, filtering is done using Taylor's "frozen field" hypothesis wherein the measured time series is used as a surrogate for a spatial record which is then filtered spatially. Tong et al. (1998) analyzed carefully the various potential sources of error in applying the Taylor approximation and concluded that they were sufficiently small to permit its use. The high frequency of the sonics (20 Hz) implies a much finer spatial resolution in the streamwise direction – from Taylor's hypothesis – than in the crosswise direction, which permits the use of a Gaussian filter in the streamwise direction. The Gaussian filter, in contrast to the top-hat filter, decays slowly in physical space but is compact in spectral space. The studies by Chen and Tong (2006) and Chen et al. (2009) found that the differences between the statistics obtained using a top-hat and a Gaussian filter in the streamwise direction are much less than those between the true statistics obtained from the field data and the statistics corresponding to different SFS models. Hence, for the purposes of testing SFS models, the use of either the top-hat or the Gaussian filter in the streamwise direction is justifiable. Finally, there is the issue of comparing statistics obtained from fields filtered in two dimensions to those obtained from LES where the fields are filtered in all three directions. Tong et al. (1998) found that two-dimensional filtering in horizontal planes is a good approximation to filtering in three dimensions. Higgins et al. (2007) found that two-dimensional horizontal filtering is a reasonable surrogate for three-dimensional filtering under unstable conditions but recommended two-dimensional filtering in vertical planes parallel to the mean wind — when possible — under near-neutral and stable conditions. The HATS experimental setup, by design, does not permit vertical filtering of the fields. Thus, in our current study, we use two-dimensional filtering in horizontal planes to process the HATS data.

Sullivan et al. (2003) demonstrated that various nondimensional statistics exhibit good collapse across a broad range of stabilities and filter widths, when plotted against the nondimensional parameter, Δ_w/Δ, where Δ_w is the peak in the vertical velocity spectrum, and Δ is the filter width. The parameter Δ_w/Δ is a measure of how well the turbulence is resolved. High values of Δ_w/Δ imply a filter width much smaller than the energy-containing scales and, thereby, conditions of well-resolved turbulence. Low values of Δ_w/Δ correspond to conditions where the filter width is of the order the integral length scales, as is the case in the near-wall region, coarse LES, stably stratified layers, etc. Thus, the parameter Δ_w/Δ captures the effects of both stability and scale. Following Sullivan et al. (2003), in our comparison of the HATS data with LES results, we plot statistics against Δ_w/Δ. In particular, we are interested in the following statistics: mean SFS stresses, SFS variances, mean SFS fluxes, and important production terms in the SFS budgets. A drawback of using Δ_w/Δ is that it contains only surface-layer information (through Δ_w) and lacks "outer scale" information — such as the boundary layer height — which have been shown to influence the structure of horizontal motions near the surface (Kaimal and Finnigan, 1994; Khanna and Brasseur, 1997, 1998). The boundary layer height wasn't measured in the HATS experiments. In spite of the lack of outer scale information in the parameter Δ_w/Δ, the studies by Sullivan et al. (2003) show that it is quite effective in describing statistics consistently across a broad range of stabilities.

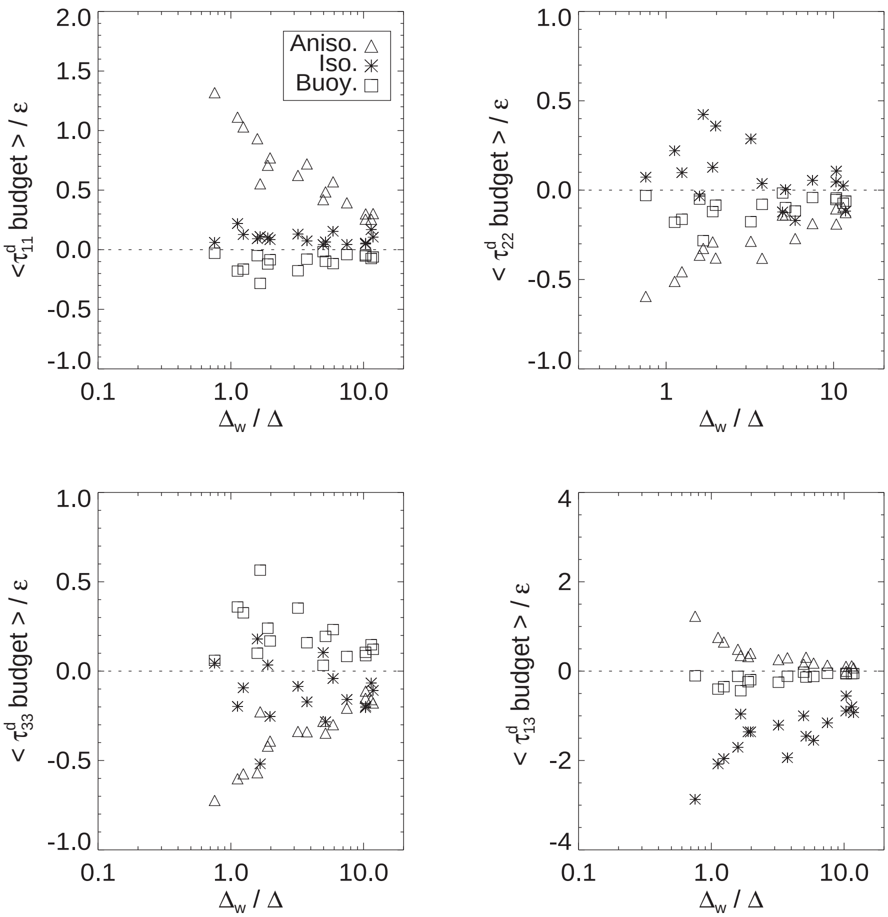

Figure 2.18. HATS data, unstable cases: The partitioning of SFS production into isotropic, anisotropic and buoyant components for the deviatoric stresses, $\tau^d_{\alpha\alpha}$, and τ^d_{13}, plotted against the nondimensional parameter Δ_w/Δ. The production terms have been scaled using $0.93\, e^{3/2}/\Delta$.

2.5.2 HATS: $\tau^d_{\alpha\alpha}$ and τ^d_{13} budgets

In Fig. (2.18), we show the scaled anisotropic, isotropic and buoyant production terms for the diagonal components, $\tau^d_{\alpha\alpha}$, and τ^d_{13}, plotted versus Δ_w/Δ. Figure (2.18) is similar to results obtained by Sullivan (2010) the only difference being that we have also included the buoyant terms. The production terms have been scaled with $\epsilon = 0.93\ e^{3/2}/\Delta$. Following Sullivan et al. (2003), we compute Δ_w using $\Delta_w = 2\pi\langle U\rangle\tau_p$, where $\langle U\rangle$ is the mean wind in the streamwise direction and τ_p is the Eulerian time scale obtained by assuming an exponential autocorrelation function for the vertical velocity, $R(t) = \exp(t/\tau_p)$.

At high values of Δ_w/Δ, the turbulence is well-resolved and the production terms in the SFS budgets are dormant. They start to become significant at lower values of Δ_w/Δ, where the subfilter scales account for a significant portion of the total stresses and fluxes. We now describe the important trends in Fig. (2.18).

2.5.2.1 $\tau^d_{\alpha\alpha}$ budgets

The magnitude of scaled anisotropic production in the $\tau^d_{\alpha\alpha}$ budgets increasingly dominates that of isotropic production as Δ_w/Δ decreases. This trend is most apparent in the τ^d_{11} budget where the scaled magnitude of isotropic production is much lower than that of anisotropic production across the entire range of Δ_w/Δ considered in our study. Isotropic production is more significant in the τ^d_{22} and τ^d_{33} budgets than in the τ^d_{11} budget, but fails to keep up with anisotropic production in magnitude at lower Δ_w/Δ. Anisotropic production is positive in the τ^d_{11} budget and negative in the $(\tau^d_{22}, \tau^d_{33})$ budgets due to its traceless nature. As expected, the trends exhibited by the scaled anisotropic and isotropic production are identical to those observed by Sullivan (2010).

The SFS buoyant terms appear as production terms in the τ^d_{33} budget and as destruction terms in the $(\tau^d_{11}, \tau^d_{22})$ budgets. Although they assume identical analytical forms in the $(\tau^d_{11}, \tau^d_{22})$ budgets, their effects are more pronounced in the τ^d_{22} budget than in the τ^d_{11} budget due to smaller magnitudes of the other production terms (anisotropic and isotropic) in the former. The trends in the variation of buoyant production with Δ_w/Δ from Fig. (2.18) are less clear when compared to that of anisotropic production. Based on scaling arguments put forth by Wyngaard (2004), the magnitude of buoyant production scaled with $\epsilon \sim (u(\Delta))^3/\Delta$ yields,

$$\frac{P^{\text{buoy}}_{ij}}{\epsilon} = \frac{g}{\Theta_0}\frac{\theta l}{u^2}\left(\frac{l}{\Delta}\right)^{-2/3} = \frac{g}{\Theta_0}\frac{\theta}{u^2}\left(\frac{l}{\Delta}\right)^{1/3}\Delta \tag{2.33}$$

where P^{buoy}_{ij} denotes the intensity scale of buoyant production for the filter scale, Δ. The variables l, θ and u denote the length, temperature and velocity scales corresponding to the energy-containing range. If the factor $(g/\Theta_0)\,(\theta/u^2)$, which has the dimensions of an inverse length scale, doesn't change appreciably, then

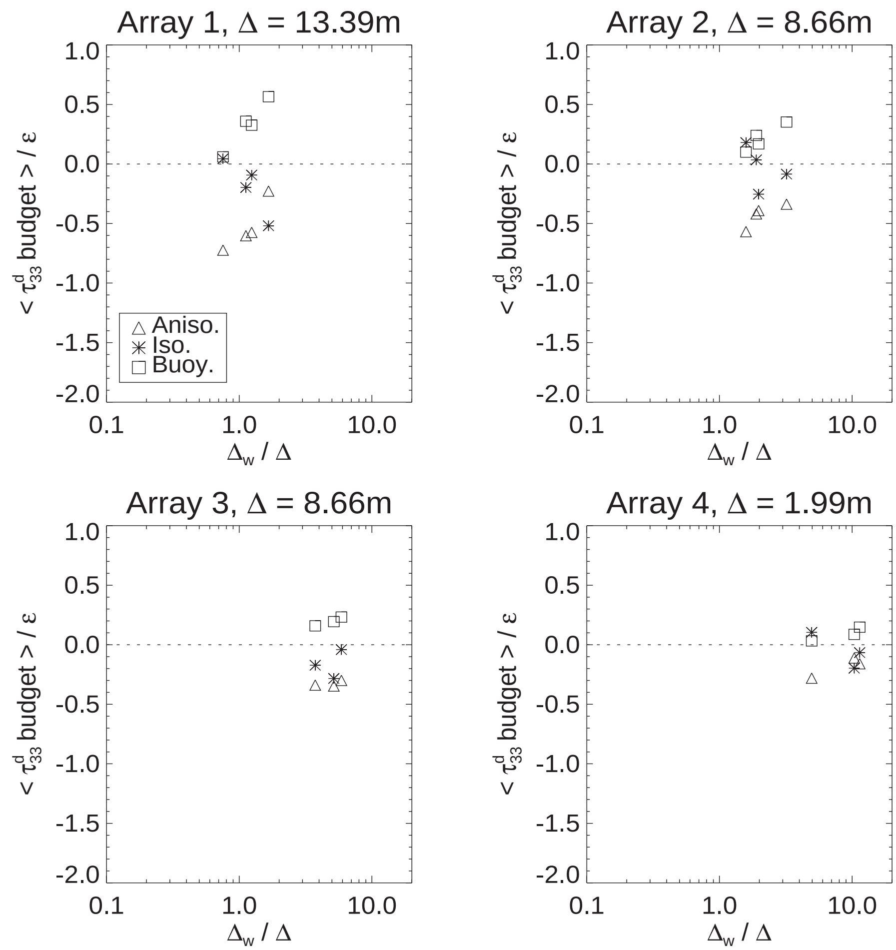

Figure 2.19. HATS data, unstable cases: Array-wise partitioning of SFS production into isotropic, anisotropic and buoyant components for the τ_{33}^{d} budget, plotted against the nondimensional parameter Δ_w/Δ. The production terms have been scaled using $0.93\, e^{3/2}/\Delta$.

Eq. (2.33) implies that the relative importance of buoyant production in the SFS budgets depends on both (l/Δ) and Δ. In Fig. (2.19), we show the τ_{33}^{d} budget for the four array configurations used in HATS, each corresponding to a fixed filter width, Δ. Note that arrays 2 and 3 correspond to different physical heights of the sonic array. As the buoyant terms in the $\tau_{\alpha\alpha}^{d}$ budgets are merely scalar multiples of each other, Fig. (2.19) is a representative case. The magnitude of scaled buoyant production attains its largest and least values for arrays 1 and 4, respectively, which also corresponds to the arrays with largest and the smallest filter widths. For fixed Δ, the role of buoyant production in the budget diminishes with decreasing l/Δ. Thus, the buoyant terms in the τ_{ij}^d budgets depend on both (l/Δ) and Δ, in agreement with Eq. (2.33).

The other terms in the budget include modeled slow pressure strain-rate covariance, advection and the transport terms. Of these terms, the first is the principal sink in the SFS budgets (Wyngaard, 2004). Based on Fig. (2.18), balance of the $\tau_{\alpha\alpha}^d$ budgets requires modeled slow pressure strain-rate covariance to be the dominant sink term in the τ_{11}^d budget, and the dominant production term in the $(\tau_{22}^d, \tau_{33}^d)$ budgets.

2.5.2.2 τ_{13}^d budget

In contrast to the $\tau_{\alpha\alpha}^d$ budgets, isotropic production dominates anisotropic production in the τ_{13}^d budget. Anisotropic production, while non-zero, is smaller in magnitude than isotropic production across the entire range of Δ_w/Δ considered in our study, although it exhibits a marked increase for $\Delta_w/\Delta < 2$. The buoyant terms assume small values and play a negligible role in the budget. For the budget to be balanced, the modeled slow pressure strain-rate has to be a gain. We infer that for $\Delta_w/\Delta > 2$, isotropic production is more significant than anisotropic production in the τ_{13}^d budget. For $\Delta_w/\Delta < 2$, anisotropic production exhibits a sharp increase but remains smaller in magnitude than isotropic production.

2.5.3 LES: $\tau_{\alpha\alpha}^d$ and τ_{13}^d budgets

In order to compare the modeled SFS budgets with those obtained from HATS, we now present results obtained from high-resolution LES using two closures: (i) the modeled SFS conservation equations; and (ii) an eddy-diffusivity closure described earlier in Sec. (2.4.1.1).

2.5.3.1 Obtaining the wavenumber corresponding to the vertical velocity spectral peak

We plot the various terms in the SFS budgets as a function of Δ_w/Δ, where $\Delta = (\Delta x \Delta y \Delta z)^{1/3}$ is the filter width and Δ_w is the peak of the two-dimensional vertical velocity spectrum, as obtained by fitting the following function, $E(\kappa)$, to

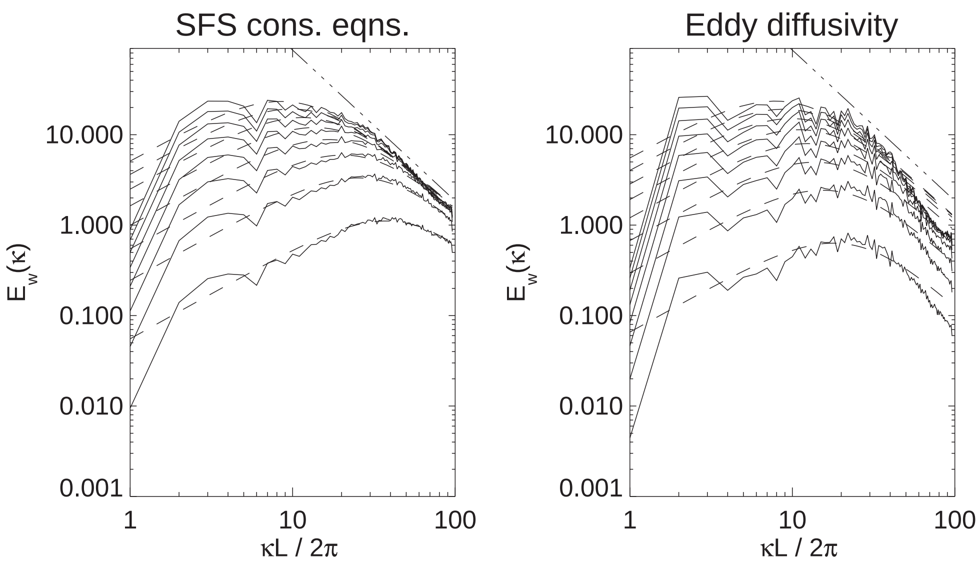

Figure 2.20. Two-dimensional vertical velocity spectra for a moderate convective ABL from a 192^2x144 simulation. The spectra are shown for the heights $0 < z/z_i < 0.1$. The dashed lines denote best fits as prescribed by Eq. (2.34). The dash-dot line has a slope of $-5/3$.

the spectrum (Peltier et al., 1996).

$$E(\kappa) = \frac{c_1 l^2 s^2 \kappa}{\left[c_2 + (\kappa l)^2\right]^{4/3}}. \tag{2.34}$$

In Eq. (2.34), (c_1, c_2) are constants and κ is the radial wavenumber. The characteristic length and intensity scales are denoted by l and s, respectively. The modeled spectrum $E(\kappa)$ has a maximum at $\kappa \sim 1/l$ and exhibits a $-5/3$ slope for $\kappa \gg l^{-1}$.

In Fig. (2.20), we plot the resolved-scale vertical velocity spectrum and the corresponding best fit from Eq. (2.20), for $0 < z/z_i < 0.1$, using both the SFS conservation equations and the eddy-diffusivity closure. Both the plots in Fig. (2.20) utilize a 192x192x144 grid and have physical conditions identical to those described in Table 2.1. The modeled spectrum, $E(\kappa)$, predicts the peak in the resolved-scale spectrum satisfactorily for both closures, although it is in slightly better agreement with spectra obtained using the SFS conservation equations at higher wavenumbers. A visual inspection of Fig. (2.20) reveals that the peak in the vertical velocity spectrum obtained using the SFS conservation equations is associated with smaller scales (higher wavenumbers) than that obtained using the eddy-diffusivity closure.

2.5.3.2 Design of LES runs

The unstable cases in HATS correspond to different surface heat fluxes, filter widths and presumably, boundary layer heights. Indeed, one of the interesting findings by Sullivan et al. (2003) is the efficacy of the scaling parameter Δ_w/Δ, as observed in the good collapse of various resolved and SFS statistics across a wide range of scale and stability. Hence, we present LES statistics as a function of Δ_w/Δ combining results from five LES runs whose specified and diagnosed characteristics are described in Table (2.3) and Table (2.4), respectively. The runs describe weakly to moderately convective ABLs with their (z/L) values ranging from -1.21 to -7.2. We label the runs as 'CONV1', 'CONV2', etc., in increasing order of their $-z_i/L$ values.

Table 2.3. A list of important prescribed physical parameters. L_x, L_y and L_z are the dimensions of the computational domain in the x, y and z directions, respectively. Q_0 is the prescribed kinematic surface potential temperature flux, z_0 is the roughness length, U_g and V_g are the geostrophic wind velocity components in the x and y directions, Γ is the lapse rate above the inversion and f is the Coriolis parameter.

	Specified physical parameters of LES runs				
	CONV1	CONV2	CONV3	CONV4	CONV5
L_x, L_y(m)	6000	3000	3000	6000	6000
L_z(m)	1600	1000	1000	2000	1600
N_x, N_y	192	192	216	192	192
N_z	144	160	192	160	144
Q_0(Kms^{-1})	0.02	0.2	0.2	0.2	0.2
U_g(ms^{-1})	15	15	15	15	15
V_g(ms^{-1})	0	0	0	0	0
z_0(m)	0.05	0.16	0.16	0.16	0.05
Γ(Km^{-1})	0.003	0.003	0.003	0.003	0.003
f(s^{-1})	0.0001	0.0001	0.0001	0.0001	0.0001

2.5.3.3 The budgets for $\tau^d_{\alpha\alpha}$ and τ^d_{13}

In Fig. (2.21), we show the terms in the modeled τ^d_{11} and τ^d_{22} budgets, scaled with $\epsilon = 0.93\ e^{3/2}/\Delta$, plotted versus Δ_w/Δ. A similar plot for the τ^d_{33} and τ^d_{13}

Table 2.4. A list of important diagnosed physical parameters. The variable z_i is the inversion height, u_* is the friction velocity, L is the Monin-Obukhov length and w_* is the mixed layer convective velocity scale.

Diagnosed physical parameters of LES runs					
	CONV1	CONV2	CONV3	CONV4	CONV5
$u_*(\mathrm{ms}^{-1})$	0.55	0.72	0.71	0.71	0.68
$w_*(\mathrm{ms}^{-1})$	0.8	1.52	1.51	1.71	1.77
$-L(\mathrm{m})$	657	142	139	140	119
$z_i(\mathrm{m})$	795	537	531	767	857
$-z_i/L$	**1.21**	**3.78**	**3.82**	**5.47**	**7.2**

budgets is shown in Fig. (2.22). The range of Δ_w/Δ considered in Figs. (2.21)–(2.22) corresponds to $0 < z/z_i < 0.1$, which is approximately the depth of the surface layer. The results from various runs collapse well and vary smoothly with Δ_w/Δ. The two major trends in Figs. (2.21)–(2.22) are: (i) the dominance of anisotropic production for the diagonal stresses, $\tau^d_{\alpha\alpha}$; and (ii) the dominance of isotropic production for the shear component, τ^d_{13}.

As we approach lower Δ_w/Δ, the modeled $\tau^d_{\alpha\alpha}$ budgets simplify to a balance mainly between anisotropic production and modeled slow pressure strain-rate covariance (labeled 'sink' in the plots), in agreement with the behavior of the observed $\tau^d_{\alpha\alpha}$ budgets as implied by Fig. (2.18). The effects of isotropic production and advection are insignificant. The buoyant terms are relatively more significant in the τ^d_{22} and τ^d_{33} budgets than in the τ^d_{11} budget, but their overall effects in all three budgets are negligible.

The τ^d_{13} budget is dominated by isotropic production and the modeled slow pressure strain-rate terms across the entire range of Δ_w/Δ considered in our runs. The sharp increase in the magnitude of anisotropic production in the HATS data for $\Delta_w/\Delta < 2$ is absent in the modeled τ^d_{13} budget. Anisotropic production in the τ^d_{13} budget is determined primarily by the term $-\tau^d_{33}\,(\partial u/\partial z)$ (Chen and Tong, 2006). Later, we see that the modeled SFS budgets underpredict τ^d_{33} compared to observations, which might partially account for the underprediction of anisotropic production.

An interesting feature of Figs. (2.21)–(2.22) is the tendency of the scaled budget terms to asymptote at lower values of Δ_w/Δ. In particular, the scaled dominant

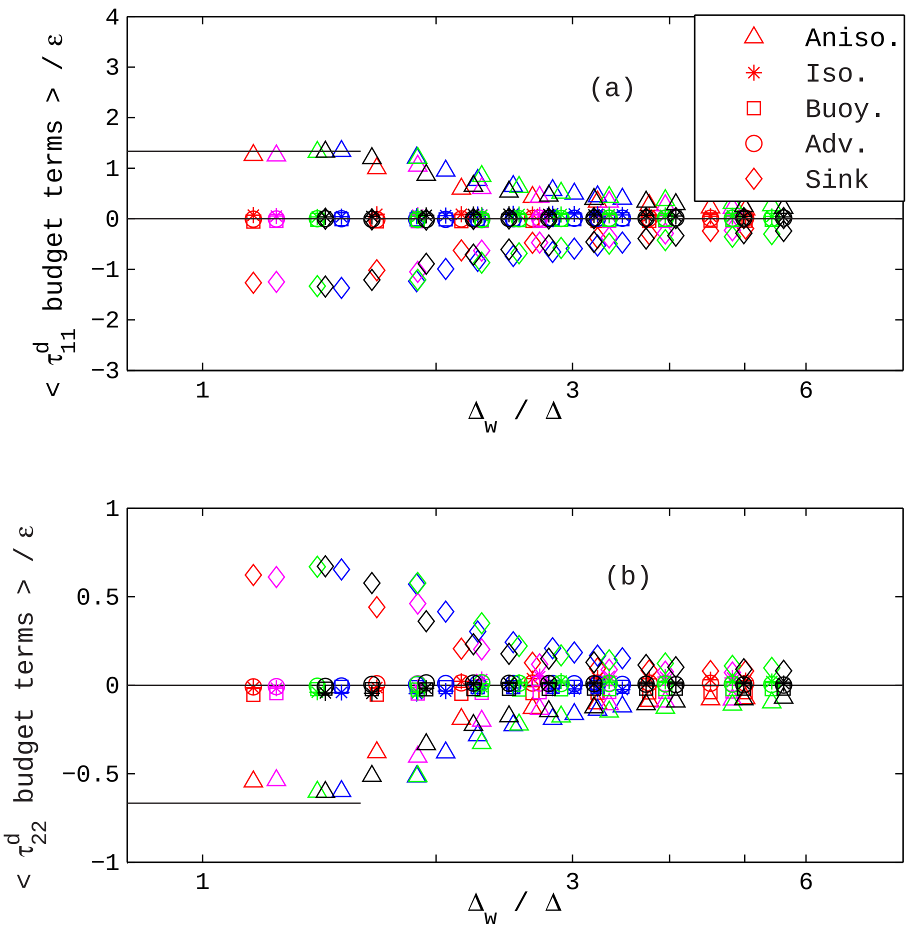

Figure 2.21. Modeled τ^d_{11} and τ^d_{22} budgets. The horizontal lines at low Δ_w/Δ indicate theoretical values in the RANS limit (refer Appendix A). Color legend: —— : $-z_i/L = 1.21$, —— : $-z_i/L = 3.78$, —— : $-z_i/L = 3.82$, —— : $-z_i/L = 5.47$, —— : $-z_i/L = 7.2$

production and destruction terms in both the $\tau^d_{\alpha\alpha}$ and τ^d_{13} budgets appear to approach constant values with decreasing Δ_w/Δ. Sullivan et al. (2003) showed that the filtering operation is equivalent to Reynolds averaging at very low values of Δ_w/Δ. In other words, $\Delta_w/\Delta \to 0$ corresponds to the "RANS limit" (RANS stands for Reynolds Averaged Navier-Stokes) and the asymptotic values of the dominant, scaled terms in the SFS budgets at low Δ_w/Δ are indicative of the SFS model's performance as we approach this limit. The horizontal solid lines shown in

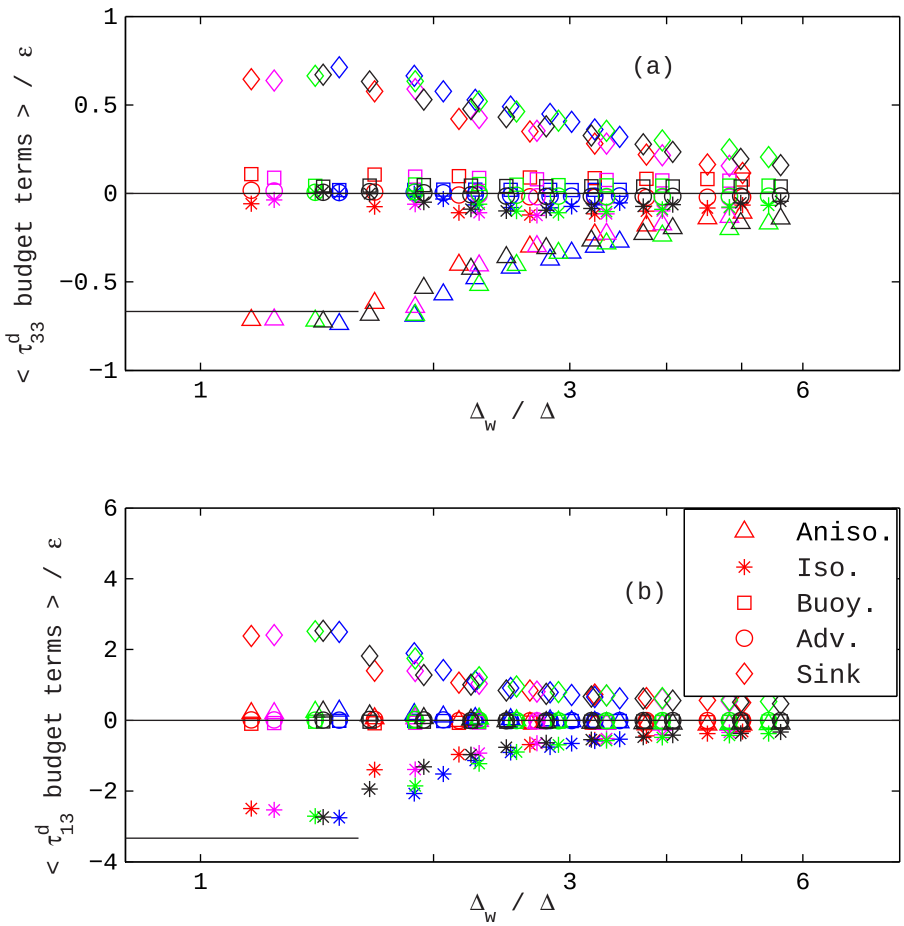

Figure 2.22. Modeled τ_{33}^d and τ_{13}^d budgets. The horizontal lines at low Δ_w/Δ indicate theoretical values in the RANS limit (refer Appendix A). Color legend: blue : $-z_i/L = 1.21$, green : $-z_i/L = 3.78$, black : $-z_i/L = 3.82$, magenta : $-z_i/L = 5.47$, red : $-z_i/L = 7.2$

Figs. (2.21)–(2.22) denote theoretical values in the RANS limit for the anisotropic production term in the case of the $\tau_{\alpha\alpha}^d$ budgets, and the isotropic production term in the case of the τ_{13}^d budget. In Appendix A, we derive analytically the limits for the anisotropic production term while infering that for the isotropic production term through HATS data. The values of the dominant production terms in the modeled τ_{11}^d and τ_{33}^d budgets at low Δ_w/Δ are in good agreement with their theoretical values in the RANS limit. Those in the modeled τ_{22}^d and τ_{13}^d budgets are underpredicted slightly. While these asymptotic limits are not observed in the HATS data for convectively unstable conditions, we recover these limits for stably stratified conditions, discussed in the next chapter. The values of Δ_w/Δ associated with stable stratification are typically lower than those for unstable stratification.

2.5.3.4 Significance of the LES to RANS transition

Near the wall, the horizontal length scale of the vertical velocity spectrum scales as z implying that turbulent motions in that region will always be under-resolved, irrespective of the grid resolution (Khanna and Brasseur, 1997). Thus, as we approach the wall, the parameter Δ_w/Δ tends to zero and the SFS model is required to represent an increasing fraction of the total turbulent stresses and fluxes. Ideally, an SFS model would provide a smooth transition from LES to RANS towards the wall. In practice, this turns out to be a challenging requirement for SFS models to meet (Sullivan et al., 1994). For instance, one of the main features of the two-part eddy-viscosity model developed by Sullivan et al. (1994) is that it is designed to achieve a transition from LES to RANS towards the wall by using a fluctuating and mean-field viscosity, the latter representing near-wall effects. In their studies, Sullivan et al. (1994) calculated the shear production term in the prognostic equation for e after subtracting the mean shear from the resolved-scale strain rate. Our results in the previous section suggest that the modeled conservation equations have the potential to enable a smooth transition from LES to RANS without using ad-hoc corrections.

2.5.4 SFS total stresses

2.5.4.1 HATS results

In Fig. (2.23) we show the magnitudes of the total (deviatoric + isotropic) SFS stresses, $\tau_{\alpha\alpha}$ and τ^d_{13}, normalized with the magnitudes of the corresponding total stresses (resolved + subfilter), as a function of Δ_w/Δ. The total stresses are denoted as $\langle u'u'\rangle_T$, $\langle v'v'\rangle_T$ and so on. Figure (2.23) is identical to results presented by Sullivan et al. (2003) except that we have shown merely the unstable cases. The magnitudes of the normalized stresses increase with decreasing Δ_w/Δ, as expected. The fraction of the total stresses residing at the subfilter scales at a given value

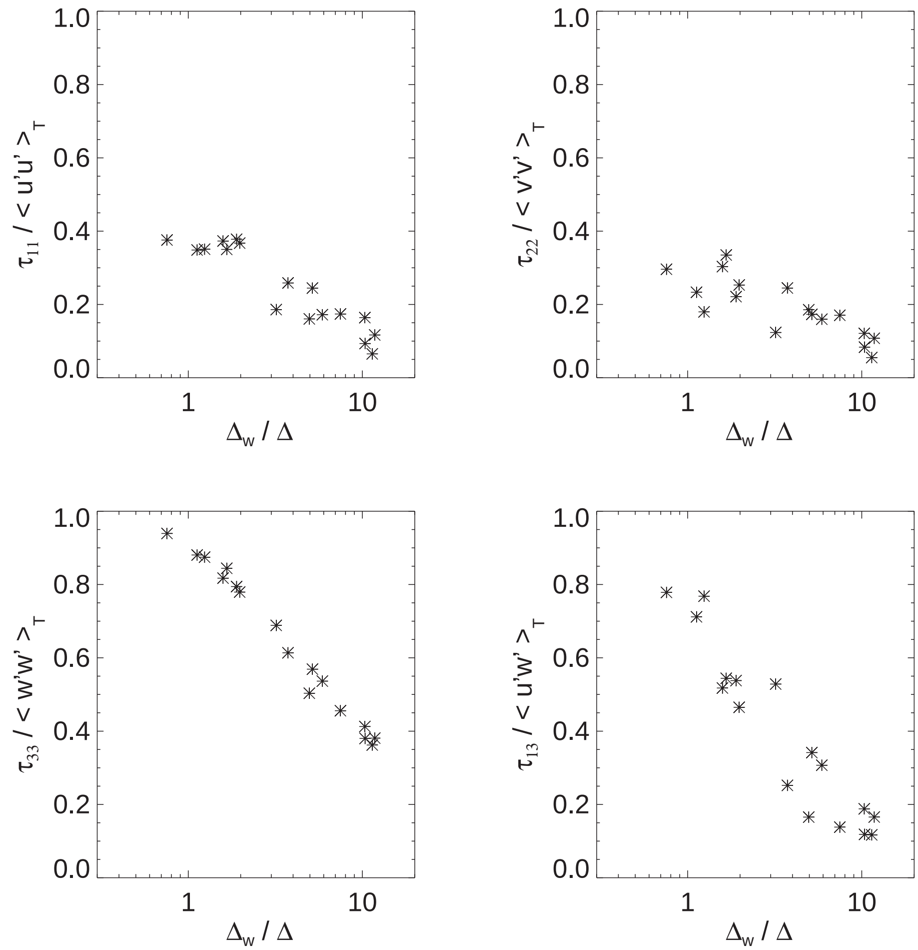

Figure 2.23. HATS: SFS stresses as a fraction of the total stresses (resolved + SFS) for convectively unstable cases.

of Δ_w/Δ is typically larger for τ_{33} than is for either τ_{11} or τ_{22} (Sullivan et al., 2003), which reflects the difference in the spectral content of horizontal and vertical velocity fluctuations. The collapse is considerably better for τ_{33} than for the other three τ_{ij} components.

2.5.4.2 LES results

Figures. (2.24)–(2.25) are plots similar to Fig. (2.23), but obtained from LES with the SFS conservation equations and the eddy-diffusivity closure. Compared to Fig. (2.23), both closures underpredict the scaled magnitudes of τ_{11} and τ_{22} at

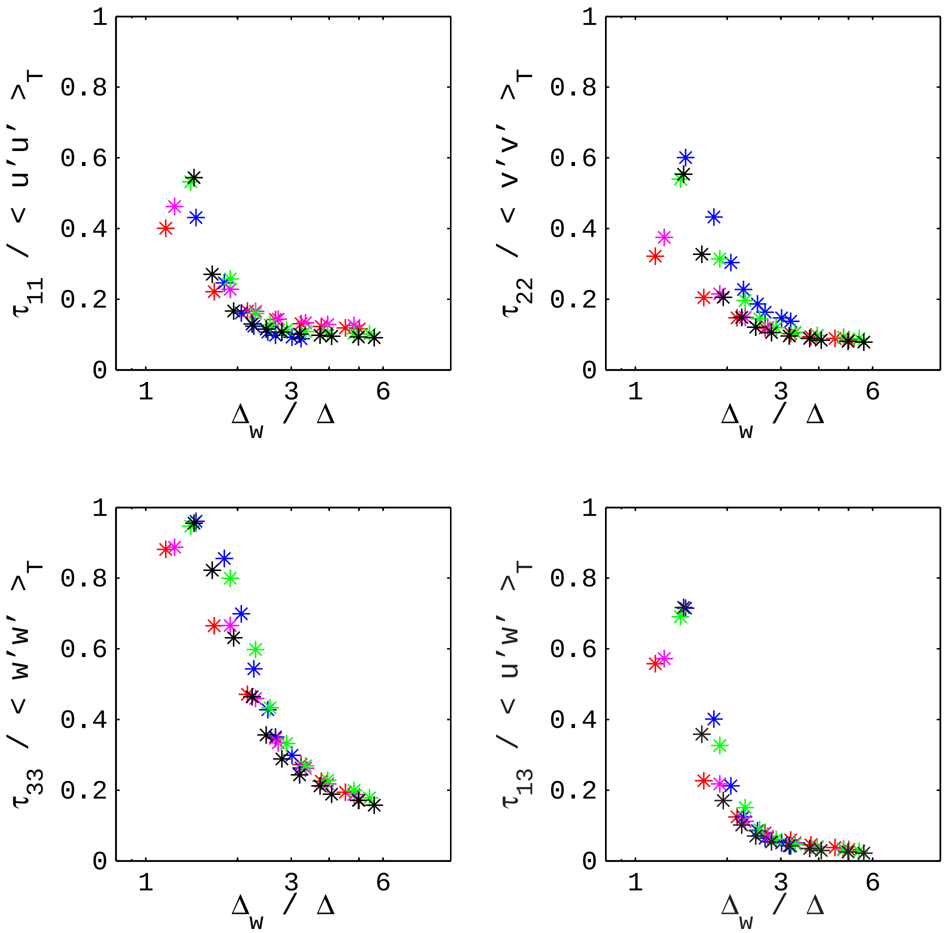

Figure 2.24. LES: SFS stresses as a fraction of the total stresses (resolved + SFS), obtained using the SFS conservation equations. Color legend: —— : $-z_i/L = 1.21$, —— : $-z_i/L = 3.78$, —— : $-z_i/L = 3.82$, —— : $-z_i/L = 5.47$, —— : $-z_i/L = 7.2$

high Δ_w/Δ but overpredict at lower values of Δ_w/Δ. The scaled magnitudes of τ_{33} and τ_{13} are predicted reasonably by the two closures at low Δ_w/Δ . At higher Δ_w/Δ, however, their magnitudes are underpredicted severely. As we shall see in later plots, this is a recurring trend in our LES resuls with both SFS models, namely, the underprediction of various statistics at high Δ_w/Δ when compared to HATS data. We speculate that this could be a consequence of the differences in the type of filtering used in LES and for the HATS data.

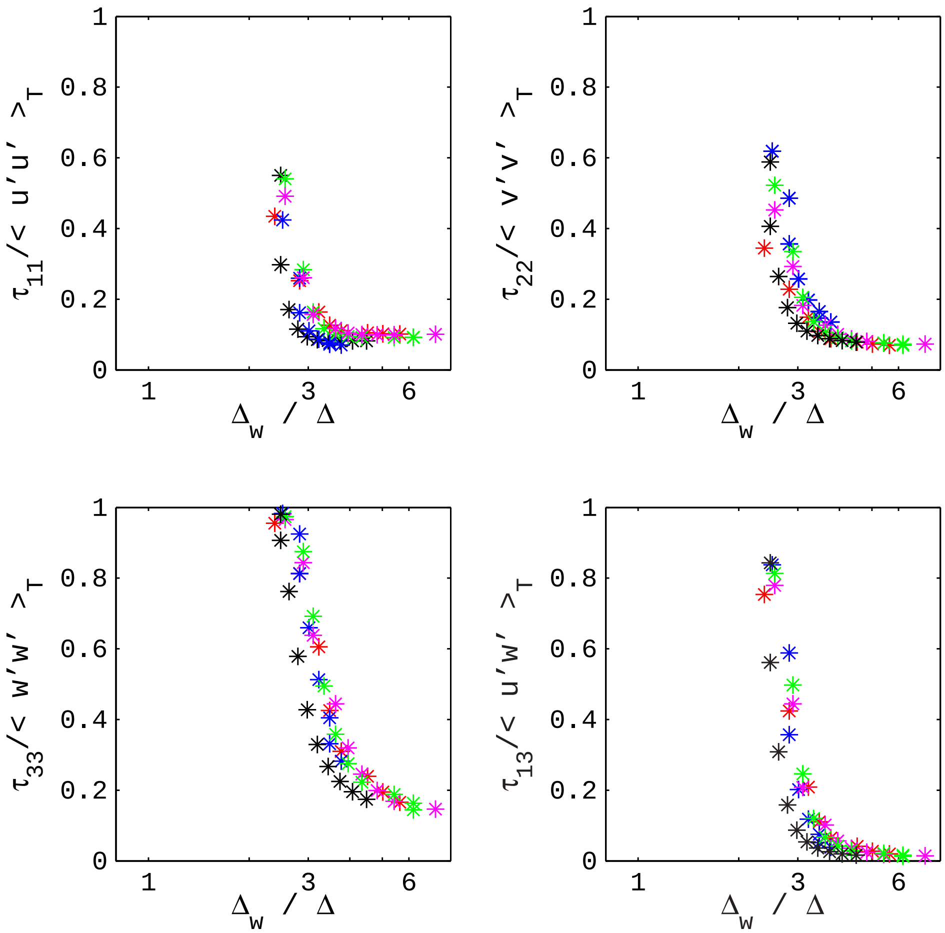

Figure 2.25. LES: SFS stresses as a fraction of the total stresses (resolved + SFS), obtained using the eddy-diffusivity closure. Color legend: —— : $-z_i/L = 1.21$, —— : $-z_i/L = 3.78$, —— : $-z_i/L = 3.82$, —— : $-z_i/L = 5.47$, —— : $-z_i/L = 7.2$

There are some differences between results obtained using the two closures. Firstly, the variations of the scaled SFS stresses with Δ_w/Δ are different for the two closures. LES results with the SFS conservation equations collapse better than those with the eddy-diffusivity closure, as a function of Δ_w/Δ. In fact, they collapse even better than the HATS data. This can be explained by noting that our LES runs cover only a limited range of z_i/L, as outlined in Table 2.4. The HATS data correspond, presumably, to a wider range of stabilities than our LES runs. In general, it appears that within this narrow range of z_i/L, the influence of the outer scales on the scaled SFS stresses leaves only a weak signature, when they are plotted against the parameter Δ_w/Δ. Thus, statistics involving horizontal velocity fluctuations exhibit greater scatter in the HATS data than in our LES studies. Another difference is that Δ_w for the eddy-diffusivity closure is consistently higher than that for the SFS conservation equations at the first few grid levels. Andren et al. (1994), in their studies of the neutral ABL, found that SFS models with reduced eddy-diffusivities and/or backscatter pushed the location of the spectral peak to smaller scales (higher wavenumbers). Thus, reducing the value of c_k in the eddy-diffusivity closure is expected to shift the spectral peak to higher wavenumbers, which would result in lower values of Δ_w/Δ.

2.5.5 SFS deviatoric components

In this section, we compare the means and the normalized standard deviations of the modeled SFS stresses and fluxes with those obtained from HATS data.

2.5.5.1 Mean values

In Fig. (2.26), we show the normalized stresses, $\tau^d_{\alpha\alpha}/u_*^2$, obtained from HATS data (Sullivan et al., 2003). A similar plot for the LES results is shown in Fig. (2.27). The HATS data show the deviatoric components tending towards zero at large Δ_w/Δ indicating the onset of isotropy. As Δ_w/Δ decreases, the SFS stresses start to exhibit strong anisotropy. The LES results in Fig. (2.27) show that the SFS conservation equations reproduce partially the anisotropy at the subfilter scales while the eddy-diffusivity closure predicts near-zero values for the scaled deviatoric components. The poor performance of the eddy-diffusivity closure is due to its lack of anisotropic production, which is an important production term in the $\tau^d_{\alpha\alpha}$ budgets at low Δ_w/Δ, as seen in Fig. (2.18).

Although the SFS conservation equations account explicitly for anisotropic production, Figs. (2.26)-(2.27) show that the SFS conservation equations underpredict the magnitudes of τ^d_{11}/u_*^2 and τ^d_{33}/u_*^2 while overpredicting that of τ^d_{22}/u_*^2. The errors in the predicted magnitudes of $\tau^d_{\alpha\alpha}$ could potentially be due to the fact that the model for the pressure-strain covariance used in this study takes into account only

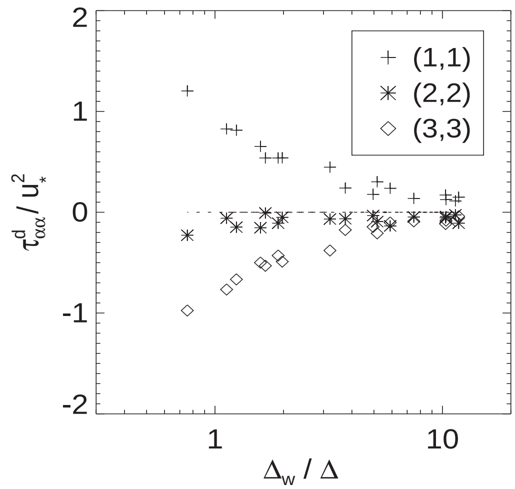

Figure 2.26. HATS: SFS normal stresses, $\tau^d_{\alpha\alpha}$, scaled with u_*^2. The dashed line corresponds to $\tau^d_{\alpha\alpha} = 0$.

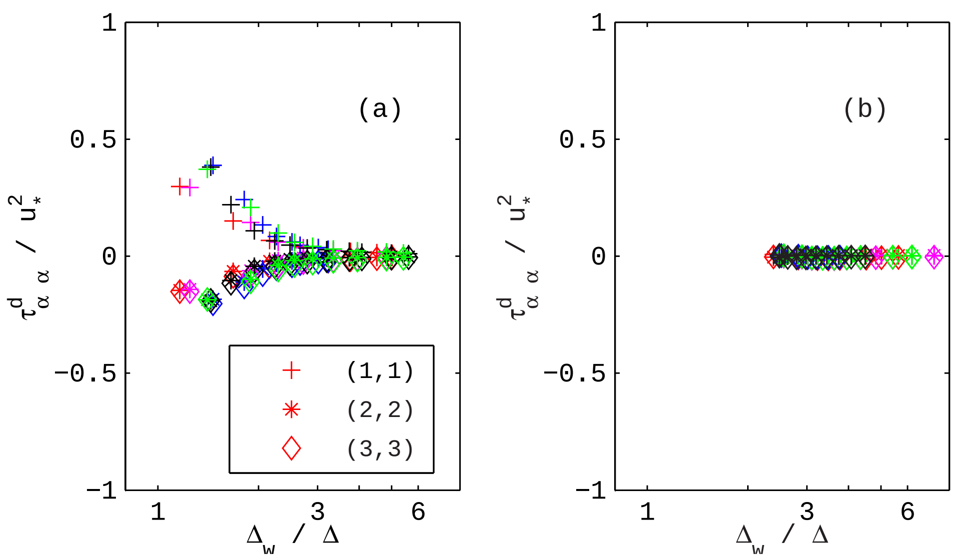

Figure 2.27. LES: Comparison of predictions of $\tau^d_{\alpha\alpha}/u_*^2$ by (a) SFS conservation equations; and (b) eddy-diffusivity closure. Color legend: —— : $-z_i/L = 1.21$, —— : $-z_i/L = 3.78$, —— : $-z_i/L = 3.82$, —— : $-z_i/L = 5.47$, —— : $-z_i/L = 7.2$

contributions from p_T.

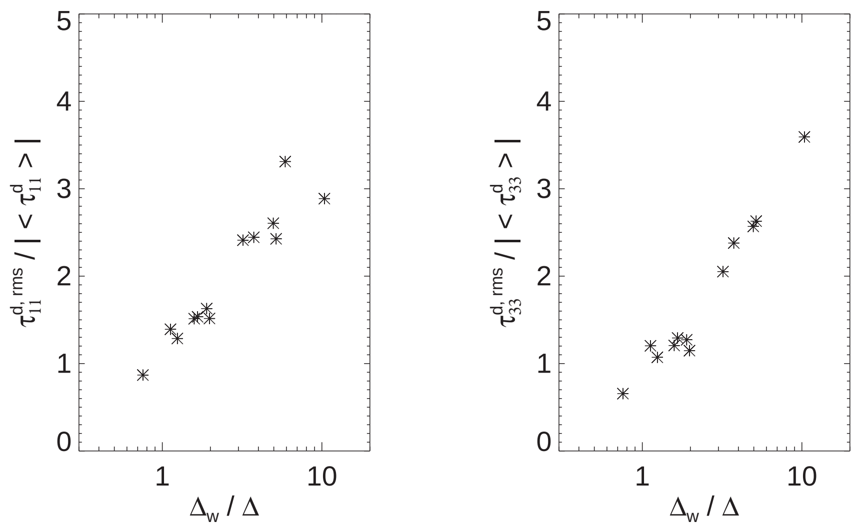

Figure 2.28. HATS: Root mean square values of SFS deviatoric stresses τ_{11}^d and τ_{33}^d, normalized with the magnitudes of their mean values.

2.5.5.2 Fluctuation levels

We discuss first the fluctuation levels of τ_{11}^d and τ_{33}^d, followed by those of τ_{13}^d. In Fig. (2.28), we show the rms (root mean square) values of τ_{11}^d and τ_{33}^d normalized with the magnitudes of their respective mean values, as obtained using HATS data. As Δ_w/Δ increases, the normalized fluctuation levels of τ_{11}^d and τ_{33}^d increase monotonically, attaining nearly equal magnitudes at higher values of Δ_w/Δ. As Δ_w/Δ decreases, the normalized fluctuations of τ_{11}^d tend to exceed slightly those of τ_{33}^d.

The normalized fluctuations of τ_{11}^d and τ_{33}^d obtained from LES are shown in Fig. (2.29). The SFS conservation equations reproduce the trends correctly, wherein the normalized fluctuations of τ_{11}^d and τ_{33}^d increase monotonically with increasing Δ_w/Δ. The normalized rms values of τ_{11}^d and τ_{33}^d are underpredicted considerably at low Δ_w/Δ but are in better agreement with observations at higher Δ_w/Δ. There appears to be a systematic dependence on z_i/L wherein the normalized fluctuations increase with increasing $-z_i/L$.

The eddy-diffusivity closure predicts very high normalized rms values of τ_{11}^d primarily because it predicts near-zero levels of $|\tau_{\alpha\alpha}^d|$, as discussed in earlier sections.

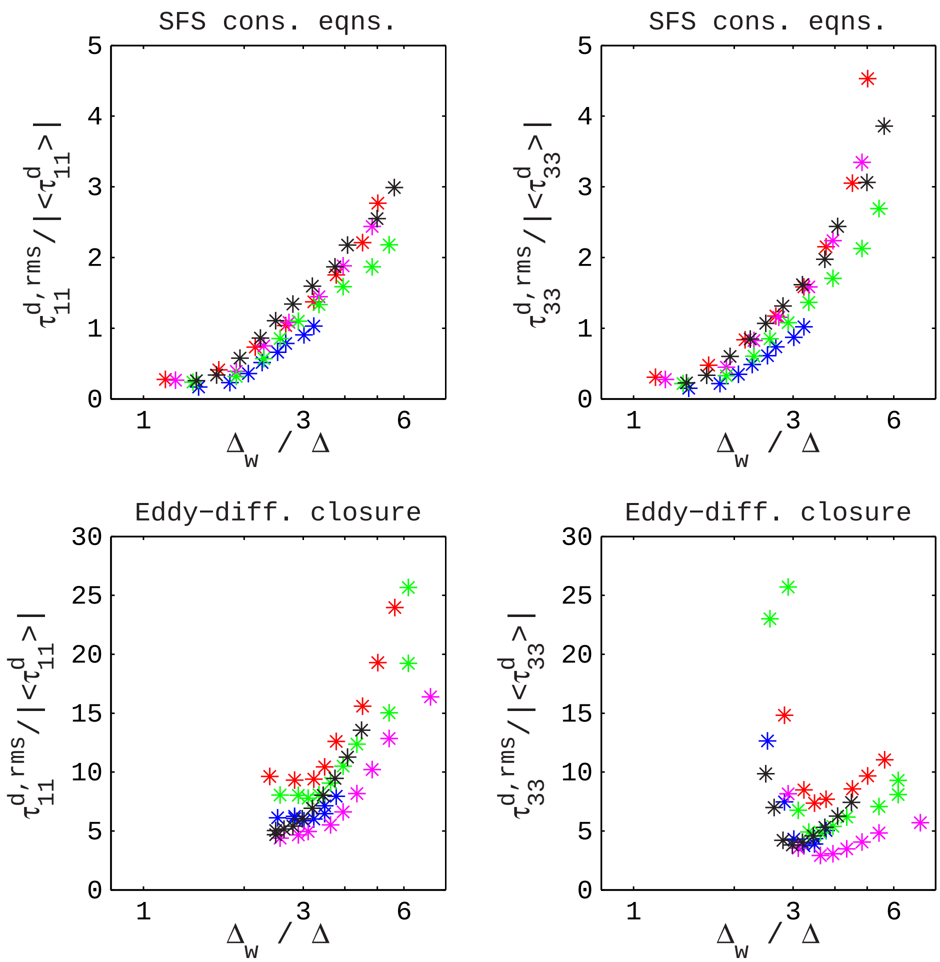

Figure 2.29. LES: Root mean square values of SFS deviatoric stresses τ_{11}^d and τ_{33}^d, normalized with the magnitudes of their mean values. Top panel: SFS conservation equations, bottom panel: eddy-diffusivity closure. Color legend: —— : $-z_i/L = 1.21$, —— : $-z_i/L = 3.78$, —— : $-z_i/L = 3.82$, —— : $-z_i/L = 5.47$, —— : $-z_i/L = 7.2$

It predicts reasonably the trends in the normalized rms values of τ_{11}^d, namely, their increase with increasing Δ_w/Δ. The predicted normalized rms values of τ_{33}^d fare poorly both in magnitude and trend when compared to observations. The dependence on z_i/L is harder to discern than in the case of the modeled SFS conservation equations.

Figure (2.30) shows the normalized rms values of τ_{13}^d obtained from HATS data. They increase in magnitude with increasing Δ_w/Δ and are nearly equal to

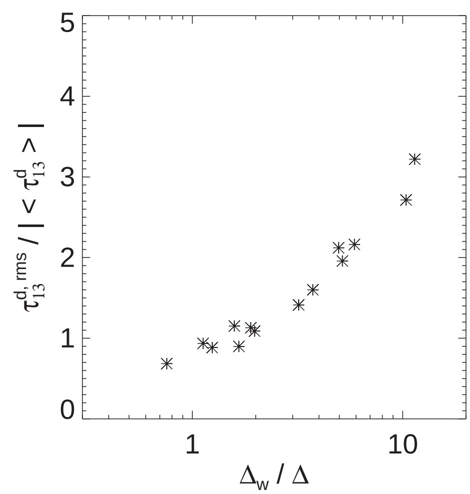

Figure 2.30. HATS: Root mean square value of τ_{13}^d, normalized with $|\langle \tau_{13}^d \rangle|$.

the normalized rms values of τ_{11}^d and τ_{33}^d at high Δ_w/Δ.

The normalized rms values of τ_{13}^d obtained using the SFS conservation equations and the eddy-diffusivity closure are shown in Fig. (2.31). Both closures reproduce correctly the trends but underpredict the magnitudes at low Δ_w/Δ. As Δ_w/Δ increases, the modeled SFS conservation equations continue to underpredict $\tau_{13}^{d,rms}/\left|\left\langle \tau_{13}^d \right\rangle\right|$ while the predictions by the eddy-diffusivity closure become increasingly sensitive to the underlying z_i/L values. At $\Delta_w/\Delta \approx 5$, for instance, the normalized τ_{13}^d fluctuations from the HATS data and LES are ≈ 2 and ≈ 1.2, respectively. The eddy-diffusivity closure yields values ranging from 1.5 to 3.2. Nevertheless, the eddy-diffusivity closure predicts the normalized rms values of τ_{13}^d better than those of $\tau_{\alpha\alpha}^d$ as it accounts for isotropic production, which is the dominant production term in the τ_{13}^d budget.

2.5.6 SFS kinetic energy

In Fig. (2.32), we show SFS turbulent kinetic energy, e_{SFS}, as a fraction of the total turbulent kinetic energy, e_{TOT}, obtained from HATS data. Corresponding plots from LES runs using the SFS conservation equations and the eddy-diffusivity closure are shown in Fig. (2.33a) and Fig. (2.33b), respectively. Compared to

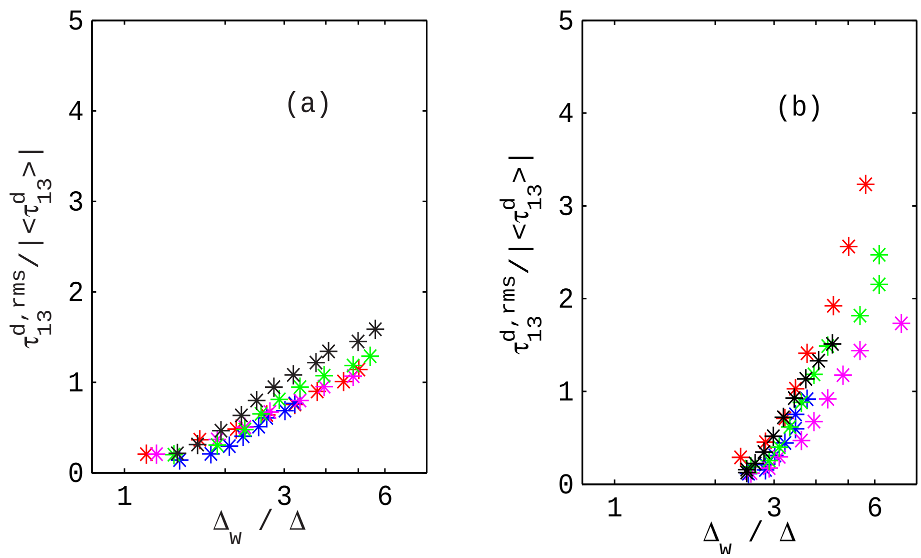

Figure 2.31. LES: Root mean square value of τ_{13}^d normalized with $|\langle\tau_{13}^d\rangle|$, using (a) SFS conservation equations; (b) eddy-diffusivity closure. Color legend: —— : $-z_i/L = 1.21$, —— : $-z_i/L = 3.78$, —— : $-z_i/L = 3.82$, —— : $-z_i/L = 5.47$, —— : $-z_i/L = 7.2$

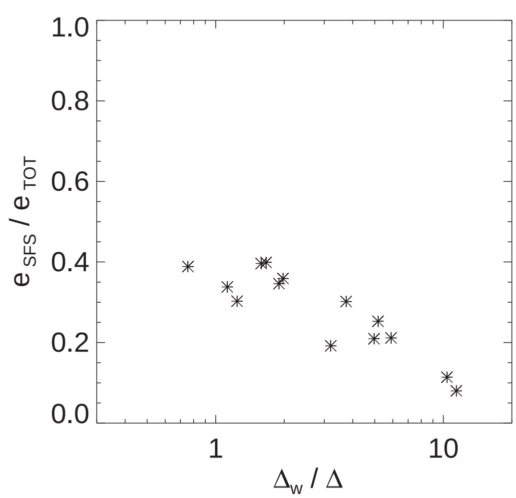

Figure 2.32. HATS: SFS turbulent kinetic energy, e_{SFS}, as a fraction of the total (resolved + SFS) turbulent kinetic energy, e_{TOT}.

HATS data, both closures overpredict $e_{\mathrm{SFS}}/e_{\mathrm{TOT}}$ at lower values of Δ_w/Δ and underpredict it at higher values of Δ_w/Δ.

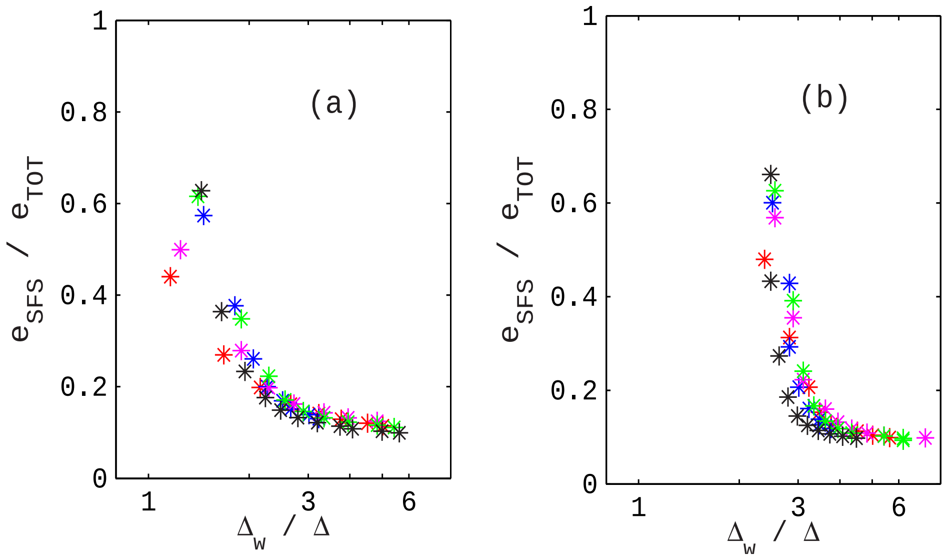

Figure 2.33. LES: SFS turbulent kinetic energy, e_{SFS}, as a fraction of the total (resolved+sfs) turbulent kinetic energy, e_{TOT}, using (a) SFS conservation equations; and (b) eddy-diffusivity closure. Color legend: —— : $-z_i/L = 1.21$, —— : $-z_i/L = 3.78$, —— : $-z_i/L = 3.82$, —— : $-z_i/L = 5.47$, —— : $-z_i/L = 7.2$

The principal production term for the SFS kinetic energy, e, is $\tau^d_{kl}\bar{S}_{kl}$, which we recognize as the rate of energy transfer from the resolved to the subfilter scales. Since the eddy-diffusivity closure is capable of downscale energy transfer at the correct mean rate, its poor representation of the SFS stresses themselves does not affect adversely the predicted magnitudes of e. Thus both the eddy-diffusivity closure and the SFS conservation equations yield more or less similar trends and magnitudes of e in Fig. (2.33).

2.5.7 HATS: f_i budgets

Among isotropic and anisotropic production, Sullivan (2010) found the latter to dominate in the f_1 budget and the former to dominate in the f_3 budget. In Fig. (2.34) we present the budgets for f_1 and f_3 obtained from HATS measurements. Figure (2.34) is similar to results obtained by Sullivan (2010), the only difference being that we also show the tilting and buoyant production terms. We discuss first the f_1 budget followed by the f_3 budget.

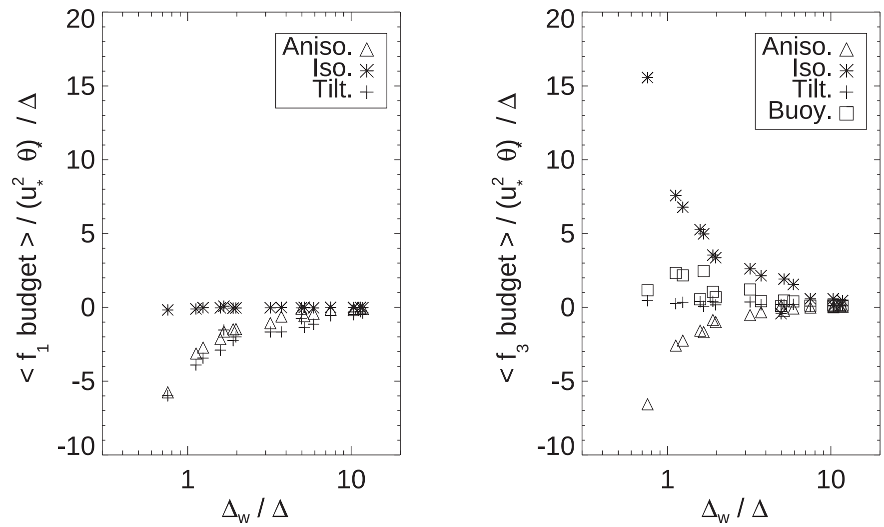

Figure 2.34. HATS: Scaled production terms in the f_1 (left) and f_3 (right) budgets.

2.5.7.1 f_1 budget

The dominant production terms in the f_1 budget are flux tilting and anisotropic gradient-production. The magnitudes of flux-tilting and anisotropic gradient-production are nearly equal with the former being slightly larger. Isotropic gradient-production is negligible at all values of Δ_w/Δ in Fig. (2.34), as shown by Sullivan (2010) and implied in studies by Hatlee and Wyngaard (2007), who found eddy-viscosity closures — which account only for isotropic production — to yield near-zero values of f_1. The other terms in the f_1 budget are advection, turbulent transport, and pressure destruction. Of these, pressure destruction is the principal sink term (Wyngaard, 2004) in the f_1 budget.

2.5.7.2 f_3 budget

For values of Δ_w/Δ in the range (4,10) the dominant production term in the f_3 budget is isotropic production while anisotropic and buoyant production are negligible. For lower Δ_w/Δ, both anisotropic- and buoyant-production increase although their magnitudes remain smaller than that of isotropic production. The increase in the magnitude of anisotropic gradient-production, in particular, is marked for $\Delta_w/\Delta < 3$. Anisotropic gradient-production in the f_3 budget contributions from $\tau_{33}^{d}\,(\partial\theta/\partial z)$. At higher values of Δ_w/Δ, the SFS stresses are nearly isotropic with $\tau_{\alpha\alpha}^{d} \approx 0$ (Sullivan et al., 2003) implying low values of anisotropic gradient-production. As Δ_w/Δ decreases, the SFS stresses become increasingly anisotropic such that the magnitudes of τ_{11}^{d} and τ_{33}^{d} increase (Sullivan et al., 2003), thereby leading to higher values of anisotropic gradient-production. Buoyant production is negligible at higher Δ_w/Δ but increases slightly as Δ_w/Δ decreases. We infer that the pressure-destruction term has to be negative to balance the f_3 budget.

To summarize, at higher Δ_w/Δ, isotropic production dominates anisotropic- and buoyant production in the f_3 budget. At lower Δ_w/Δ, buoyant-production and anisotropic gradient-production become important although they remain smaller in magnitude when compared to isotropic production. The principal sink term in the f_3 budget is pressure destruction.

2.5.8 High-resolution LES: f_i budgets

In Fig. (2.35) we present the modeled f_1 and f_3 budgets obtained using LES. We discuss first the f_1 budget.

2.5.8.1 f_1 budget

The dominant production terms in the f_1 budget are: flux tilting (loss), anisotropic gradient-production (loss) and the modeled slow pressure strain-rate covariance (gain). The flux-tilting term is larger in magnitude than the anisotropic gradient-production term at all Δ_w/Δ. Isotropic production and advection are negligible. These observations are true of all the stabilities considered in Fig. (2.35). The modeled f_1 budget is able to reproduce qualitatively the important features observed in Fig. (2.34), namely, the dominance of flux tilting and anisotropic gradient-production over isotropic gradient-production.

2.5.8.2 f_3 budget

The f_3 budget is in balance primarily between isotropic production (gain) and the modeled slow pressure strain-rate term (loss) across the entire range of Δ_w/Δ in Fig. (2.35). Anisotropic gradient-production and advection are negligible. The

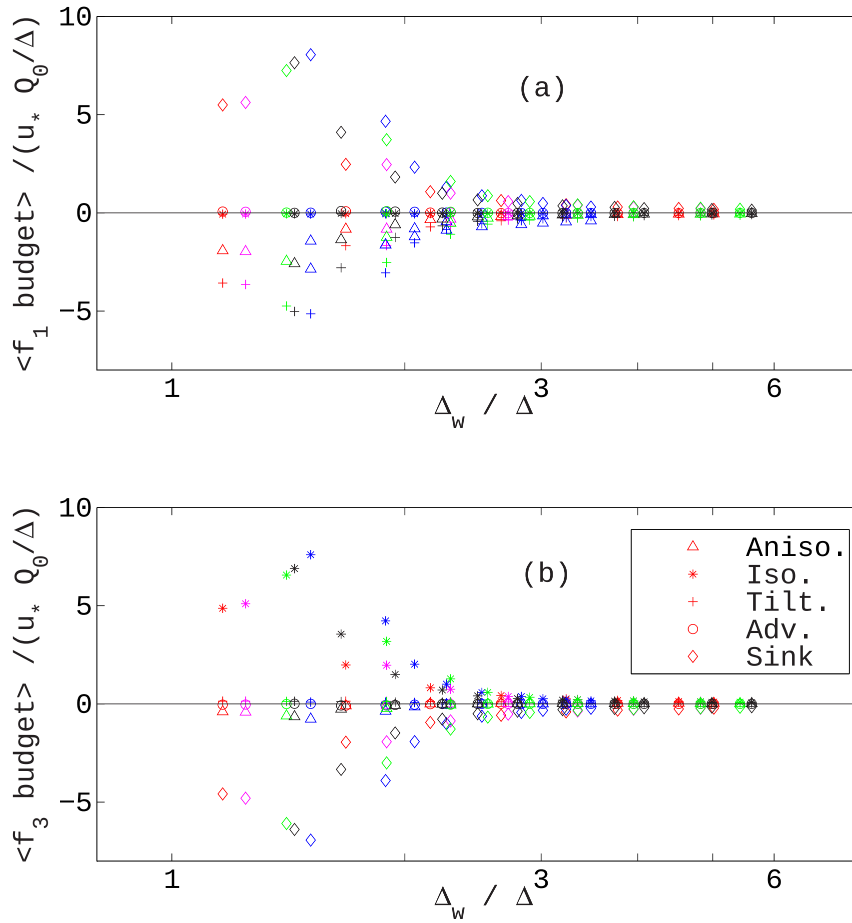

Figure 2.35. LES: Scaled terms in the modeled (a) f_1 and (b) f_3 budgets. Color legend: : $-z_i/L = 1.21$, : $-z_i/L = 3.78$, : $-z_i/L = 3.82$, : $-z_i/L = 5.47$, : $-z_i/L = 7.2$

predictions of anisotropic-gradient production differ markedly from observations where their magnitudes increase sharply at low Δ_w/Δ (Fig. (2.34). Anisotropic gradient-production in the f_3 budget is dominated by the term $\tau_{33}^d\,(\partial\theta/\partial z)$ (Chen et al., 2005). In our discussion of the SFS stresses, we observed that the SFS conservation equations while capable of exhibiting SFS anisotropy, underpredict the magnitudes of $\tau_{\alpha\alpha}^d$ in comparison to HATS data. Thus, it is likely that the underprediction of anisotropic gradient-production is caused in part due to the

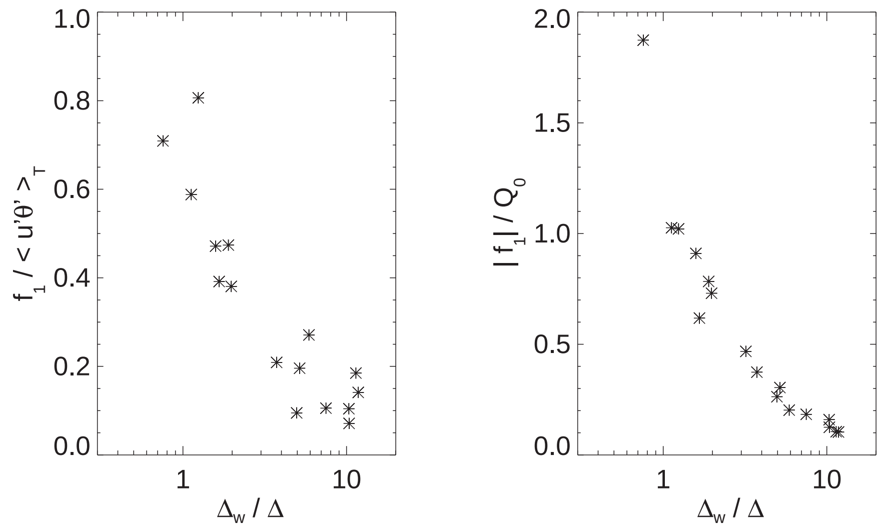

Figure 2.36. HATS: SFS horizontal scalar flux, f_1, as a fraction of the total flux (left) and the surface flux, Q_0 (right).

underprediction of τ_{33}^d.

2.5.9 SFS scalar fluxes: mean values

2.5.9.1 f_1

We plot in Fig. (2.36), the magnitude of f_1 scaled with the magnitudes of the total flux (left panel) and with that of the surface flux, Q_0 (right panel), against Δ_w/Δ. These plots are similar to those presented by Hatlee and Wyngaard (2007) in their studies. The scaled magnitudes of f_1 increase with decreasing Δ_w/Δ, as expected. At low Δ_w/Δ, f_1 attains values that are comparable to the surface flux.

In Figs. (2.37)-(2.38) we plot the scaled magnitudes of f_1, corresponding to the SFS conservation equations and the eddy-diffusivity closure. The SFS conservation equations yield results in good agreement with the HATS data at low Δ_w/Δ because they incorporate the tilting and anisotropic gradient-production mechanisms, as seen in Fig. (2.35). At high Δ_w/Δ, however, they underpredict the scaled values of f_1. The eddy-diffusivity closure depends solely on isotropic gradient-production which plays a negligible role in the f_1 budget (Fig. (2.34)), and thus, predicts near-zero values of f_1 across the entire range of Δ_w/Δ.

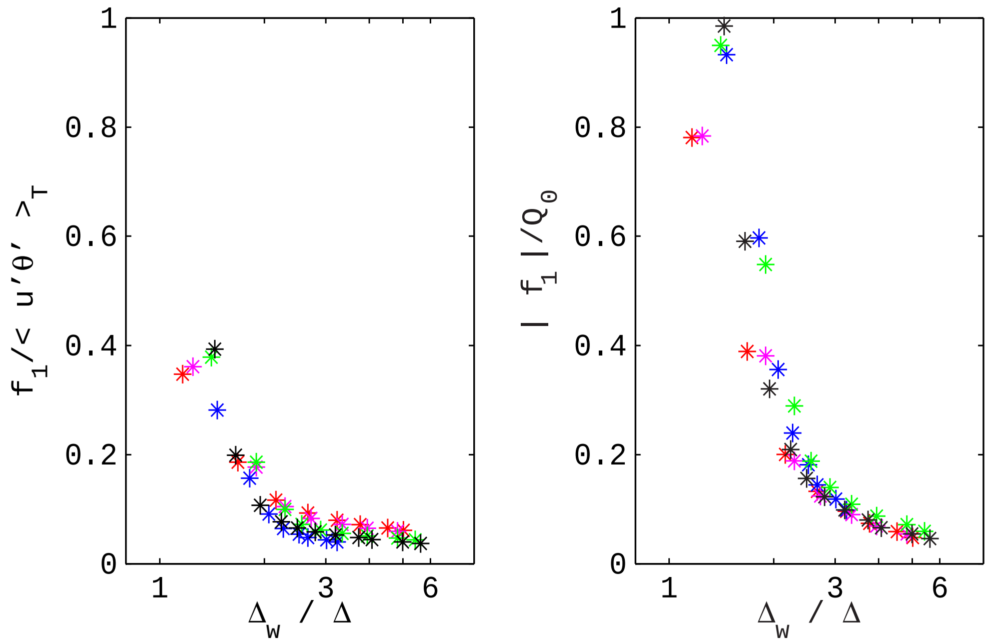

Figure 2.37. LES, SFS conservation equations: SFS horizontal scalar flux, f_1, as a fraction of the total flux, $\langle u'\theta' \rangle_T$ (left) and of the surface flux, Q_0 (right). Color legend: —— : $-z_i/L = 1.21$, —— : $-z_i/L = 3.78$, —— : $-z_i/L = 3.82$, —— : $-z_i/L = 5.47$,—— : $-z_i/L = 7.2$

2.5.9.2 f_3

In Figs. (2.39)-(2.40), we show the vertical SFS flux as a fraction of the total flux, obtained from HATS data and LES, respectively. Both closures predict satisfactorily the scaled magnitudes of the SFS vertical flux at lower Δ_w/Δ. At higher Δ_w/Δ, both closures underpredict the scaled magnitude of f_3, as was also the case for f_1.

The eddy-diffusivity closure is designed to account only for isotropic gradient-production. The SFS conservation equations possess additional production mechanisms but still yield isotropic gradient-production as the only significant mode of production in the f_3 budget, as seen in Fig. (2.35). This is because the buoyant term in the f_3 budget isn't included in our implementation of the SFS conservation equations while anisotropic gradient-production — which is included — is underpredicted due to the underprediction of $|\tau_{33}^d|$. But buoyancy and anisotropic gradient-production have opposite signs in the f_3 budget, as seen in Fig. (2.34).

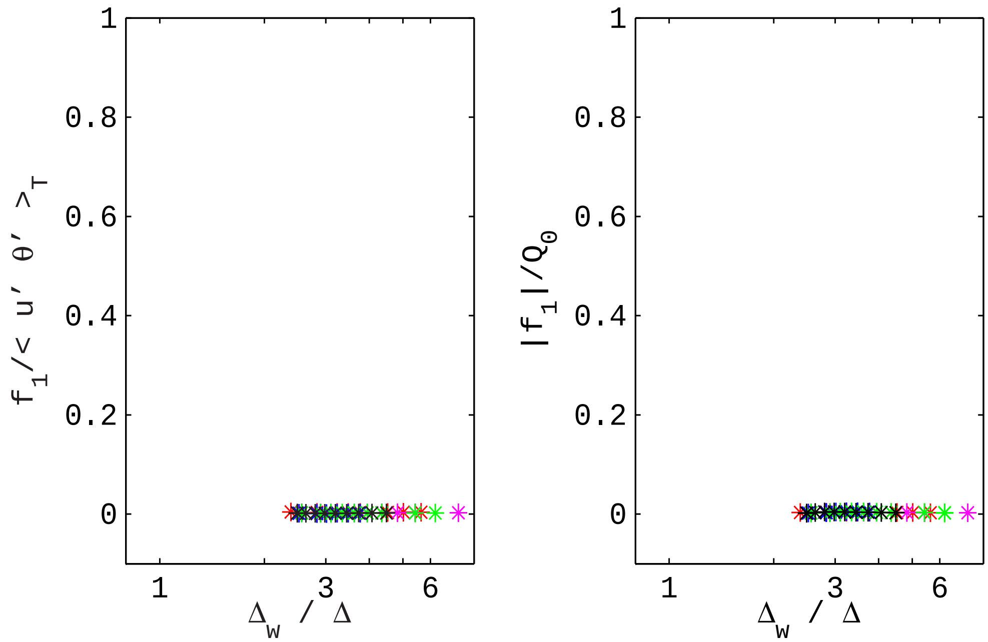

Figure 2.38. LES, eddy-diffusivity closure: SFS horizontal flux of potential temperature, f_1, as a fraction of the total flux (left) and of the surface flux, Q_0 (right). Color legend: ——— : $-z_i/L = 1.21$, ——— : $-z_i/L = 3.78$, ——— : $-z_i/L = 3.82$, ——— : $-z_i/L = 5.47$, ——— : $-z_i/L = 7.2$

As our implementation of the SFS conservation equations includes one of these terms, i.e., anisotropic gradient-production, but not the other, in principle, we should see reduced magnitudes of f_3 at lower Δ_w/Δ. This is not observed due to the underprediction of anisotropic gradient-production which minimizes — artificially — the negative impact of neglecting buoyant production. Thus, the scaled magnitudes of f_3 predicted by the two closures do not differ appreciably although they are underpredicted compared to observations.

2.5.10 SFS scalar fluxes: fluctuations

In Fig. (2.41) we show the rms values of f_1 and f_3 normalized with the magnitudes of their respective means, as obtained from HATS data. Corresponding plots from LES using the SFS conservation equations and the eddy-diffusivity closure are shown in Fig.(2.42) and Fig. (2.43), respectively.

The HATS data in Fig. (2.41) exhibit normalized fluctuations that increase

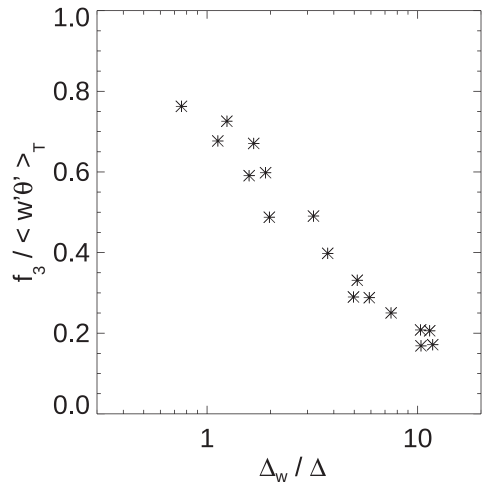

Figure 2.39. HATS: SFS vertical flux of potential temperature, f_3, normalized with the total flux, $\langle w'\theta'\rangle_T$.

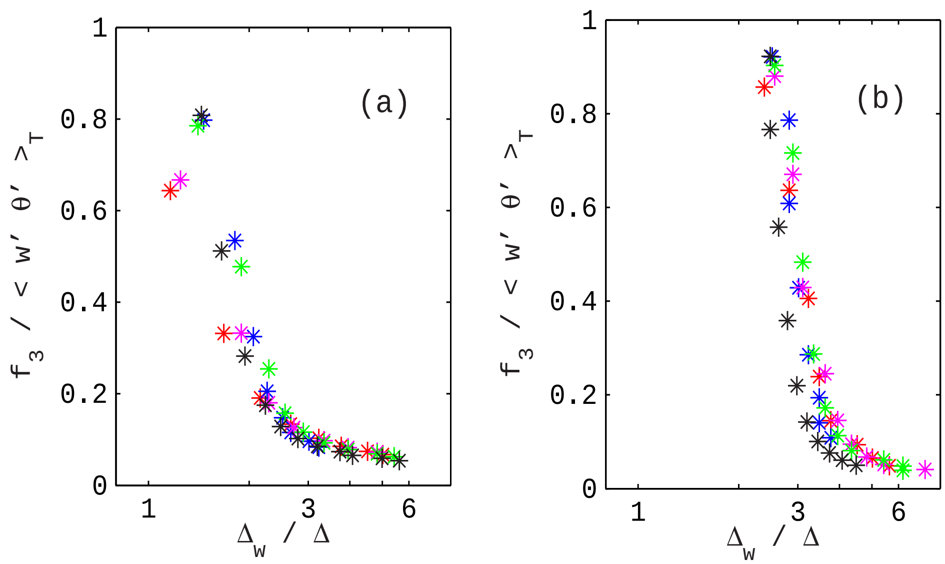

Figure 2.40. LES: SFS vertical flux of potential temperature, f_3, as a fraction of the total flux, using (a) SFS conservation equations; and (b) eddy-diffusivity closure. Color legend: —— : $-z_i/L = 1.21$, —— : $-z_i/L = 3.78$, —— : $-z_i/L = 3.82$, —— : $-z_i/L = 5.47$,—— : $-z_i/L = 7.2$

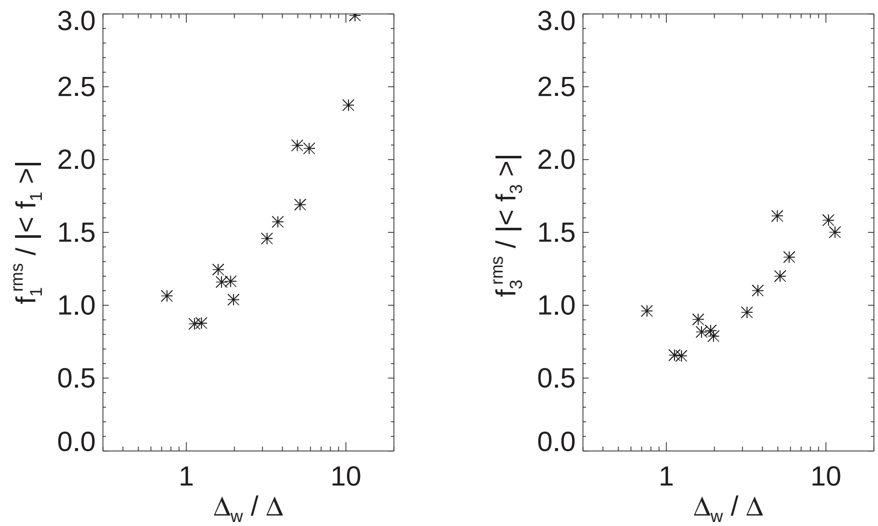

Figure 2.41. HATS: Root mean square values of f_1 (left panel) and f_3 (right panel) normalized with the magnitudes of their respective means.

monotonically with Δ_w/Δ. The SFS conservation equations underpredict the magnitudes of the normalized fluctuations at lower Δ_w/Δ but yield better predictions at higher Δ_w/Δ, although the normalized f_3 fluctuations are underpredicted slightly at higher Δ_w/Δ. The eddy-diffusivity closure yields very high magnitudes of the normalized f_1 fluctuations because it predicts near-zero mean values of f_1, as seen earlier. In contrast to HATS data, it yields symmetrical trends in the normalized f_1 fluctuations wherein they attain nearly equal values at both low and high Δ_w/Δ.

The predictions of the normalized f_3 fluctuations by the eddy-diffusivity closure become increasingly sensitive to z_i/L with decreasing Δ_w/Δ. We observe similar trends in its predictions of τ_{13}^d.

2.5.11 Summary

In this section, we used surface-layer HATS data to compare the performance of the SFS conservation equations and an eddy-diffusivity closure. In particular, we considered the following: (i) production terms in the SFS stress budgets; (ii) production terms in the SFS flux budgets; (iii) SFS stresses; (iv) SFS fluxes; and (v)

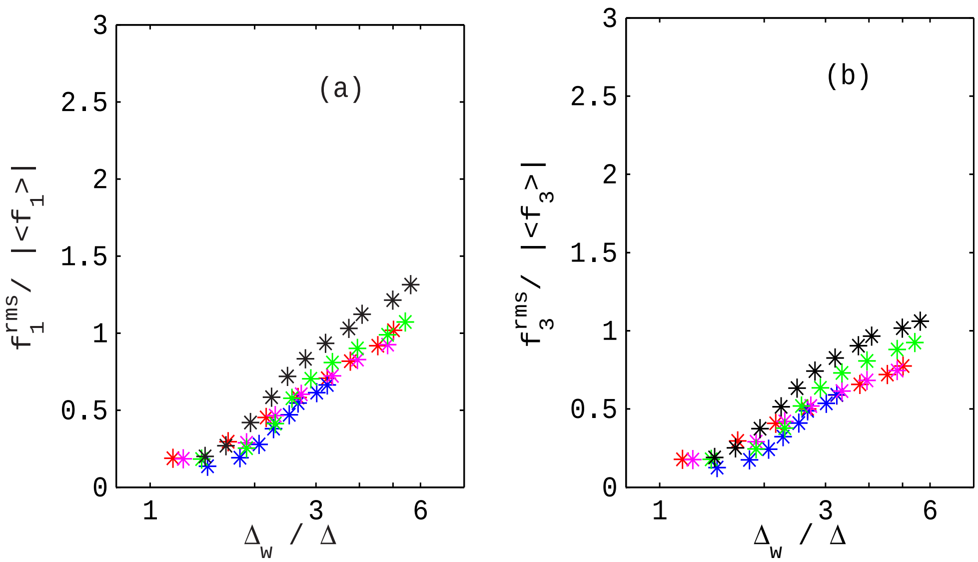

Figure 2.42. LES, SFS conservation equations: Root mean square values of (a) f_1 and (b) f_3, normalized with the magnitudes of their respective means. Color legend: —— : $-z_i/L = 1.21$, —— : $-z_i/L = 3.78$, —— : $-z_i/L = 3.82$, —— : $-z_i/L = 5.47$,—— : $-z_i/L = 7.2$

fluctuations in SFS stresses and fluxes. We obtained these statistics by combining results from high-resolution LES runs corresponding to different domain sizes, filter widths and stability conditions. The runs were designed to mimic partly the different physical conditions and filter widths associated with the HATS experiments. Following Sullivan (2010), we studied the trends in the statistics listed above by plotting them against the nondimensional parameter Δ_w/Δ, where Δ_w is the wavelength of the vertical velocity spectral peak and Δ is the filter width.

We found that the modeled SFS stress budgets were able to replicate some trends in the observed SFS stress budgets better than others. They reproduced successfully the dominance of anisotropic production in the $\tau^d_{\alpha\alpha}$ budgets and that of isotropic production in the τ^d_{13} budget, but failed to exhibit the sharp increase in the magnitude of anisotropic production in the τ^d_{13} budget at low Δ_w/Δ, as observed in the HATS data. Advection and buoyant effects were negligible in the SFS budgets. We showed that the dominant production terms in the modeled $\tau^d_{\alpha\alpha}$ and τ^d_{13} budgets, i.e., anisotropic- and isotropic-production, respectively, approach constant values at low Δ_w/Δ. We showed that these limiting values for the τ^d_{11}

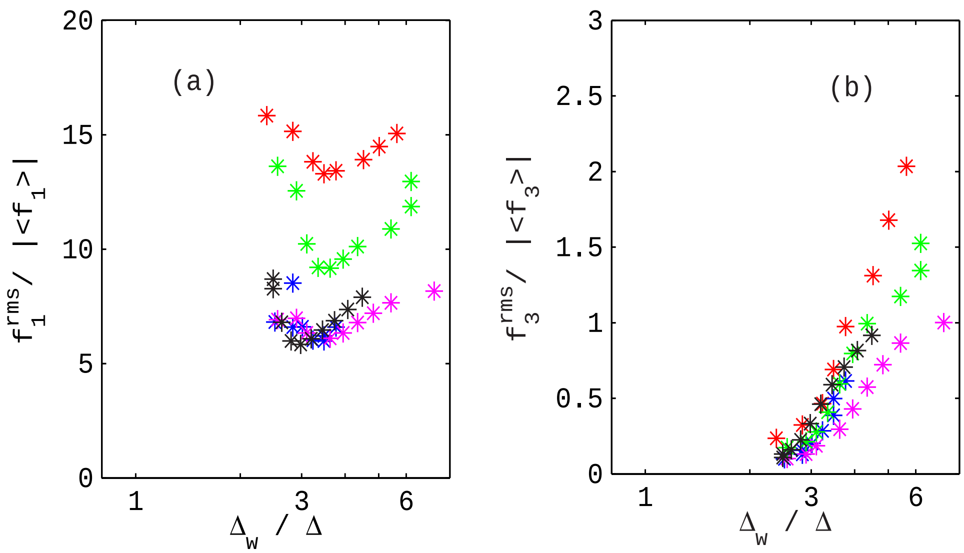

Figure 2.43. LES, eddy-diffusivity closure: Root mean square values of (a) f_1 and (b) f_3, normalized with the magnitudes of their respective means. Color legend: —— : $-z_i/L = 1.21$, —— : $-z_i/L = 3.78$, —— : $-z_i/L = 3.82$, —— : $-z_i/L = 5.47$,—— : $-z_i/L = 7.2$

and τ_{33}^d budgets are in good agreement with theoretically derived values for the dominant production terms in the limit $\Delta_w/\Delta \to 0$. The limiting values for the τ_{22}^d and τ_{13}^d budgets obtained from LES were found to be lesser in magnitude than their corresponding theoretical values.

The eddy-viscosity closure underpredicted severely the magnitudes of the deviatoric components, $|\tau_{\alpha\alpha}^d|$, and consequently the level of SFS anisotropy. This is because such closures depend solely on isotropic production, which observations show plays an increasingly insignificant role in the $\tau_{\alpha\alpha}^d$ budgets as Δ_w/Δ decreases. The SFS conservation equations yielded more realistic magnitudes of $\tau_{\alpha\alpha}^d$ reflecting the underlying SFS anisotropy, but the magnitudes were nevertheless lesser than those obtained from HATS data. One possible reason for the underprediction of SFS anisotropy by the conservation equations could be that the model for pressure-strain-rate covariance used in this study neglects contributions from the rapid pressure component, which is expected to be significant in the shear-dominated surface layer.

At low Δ_w/Δ, the normalized rms values of τ_{11}^d and τ_{33}^d are underpredicted by the SFS conservation equations and the eddy-diffusivity closure. At high Δ_w/Δ, they are better predicted by the SFS conservation equations. The normalized fluctuations of τ_{13}^d at low Δ_w/Δ tend to be underpredicted by both closures. They continue to be underpredicted by the SFS conservation equations at higher Δ_w/Δ while their predictions by the eddy-diffusivity closure become overly sensitive to z_i/L, exhibiting a spread of 100% across the range of z_i/L considered.

The HATS data revealed that the dominant production terms in the f_1 budget are tilting and anisotropic gradient-production while isotropic gradient-production is negligible. The eddy-viscosity closure used in our study, which accounted only for isotropic gradient production, predicted near-zero values for f_1 across the entire range of Δ_w/Δ, in agreement with previous studies by Hatlee and Wyngaard (2007). The modeled conservation equations account for flux tilting and anisotropic gradient-production and hence, yielded more realistic predictions of f_1.

Using HATS data, we found the dominant mode of production in the f_3 budget to be isotropic gradient-production. At low values of Δ_w/Δ, buoyant production and anisotropic gradient-production were found to be significant individually, although their magnitudes were nearly equal and opposite in sign, thereby diminishing the net influence of the two terms in the f_3 budget. This explains why the eddy-diffusivity closure, which lacks both buoyant production and anisotropic gradient-production, still predicts reasonably accurate values of f_3. The SFS conservation equations predicted isotropic production to be the dominant mode of production in the f_3 budget but failed to reproduce the marked increase in anisotropic gradient-production at lower Δ_w/Δ, seen in observations. This underprediction of anisotropic gradient-production — which is caused partly due to the underprediction of $|\tau_{33}^d|$ — compensates for the lack of buoyant production in the SFS flux conservation equations, with the net result that they yield satisfactory predictions of f_3.

The SFS conservation equations yield reasonable predictions of the normalized rms values of f_1 while the predictions by the eddy-diffusivity closure are poor in both magnitude and trend. The normalized rms values of f_3 are underpredicted by both closures at low Δ_w/Δ. As Δ_w/Δ increases, the modeled SFS conservation equations yield better predictions than the eddy-diffusivity closure, whose predictions become highly sensitive to z_i/L.

2.6 Conditional means of SFS stress and SFS production rate

In the previous sections, we analyzed the relative significance of various terms in the modeled SFS conservation equations using coarse-resolution LES and simple qualitative arguments. Using high-resolution LES, we then compared trends in the variation of SFS production terms and other SFS statistics with Δ_w/Δ, to those observed in the HATS data. In this section, we explore further the performance of the SFS conservation equations using criteria developed by Chen and Tong (2006).

2.6.1 Evolution equation for the resolved-scale velocity jpdf

In order to isolate the influence of the SFS model on resolved-scale statistics, Chen and Tong (2006) focused on the evolution equation of the one-time one-point joint probability density function (jpdf) of the resolved-scale velocity field. The significance of the one-time one-point resolved-scale velocity jpdf lies in the fact that it determines completely the entire set of resolved-scale velocity statistics (means, variances, covariances, etc.) locally in time and space. that describe the velocity field. If f denotes the jpdf of the resolvable-scale velocity field, its evolution is given by (Chen and Tong, 2006),

$$\begin{aligned}\frac{\partial f}{\partial t}+v_j\frac{\partial f}{\partial x_j} \quad = \quad & \frac{\partial^2}{\partial v_i \partial x_j}\{\langle \tau_{ij}|\mathbf{u}^r=\mathbf{v}\rangle f\}+\frac{\partial^2}{\partial v_i \partial x_i}\{\langle p^r|\mathbf{u}^r=\mathbf{v}\rangle f\} \\ & +\frac{\partial^2}{\partial v_i \partial v_j}\left\{\left\langle -\frac{1}{2}P_{ij}\middle|\mathbf{u}^r=\mathbf{v}\right\rangle f\right\} \\ & +\frac{\partial^2}{\partial v_i \partial v_j}\left\{\left\langle p^r\frac{\partial u_j^r}{\partial x_i}\middle|\mathbf{u}^r=\mathbf{v}\right\rangle f\right\} \\ & -\frac{g}{\Theta_0}\frac{\partial}{\partial v_3}\{\langle \theta^r|\,\mathbf{u}^r=\mathbf{v}\rangle f\} \end{aligned} \tag{2.35}$$

In Eq. (2.35), the superscript r, as in $\mathbf{u}^r$, denotes resolved-scale quantities and the angled brackets denote ensemble averaging. The right hand side represents, sequentially, mixed transport in physical and velocity spaces by the conditional SFS stress and the resolvable-scale pressure, and transport in velocity space by the conditional SFS stress production rate, $\langle -(1/2)P_{ij}|\mathbf{u}^r=\mathbf{v}\rangle$, the conditional resolvable-scale pressure-strain correlation, and the conditional resolvable-scale buoyancy force where,

$$P_{ij} = -\left\{\tau_{ik}\frac{\partial u_j^r}{\partial x_k} + \tau_{jk}\frac{\partial u_i^r}{\partial x_k}\right\}. \tag{2.36}$$

In Eq. (2.36), τ_{ik} refers to the total kinematic stress and not the deviatoric stress. Equation (2.35) is a modified form of the jpdf equation studied by Meneveau (1994), as it demonstrates explicitly the dependence of f, and hence resolved-scale statistics, on the SFS production rate, P_{ij}. From Eq. (2.35), the evolution equation of the resolvable-scale velocity joint-pdf has two terms that involve direct contributions from the SFS model: (i) the conditional SFS stress; and (ii) the conditional SFS production rate. Chen and Tong (2006) argued that in order to obtain realistic resolvable-scale velocity statistics, it is necessary that an SFS model yield good predictions of the conditional SFS stress and the conditional SFS production. In LES, we typically model the deviatoric stress, τ_{ij}^d, and hence, it is natural to define the SFS deviatoric production rate, P_{ij}^d:

$$P_{ij}^d = -\left\{\tau_{ik}^d\frac{\partial u_j^r}{\partial x_k} + \tau_{jk}^d\frac{\partial u_i^r}{\partial x_k}\right\}. \tag{2.37}$$

P_{ij} and P_{ij}^d are related as follows:

$$P_{ij} = P_{ij}^d - \frac{4}{3}\, eS_{ij}^r \quad ; \; S_{ij}^r = \frac{1}{2}\left(\frac{\partial u_i^r}{\partial x_j} + \frac{\partial u_j^r}{\partial x_i}\right) \tag{2.38}$$

where e is the SFS kinetic energy. As the term eS_{ij}^r doesn't depend directly on the SFS model, we will henceforth focus only on the deviatoric SFS production rate, P_{ij}^d, as we want to study the direct influence of the SFS model on the resolved-scale velocity jpdf. It is straightforward to show that the rate at which energy is extracted from the resolved scales by the SFS model is equal to one-half the trace of P_{ij}. As P_{ij} and P_{ij}^d have the same trace ($S_{ii}^r = 0$, by incompressibility), accurate predictions of P_{ij}^d are essential to ensure the right amount of energy extraction by the SFS model.

2.6.2 Procedure for obtaining conditional means

Our primary motivation behind studying the conditional means of τ_{ij}^d and P_{ij}^d is to understand how they relate to resolved-scale statistics. We present in Fig. (2.44) the following two statistics describing the velocity field: (i) $\phi_m = (\kappa z/u_*)\,(\partial\langle\bar{u}\rangle/\partial z)$, the nondimensional mean-gradient of velocity; and (ii) the vertical velocity skewness, $S_w = \langle\overline{w}^3\rangle/\langle w'w'\rangle^{3/2}$. We show LES results obtained using both the modeled SFS conservation equations and the eddy-diffusivity closure. Note that we didn't find significant differences between the velocity variance profiles for the two SFS models. The parameter $\kappa = 0.4$ denotes the von Kármán constant. The physical conditions describing the runs are identical to those described in Table 2.1. The numerator in the expression for skewness includes only the resolved-scale component of vertical velocity as we do not solve for its SFS component. Observations indicate that S_w is positive everywhere in the convective ABL, increases with height, and attains a maximum of ≈ 0.8 in the upper third of the boundary layer (Hogan et al., 2009; Lenschow et al., 1980). Figure (2.44) reveals that the predictions of ϕ_m and S_w by the SFS conservation equations are slightly better than those by the eddy-diffusivity closure.

We now proceed to compare the conditional means of τ_{ij}^d and P_{ij}^d obtained from LES with those from the HATS data. Only the (1,1), (2,2), (3,3) and (1,3) components of τ_{ij}^d and P_{ij}^d are considered in our analysis. In order to make a meaningful comparison between HATS data and LES results, we ensure that Δ/z ($\Delta/\Delta_w \sim \Delta/z$ in the surface layer) for both the HATS data and our LES runs are nearly equal, where z is the height at which the conditional means are computed. We use HATS data from the 'Array 2' configuration which has $\Delta/z \approx 2$ and $z/L = -0.4$. The LES runs have $z_1/L = -0.09$, where z_1 refers to the first grid level, and $z_i/L = -7.2$, which corresponds to a moderately convective ABL. The conditional means are obtained at $z = z_1$, such that $\Delta/z_1 = 2$. Chen and Tong (2006) found the conditional statistics to be dependent primarily on Δ/z while z/L played only a secondary role in the form of a stability correction. The values of the SFS model constants used are given by $(c_\tau, c_\theta) = (0.10, 0.19)$ for the SFS conservation equations and $c_k = 0.10$ for the eddy-diffusivity closure.

Following Chen et al. (2009), we compute conditional means by conditioning only on two velocity components instead of all three, owing to the limited amount

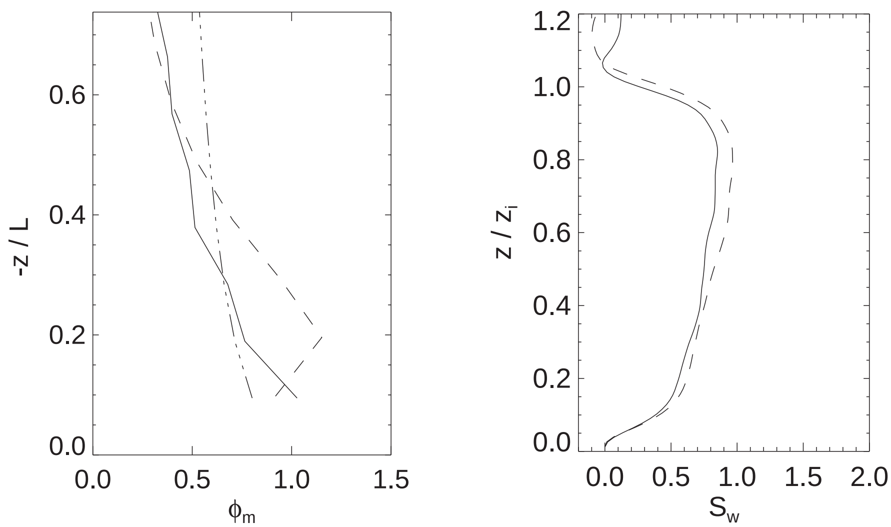

Figure 2.44. Left panel: Nondimensional mean gradient of velocity, ϕ_m, versus $-z/L$, where L is the Monin-Obukhov length. The top of the layer shown corresponds to $z/z_i = 0.1$. Legend – Solid line : modeled SFS conservation equations, dashed line : eddy-diffusivity closure, dot-dash line : empirical fit (Businger et al., 1971). Right panel: Vertical velocity skewness, $S_w = \langle \overline{w}^3 \rangle / \langle w'w' \rangle^{3/2}$. Legend – Solid line : modeled SFS conservation equations, dashed line : eddy-diffusivity closure.

of HATS data. They showed that conditioning using only two velocity components was sufficient to ensure statistical convergence. For P^d_{11}, P^d_{33} and P^d_{13} we choose u and w as the conditioning variables while for P_{22} we pick v and w as the conditioning variables. We plot the conditional means against the first conditioning variable for different values of the second conditioning variable. We split the first conditioning variable into 8 data bins covering $\pm$ 1.8 standard deviations and the second conditioning variable into 5 data bins also covering $\pm$ 1.8 standard deviations.

There are some constraints on choosing the number of bins and the width of the conditioning variable. A large number of bins (i.e., small bin sizes) yields the underlying trend but makes statistical convergence harder to achieve as each bin might not have a sufficient number of samples. Too few bins will ensure convergence but might smooth out trends of interest. Choosing a large width (i.e., many standard deviations wide) for the conditioning variables gives us more information about events at the tails of their pdfs but that information is also less reliable due to decreased convergence, as events at the tails occur rarely. In spite of these constraints, Chen and Tong (2006) achieved reasonable convergence in their statistics and demonstrated that we can draw important conclusions based on the trends exhibited by the conditional means of τ_{ij}^d and P_{ij}^d. In the ensuing discussion, we denote u, v and w as u_1^r, u_2^r and u_3^r, respectively.

2.6.3 HATS: Conditional means of P_{ij}^d

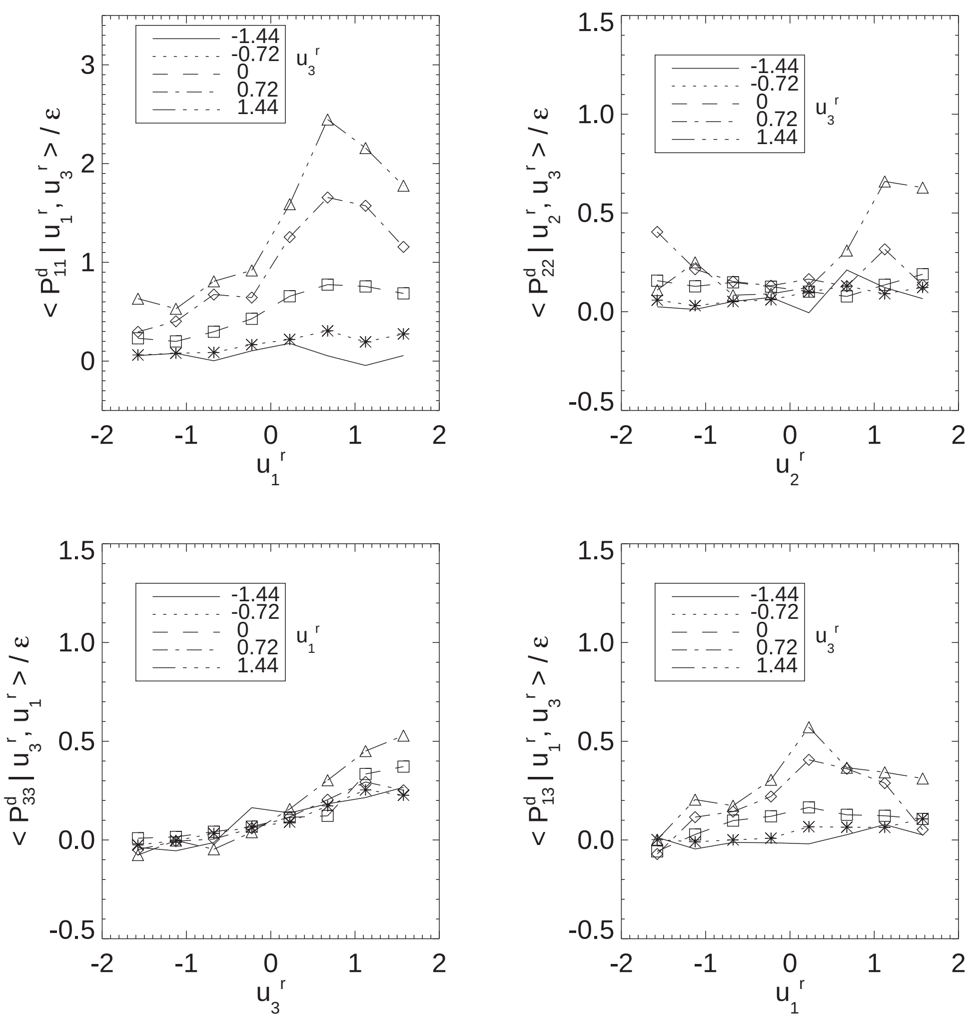

Figure 2.45. HATS: Conditional means of SFS production rate.

In Fig. (2.45), we show the conditional means of the deviatoric production rate, obtained from HATS data. Only the diagonal and (1,3) components are shown.

We now summarize arguments put forth by Chen and Tong (2006) in order to understand the trends exhibited in Fig. (2.45).

2.6.3.1 $\left\langle P_{11}^{d} \middle| u_1^r, u_3^r \right\rangle$

The conditional mean of P_{11}^d, denoted by $\langle P_{11}^d | u_1^r, u_3^r \rangle$, increases with increasing u_3^r. Its dependence on u_1^r is weak for negative u_3^r but considerably more pronounced for positive u_3^r. Expanding $\langle P_{11}^d | u_1^r, u_3^r \rangle$, we obtain,

$$\left\langle P_{11}^d | u_1^r, u_3^r \right\rangle = -2 \left\langle \tau_{11}^d \frac{\partial u_1^r}{\partial x_1} + \tau_{12}^d \frac{\partial u_1^r}{\partial x_2} + \tau_{13}^d \frac{\partial u_1^r}{\partial x_3} \middle| u_1^r, u_3^r \right\rangle \tag{2.39}$$

For positive u_3^r, $(\partial u_3^r / \partial x_3) > 0$ on average in an unstable ABL due to positive buoyant forcing, which implies $(\partial u_1^r / \partial x_1) < 0$ and $(\partial u_2^r / \partial x_2) < 0$, from incompressibility. Positive u_3^r also represents advection of τ_{11}^d from near the ground where $\left\langle \tau_{11}^d \right\rangle > 0$, due to strong SFS anisotropy induced by the presence of a mean wind along the x_1 direction. Thus, the term associated with the normal strain, $-\left\langle \tau_{11}^d \left(\partial u_1^r / \partial x_1 \right) \middle| u_1^r, u_3^r \right\rangle$, is positive on average. Among the terms associated with the shear strain, $-\left\{ \tau_{12}^d \left(\partial u_1^r / \partial x_2 \right) + \tau_{13}^d \left(\partial u_1^r / \partial x_3 \right) \right\}$, the second is strongly dependent on u_3^r. When $u_3^r > 0$, τ_{13}^d is advected from near the surface, where it is negative and assumes large magnitudes. Simultaneously, $u_3^r > 0$ is associated with positive values of $(\partial u_1^r / \partial x_3)$ on average, as the updrafts are originating from near the ground, a region of high shear. As u_3^r becomes more positive, the above effects on both the normal- and shear-strain terms are enhanced. Thus, when $u_3^r > 0$, $\langle P_{11}^d | u_1^r, u_3^r \rangle$ is generally positive and its magnitude increases with increasing u_3^r.

When u_3^r is negative, $(\partial u_3^r / \partial x_3) < 0$ on average and from incompressibility it follows that $(\partial u_1^r / \partial x_1) > 0$ and $(\partial u_2^r / \partial x_2) > 0$. Thus, the term associated with the normal strain is negative. The shear-strain related terms remain positive for reasons similar to those discussed above for $u_3^r > 0$. Observations (Chen and Tong, 2006) show that the terms associated with the shear strain are greater in magnitude than those associated with the normal strain, with the net effect that $\langle P_{11}^d | u_1^r, u_3^r < 0 \rangle$ is positive, although the competition among its various terms implies that it is lesser in magnitude when $u_3^r < 0$ than when $u_3^r > 0$. As u_3^r becomes more negative, the magnitude of $\partial u_1^r / \partial x_1$ increases, from incompressibility. The advection effect, however, is much weaker as τ_{11}^d and τ_{13}^d are being advected from the higher regions where the SFS stresses are negligible. For similar reasons, the values of $(\partial u_1^r/\partial x_3)$ associated with $u_3^r < 0$, on average, are lesser than those associated with $u_3^r > 0$. Consequently, $\langle P_{11}^d | u_1^r, u_3^r \rangle$ exhibits a weaker dependence on u_3^r when $u_3^r < 0$ than when $u_3^r > 0$.

Fig. (2.45) shows that $\langle P_{11}^d | u_1^r, u_3^r \rangle$ depends weakly on u_1^r for $u_3^r < 0$ but this dependence is enhanced for $u_3^r > 0$. Compared to $-\tau_{11}^d \left(\partial u_1^r/\partial x_1 \right)$, the terms associated with the shear strain vary more strongly with u_1^r (Chen and Tong, 2006). In particular, when $u_3^r > 0$, a larger value of u_1^r is associated with a larger magnitude of $\partial u_1^r/\partial x_3$, due to "no-slip" at the wall. This effect is further enhanced as u_3^r increases. In contrast, when $u_3^r < 0$, a larger value of u_1^r is not associated with greater shear on average, as the shear in the region above 'z' is lesser, on average, than that in the region below 'z' due to the presence of a lower boundary. This is true of increasingly negative u_3^r as well. Thus, the dependence of $\left\langle P_{11}^d | u_1^r, u_3^r \right\rangle$ on u_1^r is enhanced more by positive u_3^r than by negative u_3^r.

Finally, we note that $\left\langle P_{11}^d \middle| u_1^r, u_3^r \right\rangle$ is almost always positive. Recall that the rate of transfer of energy from the resolved to the subfilter scales is equal to one-half the trace of P_{ij}^d. Thus the abundance of positive values of $\left\langle P_{11}^d \middle| u_1^r, u_3^r \right\rangle$ indicates negligible amounts of conditional backscatter associated with τ_{11}^d.

2.6.3.2 $\left\langle P_{22}^d \middle| u_2^r, u_3^r \right\rangle$

From Fig. (2.45), $\left\langle P_{22}^d \middle| u_2^r, u_3^r \right\rangle$ has smaller magnitudes than $\left\langle P_{22}^d \middle| u_2^r, u_3^r \right\rangle$ and exhibits weaker dependencies on u_2^r and u_3^r. This is due to the lack of mean wind in the x_2 direction which leads to reduced magnitudes of τ_{23}^d and $(\partial u_2^r/\partial x_3)$. The dependence of $\langle P_{22}^d | u_2^r, u_3^r \rangle$ on u_3^r can be explained using arguments similar to those applicable to $\langle P_{11}^d | u_1^r, u_3^r \rangle$. The trends in $\left\langle P_{22}^d \middle| u_2^r, u_3^r \right\rangle$ with respect to u_2^r are weakly symmetrical such that its magnitude depends on $|u_2^r|$. If there were no Coriolis force, we would expect symmetry in the x_2 direction due to the absence of mean wind in that direction. In the ABL, however, the presence of Coriolis force disturbs the lateral symmetry.

2.6.3.3 $\left\langle P_{33}^d \middle| u_3^r, u_1^r \right\rangle$

The conditional mean of P_{33}^d exhibits a marked asymmetric dependence on u_3^r wherein it attains higher values for $u_3^r > 0$ than for $u_3^r < 0$, which can be explained as follows. The dominant term in P_{33}^d is $-\tau_{33}^d \left(\partial u_3^r / \partial x_3\right)$ (Chen and Tong, 2006), which on average, is positive for $u_3^r > 0$ and negative for $u_3^r < 0$, due to continuity and strong anisotropy near the surface. As u_3^r becomes more positive, both τ_{33}^d and $(\partial u_3^r / \partial x_3)$ increase in magnitude on average, due to stronger advection effects and positive buoyant acceleration, respectively. It follows that P_{33}^d increases in magnitude with positively increasing u_3^r. As u_3^r becomes increasingly negative, the magnitude of $(\partial u_3^r / \partial x_3)$, on average, increases but that of τ_{33}^d decreases due to advection from higher regions with negligible SFS stresses. These two competing effects yield magnitudes of P_{33}^d that are much lesser for $u_3^r < 0$ than for $u_3^r > 0$.

The negative values of u_3^r are associated with negative $\left\langle P_{33}^d \middle| u_3^r, u_1^r \right\rangle$, which represents conditional backscatter.

2.6.3.4 $\left\langle P_{13}^d \middle| u_1^r, u_3^r \right\rangle$

The conditional mean of P_{13}^d is largely positive and increases weakly with u_1^r for $u_3^r < 0$ but $u_3^r > 0$ enhances its dependence on u_1^r. The dominant term in P_{13}^d is $-\tau_{33}^d \left(\partial u_1^r / \partial x_3\right)$ (Chen and Tong, 2006), which is positive on average, for both $u_3^r > 0$ and $u_3^r < 0$, due to strong anisotropy $(\left\langle \tau_{33}^d \right\rangle < 0)$ and positive vertical shear. The trends, however, are qualitatively different for $u_3^r > 0$ and $u_3^r < 0$. When $u_3^r > 0$, a larger value of u_1^r implies on average, larger magnitudes of $(\partial u_1^r / \partial x_3)$. For higher values of u_3^r, these effects are more pronounced due to stronger advection effects and thus, the dependence of $\left\langle P_{13}^d \middle| u_1^r, u_3^r \right\rangle$ on u_1^r is enhanced by positive values of u_3^r. When $u_3^r < 0$, advection from the higher regions is much weaker due to decreased magnitudes of SFS stresses and vertical shear. Hence, $\left\langle P_{13}^d \middle| u_1^r, u_3^r \right\rangle$ exhibits a weaker dependence on u_3^r when $u_3^r < 0$.

2.6.4 LES: Conditional means of P_{ij}^d

In the previous section, we summarized the arguments of Chen and Tong (2006) explaining the trends exhibited by the conditional means of P_{ij}^d in Fig. (2.45). In this section, we compute the same using LES with two SFS models: the SFS conservation equations and an eddy-diffusivity closure. Chen et al. (2009) have presented LES results using an eddy-diffusivity closure identical to the one in our study. We include results from the eddy-diffusivity closure, nevertheless, for the sake of comparison. Our goal here is to examine whether the SFS conservation equations are able to reproduce the trends in Fig. (2.45), and to contrast their performance with that of an eddy-diffusivity closure.

In Figs. (2.46)-(2.47), we plot the conditional means of P^d_{ij} using the eddy-diffusivity closure and the SFS conservation equations, respectively. As in Fig. (2.45), only the diagonal and (1,3) components of P^d_{ij} are shown.

2.6.4.1 $\left\langle P^d_{11} \middle| u^r_1, u^r_3 \right\rangle$

Both closures yield reasonable magnitudes of $\left\langle P^d_{11} \middle| u^r_1, u^r_3 \right\rangle$ but overstate its dependence on u^r_1 when $u^r_3 < 0$. We recall that in the case of HATS data, $\left\langle P^d_{11} \middle| u^r_1, u^r_3 \right\rangle$ varies strongly with u^r_1 only for positive u^r_3. The tendency of $\left\langle P^d_{11} \middle| u^r_1, u^r_3 \right\rangle$ to increase with u^r_3 — due to advection effects — is captured by both the closures. The influence of advection for $u^r_3 > 0$ is more marked for the SFS conservation equations as they account explicitly for SFS advection. In the HATS data, $\left\langle P^d_{11} \middle| u^r_1, u^r_3 \right\rangle$ exhibits very little conditional backscatter. The eddy-diffusivity closure is incapable of exhibiting backscatter, a constraint which follows from its definition. Figure. (2.47) shows that the SFS conservation equations, which are capable of exhibiting backscatter, also fail to yield any conditional backscatter over the range of (u^r_1, u^r_3) considered.

2.6.4.2 $\left\langle P^d_{22} \middle| u^r_2, u^r_3 \right\rangle$

The conditional means of P^d_{22} predicted by both closures are very similar to each other. $\left\langle P^d_{22} \middle| u^r_2, u^r_3 \right\rangle$ is nearly symmetric with respect to u^r_2 as its magnitude increases with u^r_2. The conditional means exhibit weak dependence on u^r_3 as the advection effects are much smaller for P^d_{22} than for P^d_{11}. These trends agree with the HATS data qualitatively, except at the extremes of the u^r_2 distribution where the conditional means obtained from LES are lesser than those obtained from HATS.

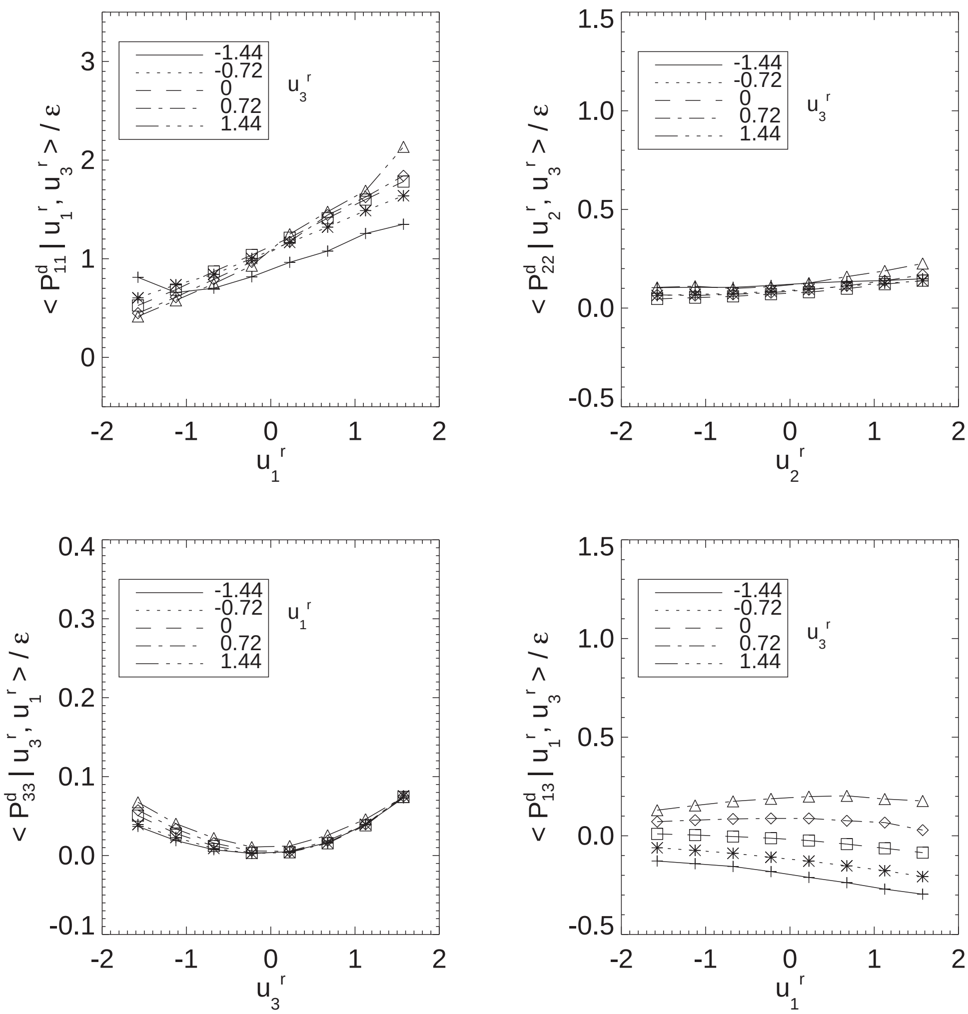

Figure 2.46. LES: Conditional means of SFS deviatoric production rate using an eddy-diffusivity closure.

2.6.4.3 $\left\langle P_{33}^{d} \middle| u_3^r, u_1^r \right\rangle$

Both closures underpredict $\left\langle P_{33}^{d} \middle| u_1^r, u_3^r \right\rangle$ compared to HATS data, at the positive end of the u_3^r distribution. The eddy-diffusivity closure is unable to differentiate between the qualitatively different effects of updrafts and downdrafts, as evident from the nearly symmetrical shape of $\left\langle P_{33}^{d} \middle| u_1^r, u_3^r \right\rangle$. The SFS conservation equations reproduce to some degree the asymmetry in $\left\langle P_{33}^{d} \middle| u_3^r, u_1^r \right\rangle$. The SFS conservation equations exhibit very small amounts of conditional backscatter for $u_3^r < 0$ that is

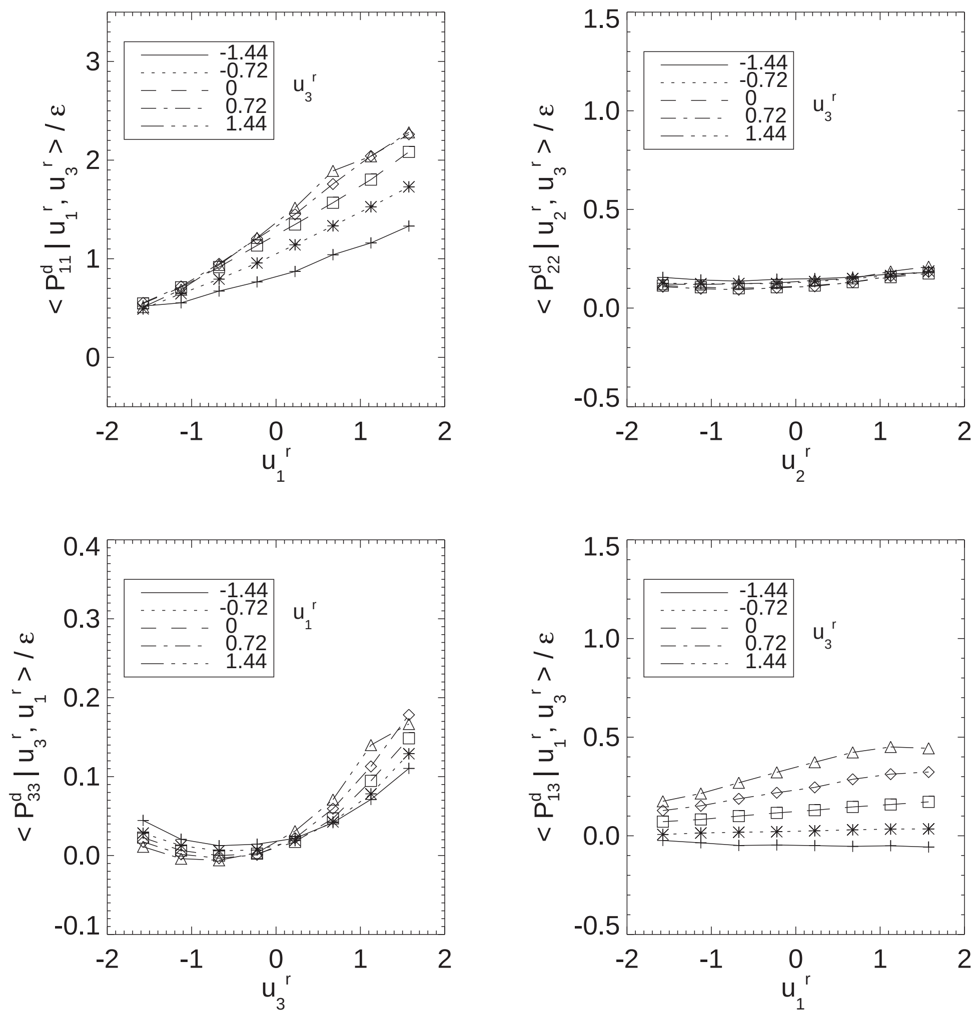

Figure 2.47. LES: Conditional means of SFS deviatoric production rate using the SFS conservation equations.

considerably lesser than that observed in the HATS data.

2.6.4.4 $\left\langle P_{13}^d \middle| u_1^r, u_3^r \right\rangle$

The eddy-diffusivity closure predicts incorrectly both the magnitudes and trends of $\left\langle P_{13}^d \middle| u_1^r, u_3^r \right\rangle$. The positive magnitudes are under-predicted while the negative magnitudes are over-predicted, in comparison to observations. The variation of $\left\langle P_{13}^d \middle| u_1^r, u_3^r \right\rangle$ with u_3^r is slightly stronger for negative u_3^r than for positive u_3^r, which is qualitatively opposite to what we see in observations.

The SFS conservation equations yield reasonable predictions of $\left\langle P_{13}^d \middle| u_1^r, u_3^r \right\rangle$, both in magnitude and trend. The magnitudes are in good agreement with observations, while the dependence on u_3^r reproduces correctly the effects of advection on $\left\langle P_{13}^d \middle| u_1^r, u_3^r \right\rangle$.

2.6.5 HATS: Conditional means of τ_{ij}^d

In the previous section, we contrasted the conditional means of P_{ij}^d obtained from HATS data and from LES. In this section, we analyze the other term in the evolution equation for the resolved-scale jpdf that is influenced directly by the SFS model: the conditional mean of τ_{ij}^d.

In Fig. (2.48) we show the conditional means of the SFS stresses obtained from HATS data. Only the diagonal and (1,3) components are shown. Before comparing the HATS results with LES, we review briefly the explanations provided by Chen and Tong (2006) for the trends observed in Fig. (2.48).

2.6.5.1 $\langle \tau_{11}^d | u_1^r, u_3^r \rangle$

The conditional means of τ_{11}^d attain mostly positive magnitudes due to strong SFS anisotropy near the surface, where $\langle \tau_{11}^d \rangle > 0$ and $\langle \tau_{33}^d \rangle < 0$. The dependence of $\langle \tau_{11}^d \rangle$ on u_1^r is weak for negative u_3^r and stronger for positive u_3^r, similar to the trends observed in $\langle P_{11}^d | u_1^r, u_3^r \rangle$. The enhanced dependence of $\langle \tau_{11}^d | u_1^r, u_3^r \rangle$ on u_1^r for $u_3^r > 0$ is due to advection of τ_{11}^d from near the surface where it attains high values.

2.6.5.2 $\langle \tau_{22}^d | u_2^r, u_3^r \rangle$

The conditional means of τ_{22}^d, like those of P_{22}^d, fail to exhibit symmetry with respect to u_2^r. The advection effects are considerably weaker than for τ_{11}^d as magnitudes of τ_{22}^d near the surface are much less than those of τ_{11}^d.

2.6.5.3 $\langle \tau_{33}^d | u_1^r, u_3^r \rangle$

Strong anisotropy near the surface yields mostly negative values for $\langle \tau_{33}^d | u_1^r, u_3^r \rangle$. The magnitude of $\langle \tau_{33}^d | u_1^r, u_3^r \rangle$ increases with u_3^r due to advection from near the surface. When $u_3^r > 0$, increasingly positive values of u_1^r, on average, are associated

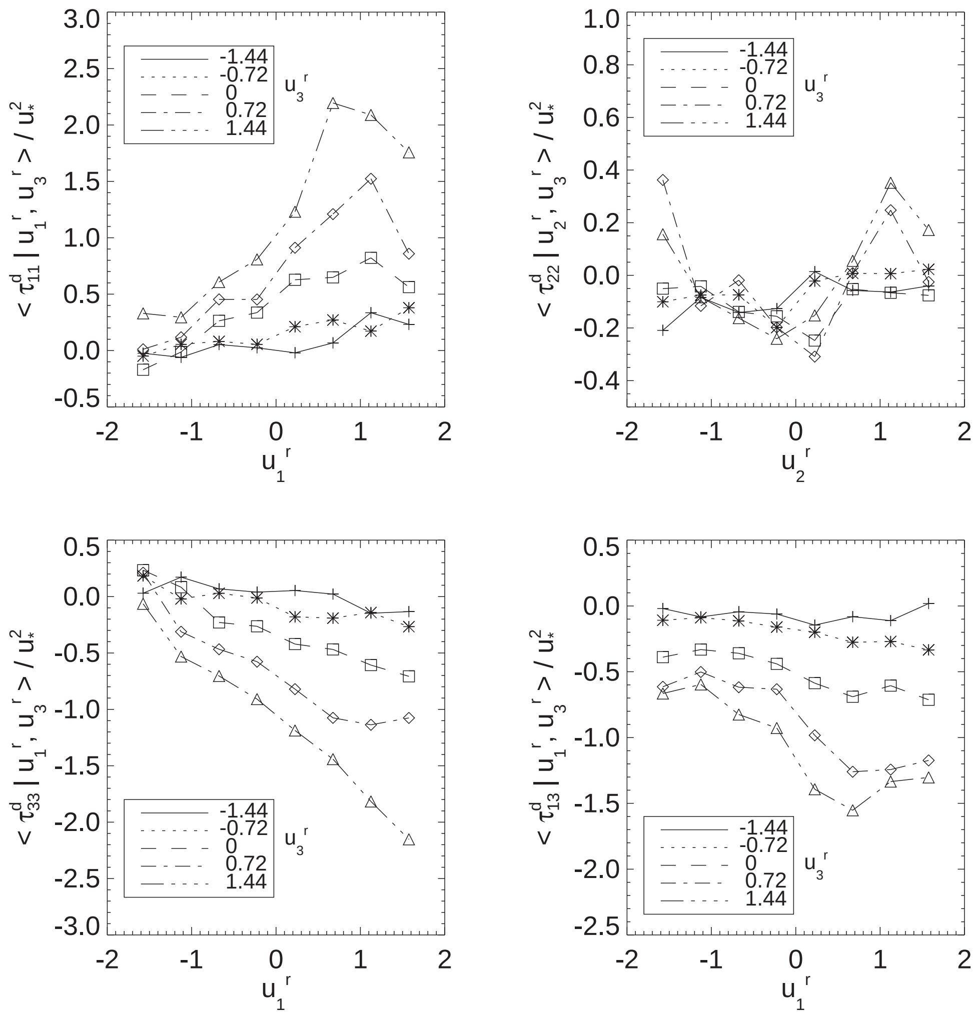

Figure 2.48. HATS: Conditional means of SFS deviatoric stresses.

with higher levels of SFS anisotropy (Chen and Tong, 2006), and consequently, larger magnitudes of the deviatoric stresses. The above arguments explain the trends in $\langle \tau_{33}^d \big| \, u_1^r, u_3^r \rangle$.

2.6.5.4 $\langle \tau_{13}^d \big| \, u_1^r, u_3^r \rangle$

The conditional means of τ_{13}^d are almost entirely negative which is consistent with the dynamics of the unstable surface layer (Haugen et al., 1971) and represents the upward ejection of fluid parcels with a horizontal velocity deficit. Their weak dependence on u_1^r for $u_3^r < 0$ is enhanced by $u_3^r > 0$. The observed increase in the magnitude of $\langle \tau_{13}^d \big| u_1^r, u_3^r \rangle$ with increasing u_3^r is due to advection of τ_{13}^d from near the surface. The trends exhibited by $\langle \tau_{13}^d \big| u_1^r, u_3^r \rangle$ are quite different from those exhibited by $\langle P_{13}^d \big| u_1^r, u_3^r \rangle$. This is because the dominant production term in the τ_{13}^d budget is isotropic production, $-(4/3)e\overline{S}_{13}$, which (not shown) does exhibit the same trends as $\langle \tau_{13}^d \big| u_1^r, u_3^r \rangle$ (Chen and Tong, 2006).

2.6.6 LES: Conditional means of τ_{ij}^d

In this section, we examine the trends in $\langle \tau_{13}^d \big| u_1^r, u_3^r \rangle$ obtained from LES using the modeled SFS conservation equations and an eddy-diffusivity closure.

Figures (2.49)–(2.50) show the conditional means of the SFS deviatoric stresses using the eddy-diffusivity closure and the SFS conservation equations, respectively. Only the diagonal and the (1,3) components of $\langle \tau_{ij}^d \big| \mathbf{u}^r = \mathbf{v}^r \rangle$ are shown.

2.6.6.1 $\langle \tau_{11}^d \big| u_1^r, u_3^r \rangle$

Both closures underpredict the magnitude of $\langle \tau_{11}^d \big| u_1^r, u_3^r \rangle$ compared to observations, the eddy-diffusivity closure doing so more severely as it doesn't account for anisotropic production, the dominant production mechanism in the τ_{11}^d budget. The modeled SFS conservation equations account explicitly for anisotropic production which explains why their predictions of $\langle \tau_{11}^d \big| u_1^r, u_3^r \rangle$ are better than those by the eddy-diffusivity closure. They are still lesser in magnitude compared to observations as they underestimate the SFS anisotropy, plausibly due to deficiencies in the model for the pressure-strain covariance.

2.6.6.2 $\langle \tau_{22}^d \big| u_2^r, u_3^r \rangle$

The predictions of $\langle \tau_{22}^d \big| u_2^r, u_3^r \rangle$ by the eddy-diffusivity closure and the SFS conservation equations are similar in their variations with u_2^r and u_3^r. They differ in that the former predicts conditional means that are nearly symmetric about zero while the SFS conservation equations yield values that are predominantly negative. The corresponding predictions for the HATS data in Fig. (2.48) exhibit mostly negative values for the central u_2^r bins but large positive values for the extreme bins. Neither of the two closures reproduces this trend.

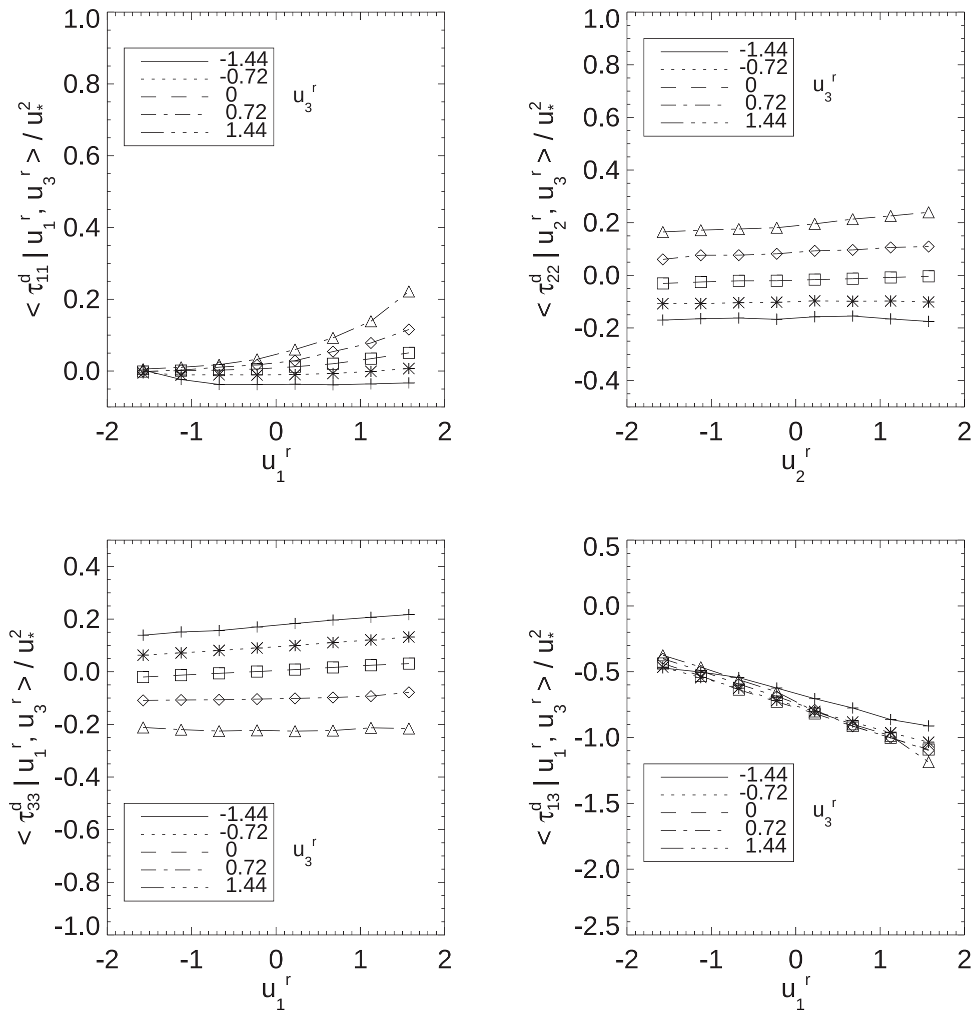

Figure 2.49. LES: Conditional means of SFS deviatoric stresses using an eddy-diffusivity closure.

We note that the HATS values for $\langle \tau_{\alpha\alpha}^d \rangle$ in Fig. (2.26) display increasingly negative values of $\langle \tau_{22}^d \rangle$ as Δ_w/Δ decreases. We can thus argue that its magnitude must be enhanced by positive u_3^r as high magnitudes of τ_{22}^d (negative in sign) are advected upwards from near the surface. Both the SFS conservation equations and the eddy-diffusivity closure yield predictions of $\langle \tau_{22}^d \big| u_2^r, u_3^r \rangle$ that become increasingly positive for positive $u_3^r > 0$, which is opposite to what we expect. Note that the SFS conservation equations yield values of $\langle \tau_{22}^d \rangle$ at low Δ_w/Δ (Fig. (2.27)) that are in reasonable agreement with observations. It follows that the conser-

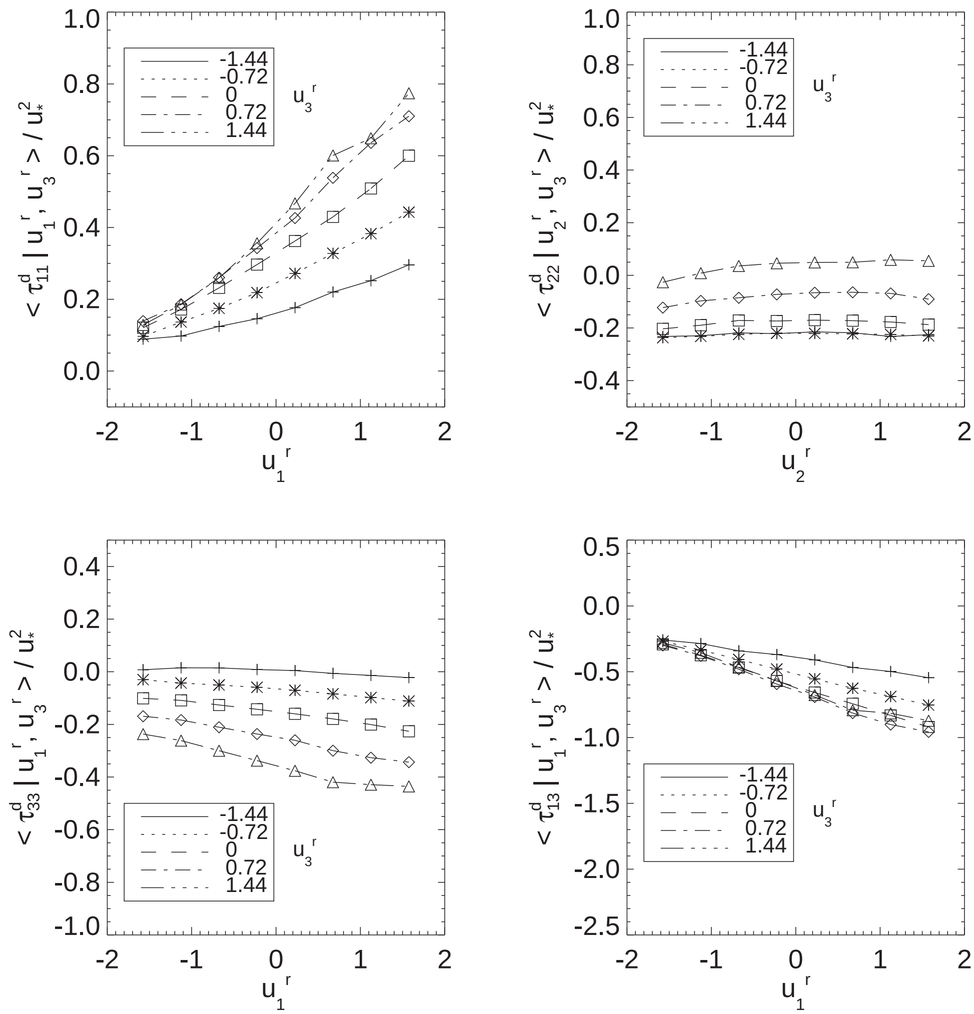

Figure 2.50. LES: Conditional means of SFS deviatoric stresses using the SFS conservation equations.

vation equations represent the τ_{22}^d field satisfactorily in the mean but not in its overall structure, as evidenced by Fig. (2.50).

2.6.6.3 $\langle \tau_{33}^d | \, u_1^r, u_3^r \rangle$

Compared to HATS data, both closures under-predict magnitudes of $\langle \tau_{33}^d | \, u_1^r, u_3^r \rangle$ but differ in their predicted trends of the same. The eddy-diffusivity closure yields conditional means that are almost symmetric about zero, a trend consistent with its near-zero prediction of $\langle \tau_{33}^d \rangle$. The SFS conservation equations yield $\langle \tau_{33}^d | \, u_1^r, u_3^r \rangle$

that are predominantly negative, in qualitative agreement with observations. Their magnitudes are, however, underpredicted considerably when compared to observations which is consistent with the underprediction of $\left|\tau^d_{\alpha\alpha}\right|$ by the SFS conservation equations.

The variations of $\langle \tau^d_{33} \,|\, u^r_1, u^r_3 \rangle$ with u^r_1 and u^r_3 are better predicted by the SFS conservation equations. In particular, they capture the enhanced sensitivity of $\langle \tau^d_{33} \,|\, u^r_1, u^r_3 \rangle$ to u^r_1 for positive u^r_3, a trend the eddy-diffusivity closure fails to reproduce.

2.6.6.4 $\langle \tau^d_{13} \,|\, u^r_1, u^r_3 \rangle$

The predictions of $\langle \tau^d_{13} \,|\, u^r_1, u^r_3 \rangle$ by both closures are mostly similar in trend and magnitude as the dominant production term in the τ^d_{13} budget — isotropic production — is accounted for in both closures. The advection effects for $u^r_3 > 0$ are weaker in both closures, when compared to observations. This could be caused partly by the influence of the surface stress model. We are plotting the conditional statistics at the first grid level, $z = \Delta z$, where the advection term in the τ^d_{13} rate equation utilizes values of τ^d_{13} at $z = 2\Delta z$ and $z = 0$, i.e., the surface. The surface value of τ^d_{13} (and τ^d_{23}) is set by the surface stress model. It follows that the formulation of the surface stress model influences $\langle \tau^d_{13} \,|\, u^r_1, u^r_3 \rangle\big|_{z=z_1}$ directly.

2.6.7 Summary

In the previous section, we analyzed the conditional means of the SFS stresses and the SFS production rate using HATS data and two closures: the SFS conservation equations and an eddy-diffusivity closure. These two conditional means represent the direct influence of the SFS model on the resolved-scale velocity joint pdf, and hence, on the resolved-scale statistics (Chen et al., 2009; Chen and Tong, 2006). Consequently, it is desirable for an SFS model to yield accurate predictions of the conditional means of the SFS stress and the SFS production rate. We summarize below our main findings.

The eddy-diffusivity closure yields reasonable predictions of $\left\langle P^d_{11} \,\middle|\, u^r_1, u^r_3 \right\rangle$ and $\left\langle P^d_{22} \,\middle|\, u^r_2, u^r_3 \right\rangle$ but predicts $\left\langle P^d_{33} \,\middle|\, u^r_3, u^r_1 \right\rangle$ and $\left\langle P^d_{13} \,\middle|\, u^r_1, u^r_3 \right\rangle$ poorly. The poor prediction of $\left\langle P^d_{33} \,\middle|\, u^r_3, u^r_1 \right\rangle$ by the eddy-diffusivity closure is linked to its inability to reproduce the differential influence of updrafts and downdrafts on $\left\langle P_{33}^d \middle| u_3^r, u_1^r \right\rangle$. The predictions of $\left\langle P_{13}^d \middle| u_1^r, u_3^r \right\rangle$ by the eddy-diffusivity closure are overly negative and fail to display the correct trends when compared to observations.

In general, the SFS conservation equations predict trends in the conditional means of the SFS production rate better when compared to the eddy-diffusivity closure. They are able to capture the asymmetric nature of $\left\langle P_{33}^d \middle| u_3^r, u_1^r \right\rangle$ and the correct trends in $\left\langle P_{13}^d \middle| u_1^r, u_3^r \right\rangle$ as they account explicitly for advection of the SFS stresses.

The eddy-diffusivity closure doesn't take into account anisotropic production, the dominant production term in the $\tau_{\alpha\alpha}^d$ budgets. Thus, it underpredicts $\langle \tau_{11}^d | u_1^r, u_3^r \rangle$ and fails to reproduce the correct trends in $\langle \tau_{22}^d | u_2^r, u_3^r \rangle$, and $\langle \tau_{33}^d | u_1^r, u_3^r \rangle$. It predicts $\langle \tau_{13}^d | u_1^r, u_3^r \rangle$ reasonably well as the principal production term in the τ_{13}^d budget is isotropic production, which is accounted for in eddy-diffusivity closures.

The SFS conservation equations predict the conditional means of $\tau_{\alpha\alpha}^d$ better compared to the eddy-diffusivity closure as they include anisotropic production. They also reproduce better the effects of advection on the conditional means of $\tau_{\alpha\alpha}^d$. The predictions of $\langle \tau_{13}^d | u_1^r, u_3^r \rangle$ by the SFS conservation equations differ negligibly from those by the eddy-diffusivity closure, in both trend and magnitude.

Chapter 3

The moderately stable boundary layer: analysis using HATS data and LES

In the previous chapter, we examined the performance of an SFS model based on a truncated version of the full SFS conservation equations (Hatlee and Wyngaard, 2007), using LES of the moderately convective ABL. In the current chapter, we continue to explore the SFS conservation equations through analysis of HATS data and Large-eddy Simulation (LES) of a moderately stable boundary layer.

3.1 Introduction

Stable stratification refers to lighter fluid overlying heavier fluid. In such a configuration, the effect of buoyancy is to inhibit vertical motions and suppress turbulent activity. Consequently, the stable boundary layer (SBL) is shallower than the unstable daytime boundary layer. The SBL can be highly nonstationary owing to its "patchy" and intermittent nature, thereby making it harder to obtain reliable statistics from observations (Caughey et al., 1979). The study of SBLs is further complicated by their sensitivity to the following factors: terrain slope (Brost and Wyngaard, 1978), internal waves (Hunt et al., 1985), "global" intermittency (Mahrt, 1989) and mesoscale influences (Mason and Derbyshire, 1990). From a practical viewpoint, modeling the SBL is necessary for nighttime surface temperature predictions, modeling pollutant transport (Banta et al., 1998), fog prediction (Duynkerke, 1999), understanding polar climates (King et al., 2001), and more recently, wind energy applications (Pichugina et al., 2008; Sim et al., 2009). Evidently, the parameterization of stably stratified boundary layers is an essential but daunting exercise.

LES, where in principle, the dominant energy-carrying scales can be computed explicitly, has emerged as an attractive option to study the SBL (Basu and Porté-Agel, 2006; Galmarini et al., 1998; Kosović and Curry, 2000; Mason and Derbyshire, 1990; Saiki et al., 2000; Stoll and Porté-Agel, 2008). The turbulent eddies in the SBL, however, are confined to much smaller length scales (Jimenez and Cuxart, 2005; Kaimal et al., 1972) than in the unstable boundary layer where buoyancy aids their growth into large structures that scale on the boundary layer depth. The confinement of turbulent activity in the SBL to smaller scales implies a greater role for the SFS model. While simulating the SBL in all its generality is not an easy task, the quasi-steady SBL with weak-to-moderate stratification over flat terrain has received considerable attention in the literature. Mason and Derbyshire (1990) are credited with having performed the first LES of the SBL. For weak stratification, their results showed general agreement with the analytical model developed by Nieuwstadt (1984) and, the second-order closure model of Brost and Wyngaard (1978). For highly negative surface fluxes, though, their LES runs exhibited "runaway cooling", which refers to a spurious, rapid decrease in the surface temperature (30K over 90 min). They identified one of the potential factors behind runaway cooling as the inability of the SFS model to represent strongly stratified boundary layers at coarse resolutions. More recently, Van de Wiel et al. (2007) have argued that runaway cooling has a physical basis but is arrested in nature by negative feedbacks arising from vegetation and radiative effects. Nevertheless, the pioneering work by Mason and Derbyshire (1990) demonstrated for the first time the feasibility of simulating SBLs with LES. Building on those results, Derbyshire (1990) extended further Nieuwstadt's theory (Nieuwstadt, 1984) and showed that Nieuwstadt's model can be interpreted as a limiting case associated with a maximum value of the downward surface heat flux that can support turbulence. Kosović and Curry (2000) simulated the moderately stratified quasi-steady

SBL using a nonlinear SFS model (Kosović, 1997) and initial conditions similar to the BASE (Beaufort Sea Arctic Stratus Experiment) observations. They found their results to be in good agreement with observations and Nieuwstadt's model for the SBL (Nieuwstadt, 1984). Saiki et al. (2000) performed LES of the moderately stable boundary layer and found that the original formulation of the two part SFS model by Sullivan et al. (1994) triggered a collapse of the vertical SFS heat flux near the surface, which led to unphysical profiles of turbulent statistics. They tracked the cause for this behavior to an incorrect formulation of the SFS heat flux and obtained good results after using a two part eddy-viscosity model for the SFS heat flux, similar to their model for the SFS stresses. Even with the improved SFS model, they found the simulations to be sensitive to rapid changes in the surface flux. Basu and Porté-Agel (2006) simulated the moderately stable boundary layer using the locally-averaged scale-dependent dynamic model and found good agreement with observations and theory. The Global Energy and Water Cycle Experiment Atmospheric Boundary Layer Study or GABLS (Beare et al., 2006), an intercomparison study of different SFS models for the moderately stable boundary layer, found that the SFS models reproduced reasonably the essential features of a quasi-steady SBL. While the results from the high-resolution runs (≤ 3.125m) showed good convergence, there was significant sensitivity to the SFS model at coarse resolutions (> 6.25m). Due to the computational expense of the high-resolution runs, the GABLS experiment noted that SFS model development will continue to play a crucial role in improving SBL simulations, especially at coarse resolutions.

3.1.1 Motivation

As discussed in the previous chapter, the SFS conservation equations present a natural way to describe the evolution of the SFS stresses and fluxes. Eddy-diffusivity closures assume implicitly a balance between isotropic production and pressure destruction in the SFS conservation equations. This assumption is violated in regions where the turbulence is poorly-resolved as the budgets of the diagonal SFS deviatoric stress components are dominated by anisotropic production with isotropic production playing a negligible role (Sullivan, 2010). Similarly, in the horizontal SFS flux budgets, the main production mechanisms are flux tilting and anisotropic gradient-production with isotropic gradient-production playing an insignificant role. Consequently, eddy-diffusivity closures perform poorly in parameterizing the diagonal SFS deviatoric stresses and horizontal SFS fluxes. While the above arguments were demonstrated for unstable conditions in the previous chapter, they are equally valid for the SBL where in fact, the role of the SFS model is enhanced due to the effects of stratification. In strongly stratified environments, the turbulence can be highly anisotropic (Jimenez and Cuxart, 2005), implying that SFS models need to account for anisotropy at the subfilter scales. Eddy-diffusivity closures, unlike the SFS conservation equations, lack any mechanism for generating SFS anisotropy. Finally, the SFS conservation equations retain important SFS production mechanisms in their exact analytical form. Thus, in principle, we expect a model based on the SFS conservation equations to require less tweaking from one stability regime to another.

If the SFS conservation equations hold promise, they are also complex and merit further study. Wyngaard (2004) and Hatlee and Wyngaard (2007) have studied the SFS conservation equations for the convectively unstable regime. In the current chapter, we build on their work by gaining insight into the SFS conservation equations for the moderately stable regime, using a combination of observations and LES.

3.1.2 Outline of chapter

A brief outline of the current chapter follows. In the next section, we use HATS data corresponding to stably-stratified conditions, in order to examine the relative importance of different production terms in the SFS stress and flux budgets. We then investigate the sources of fluctuations in the SFS stresses and fluxes by determining directly the contribution from the various production terms. We also compare the fluctuation levels of different SFS stress and flux components among themselves.

The HATS analysis is followed by an LES study of the moderately stable boundary layer using an SFS model that uses prognostic equations to determine the SFS stresses and fluxes. The initial conditions and physical parameters in our LES runs are identical to those used in the GABLS LES intercomparison study (Beare et al., 2006) although we also perform LES for cooling rates other than that used by Beare et al. (2006). We examine timeseries and steady-state profiles of important bulk parameters and other variables of interest. Where possible, we compare our LES results with past experimental, numerical and analytical studies. We conclude with a discussion on the influence of the surface cooling rate on our LES results.

3.2 HATS: $\tau^d_{\alpha\alpha}$ and τ^d_{13} budgets

In this section, we study the dominant production terms in the $\tau^d_{\alpha\alpha}$ and τ^d_{13} budgets. The details of the HATS experiment and the filtering procedures used are described in Ch. 2.

Figure (3.1) shows the scaled anisotropic, isotropic and the buoyant production terms in the $\tau^d_{\alpha\alpha}$ and τ^d_{13} budgets, plotted versus the nondimensional parameter Δ_w/Δ, where Δ_w is the wavelength associated with the peak in the vertical velocity spectrum and Δ is the filter width. Using HATS data, Sullivan (2010) examined the partitioning of SFS production into anisotropic and isotropic components. He showed the dominance of anisotropic production in the $\tau^d_{\alpha\alpha}$ budgets and that of isotropic production in the τ^d_{13} budget, at low Δ_w/Δ. In Fig. (3.1), we plot the scaled anisotropic, isotropic and buoyant production terms for $\tau^d_{\alpha\alpha}$ and τ^d_{13}, as functions of Δ_w/Δ. High values of Δ_w/Δ correspond to well-resolved turbulence while low values correspond to poorly-resolved turbulence. The various budget terms have been scaled with $\epsilon = \phi_\epsilon(u_*^3/kz_d)$, where $\phi_\epsilon = \left[1 + 2.5(z/L)^{3/5}\right]^{3/2}$ (Wyngaard and Coté, 1971), $k = 0.4$ is the von Kármán constant and z_d is the height of the primary sonic array. Following Sullivan et al. (2003), we compute Δ_w using $\Delta_w = 2\pi\langle U\rangle\tau_p$, where $\langle U\rangle$ is the mean wind in the streamwise direction and τ_p is the Eulerian time scale obtained by assuming an exponential autocorrelation function for the vertical velocity, $R(t) = \exp(t/\tau_p)$.

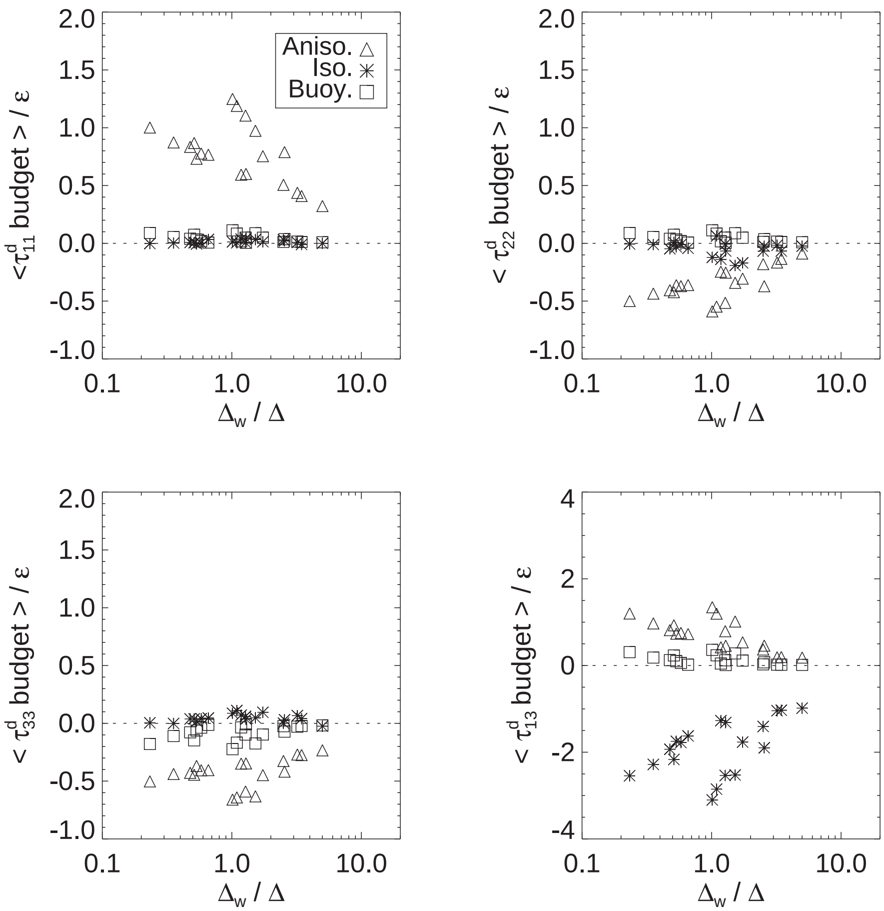

Figure 3.1. HATS data, stable cases: The partitioning of SFS deviatoric production into isotropic, anisotropic and buoyant components, scaled with $\epsilon = \phi_\epsilon(u_*^3/kz_d)$. The terms are plotted versus the nondimensional parameter, Δ_w/Δ .

3.2.1 $\tau^d_{\alpha\alpha}$ budgets

From Fig. (3.1), scaled anisotropic production far exceeds scaled isotropic- and buoyant- production in the $\tau^d_{\alpha\alpha}$ budgets, especially at low Δ_w/Δ. Scaled isotropic production is relatively insignificant almost across the entire range of Δ_w/Δ. Buoyancy is associated with production in the τ^d_{11} and τ^d_{22} budgets, and destruction in the τ^d_{33} budget, due to stable stratification. Among the three diagonal components, the effects of buoyancy are felt most in the τ^d_{33} budget underlining the influence of stratification on the vertical eddies. The magnitude of buoyant destruction in the τ^d_{33} budget increases with decreasing Δ_w/Δ but at a much slower rate when compared to anisotropic production.

3.2.2 τ_{13}^d budget

The τ_{13}^d budget, in contrast to those of $\tau_{\alpha\alpha}^d$, is dominated by isotropic production. Anisotropic production increases with decreasing Δ_w/Δ but at a rate slower than that of isotropic production, at all values of Δ_w/Δ. Buoyant production (gain) also increases with decreasing Δ_w/Δ but at a rate slower than even that of anisotropic production.

The dominance of anisotropic production in the $\tau_{\alpha\alpha}^d$ budgets and that of isotropic production in the τ_{13}^d budget were also observed for the convectively unstable cases, discussed earlier in Ch. 2.

3.2.3 Asymptotic values in the "RANS" limit

In our discussion of LES results for the unstable cases, we observed that the dominant production terms in the $\tau_{\alpha\alpha}^d$ and τ_{13}^d budgets tend to asymptote at lower values of Δ_w/Δ. Such trends were absent in the unstable HATS cases as they are in Fig. (3.1). We replot the production terms for the stable cases in Fig. (3.2) after scaling them with $\langle -\tau_{ij}^d \bar{S}_{ij} \rangle$, where $\bar{S}_{ij}$ (denoted by S_{ij}^r in Fig. 3.2) is the resolved-scale strain rate tensor and $\langle\rangle$ denotes time-averaging. The horizontal solid lines at low Δ_w/Δ represent analytically derived values of scaled anisotropic production in the $\tau_{\alpha\alpha}^d$ budgets and that of scaled isotropic production in the τ_{13}^d budget in the limit $\Delta_w/\Delta \to 0$, also called the "RANS" limit (Appendix A). The asymptotes of the scaled production terms in Fig. (3.2) at low Δ_w/Δ are in reasonable agreement with our theoretical predictions. The stable cases in the HATS data with low Δ_w/Δ are associated typically with highly stable environments. Our analysis in Appendix A does not make any assumptions regarding the stratification of the flow. The key to obtaining values for the scaled production terms in the RANS limit is the observation by Sullivan et al. (2003) that the filtering operation is equivalent to Reynolds averaging at very low values of Δ_w/Δ. That analytical predictions based on this observation are valid for two strikingly different flows — moderately unstable (from LES in Ch. 2) and very stable — highlights the effectiveness of Δ_w/Δ in describing SFS statistics across a wide range of stability

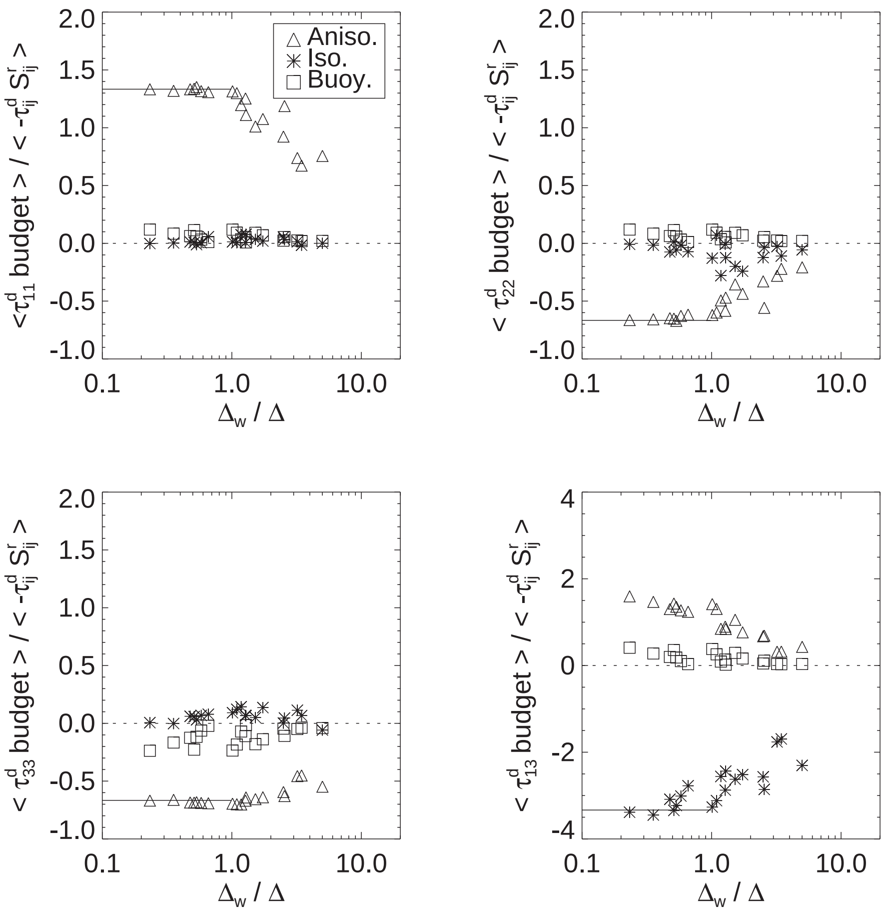

Figure 3.2. HATS data, stable cases: The partitioning of SFS deviatoric production into isotropic, anisotropic and buoyant components, scaled with $\langle -\tau_{ij}^d S_{ij}^r \rangle$, where S_{ij}^r is the resolved-scale strain rate tensor. The terms are plotted versus the nondimensional parameter, Δ_w/Δ. The horizontal solid lines denote theoretical values in the "RANS limit," discussed in Appendix A.

regimes.

A possible reason for the absence of any asymptotic trends in Fig. (3.1) could be the irrelevance of z_d as a length scale at low values of Δ_w/Δ, which as mentioned earlier correspond to strong stratification. A more appropriate length scale under such conditions might be $l_b = \sigma_w/N$ (Brost and Wyngaard, 1978), where σ_w is the vertical velocity standard deviation and $N = \sqrt{(g/\Theta_0)(\partial\theta/\partial z)}$ is the Brunt-Väisälä frequency. The length scale l_b decreases as N increases, which reflects the diminishing size of turbulent eddies as the flow becomes increasingly

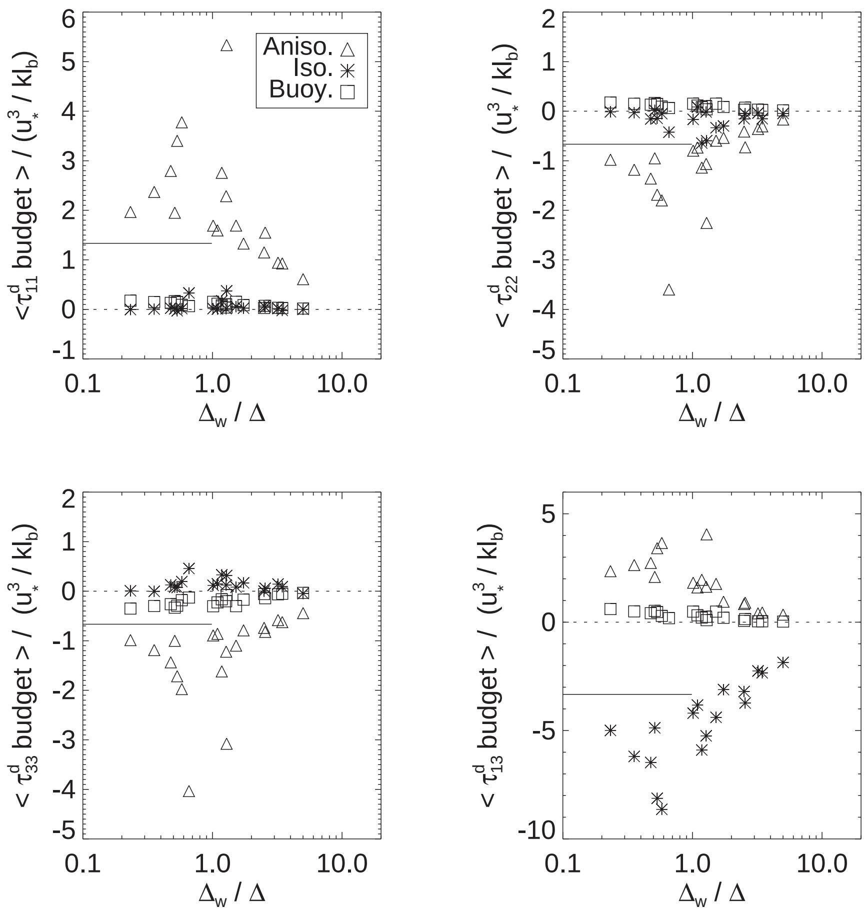

Figure 3.3. HATS data, stable cases: The partitioning of SFS deviatoric production into isotropic, anisotropic and buoyant components, scaled with (u_*^3/kl_b), where l_b is a buoyancy length scale, dependent on the Brunt-Väisälä frequency. The terms are plotted versus the nondimensional parameter, Δ_w/Δ. The horizontal solid lines denote theoretical values in the "RANS limit," discussed in Appendix A.

stable. In Fig. (3.3) we plot the SFS deviatoric production scaled with (u_*^3/kl_b). The anisotropic- and isotropic-production terms in the $\tau_{\alpha\alpha}^d$ and τ_{13}^d budgets, respectively, exhibit a common trend wherein they increase in magnitude with decreasing Δ_w/Δ for $\Delta_w/\Delta > 1$ and then decrease sharply for further decreases in Δ_w/Δ. Compared to Fig. (3.1), the scaled anisotropic and isotropic production terms in Fig. (3.3) appear more likely to approach constant values at low Δ_w/Δ. But based on Fig. (3.3) alone, it is unclear whether they indeed do asymptote at low Δ_w/Δ and even if they do, whether the asymptotes are equal to those derived analytically in the RANS limit and observed in Fig. (3.2).

3.2.4 RMS values of production terms in the τ_{ij}^d budgets

In the previous section, we examined the trends exhibited by the mean values of scaled production terms in the τ_{ij}^d budgets, when plotted versus Δ_w/Δ. The mean and variance of τ_{ij}^d are the two lowest moments that contribute to its probability density function (pdf) (Wyngaard, 2010). Thus, it is of interest to study the contributions of the measured production terms to the fluctuation level of $\left(\partial\tau_{ij}^d/\partial t\right)$, denoted by $\left(\partial\tau_{ij}^d/\partial t\right)_{\mathrm{rms}}$. We demonstrate later that $\left(\partial\tau_{ij}^d/\partial t\right)_{\mathrm{rms}}$ is a good indicator of the fluctuation level of τ_{ij}^d. The variable $\left(\partial\tau_{ij}^d/\partial t\right)_{\mathrm{rms}}$ involves contributions from unmeasured and measured terms. The unmeasured terms comprise advection, turbulent transport and pressure destruction while the measured terms comprise anisotropic-, isotropic- and buoyant-production. In general, it is not possible to infer the contributions from the unmeasured terms to $\left(\partial\tau_{ij}^d/\partial t\right)_{\mathrm{rms}}$ based on those from the measured terms due to cross-correlations between the two groups of terms.

In Fig. (3.4), we present the rms values of anisotropic production, isotropic production, buoyant production and the rms value of their sum, normalized with $\left(\partial\tau_{ij}^d/\partial t\right)_{\mathrm{rms}}$. Although the advection, turbulent transport and pressure terms aren't available to us, the rms value of $\left(\partial\tau_{ij}^d/\partial t\right)$ can be obtained directly using the time series of τ_{ij}^d.

3.2.4.1 $\tau_{\alpha\alpha}^d$ budgets

We discuss first the rms value of the time derivative of τ_{11}^d followed by those of the time derivatives of the other two diagonal components. From Fig. (3.4), as Δ_w/Δ decreases, the fluctuation levels of anisotropic production as a fraction of $\left(\partial\tau_{11}^d/\partial t\right)_{\mathrm{rms}}$ increase in relation to those of isotropic production and buoyant production. Furthermore, the normalized rms values of the sum of these three production terms increase with decreasing Δ_w/Δ. As Δ_w/Δ increases, anisotropic production, isotropic production and buoyant production together account for a decreasing fraction of $\left(\partial\tau_{11}^d/\partial t\right)_{\mathrm{rms}}$. As noted earlier they could, in principle, influence $\left(\partial\tau_{11}^d/\partial t\right)_{\mathrm{rms}}$ through cross-correlations with the unmeasured terms.

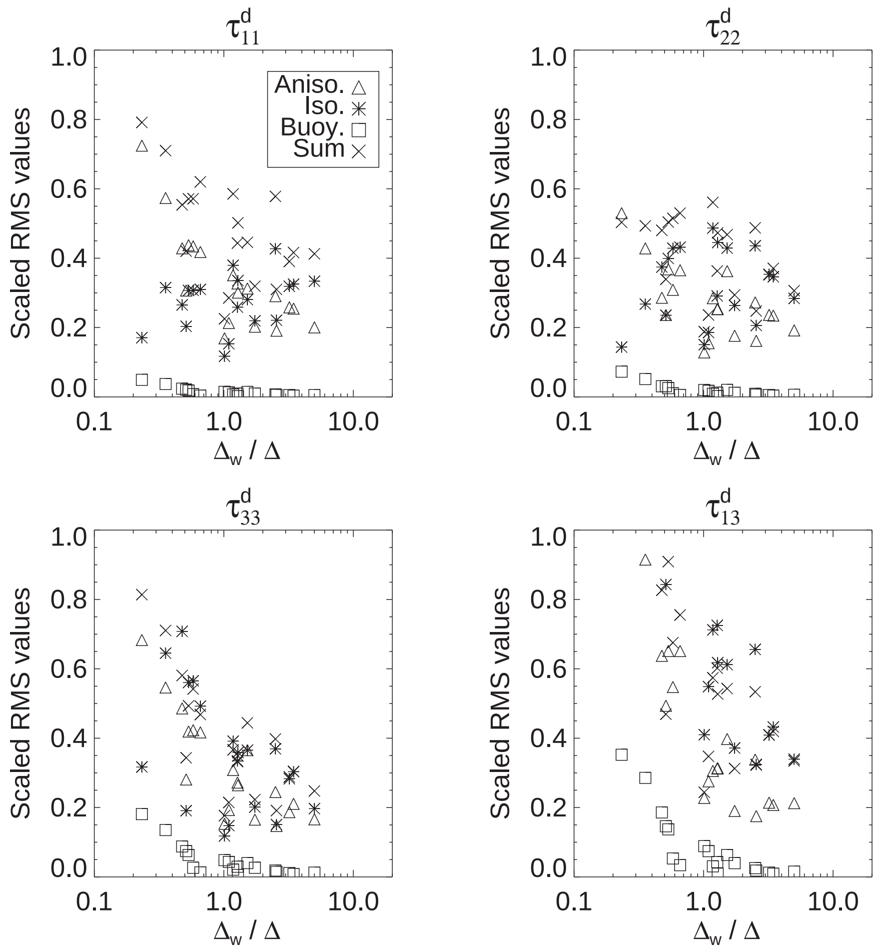

Figure 3.4. HATS data, stable cases: rms values of anisotropic production, isotropic production, buoyant production and their sum, normalized with the rms value of the time derivative of τ^d_{ij}.

The trends in the fluctuation levels of terms in the τ^d_{22} budget are similar in some respects to those observed in the τ^d_{11} budget, but differ in others. For instance, the normalized rms values of anisotropic production increase with decreasing Δ_w/Δ, as in the τ^d_{11} budget. In contrast to the τ^d_{11} budget, however, the fluctuations of isotropic production are greater than those of anisotropic production for all but the lowest values of Δ_w/Δ. Buoyant production contributes negligibly to the fluctuation level across the entire range of Δ_w/Δ in Fig. (3.4). Thus, at low values of Δ_w/Δ, anisotropic production emerges as an important contributor to the fluctuation level but even at the lowest value of Δ_w/Δ, the sum of anisotropic, isotropic and buoyant production account only for half the total fluctuation level. This shows that advection, turbulent transport or pressure destruction are responsible for a significant fraction of $\left(\partial\tau_{22}^d/\partial t\right)_{\text{rms}}$ at low Δ_w/Δ, either directly or through cross-correlations with the measured terms. As Δ_w/Δ increases, the contributions of anisotropic, isotropic and buoyant production to $\left(\partial\tau_{22}^d/\partial t\right)_{\text{rms}}$ decrease.

In the τ_{33}^d budget, as Δ_w/Δ decreases, anisotropic production, isotropic production and buoyant production together account for an increasingly large fraction of $\left(\partial\tau_{33}^d/\partial t\right)_{\text{rms}}$. Among these three terms, anisotropic production emerges as the principal contributor at low Δ_w/Δ. As in the τ_{22}^d budget, the normalized rms values of anisotropic- and isotropic-production are comparable but the latter is typically greater than the former except at very low Δ_w/Δ. For $\Delta_w/\Delta < 1$, the normalized fluctuations of buoyant production increase sharply from near-zero values to around 20% but remain smaller than that of anisotropic- and isotropic-production. As Δ_w/Δ increases, the sum of anisotropic production, isotropic production and buoyant production accounts for a decreasing fraction of $\left(\partial\tau_{33}^d/\partial t\right)_{\text{rms}}$.

3.2.4.2 τ_{13}^d budget

We recall from our discussion of the τ_{ij}^d budgets that the dominant production term in the τ_{13}^d budget is isotropic production. Fig. (3.4) shows that isotropic production is also a significant contributor to $\left(\partial\tau_{13}^d/\partial t\right)_{\text{rms}}$. As Δ_w/Δ decreases, the normalized rms values of isotropic production, anisotropic production, buoyant production and the rms value of their sum, increase steeply. Among the three production terms, normalized fluctuations levels are highest for isotropic production and lowest for buoyant production. There is a marked increase in the normalized rms values of buoyant production for $\Delta_w/\Delta < 1$, but it is considerably lesser than those of isotropic- or anisotropic-production.

A couple of observations regarding the fluctuation levels in the τ_{13}^d budget merit some discussion as they are mostly absent in the $\tau_{\alpha\alpha}^d$ budgets:

1. The normalized rms value of isotropic production, anisotropic production and buoyant production together is in some instances greater than 1. This is especially pronounced at very low Δ_w/Δ.

2. The normalized rms value of isotropic production is in some instances, greater

than that of the sum of isotropic production, anisotropic production and buoyant production. This is observed at low to intermediate values of Δ_w/Δ. The terms in the τ^d_{22} budget do exhibit such behavior although in very few instances. For instance, at the lowest value of Δ_w/Δ, the dominant production term in the τ^d_{22} budget, i.e., anisotropic production, has an rms value slightly greater than that of the sum of the three production terms.

We explain the second of these observations first. For it to be true, we require either buoyant- or anisotropic-production in the τ^d_{13} budget to exhibit high negative correlation with isotropic production. In Fig. (3.5), we plot the correlation coefficients between the dominant production term and the other two production terms for each of the $\tau^d_{\alpha\alpha}$ and τ^d_{13} budgets. The dominant production terms in the $\tau^d_{\alpha\alpha}$ and τ^d_{13} budgets are anisotropic- and isotropic-production, respectively. The correlation coefficients have been plotted versus Δ_w/Δ. We see high negative correlations in both the τ^d_{22} and τ^d_{13} budgets, although the correlation coefficients in the latter are considerably more negative than in the former. This is most evident at low Δ_w/Δ where the correlation coefficient between isotropic- and anisotropic-production in the τ^d_{13} budget is nearly -0.9. Such high negative correlation enables isotropic production to attain rms values much higher than that of isotropic, buoyant and anisotropic production together.

It is now possible to offer a similar explanation for the fact that the normalized rms value of isotropic production, anisotropic production and buoyant production together is in some instances greater than 1. We infer from Fig. (3.5) that either advection, turbulent transport or pressure destruction (or a linear combination thereof) exhibits high negative correlation with the sum of isotropic production, buoyant production and anisotropic production.

3.2.4.3 Relative rms values of $\left(\partial\tau^d_{ij}/\partial t\right)$

In the previous section, we identified the primary sources of fluctuations in the $\tau^d_{\alpha\alpha}$ and τ^d_{13} budgets across a broad range of Δ_w/Δ. While this provided insight into the individual τ^d_{ij} budgets, it is also of interest to compare the fluctuation levels of τ^d_{ij} amongst themselves. We plot in Fig. (3.6) the rms values of τ^d_{ij} normalized with that of τ^d_{33} versus Δ_w/Δ. The normalized rms values of τ^d_{11} are the highest while

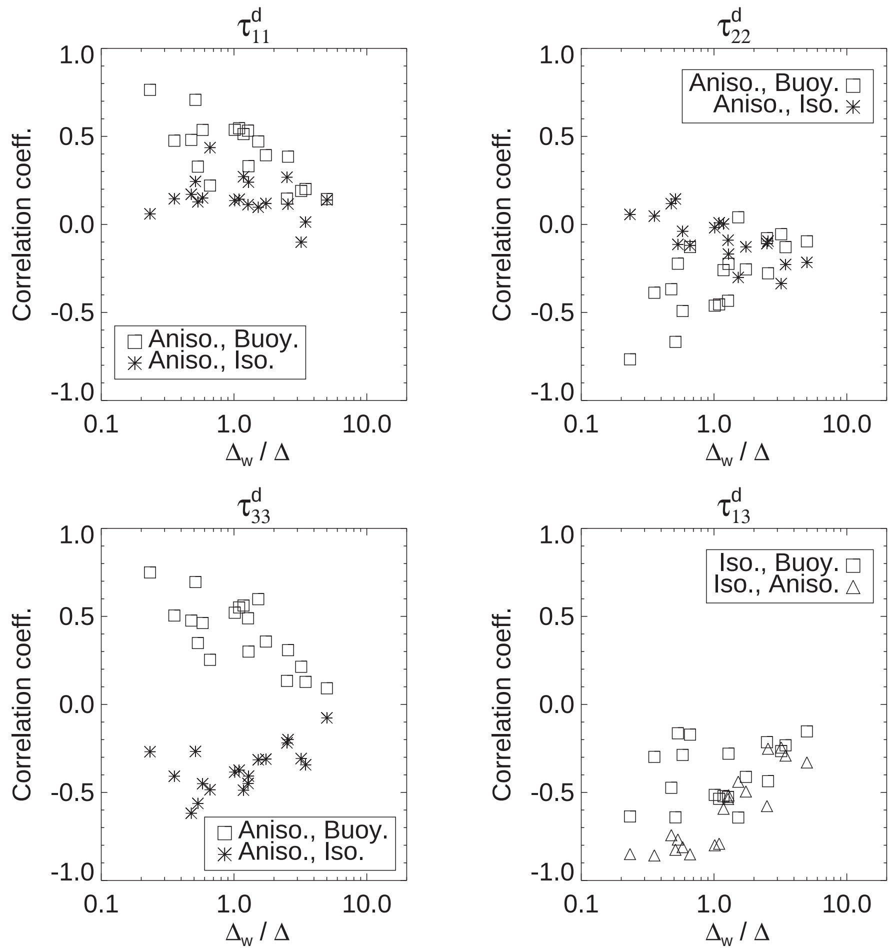

Figure 3.5. HATS data, stable cases: (i) Correlation coefficient of anisotropic production in the $\tau^d_{\alpha\alpha}$ budgets with isotropic- and buoyant-production; (ii) Correlation coefficient of isotropic production in the τ^d_{13} budget with anisotropic- and buoyant-production.

those of τ^d_{22} and τ^d_{13} are comparable with the former slightly larger than the latter. In order to relate these trends to our discussions in previous sections, we plot in Fig. (3.7) the rms values of $\left(\partial\tau^d_{11}/\partial t\right)$, $\left(\partial\tau^d_{22}/\partial t\right)$ and $\left(\partial\tau^d_{13}/\partial t\right)$, normalized with that of $\left(\partial\tau^d_{33}/\partial t\right)$. The normalized fluctuations have been plotted versus Δ_w/Δ. The observed trends are similar to that observed in Fig. (3.6) which suggests that the normalized fluctuation levels of $\left(\partial\tau^d_{ij}/\partial t\right)$ are good indicators of the normalized fluctuation levels of τ^d_{ij}, as hypothesized earlier.

At the largest value of Δ_w/Δ, the normalized rms values of $\left(\partial\tau^d_{11}/\partial t\right)$ and $\left(\partial\tau^d_{22}/\partial t\right)$ are 1.2 and 1, respectively. As Δ_w/Δ decreases, they both increase

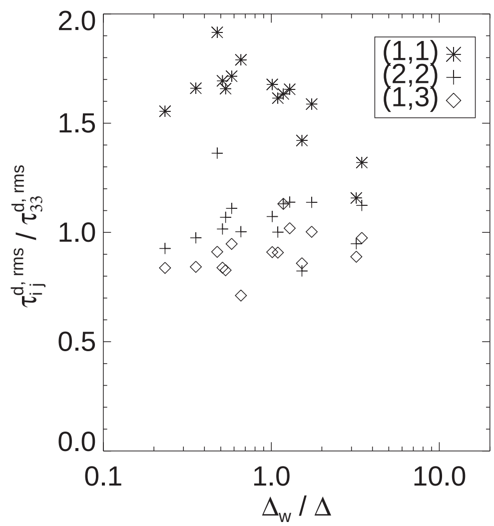

Figure 3.6. HATS, stable cases: RMS values of τ_{ij}^d normalized with that of τ_{33}^d, plotted versus Δ_w/Δ.

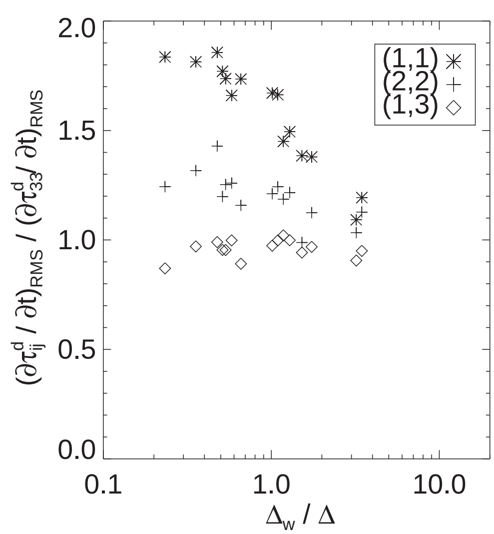

Figure 3.7. HATS, stable cases: RMS values of $\left(\partial\tau_{ij}^d/\partial t\right)$ normalized with that of $\left(\partial\tau_{33}^d/\partial t\right)$, plotted versus Δ_w/Δ.

such that the fluctuation levels of $\left(\partial\tau_{11}^d/\partial t\right)$ increase more rapidly than that of $\left(\partial\tau_{22}^d/\partial t\right)$. The normalized rms values of $\left(\partial\tau_{13}^d/\partial t\right)$ are close to unity and exhibit a spread of only 10-15% across the entire range of Δ_w/Δ.

3.2.5 Summary

We summarize briefly our observations regarding the mean values of the production terms followed by those regarding their fluctuations.

Anisotropic production dominates isotropic- and buoyant-production in the $\tau^d_{\alpha\alpha}$ budgets while isotropic production plays the dominant role in the τ^d_{13} budget. The buoyant production terms are relatively insignificant in the τ^d_{11}, τ^d_{22} and τ^d_{13} budgets but can be comparable to anisotropic production in the τ^d_{33} budget, at very low Δ_w/Δ. These trends are qualitatively similar to those observed in the unstable HATS cases, discussed in Ch. (2).

At high Δ_w/Δ, anisotropic production, isotropic production and buoyant production together account only for a small fraction of the fluctuations in $\left(\partial\tau^d_{ij}/\partial t\right)$, implying significant contributions from advection, turbulent transport or pressure destruction, either directly or through cross-correlations with the measured terms. With decreasing Δ_w/Δ, the three measured production terms together account for an increasingly large fraction of the total fluctuation level although this still does not rule out cross-correlations with the unmeasured terms. In the $\tau^d_{\alpha\alpha}$ budgets, anisotropic production emerges as the principal source of fluctuations among the three production terms at low Δ_w/Δ. In the τ^d_{13} budget, isotropic production is the principal source of fluctuations among the three production terms at low Δ_w/Δ. Among the diagonal components, $\left(\partial\tau^d_{11}/\partial t\right)$ fluctuates the most and $\left(\partial\tau^d_{33}/\partial t\right)$ the least. The fluctuations in $\left(\partial\tau^d_{13}/\partial t\right)$ are nearly equal to those in $\left(\partial\tau^d_{13}/\partial t\right)$ and don't change significantly with Δ_w/Δ.

3.3 HATS: f_1 and f_3 budgets

In this section, we examine the f_1 and f_3 budgets in order to determine how the following terms vary with Δ_w/Δ: isotropic gradient-production, anisotropic gradient-production, flux tilting and buoyant production. Among isotropic and anisotropic production, Sullivan (2010) found the latter to dominate in the f_1 budget and the former to dominate in the f_3 budget.

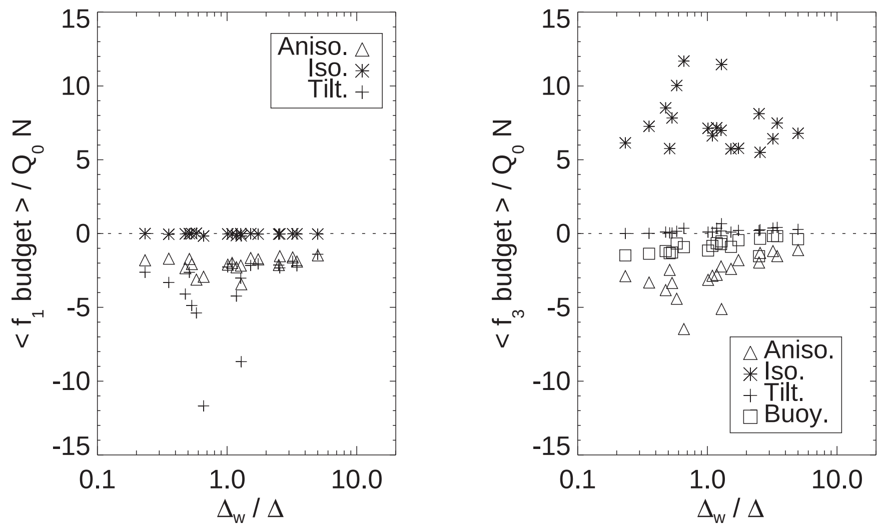

Figure 3.8. HATS, stable cases: Scaled production terms in the f_1 (left) and f_3 (right) budgets, plotted versus Δ_w/Δ. The terms have been scaled with Q_0N where Q_0 is the surface heat flux and N is the Brunt-Väisälä frequency.

In Fig. (3.8) we plot the following terms in the f_1 and f_3 budgets after scaling them appropriately: isotropic- and anisotropic-gradient production, flux tilting and buoyant production. We scale these terms with Q_0N, where Q_0 is the surface heat flux and N is the Brunt-Väisälä frequency. Figure (3.8) is similar to results obtained by Sullivan (2010), the only difference being that we have also plotted the tilting and buoyant production terms. Similar to the τ^d_{ij} budgets, the scaled production terms in Fig. (3.8) increase with decreasing Δ_w/Δ for $\Delta_w/\Delta > 1$ and then decrease sharply for further decreases in Δ_w/Δ. We now discuss the f_1 budget followed by the f_3 budget.

3.3.1 f_1 budget

In the f_1 budget, flux tilting and anisotropic-gradient production are the dominant production terms. For $\Delta_w/\Delta > 2$, these two terms are comparable in magnitude but as Δ_w/Δ decreases further, flux tilting tends to dominate anisotropic-gradient production till $\Delta_w/\Delta \approx 0.2$, when the two production terms converge and appear to asymptote approximately to a value of 2 for lower values of Δ_w/Δ. Isotropic

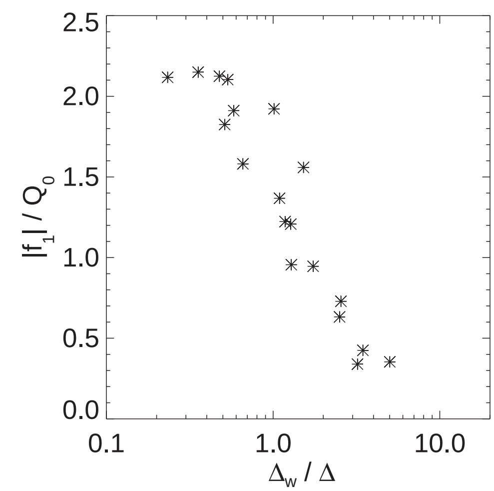

Figure 3.9. HATS, stable cases: Plot of $|f_1|/Q_0$ versus Δ_w/Δ, where Q_0 is the surface heat flux.

gradient-production is negligible across the entire range of Δ_w/Δ. We plot in Fig. (3.9) $|f_1|$ normalized with the surface heat flux, Q_0, versus Δ_w/Δ. The normalized values of $|f_1|$ increase with decreasing Δ_w/Δ and tend towards a value of 2.1 at low Δ_w/Δ. Figures (3.8)-(3.9) show that the horizontal SFS scalar flux can be significant even in the absence of horizontal mean gradients in the scalar field. Using HATS data for the unstable cases, Hatlee and Wyngaard (2007) found that eddy-viscosity closures — which account only for isotropic gradient-production — fare poorly in their prediction of SFS horizontal fluxes Hatlee and Wyngaard (2007). Thus Figs. (3.8)–(3.9) are consistent with their findings.

3.3.2 f_3 budget

Isotropic gradient-production plays a significant role in the f_3 budget as it is proportional to the vertical gradient of potential temperature. Anisotropic gradient-production and buoyant production are non-zero but have smaller magnitudes than isotropic gradient-production. Anisotropic gradient-production is typically larger in magnitude than buoyant production but they appear to converge as Δ_w/Δ decreases. It is harder to discern the asymptotes for the production terms at low Δ_w/Δ but crude visual extrapolation suggests a value slightly lesser than 5 for isotropic gradient-production and a value of ≈ -2 for anisotropic gradient-production and buoyant production.

It is interesting to note that the implied asymptotes at low Δ_w/Δ for terms in the f_1 budget are equal approximately to those observed in our high-resolution LES results for the unstable boundary layer in Ch. (2) (see Fig. (2.35)). This is also true of the implied low Δ_w/Δ asymptote for isotropic gradient-production in the f_3 budget. The common asymptote for anisotropic gradient-production and buoyant production (≈ -2), however, is absent from our LES results due to two reasons: (i) we neglect the buoyant terms in the f_3 conservation equation, modeling which would require an additional model for the SFS θ variance; (ii) the modeled SFS conservation equations underpredict the levels of SFS anisotropy close to the surface, which in turn leads to underprediction of anisotropic gradient-production in the SFS scalar flux budgets. Nevertheless, the parallels between Fig. (3.8) and our LES results for the unstable boundary layer show once again that the parameter Δ_w/Δ is quite effective in describing turbulence statistics across a wide range of stabilities.

3.3.3 RMS values of production terms in the f_1 and f_3 budgets

In the present section, we discuss trends in the rms values of production terms in the f_i budgets, scaled with the rms values of $(\partial f_i/\partial t)$, denoted by $(\partial f_i/\partial t)_{\mathrm{rms}}$. In particular, we consider tilting, isotropic gradient-production, anisotropic gradient-production and buoyant production. We discuss first the f_1 budget followed by the f_3 budget.

3.3.3.1 f_1 budget

In Fig. (3.10a), we show the rms values of flux tilting, isotropic gradient-production, anisotropic gradient-production and of their sum, normalized with $(\partial f_1/\partial t)_{\mathrm{rms}}$. Of the three production terms, flux tilting has the highest normalized fluctuation levels. This shows that flux tilting influences significantly not only the mean value of f_1 but also its fluctuation level. As Δ_w/Δ decreases, the three production terms together account for an increasing fraction of $(\partial f_1/\partial t)_{\mathrm{rms}}$. For low Δ_w/Δ, the normalized rms values of the sum of the three production terms, in some instances, exceeds considerably that of either of the individual terms. For this to be possible, two or more of the three production terms must have high positive correlation. In Fig. (3.10b) we show the correlation coefficients between two pairs of production terms: (i) flux tilting and isotropic gradient-production (ii) flux tilting and anisotropic gradient-production. With decreasing Δ_w/Δ, the correlation coefficient between flux tilting and anisotropic gradient-production increases to values as high as 0.8, which explains why in some instances, the sum of the three production terms has rms values much higher than do either one of them. At higher values of Δ_w/Δ, the three production terms account for only a small fraction of the total fluctuation rate (≈ 0.3). It follows that advection, turbulent transport or pressure destruction contributes significantly to $(\partial f_1/\partial t)_{\mathrm{rms}}$ at high Δ_w/Δ, either directly or through cross-correlations with the measured terms.

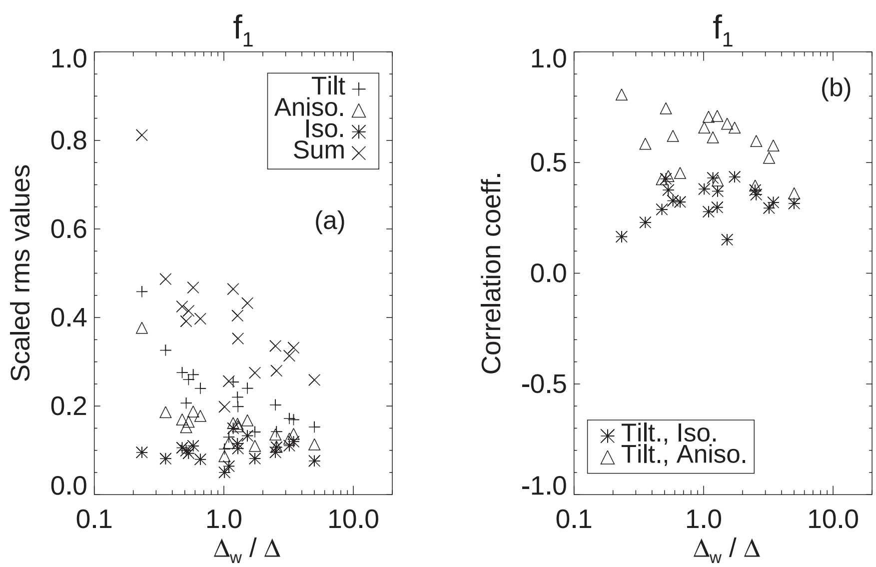

Figure 3.10. HATS, stable cases: (a) rms values of flux tilting, isotropic gradient-production, anisotropic gradient-production and of their sum, normalized with that of $(\partial f_1/\partial t)$ (b) Correlation coefficient between flux tilting and isotropic gradient-production, and flux tilting and anisotropic gradient-production

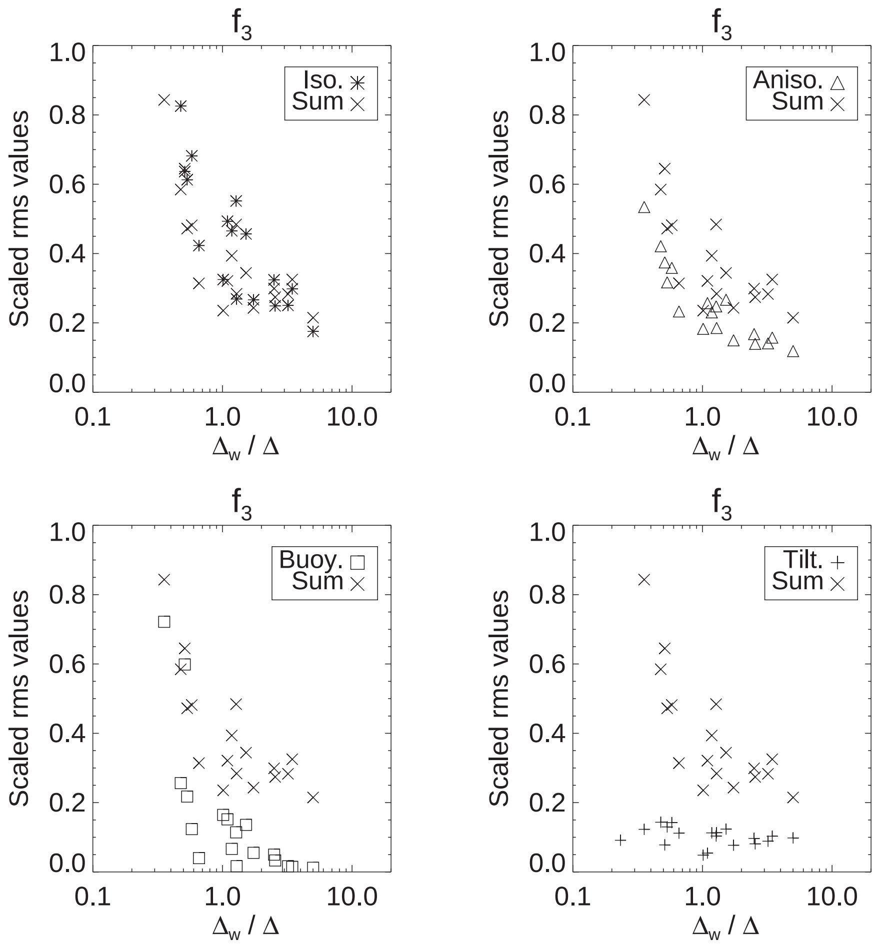

Figure 3.11. HATS, stable cases: normalized rms values of isotropic gradient-production, anisotropic gradient-production, buoyant production and flux tilting shown plotted alongside the normalized rms values of their sum. The normalization factor is the rms value of $(\partial f_3/\partial t)$.

3.3.3.2 f_3 budget

In Fig. (3.11), we show the rms values of flux tilting, buoyant production, isotropic gradient-production, anisotropic gradient-production and of their sum, normalized with $(\partial f_3/\partial t)_{\mathrm{rms}}$. For easy interpretation, we show in separate plots the normalized fluctuation levels of each of these four production terms along with that of their sum. We recall from earlier discussions that the principal production term in the f_3 budget is isotropic gradient-production. Figure (3.11) shows that it is also the dominant source of fluctuations in $(\partial f_3/\partial t)$. As Δ_w/Δ decreases, the normalized

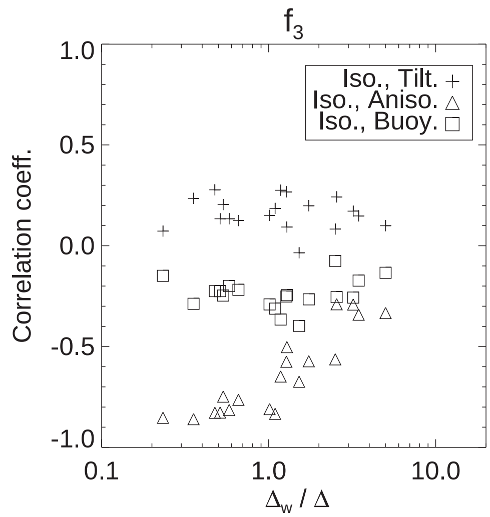

Figure 3.12. HATS, stable cases: Correlation coefficient between isotropic gradient-production in the f_3 budget and – (i) flux tilting (ii) anisotropic gradient-production (iii) buoyant production.

rms values of isotropic gradient-production, anisotropic gradient-production and buoyant production increase sharply with the latter two lagging behind the first. The normalized rms values of buoyant production in particular, increase rapidly from near-zero values to ≈ 0.7 at low Δ_w/Δ. The contributions from flux tilting remain insignificant ($\approx$ 0.1–0.2) across the entire range of Δ_w/Δ. The dominant production term — isotropic gradient-production — has fluctuation levels that in some instances exceed that of the sum of all four production terms. This is consistent with increasingly high negative correlation between isotropic gradient-production and anisotropic gradient-production with decreasing Δ_w/Δ, as shown in Fig. (3.12). Close observation of Fig. (3.11) reveals that for the lowest value of Δ_w/Δ in the HATS data (≈ 0.23, see the fluctuations of the tilting term in Fig. (3.11)), the normalized fluctuation of the sum of the four production terms is greater than unity and hence, not visible in the plot. This implies that the unmeasured terms exhibit significant negative correlation with the sum of the four production terms at very low Δ_w/Δ.

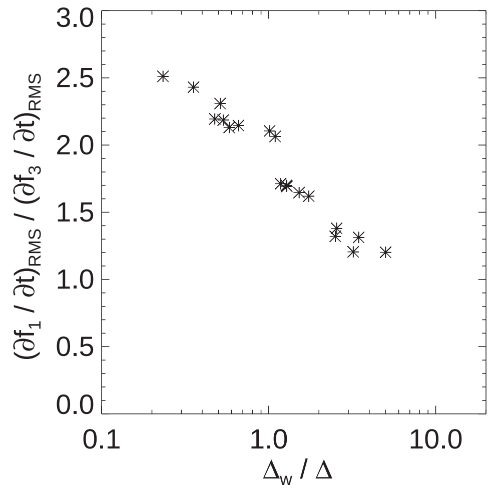

Figure 3.13. HATS, stable cases: RMS values of $(\partial f_1/\partial t)$ normalized with that of $(\partial f_3/\partial t)$, plotted versus Δ_w/Δ.

3.3.3.3 Relative rms values of $(\partial f_i/\partial t)$

In Fig. (3.13), we plot $(\partial f_1/\partial t)_{\text{rms}}$ normalized with $(\partial f_3/\partial t)_{\text{rms}}$, as a function of Δ_w/Δ. It increases from ≈ 1.2 at the highest value of Δ_w/Δ to ≈ 2.5 at low Δ_w/Δ. The four production terms — tilting, isotropic gradient-production, anisotropic gradient-production and buoyant production — account for an increasingly large fraction of the fluctuations with decreasing Δ_w/Δ. As discussed in the previous section, however, unlike in the τ_{ij}^d budgets, we have more than one significant source of fluctuations in the f_i budgets even at the lowest value of Δ_w/Δ. The steep increase in the normalized rms values of $(\partial f_1/\partial t)$ with decreasing Δ_w/Δ imply that at low Δ_w/Δ, the dominant sources of fluctuations in the f_1 budget fluctuate more than those in the f_3 budget.

3.3.4 Summary

As Δ_w/Δ decreases, the f_1 budget is dominated by flux tilting and anisotropic gradient-production with isotropic gradient-production playing a negligible role. The principal source of production in the f_3 budget is isotropic gradient-production but anisotropic gradient-production and buoyant production also play a significant role at low Δ_w/Δ. Flux tilting plays a negligible role in the f_3 budget for all Δ_w/Δ.

At high Δ_w/Δ, isotropic gradient-production, anisotropic gradient-production and flux tilting together account only for a small fraction of the rms value of $(\partial f_1/\partial t)$, implying significant contributions from advection, turbulent transport or pressure destruction, either directly or through cross-correlations with the measured terms. As Δ_w/Δ decreases, the three production terms together account for an increasingly large fraction of the total fluctuation level although this still does not rule out cross-correlations with the unmeasured terms. Isotropic gradient-production contributes negligibly to the total fluctuation level across the entire range of Δ_w/Δ.

In the f_3 budget, as Δ_w/Δ decreases, the normalized rms values of isotropic gradient-production, anisotropic gradient-production, buoyant production and their sum increase while those of flux tilting are relatively insignificant ($\approx$ 0.1–0.15). Among the four production terms, isotropic gradient-production has the highest normalized rms values. At high values of Δ_w/Δ, the four production terms together represent only a small fraction ($\approx$ 0.2) of the rms value of $(\partial f_3/\partial t)$ and we infer significant contributions from advection, turbulent transport or pressure destruction, either directly or through cross-correlations with the measured terms. Finally, the fluctuations in $(\partial f_1/\partial t)$ exceed those in $(\partial f_3/\partial t)$ and at very low Δ_w/Δ, the former is more than twice the latter which shows that the dominant sources of fluctuations in the f_1 budget fluctuate more than do their counterparts in the f_3 budget.

Our results in the current and preceding section show that as Δ_w/Δ decreases, SFS production terms in the τ_{ij}^d and f_i budgets that dominate in the mean also account for a significant fraction of the fluctuations in τ_{ij}^d and f_i, respectively.

3.4 SFS model

In the previous sections, we used HATS data for the stable boundary layer to gain insight into the conservation equations for the SFS stresses and fluxes. We determined that at low Δ_w/Δ, the principal production terms in the SFS budgets (for both stresses and fluxes) are also an important source of fluctuations in the SFS stresses and fluxes. Our HATS analysis suggests that traditional eddy-viscosity closures that account only for isotropic production are expected to represent poorly the diagonal SFS deviatoric stresses, $\tau^d_{\alpha\alpha}$, and the horizontal SFS scalar flux, f_1, in whose budgets isotropic production plays a negligible role.

In the present section, we investigate the performance of an SFS model that uses conservation equations by implementing it in LES of a moderately stable boundary layer. The SFS model we employ is identical to the one developed by Hatlee and Wyngaard (2007) and was used in Ch. (2) for LES of the unstable ABL. Equations (3.1)–(3.2) comprise the SFS model:

$$\frac{\partial f_i}{\partial t} + \bar{u}_j \frac{\partial f_i}{\partial x_j} = -f_j \frac{\partial \bar{u}_i}{\partial x_j} - \tau^d_{ij} \frac{\partial \bar{\theta}}{\partial x_j} - \frac{2}{3} e \frac{\partial \bar{\theta}}{\partial x_i} - \frac{f_i}{T_\theta}. \tag{3.1}$$

$$\begin{aligned} \frac{\partial \tau^d_{ij}}{\partial t} + \bar{u}_k \frac{\partial \tau^d_{ij}}{\partial x_k} &= -\frac{2}{3} e \left(\frac{\partial \bar{u}_i}{\partial x_j} + \frac{\partial \bar{u}_j}{\partial x_i} \right) \\ &- \left[\tau^d_{ik} \frac{\partial \bar{u}_j}{\partial x_k} + \tau^d_{jk} \frac{\partial \bar{u}_i}{\partial x_k} - \frac{1}{3} \delta_{ij} \tau^d_{kl} \left(\frac{\partial \bar{u}_k}{\partial x_l} + \frac{\partial \bar{u}_l}{\partial x_k} \right) \right] \\ &+ \frac{g}{T_0} \left[\delta_{j3} f_i + \delta_{i3} f_j - \left(\frac{2}{3} \right) \delta_{ij} f_3 \right] - \frac{\tau^d_{ij}}{T_\tau}. \end{aligned} \tag{3.2}$$

The nomenclature is the same as defined in previous Ch. (2). The terms in Eq. (3.1) are (from left to right): time derivative, advection, flux tilting, anisotropic gradient-production, isotropic gradient-production and modeled slow pressure strain-rate covariance. The terms in Eq. (3.2) are (from left to right): time derivative, advection, isotropic production, anisotropic production, buoyant production and modeled slow pressure strain-rate covariance.

The SFS time scales $T_{\theta,\tau}$ are modeled as being proportional to $l_{\rm SFS}/e^{1/2}$ where $l_{\rm SFS}$ is the length scale for the SFS eddies. We denote the proportionality constants in the expressions for T_θ and T_τ by c_θ and c_τ, respectively. We set $l_{\rm SFS} = \Delta = (\Delta x \Delta y \Delta z)^{1/3}$ in regions of unstable stratification and $l_{\rm SFS} = 0.76\sqrt{e}/N$ (Deardorff, 1973) under stable stratification where $N = \sqrt{(g/\Theta_0)(\partial\theta/\partial z)}$ is the Brunt-Väisälä frequency. Use of the stability dependent length scale is critical to prevent Eqs. (3.1)–(3.2) from blowing up in stably stratified regions.

3.5 Set-up of LES runs

The GABLS experiment (Beare et al., 2006) was the first major intercomparison study that assessed the ability of different SFS models to simulate the moderately stable boundary layer. We describe briefly the main parameters of the LES runs used in GABLS, as we use an identical set-up for our LES runs in this chapter. The set-up used in GABLS is similar to that used by Kosović and Curry (2000), who in turn modeled their runs on the BASE (Beaufort Sea Arctic Stratus Experiment) observations.

The domain size is 400 m in all three directions. The surface cooling rate is prescribed to be 0.25 K/hr. The geostrophic wind in the x-direction is 8m/s with the Coriolis parameter set to 1.39 x 10^{-4} s^{-1} (corresponding to latitude 73°N). To initiate turbulence, a random potential temperature perturbation of amplitude 0.1 K and zero mean is applied to vertical levels below a height of 50 m. The initial SFS turbulent kinetic energy is initialized as $0.4(1 - z/250)^3$ m^2s^3, for $z < 250$m and is set to zero for $z > 250$m. Gravity wave damping is applied above $z = 300$m to suppress reflection of gravity waves from the top of the domain. The damping is achieved by nudging the instantaneous velocities linearly towards their geostrophic values. The surface roughness length is 0.1 m and the initial surface potential temperature is 265 K. The terrain is assumed to be flat and homogeneous. The simulations are run for a total of 9 hours (model time) and statistics are collected over the last one hour. The long simulation times are necessary in order to obtain a quasi-steady SBL which then enables comparisons between the LES results and Nieuwstadt's predictions (Nieuwstadt, 1984). In following the GABLS set-up for our LES runs, our goal is admittedly modest: to assess the performance of the modeled SFS conservation equations in simulating the quasi-steady moderately stable boundary layer. Consequently, factors such as terrain slope, gravity waves and very strong stratification (the "very stable boundary layer" (Mahrt, 1998)), while certainly relevant to a more general treatment of the SBL, are beyond the scope of our LES study.

Before presenting the results, we comment briefly on our use of a surface cooling rate rather than the surface heat flux as the lower boundary condition. Basu et al. (2008) have demonstrated theoretically and numerically that prescribing the surface heat flux is suitable only for near-neutral to weakly-stable conditions as it leads to erroneous values of u_* for strong stratifications. They showed that prescribing the surface potential temperature is more appropriate and recommended avoiding the specification of the surface heat flux as a lower boundary condition in LES of the SBL.

3.6 Results

In this section, we present LES results using three different grid sizes: 128x128x128, 64x64x64 and 32x32x32, which correspond to resolutions 3.125m, 6.25m and 12.5m, respectively. We denote the corresponding LES runs as SBL1, SBL2 and SBL3, in increasing order of coarseness. All participants in the GABLS experiment (Beare et al., 2006) submitted results from LES runs at the above three resolutions. A couple of participants also submitted results at a resolution of 1 m. We begin with a brief discussion of the modeled SFS budgets of τ_{ij}^d followed by those of f_i, as described by Eqs. (3.1)–(3.2). We plot the budgets only for SBL2 as an illustrative case.

We define the boundary layer height in a manner similar to Kosović and Curry (2000) and Beare et al. (2006), wherein $z_i = z_{0.95}/0.95$, $z_{0.95}$ being the height at which the total (resolved + SFS) resultant shear stress, $\sqrt{\langle u'w'\rangle^2 + \langle v'w'\rangle^2}$, falls to a small fraction (5%) of its surface value, u_*^2. In the SBL, it is preferable to define z_i in terms of the momentum fluxes rather than the heat flux as the latter is influenced significantly by gravity waves near the top of the SBL (Kosović and Curry, 2000) and thus, the height corresponding to zero heat flux might not be an accurate indicator of the boundary layer top.

3.6.1 Modeled τ_{ij}^d budgets

In Fig. (3.14) are shown the various terms in the modeled τ_{ij}^d budgets, scaled with $\left\langle -\tau_{ij}^d \bar{S}_{ij} \right\rangle$ and plotted versus z/z_i, where $z_i = 182$m is the inversion height. At equilibrium, the dissipation of turbulent kinetic energy, ϵ is approximately equal to $\left\langle -\tau_{ij}^d \bar{S}_{ij} \right\rangle$. In the HATS data, the stably-stratified cases are associated with lower values of Δ_w/Δ than are the unstable cases. In our LES runs of the SBL,

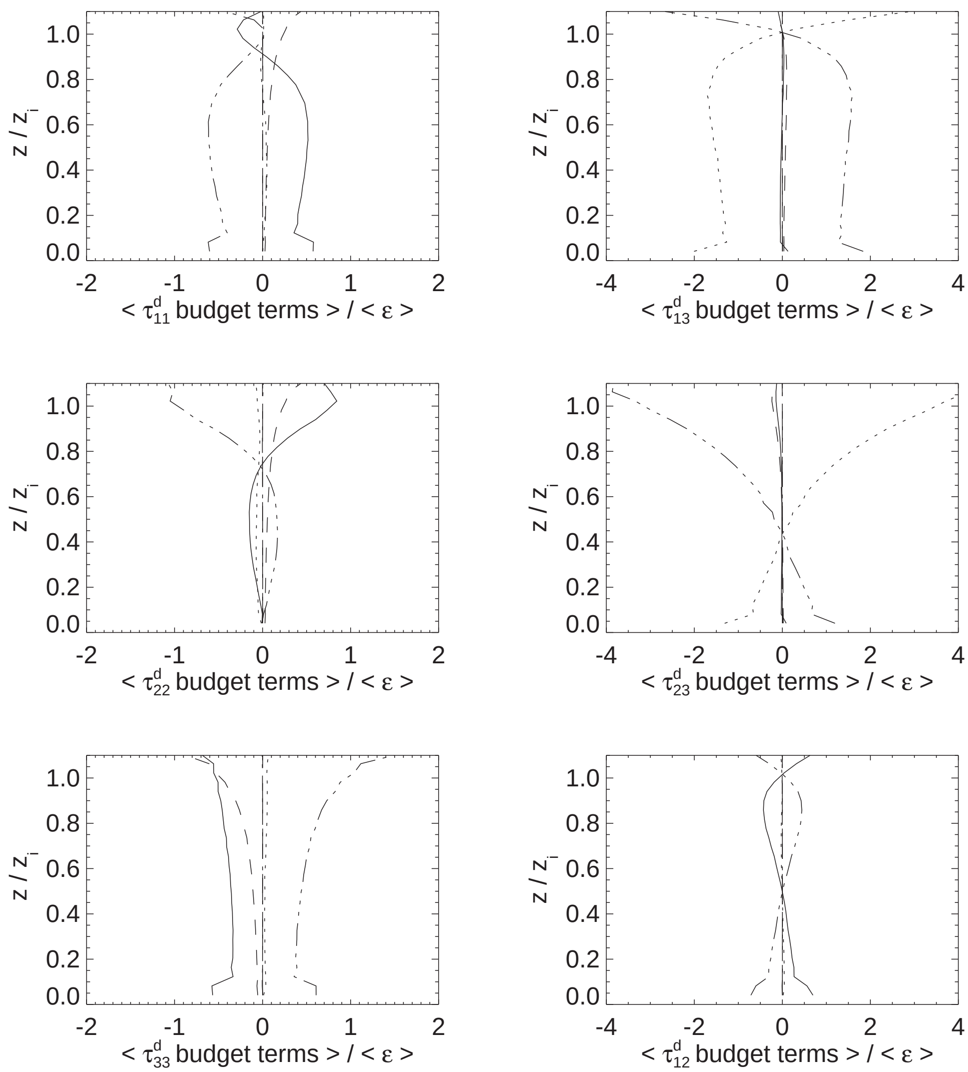

Figure 3.14. Plane-averaged values of terms in the SFS stress budgets scaled with $\left\langle -\tau_{ij}^{d}\bar{S}_{ij}\right\rangle$, for the run SBL2 ($64^3$). Left column: diagonal components, right column: off-diagonal components. The scaled terms are plotted versus z/z_i, where $z_i = 182$m is the inversion height. Plot legend: (—) Anisotropic production, ($\cdots$) Isotropic production, ($--$) Buoyant production, ($-\cdot$) Advection, ($-\cdots-$) Pressure-strain covariance, (— —) Time tendency

we expect the lowest values of Δ_w/Δ to occur in the surface layer, where $\Delta_w \sim z$ (Lenschow et al., 1988)

3.6.1.1 $\tau^d_{\alpha\alpha}$ budgets

The HATS data show anisotropic production to be the principal production term in the $\tau^d_{\alpha\alpha}$ budgets and buoyant production to be non-negligible in the τ^d_{33} budget at low Δ_w/Δ. Fig. (3.14) shows the dominance of anisotropic production over isotropic production in the $\tau^d_{\alpha\alpha}$ budgets. Due to stable stratification, buoyancy appears as a loss in the τ^d_{33} budget and, as a gain in the τ^d_{11} and τ^d_{22} budgets. The effects of buoyancy are most significant near the inversion, a region of strong stratification due to steep gradients in mean potential temperature. Modeled slow pressure-strain covariance is the principal destruction term that balances anisotropic production in the $\tau^d_{\alpha\alpha}$ budgets. The advection terms are negligible in the mean. They are, however, necessary for the SFS model to extract energy meaningfully from the resolved-scales and avoid a spurious build-up of resolved-scale energy close to the filter cut-off, as discussed earlier in Ch. (2).

To see the effect of the anisotropic production term, we examine the mean values of $\tau^d_{\alpha\alpha}$ as predicted by LES and compare them to observations. We show results obtained using two closures: (i) an eddy-diffusivity closure; and (ii) the modeled SFS conservation equations. The eddy-diffusivity closure is identical to the one used in Ch. (2), wherein the eddy-diffusivity, K_m, is defined to be $K_m = c_k\sqrt{e}\ \Delta$. For our LES runs of the unstable ABL, we used $c_k = 0.1$, a value first derived by Lilly (1967) assuming homogeneous and isotropic turbulence. In LES of the SBL, however, we found $c_k = 0.1$ to be too high as it leads to incorrect mean potential-temperature profiles that were almost linear while past LES studies (Basu and Porté-Agel, 2006; Beare et al., 2006) and field observations (Caughey et al., 1979; Lenschow et al., 1988; Newsom and Banta, 2003; Nieuwstadt, 1984) show the mean potential temperature profile to have a positive curvature in the middle portion of the boundary layer. We found that reducing c_k was necessary to obtain more realistic mean potential temperature profiles. Thus, we use $c_k = 0.06$ in all our LES runs using the eddy-diffusivity closure.

In Fig. (3.15), we plot $\tau^d_{\alpha\alpha}/u_*^2$ as a function of Δ_w/Δ for the stable HATS cases. As Δ_w/Δ decreases, τ^d_{11}/u_*^2 (> 0) and τ^d_{33}/u_*^2 (< 0) increase sharply in magnitude while τ^d_{22}/u_*^2 attains small negative values. Thus, the SFS stresses are strongly anisotropic at low Δ_w/Δ, which we recall describes conditions of under-resolved turbulence such as the near-wall region, strongly stratified flow, etc. In Fig. (3.16), we plot $\tau^d_{\alpha\alpha}/u_*^2$ obtained from LES. A qualitative comparison of Figs. (3.15)-(3.16) reveals that the modeled SFS conservation equations are capable of reproducing anisotropy at the subfilter scales but severely underpredict $\tau^d_{\alpha\alpha}$ when compared to observations. The eddy-diffusivity closure predicts near-zero values of $\tau^d_{\alpha\alpha}/u_*^2$ throughout the boundary layer, as it fails to account for SFS anisotropy.

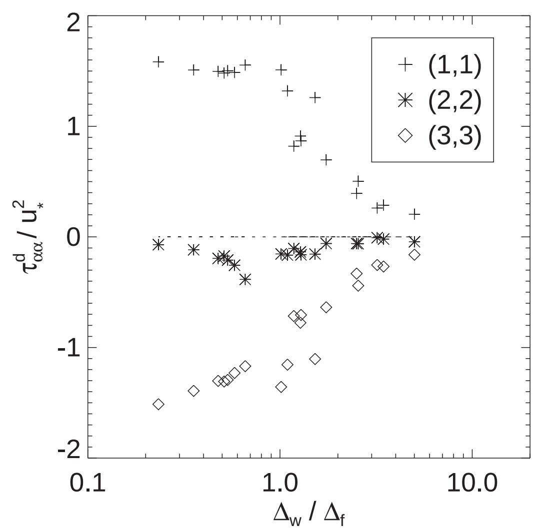

Figure 3.15. HATS, stable cases: SFS deviatoric stresses, $\tau^d_{\alpha\alpha}/u_*^2$, plotted versus Δ_w/Δ.

3.6.1.2 $\tau^d_{\alpha\beta}$ budgets

In the τ^d_{13} budget, the HATS data yield isotropic production as the principal production term but anisotropic production and buoyant production are also significant, especially at low values of Δ_w/Δ. Our LES results yield isotropic production to be the dominant production term in the τ^d_{13} budget but yield negligible values for both anisotropic- and buoyant-production, in comparison to observations. The underprediction of anisotropic production in the τ^d_{13} budget was also observed in our LES simulations of the unstable boundary layer in Ch. (2). Anisotropic production in the τ^d_{13} budget is determined primarily by the term $-\tau^d_{33}\left(\partial\bar{u}/\partial z\right)$ (Chen et al., 2005). Thus, the underprediction of anisotropic production is likely due to the underprediction of τ^d_{33}. In Ch. (2), we speculated that the modeled SFS conservation equations underpredict the magnitude of $\tau^d_{\alpha\alpha}$ at low Δ_w/Δ due to the

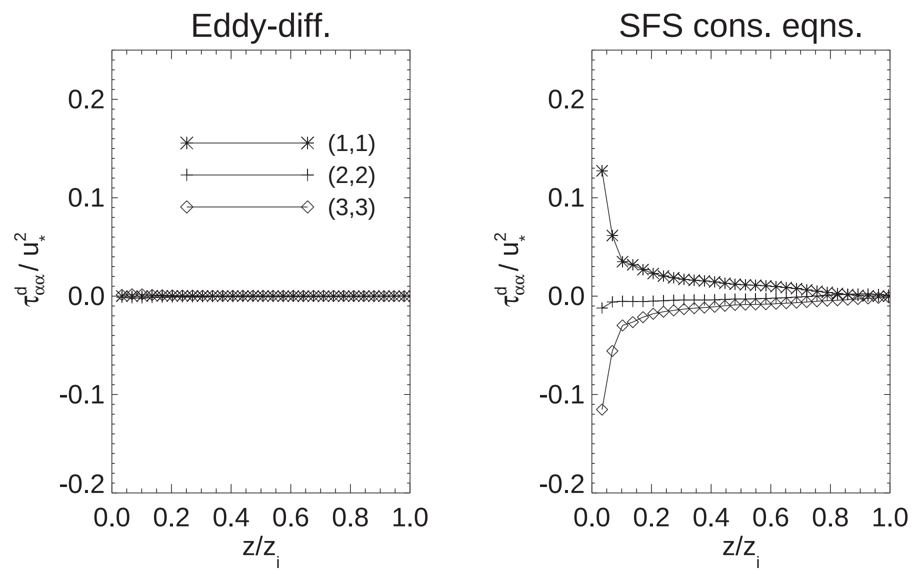

Figure 3.16. LES: SFS deviatoric stresses, $\tau_{\alpha\alpha}/u_*^2$, plotted versus z/z_i, using an eddy-diffusivity closure (left) and the modeled SFS conservation equations (right).

inadequacy of the model for the pressure-strain covariance terms. Thus, it is plausible that the modeled pressure strain covariance term influences the predictions of anisotropic production adversely in the SBL as well.

The τ_{23}^d budget is qualitatively similar to the τ_{13}^d budget wherein it is in balance between isotropic production and modeled slow pressure strain-rate covariance. The τ_{12}^d budget has anisotropic production as the principal production mechanism which is balanced by modeled slow pressure strain-rate covariance. The mean SFS advection terms are negligible in the $\tau_{\alpha\beta}$ budgets. Although we have shown the modeled SFS budgets for all six τ_{ij}^d components, τ_{23}^d and τ_{12}^d are much smaller in magnitude than the other components.

3.6.2 Modeled f_i budgets

In Fig. (3.17), we plot the plane-averaged terms in the modeled f_i budget scaled with Q_0N, as a function of z/z_i. We now qualitatively compare Fig. (3.17) with corresponding results from HATS data, shown in Fig. (3.8).

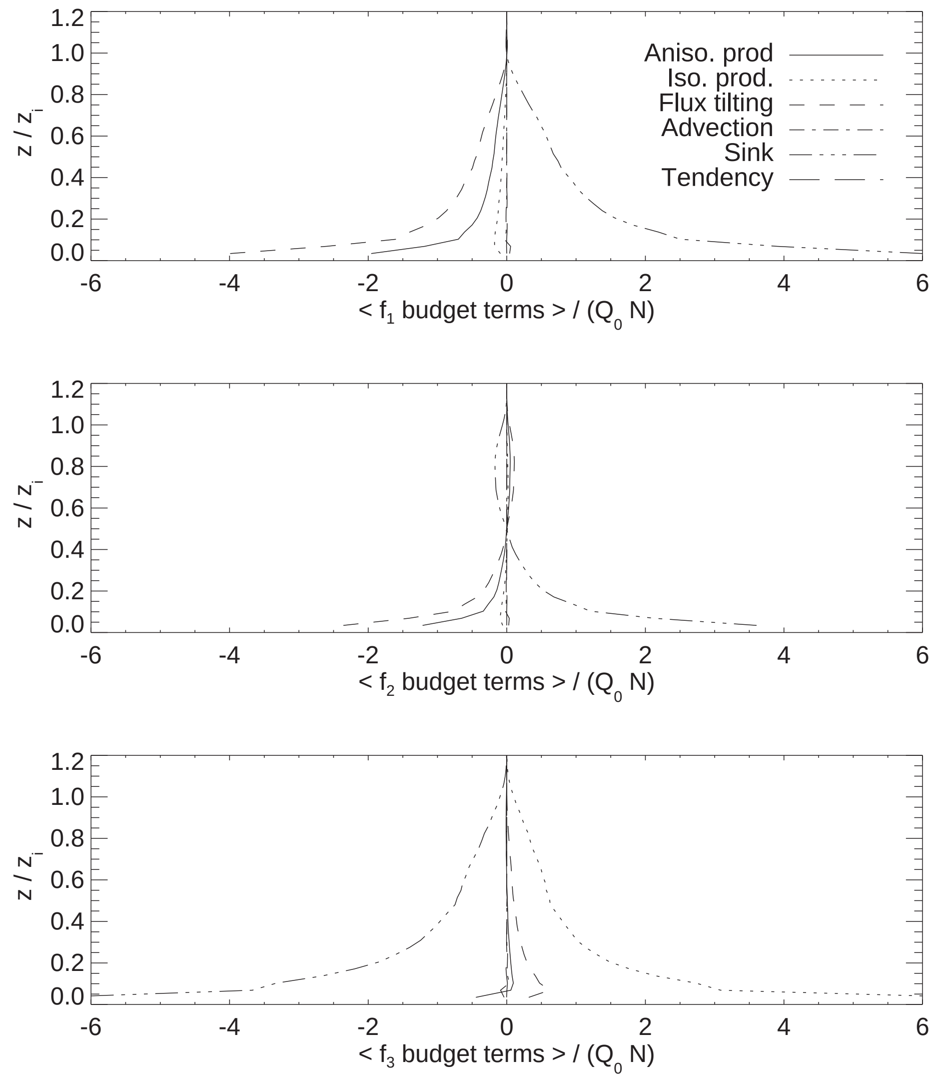

Figure 3.17. LES: Plane-averaged terms in the f_i budgets scaled with Q_0N and plotted versus z/z_i, for the run SBL2 (64^3). The variable Q_0 is the surface heat flux, N is the Brunt-Väisälä frequency, and $z_i = 182$m is the inversion height.

3.6.2.1 f_1 and f_2 budgets

Our LES results show that the principal production terms in the f_1 budget are flux tilting and anisotropic gradient-production, in agreement with Fig. (3.8). Isotropic gradient-production and advection in the modeled f_1 budget are negligible. The advection term, while negligible in the mean, is necessary to prevent an unphysical

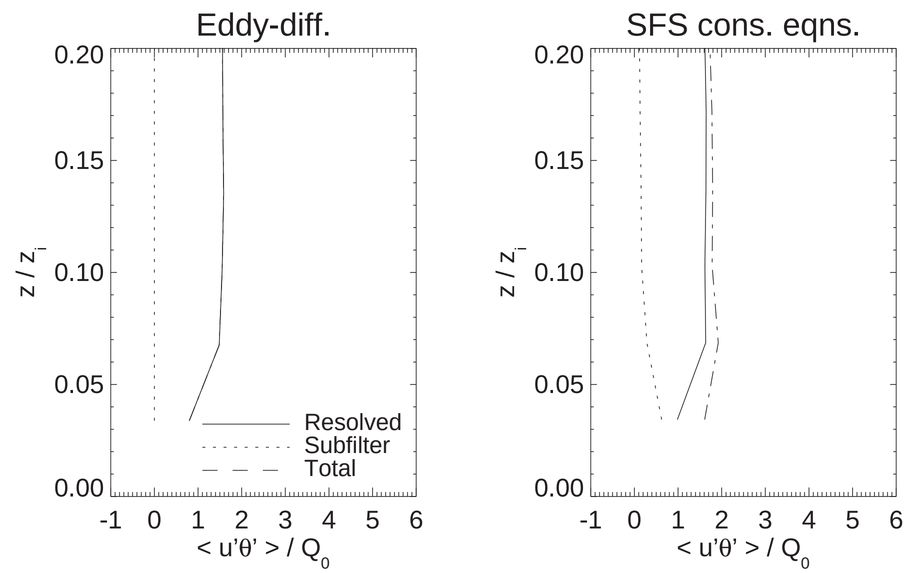

Figure 3.18. LES: Horizontal flux of potential temperature versus z/z_i, for the run SBL2 using an eddy-diffusivity closure and the modeled SFS conservation equations.

build-up of resolved-scale potential temperature variance at scales close to the filter cut-off. The modeled slow pressure-strain covariance is the principal destruction term. The trends in the f_2 budget are mostly similar to those in the f_1 budget but the magnitudes of the mean production and sink terms are smaller in magnitude.

In Fig. (3.18), we plot f_1/Q_0 as a function of z/z_i. The modeled SFS conservation equations predict a non-zero value for f_1, in agreement with observations (see Fig. (3.9)). The eddy-diffusivity closure is unable to produce any horizontal SFS flux due to its sole dependence on isotropic gradient-production, which according to Fig. (3.8), plays a negligible role in the f_1 budget.

In general, the nature of balance in the modeled f_1 and f_2 budgets for the SBL mirrors that observed in our LES results for the unstable boundary layer, discussed in Chapter (2).

3.6.2.2 f_3 budget

The f_3 budget has isotropic gradient-production as its principal production term which is balanced by the modeled pressure-strain covariance. Anisotropic gradient-production and advection are negligible. Flux tilting while non-zero is much

Table 3.1. Boundary layer height (z_i), Monin-Obukhov (MO) length (L), surface flux (Q_0), MO scales u_* and θ_*, and the Zilitinkevich parameter, γ, where $\gamma = z_i/(u_*\,L/f)^{1/2}$. The statistics are averaged over the last hour of simulation. Where possible, we also list for each parameter the corresponding minimum and maximum values observed in the GABLS LES-intercomparison study (Beare et al., 2006).

Diagnosed physical parameters of LES runs				
Resolution (m)	**3.125**	**6.25**	**12.5**	**3.125** (GABLS)
z_i(m)	173	182	188	$(168, 204)$
L(m)	107	107	102	$(100, 150)$
$Q_0(\mathrm{W\,m^{-2}})$	-14.62	-15.95	-15.95	$(-12.5, -19.6)$
$u_*(\mathrm{ms^{-1}})$	0.262	0.268	0.267	$(0.245, 0.283)$
θ_*(K)	0.043	0.045	0.047	–
γ	0.38	0.40	0.42	–

smaller than isotropic gradient-production everywhere in the ABL. The dominance of isotropic gradient-production in the modeled f_3 budget is also observed in the HATS data. Anisotropic-gradient production, however, is severely under-predicted in the modeled f_3 budget compared to observations, which show it to be a significant loss term even if lesser in magnitude than isotropic gradient-production. This under-prediction of anisotropic gradient-production was also observed in our LES results for the unstable boundary layer. We now proceed to discuss in detail our results obtained from LES runs SBL1, SBL2 and SBL3.

3.6.3 Bulk parameters

Table (3.1) lists the boundary layer height (z_i), Monin-Obukhov (MO) length (L), surface heat flux (Q_0), the MO scales θ_* and u_*, and the Zilitinkevich parameter, $\gamma = z_i/(u_*\,L/f)^{1/2}$ (Zilitinkevich, 1972). As one of the aims in the GABLS experiment (Beare et al., 2006) was to test the sensitivity of various SFS models to grid resolution, we tabulate values from LES runs at three resolutions: (i) 3.125m; (ii) 6.25m; and (iii) 12.5m. For comparison, we also list the corresponding minimum and maximum values — where available — observed by Beare et al. (2006) at a resolution of 3.125m.

To convert the surface flux values from K-m to $\mathrm{W\,m^{-2}}$, we have used the relation, $H = -\rho\, c_p\, \theta_*\, u_*$, where H is the heat flux in $\mathrm{W\,m^{-2}}$, $\rho = 1.3223\,\mathrm{kg\,m^{-3}}$ and $c_p = 1.005\,\mathrm{kJ\,kg^{-1}\,K^{-1}}$. We obtained the values of L from the time series provided on the official GABLS webpage (www.gabls.org). The CASES experiment (Poulos et al., 2003) observed u_* and Q_0 to lie within $(0.22, 0.59)\,\mathrm{m\,s^{-1}}$ and $(-5.7, -48.4)\,\mathrm{W\,m^{-2}}$, respectively, for continuously turbulent boundary layers. Thus, the values of the bulk parameters from our LES runs at all three resolutions are consistent with the GABLS experiment and the CASES-99 experiment.

Among the parameters shown in Table (3.1), z_i exhibits the greatest sensitivity to resolution. Beare et al. (2006) found a majority of SFS models to display a similar trend wherein z_i increases with coarsening resolution. The change (increase or decrease) in predicted z_i at $\Delta = 12.5$m from that at $\Delta = 6.25$m averaged to a value of 14% across all the SFS models. Indeed, for some SFS models, the percentage increase in z_i was as high as 30% which led to a smearing out of the inversion at the coarse resolutions. In comparison, the modeled SFS conservation equations exhibit a modest increase (3%) in z_i as the resolution increases from $\Delta = 6.25$m to $\Delta = 12.5$m. The values of the other parameters in Table (3.1) differ by less than 10% for any two resolutions. Nieuwstadt (1985) derived analytically an expression for the Zilitinkevich parameter which yielded $\gamma = 0.37$. Observations reveal a slightly higher value of 0.4 (Garratt, 1982).

In Fig. (3.19) we show the time evolution of u_*, Q_0 and z_i over the entire simulation length of 9 hours. We also indicate nondimensional time, $t^* = tz_i/u_*$, on the top axis of each plot. Since our simulations include the Coriolis effect, we expect all statistics to exhibit gradual variations over a timescale $1/f$ ($\sim 10^4$ sec.), even after the flow has reached quasi-steady state.

Fig. (3.19) shows that u_* undergoes significant variations until $t \approx 15000$s ($t^* \approx 25$) after which the changes are more gradual. The boundary layer height z_i increases sharply till $t \approx 14000$s ($t^* \approx 21$). For $t > 14000$s, z_i continues to fluctuate more or less about a constant value. The fluctuations are consistent with the intermittent nature of the boundary layer top (Kosović and Curry, 2000). As our lower boundary condition employs a prescribed cooling rate instead of a prescribed surface heat flux, Q_0 varies with time although its rate of change decreases in magnitude gradually over time. By the end of the simulation Q_0 is nearly constant. Thus, to a good approximation we have quasi-steady state conditions during the final hour of simulation, which is our window for gathering statistics.

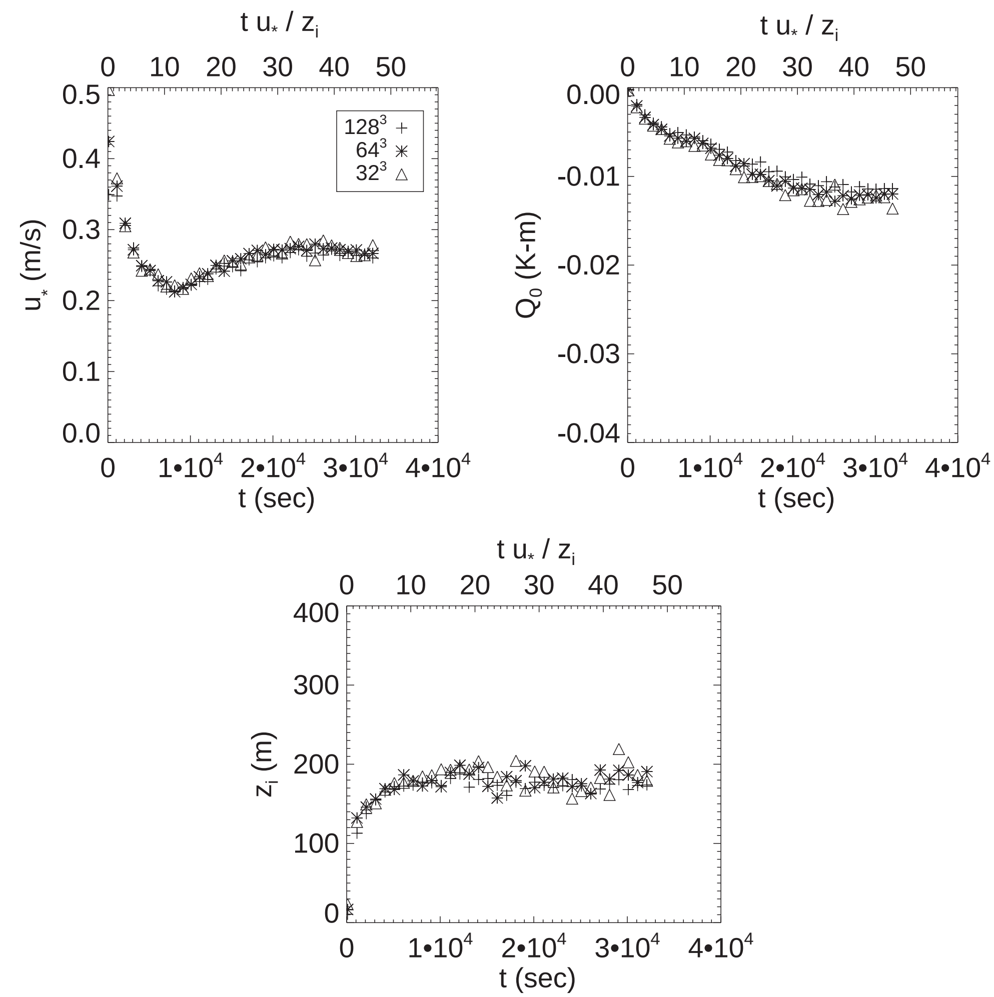

Figure 3.19. Time series of u_*, surface flux Q_0 and z_i over the entire simulation length of 9 hours. On the top axis of each plot is shown the time scaled with z_i/u_*.

3.6.4 Evolution of mean profiles of potential temperature and velocity

In Fig. (3.20) we plot the vertical profiles of mean potential temperature and resultant horizontal velocity at $t_* = (5, 15, 25, 30)$ to show their evolution with time. The profiles at $t_* = (5, 15, 25)$ are considerably different (especially $\langle\Theta\rangle$) as the flow is still transitioning towards equilibrium. The profiles at $t_* = 25$ and $t_* = 30$ are similar suggesting that the flow is nearing equilibrium. This observation

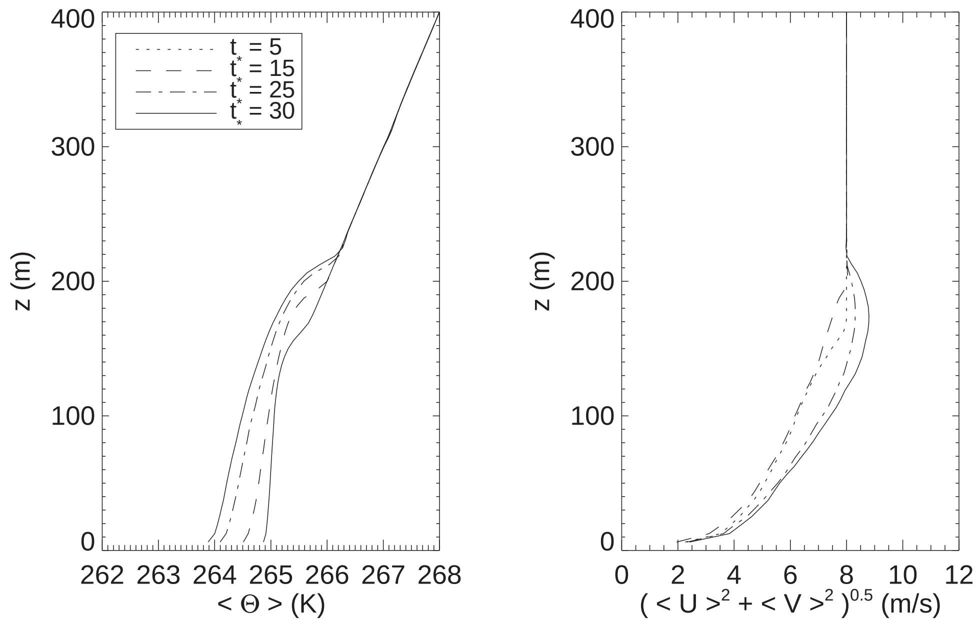

Figure 3.20. Profiles of mean potential temperature (left panel) and resultant mean velocity (right panel) at $t_* = (5, 15, 25, 30)$, where $t_* = tu_*/z_i$, is the nondimensional time.

combined with the fact that u_* stabilizes at $t_* \approx 25$ suggests that the transient phase ends approximately at $25 < t_* < 30$.

We can also see the nocturnal jet (also called the low level jet) evolving in time with the "nose" of the jet accelerating to super-geostrophic speeds, as seen in the profiles at $t_* = 25$ and $t_* = 30$. The jet continues to accelerate even beyond $t_* = 30$, as the peak jet velocity at equilibrium is higher than that implied by Fig. (3.20). As the nocturnal jet plays an important role in the SBL, we now discuss it at greater length.

3.6.4.1 The nocturnal jet

The nocturnal jet is a common feature of the nighttime boundary layer (Andreas et al., 2000; Banta et al., 2002; Davies, 2000) and refers to a shallow layer of air ($\sim$ 100m) with high shear, which is produced as a result of the dynamical decoupling of the flow aloft from the surface (Blackadar, 1957). Banta et al. (1998) showed that it influences the transport of pollutants such as Ozone in the urban boundary layer. Using data from the CASES-99 experiment, Banta et al. (2003) found that the strength of the nocturnal jet modulates the turbulence in the region below it and subsequent studies by Banta et al. (2006) showed that high jet speeds (> 15m/s) give rise to the so-called "upside down boundary layer" (Mahrt, 1999; Mahrt and Vickers, 2002), in which turbulence generated aloft due to shear propagates downwards to the surface. In such boundary layers, the turbulent fluctuations typically increase with height within the boundary layer and the peak jet velocity, U_J, scales the velocity fluctuations better than does u_*, even near the surface. Understanding the evolution of the nocturnal jet also has practical relevance for wind energy applications (Banta et al., 2008; Sim et al., 2009).

Blackadar (1957) proposed a mechanism for the evolution of the nocturnal jet, wherein the decay of the turbulent stresses aloft — and consequently, their divergence — during the early-evening period leads to an imbalance in the horizontal momentum equation, which in turn causes the jet to accelerate to super-geostrophic speeds. We now review briefly Blackadar's solution describing the nocturnal jet (Wyngaard, 2010). The horizontal mean momentum equations for an incompressible, horizontally homogeneous flow are,

$$\frac{\partial \langle U \rangle}{\partial t} = f\left(\langle V \rangle - V_g\right) - \frac{\partial \left\langle u'w' \right\rangle}{\partial z} \tag{3.3}$$

$$\frac{\partial \langle V \rangle}{\partial t} = f\left(U_g - \langle U \rangle\right) - \frac{\partial \left\langle v'w' \right\rangle}{\partial z}. \tag{3.4}$$

Neglecting the stress divergence terms, it is straightforward to show that the solution to Eqs. (3.3)–(3.4) is given by $\Delta U = U_0 e^{-if(t-t_0)}$ and $\Delta V = V_0 e^{-if(t-t_0)}$, where $\Delta U = \langle U \rangle - U_g$, $\Delta V = \langle V \rangle - V_g$, t_0 is the time at which the stress divergence terms collapse and (U_0, V_0) are the mean velocities at $t = t_0$. The above solution states that for $t > t_0$, the velocity difference vector $(\Delta U, \Delta V)$ traces out the tip of a circle of radius $\sqrt{U_0^2 + V_0^2}$ with frequency f. The nocturnal jet can also be explained as a feature of the quasi-steady SBL wherein it is a consequence of the equilibrium between the Coriolis terms and the stress divergence terms in the horizontal momentum equations (Kosović and Curry, 2000; Nieuwstadt, 1984), i.e., the first and second terms on the right hand side of Eqs. (3.3)–(3.4). This view is in agreement with past studies that found that the peak jet velocity might depend on the stress divergence terms (Mahrt, 1981). Davies (2000) have argued that the

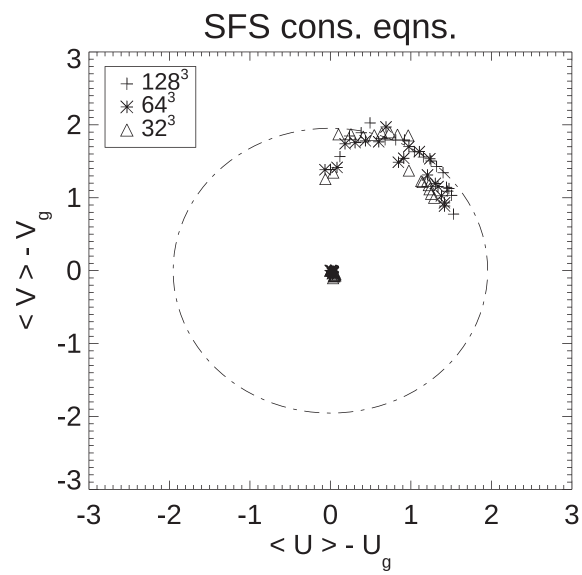

Figure 3.21. Time-evolution of the peak jet velocity shown in $(\Delta U, \Delta V)$-space where $\Delta U = \langle U \rangle - U_g$ and $\Delta V = \langle V \rangle - V_g$. The dash-dot lines in the left and right panels are circles of radii 2 and 2.2, respectively. These radii denote the magnitude of the $(\Delta U, \Delta V)$ vector at approximately the beginning of the inertial oscillation. The individual points correspond to samples collected at 1000-second intervals over the course of the simulation (9 hours).

nocturnal jet is influenced by both the above mechanisms, which implies that all terms in Eqs. (3.3)–(3.4) play a role in the evolution of the jet.

In Fig. (3.21), we plot the time-evolution of the peak jet velocity in $(\Delta U, \Delta V)$-space. The dash-dot line in Fig. (3.21) denotes a circle of radius 1.95, whose significance we explain below. To illustrate the onset of the inertial oscillation we plot the timeseries of: (i) $(\sqrt{\Delta U^2 + \Delta V^2})$ in Fig. (3.22a); (ii) the scaled Coriolis and stress divergence terms in the $(\partial\langle V\rangle/\partial t)$ equation in Fig. (3.22b); and (iii) the scaled Coriolis and stress divergence terms in the $(\partial\langle U\rangle/\partial t)$ in Fig. (3.22c). We have scaled the momentum equation terms shown in Figs. (3.22b)-(3.22c) using z_i/u_*^2. For $t_* < 22$, $\sqrt{\Delta U^2 + \Delta V^2} \approx 0$ which implies that the peak mean velocities of the jet are nearly identical to their geostrophic values. In $(\Delta U, \Delta V)$-space, this is equivalent to the velocity-difference vector occupying the origin. Shortly after $t_* > 22$, we see a sharp increase in the magnitudes of $(\Delta U, \Delta V)$ and the scaled stress divergence terms, which corresponds to the velocity-difference vector moving vertically upward from the origin in Fig. (3.21). From $t_* \approx 25$ till $t_* \approx 42$, the

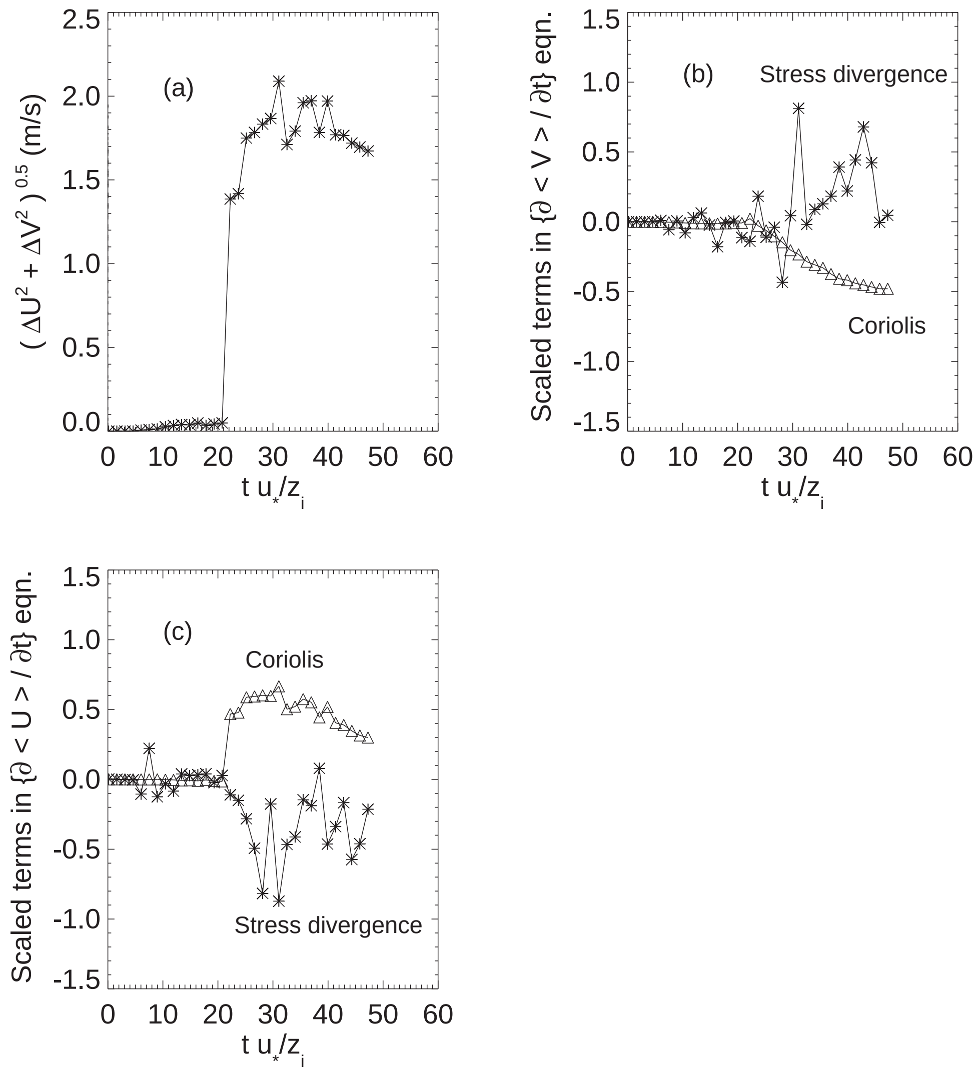

Figure 3.22. (a) Timeseries of $\sqrt{\Delta U^2 + \Delta V^2}$; (b) timeseries of scaled Coriolis and stress divergence terms in the $(\partial\langle V\rangle/\partial t)$ equation; (c) timeseries of scaled Coriolis and stress divergence terms in the $(\partial\langle U\rangle/\partial t)$. The terms shown in (b) and (c) have been scaled with z_i/u_*^2. The individual points correspond to samples collected at 1000-second intervals over the course of the simulation (9 hours). Only results from the run SBL2 have been shown.

magnitude of the $(\Delta U, \Delta V)$ vector appears to stabilize and averages approximately to a value of 1.95 and thereafter, starts tracing out a path that ideally would be a circle, as predicted by Blackadar (1957). Fig. (3.21) shows that results from the run SBL3 (128^3) agree better with Blackadar's analysis compared to the other two runs

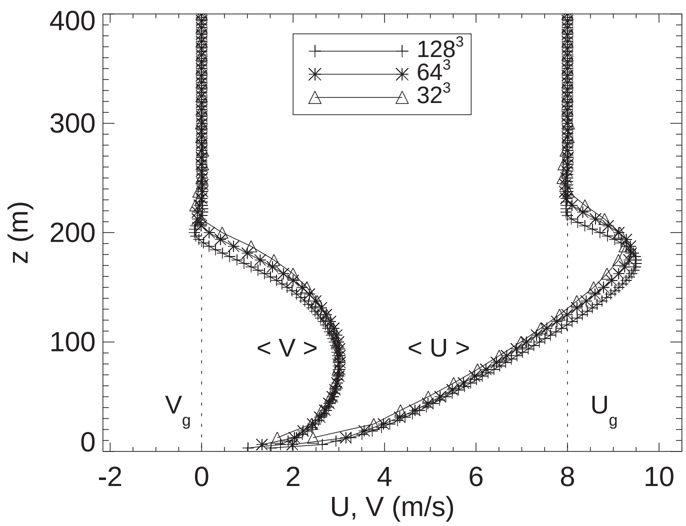

Figure 3.23. Profiles of mean velocity components, $\langle U\rangle$ and $\langle V\rangle$, obtained using the modeled SFS conservation equations. The dotted lines denote the geostrophic values, $U_g = 8$ m/s and $V_g = 0$ m/s. The profiles are averages over the last hour of simulation.

although even in the case of SBL3, the values of $(\Delta U, \Delta V)$ start to deviate from Blackadar's solution towards the final stages of the simulation. We show in later sections that higher surface cooling rates yield better agreement with Blackadar's analysis.

Although Blackadar's analysis assumes that the stress divergence terms are zero, Fig. (3.22) shows that they are non-negligible precisely when the $(\Delta U, \Delta V)$ vector appears to obey Blackadar's solution. Thus, it appears that both the Coriolis and stress divergence terms influence the dynamics of the inertial oscillation Davies (2000). We can reconcile Blackadar's analysis with our results by noting that non-zero stress divergence terms do not preclude an oscillatory solution to Eqs. (3.3)–(3.4). This is because the necessary condition for oscillatory behavior in Eqs. (3.3)–(3.4) is the presence of the time-derivative and the Coriolis terms — which together represent a linear, harmonic oscillator — and not the absence of the stress-divergence terms, although assuming the latter has the benefit of rendering the momentum equations analytically tractable. Thus, we can imagine the stress divergence terms modulating the amplitude and frequency of the oscillation without disrupting it completely.

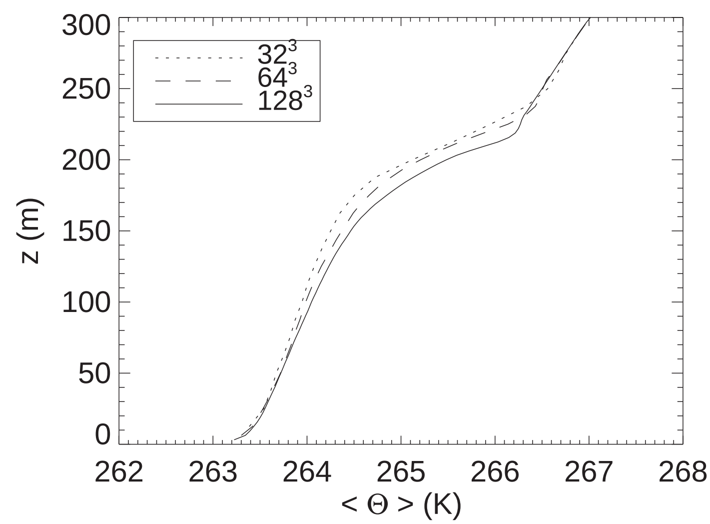

Figure 3.24. Profiles of mean potential temperature averaged over the last hour of simulation.

In Fig. (3.23), we show the profiles of the mean velocity components averaged over the last hour of simulation. We observe a deepening of the boundary layer and slight weakening of the peak jet velocity with decreasing resolution. Similar trends were also recorded in the GABLS experiment (Beare et al., 2006) and by Basu and Porté-Agel (2006) in their LES simulations using the locally-averaged scale-dependent dynamic model. The peak jet velocities are in close agreement with those observed by Beare et al. (2006).

3.6.4.2 Profile of mean potential temperature

In Fig. (3.24) we plot the profiles of mean potential temperature averaged over the final hour of simulation. A marked characteristic of the potential temperature profile in the nocturnal SBL with weak to moderate stratification is its positive curvature, i.e., $d^2\langle\Theta\rangle/dz^2 > 0$ (Caughey et al., 1979; Lenschow et al., 1988; Nieuwstadt, 1984), except very close to the surface. André and Mahrt (1982) found that SBLs associated with high wind speeds and strong mixing displayed a positive curvature in the potential temperature profile. Those associated with weak winds and dominated by clear-air radiative cooling were found to exhibit a negative curvature.

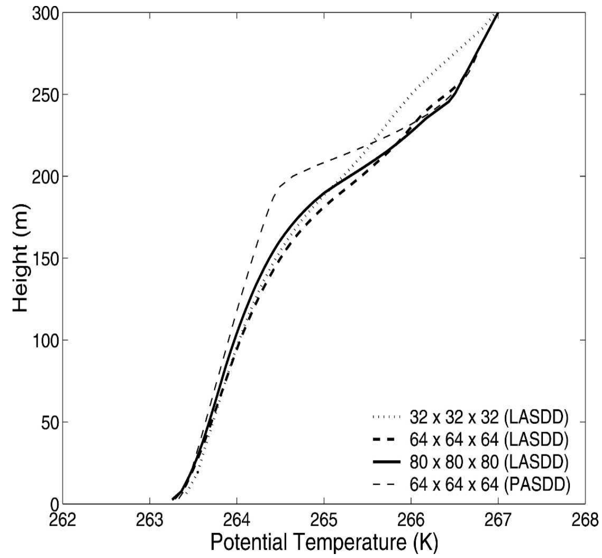

Figure 3.25. Reproduced from Basu and Porté-Agel (2006). Profiles of mean potential temperature averaged over the last hour of simulation using the locally-averaged (LASDD) and plane-averaged (PASDD) scale-dependent dynamic models.

Hyun et al. (2005) used CASES-99 data to show that the development of a strong nocturnal jet on some nights caused the curvature in the potential temperature profile to change sign from negative to positive. Analytical profiles (Nieuwstadt, 1985) and LES studies (Basu and Porté-Agel, 2006; Beare et al., 2006; Stoll and Porté-Agel, 2008) also indicate a positive curvature in the potential temperature profile for well-mixed SBLs with weak to moderate stratifications.

Figure (3.24) shows that the profiles at all three resolutions exhibit a positive curvature, which is consistent with the moderate stratification of our simulated SBLs. There is reasonable convergence between the profiles for the lowest 100 m but they exhibit differences as we approach the inversion. The GABLS experiment (Beare et al., 2006) found maximum sensitivity to the SFS model near the inversion. There is a slight decrease in curvature with the coarsening of grid resolution but the effect is less severe than that observed in some of the SFS models tested by Beare et al. (2006).

For comparison, we reproduce in Fig. (3.25), the mean potential temperature profile obtained using the locally-averaged (LASDD) and plane-averaged scale-dependent models (Basu and Porté-Agel, 2006). Both these models belong to the family of dynamic SFS models wherein the SFS model coefficient is computed dynamically from the resolved scales. The LASDD model was developed as an improvement over the PASDD model which was found to be insufficiently dissipative in regions of strong stratification (Basu and Porté-Agel, 2006). Some of the deficiencies in the LASDD model, in turn, have been addressed in the Lagrangian averaged formulation of Stoll and Porté-Agel (2008). The LES simulations of Stoll and Porté-Agel (2008) use a computational domain whose dimensions and aspect ratio are different from those used in the GABLS study. Moreover, the coarsest resolution used in the LES study by Stoll and Porté-Agel (2008) (9.92m) is finer than that (12.5m) used in the GABLS numerical experiment (Beare et al., 2006) and by Basu and Porté-Agel (2006). The physical parameters for the LES runs by Basu and Porté-Agel (2006) are identical to those used in the GABLS numerical experiment (Beare et al., 2006), which enables a direct comparison between our results and theirs. Thus, we focus here on the results obtained using the LASDD model and compare them to those obtained using the modeled SFS conservation equations. Figures (3.24)–(3.25) reveal that there is negligible difference between the results from the two SFS models at the finer resolutions. There is, however, significant deterioration in the performance of the LASDD model for the 32^3 run, as witnessed in the smearing out of the mean profile near the inversion.

3.6.5 Time series of velocity and potential temperature fluctuations

In Fig. (3.26), we plot the timeseries of the total velocity variances (resolved + SFS) scaled with u_*^2 and the resolved-scale variance of potential temperature, scaled with θ_*^2, at $z/z_i = 0.1$. The location $z/z_i = 0.1$ isn't fixed as we use the instantaneous values of z_i. Once equilibrium is attained, however, the variations in z_i are considerably lesser than in the initial stages of the simulation. The timeseries have been plotted versus t/t_*. We have used the equilibrium values of u_* and θ_* for scaling purposes.

The scaled variances of u, v and w decrease initially and reach a minimum at around $t_* \approx 13$. For $t_* > 13$, $(\langle u^2\rangle/u_*^2, \langle v^2\rangle/u_*^2, \langle w^2\rangle/u_*^2)$ increase until they attain maxima at times approximately between $t_* = 35$ and $t_* = 40$. The pre-

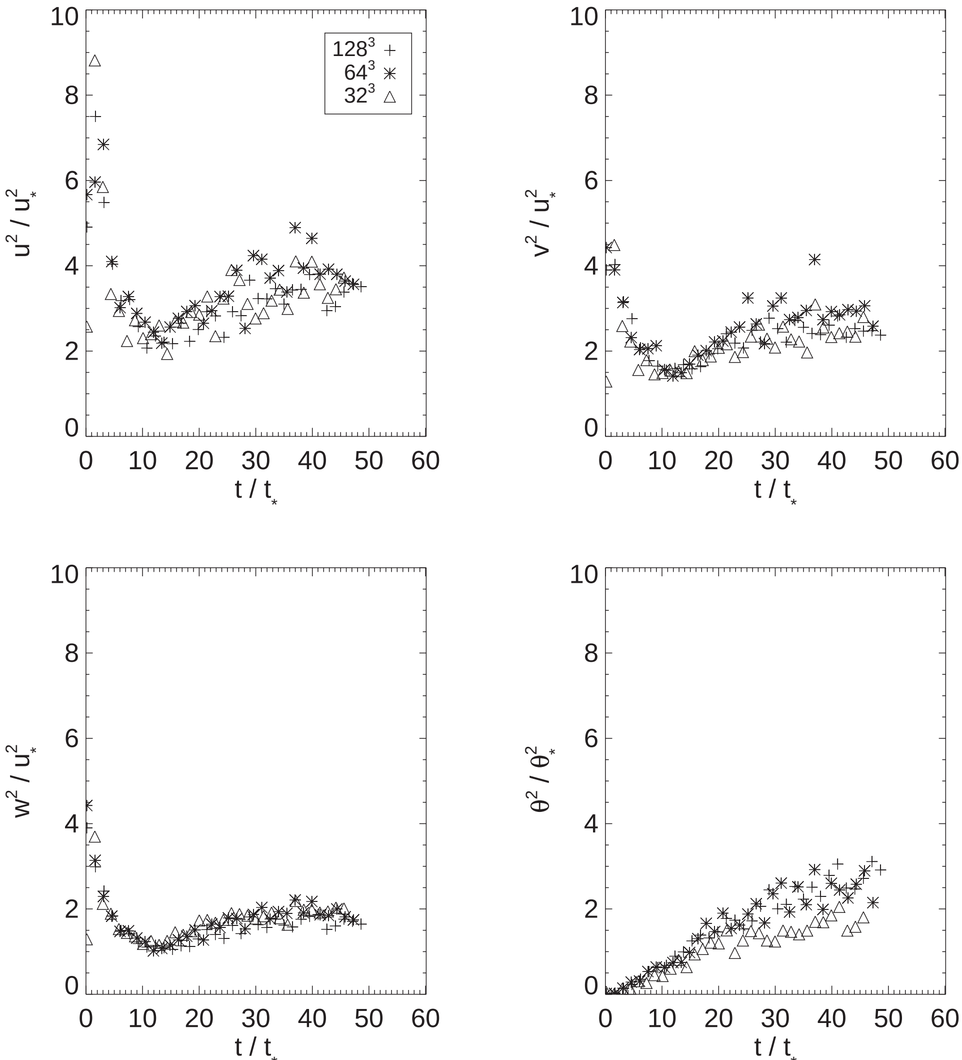

Figure 3.26. Time series of (i) $\langle u^2 \rangle$, $\langle v^2 \rangle$, $\langle w^2 \rangle$ (resolved + SFS) scaled with u_*^2; and (ii) $\langle \theta^2 \rangle$ (resolved only) scaled with θ_*^2, plotted versus t/t_* at $z/z_i = 0.1$, where $t_* = z_i/u_*$. The individual points correspond to samples collected at 1000-second intervals over the course of the simulation (9 hours).

dictions of $(\langle u^2 \rangle/u_*^2, \langle v^2 \rangle/u_*^2)$ are considerably more sensitive to grid resolution compared to those of $\langle w^2 \rangle/u_*^2$. The values of resolved-scale potential temperature variance increase almost linearly versus time till around $t/t_* \approx 25$. For $t/t_* > 25$, their growth rate is resolution-dependent. The scaled variances for the runs SBL1 and SBL2 increase at a rate faster than that for the coarsest run, SBL3, and appear to stabilize at around $t/t_* \approx 40$, which is approximately when the surface flux, Q_0, stabilizes. Their steady-state values are greatest for the run SBL1 and least for SBL3 which is consistent with the notion of a finer grid yielding greater resolved-scale variances. The Minnesota experiments (Caughey et al., 1979) yielded values of 3.8, 1.8 and 3.0 for $\langle u^2 \rangle / u_*^2$, $\langle w^2 \rangle / u_*^2$ and $\langle \theta^2 \rangle / \theta_*^2$ (resolved + SFS), respectively, at $z/z_i = 0.1$. Aircraft measurements during the Severe Environmental Storms and Mesoscale Experiment (Lenschow et al., 1988) found $\left(\langle u^2 \rangle, \langle v^2 \rangle, \langle w^2 \rangle \right) / u_*^2 \approx (3.8, 3.8, 2.2)$ at $z/z_i = 0.1$. The scaled potential temperature variances obtained by Lenschow et al. (1988) exhibited considerable scatter and yielded values of 4–4.5 at $z/z_i = 0.1$. Our values of $\left(\langle u^2 \rangle, \langle w^2 \rangle \right) / u_*^2$ during the last hour of simulation agree satisfactorily with observations while those of $\langle v^2 \rangle / u_*^2$ are underpredicted. We use values of resolved-scale $\langle \theta^2 \rangle / \theta_*^2$ from run SBL1 for comparison with observations as the SFS contribution is least for SBL1 among the three runs. The resolved-scale potential temperature variances from LES agree well with field measurements (Caughey et al., 1979) but are underpredicted when compared to aircraft measurements (Lenschow et al., 1988). To provide further context to our results, we now cite results from a few DNS studies.

Nieuwstadt (2005) performed DNS of stably stratified channel flow with no rotation for a range of stratifications. In his DNS study, the Reynolds number, $Re_* = u_* z_i / \nu = 360$, was quite low but he invoked Reynolds number similarity to postulate that his results might be relevant for higher Reynolds numbers as well. The CASES-99 experiment (Poulos et al., 2003; Van de Wiel et al., 2003) in Kansas found u_* to lie in the range $(0.22, 0.59)$m/s for continuously turbulent stable boundary layers spanning a wide range of stratifications. Corresponding values of z_i range from 70m and 200m. Choosing $u_* = 0.4$m/s and $z_i = 150$m as representative values, and using $\nu \sim 10^{-5}$, we obtain $Re_* \sim 10^6$ which is four orders of magnitude higher than its value in Nieuwstadt's DNS studies (Nieuwstadt, 2005). He found the maximum value of z_i/L — a measure of the stratification — that could sustain continuous turbulence in the channel[1], to be 0.6. This value is much lower than the z_i/L values in our LES runs (≈ 1.7) and in past LES studies (Basu and Porté-Agel, 2006; Beare et al., 2006) which report z_i/L values of ≈ 2. For $z_i/L < 0.6$,

[1]Nieuwstadt originally reported the critical value of z_i/L to be 1.2 but he defined L without using the von Kármán constant, $k = 0.4$, in the denominator. We have recalculated Nieuwstadt's z_i/L values using the traditional definition of L.

Nieuwstadt (2005) found $\langle u^2 \rangle / u_*^2$, $\langle v^2 \rangle / u_*^2$ and $\langle w^2 \rangle / u_*^2$ to attain steady-state values of 4, 1.5 and 0.8, respectively, at $z/z_i = 0.1$ for $t_* > 25$. The DNS values of $\langle u^2 \rangle / u_*^2$ agree reasonably with observations (Caughey et al., 1979; Lenschow et al., 1988) and our LES results but those of $\langle v^2 \rangle / u_*^2$ and $\langle w^2 \rangle / u_*^2$ are significantly lower in comparison. From Fig. (3.26), the LES values of $\langle w^2 \rangle / u_*^2$ stabilize at $t_* \approx 25$, in agreement with Nieuwstadt's (2005) DNS studies. We recall that u_* also stabilizes around $t/t_* \approx 25$ (see Fig. (3.19)).

DNS by Iida et al. (2002) corresponding to $Re_* = 150$ and $Ri_b = 0.35$ (defined below) yielded values of the scaled velocity variances at $z/z_i = 0.1$ that are nearly equal to those obtained by Nieuwstadt. They found $\langle \theta^2 \rangle / \theta_*^2 \approx 5.7$ at $z/z_i = 0.1$ which is high compared to field measurements (Caughey et al., 1979). The variable $Ri_b = (g\Theta_0)(\Delta\theta \; z_i/U_g^2)$, where $\Delta\theta$ is the change in θ across the boundary layer, denotes the bulk Richardson number and is a measure of the global stratification. In our LES runs, we estimate Ri_b to be 0.16. Iida et al. (2002) found that $Ri_b > 0.54$ caused the flow to re-laminarize.

Thus, although a strict comparison between DNS and our LES results might not be possible due to the differences in Re, there appears to be limited agreement between the two in select aspects of the flow dynamics.

3.6.6 Profiles of flux- and gradient-Richardson number

The flux Richardson number, Ri_f, is defined to be the ratio of buoyant destruction to shear production of turbulent kinetic energy. A related nondimensional quantity is the gradient Richardson number, Ri_g, which can be derived from Ri_f assuming a gradient-diffusion form for the turbulent fluxes. Both Ri_g and Ri_f are indicators of the level of stratification in a flow.

In Fig. (3.27), we plot Ri_g and Ri_f averaged over the last hour of simulation. They are found to increase smoothly with height within the boundary layer ($173\,\mathrm{m} < \mathrm{z_i} < 188\,\mathrm{m}$). All three runs yield a value of Ri_g between 0.25 and 0.30 near the inversion. Miles (1961) used linear stability analysis to show that a stratified flow is stable for $Ri_g > 0.25$. Field studies (Caughey et al., 1979) and wind tunnel measurements (Ohya, 2001; Ohya et al., 1997) show that for weak to moderate stratification, Ri_g increases gradually with height and attains values

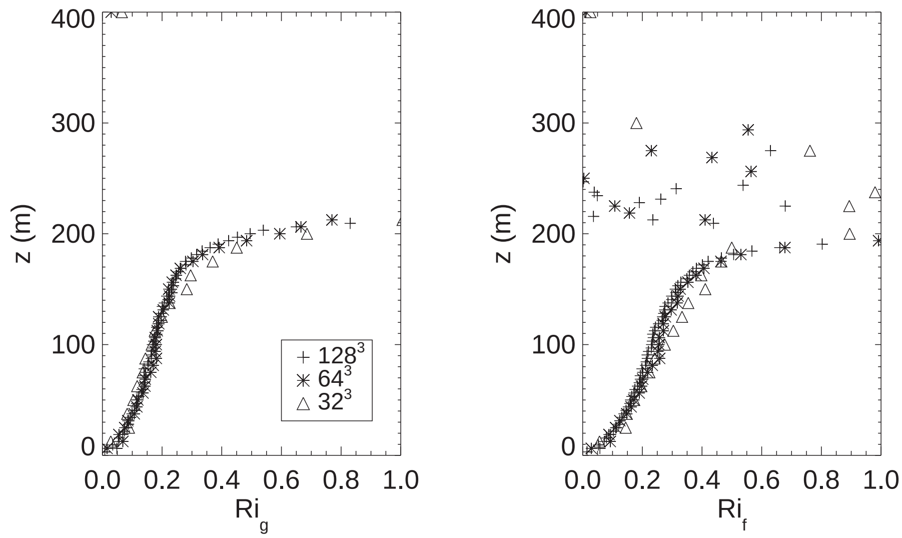

Figure 3.27. Vertical profiles of gradient Richardson number, Ri_g, and flux Richardson number, Ri_f. The mean inversion height for the runs SBL1-SBL3 is $\approx$ 181 m. The profiles are averages over the last hour of simulation.

close to the critical value (0.25) near the inversion. Thus, our Ri_g values near the inversion are consistent with theory and observations. Above the inversion, Ri_g is unbounded because the gradient of mean velocity tends towards zero while that of mean potential temperature stays finite. In contrast, the definition of Ri_f involves fluxes as opposed to gradients and hence, is ill-defined above the inversion due to negligible levels of turbulence there. For comparison, we show the vertical profile of Ri_g obtained using the LASDD model (Basu and Porté-Agel, 2006) in Fig. (3.28). The sensitivity to resolution in Fig.(3.28) is greater than in the case of the modeled SFS conservation equations. We found that similar conclusions hold for Ri_f as well (plot not shown).

Our LES values of Ri_g/Ri_f, which is equal to the turbulent Prandtl number, Pr, are 0.6–0.7 throughout most of the boundary layer for all three grid resolutions. The turbulent Prandtl number is a measure of the relative mixing efficiencies of momentum and heat. Townsend (1976) and Yakhot and Orszag (1986) predicted a value of 0.7 for the Prandtl number analytically. For weak stratification, Schumann and Gerz (1995) estimated Pr to lie between 0.8 and 1.2. Howell and Sun (1999) found Pr to be $O(1)$ in the stable surface layer from field experiments. They also

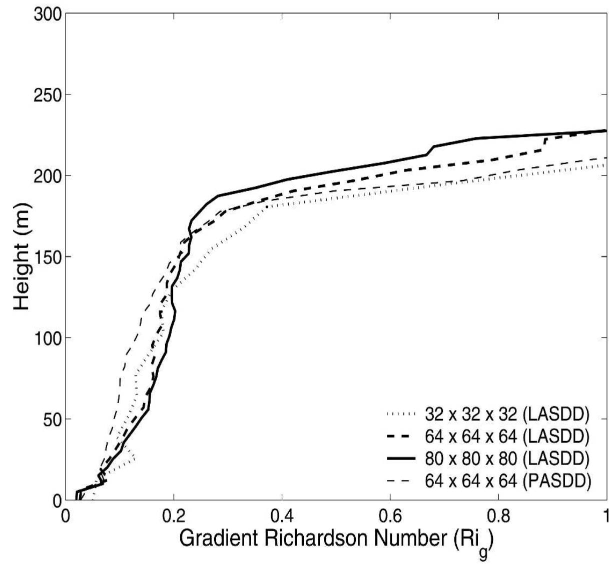

Figure 3.28. Reproduced from Basu and Porté-Agel (2006). Vertical profile of gradient Richardson number, Ri_g, averaged over the last hour of simulation using the locally-averaged (LASDD) and plane-averaged (PASDD) scale-dependent dynamic models.

observed an increase in the value of Pr towards the surface implying more efficient mixing of momentum relative to heat near the wall. Ha et al. (2007) noticed similar trends in their analysis of CASES-99 data. Our LES values of Pr do not increase towards the surface. The LASDD model does exhibit such an increase in Pr towards the surface (Basu and Porté-Agel, 2006).

3.6.6.1 Ri_f as a function of Ri_g

The flux Richardson number is an important modeling parameter in mesoscale codes and is parameterized typically as a function of Ri_g (Pardyjak et al., 2002). Thus, it is of interest to examine the relationship between Ri_f and Ri_g. In Fig. (3.29) we plot Ri_f as a function of Ri_g. We have shown only the points inside the boundary layer as Ri_f is not well-defined in regions where the turbulent fluxes are negligible. We recall that $Ri_g < 0.25$ within the boundary layer except near the inversion where it increases sharply to super-critical values. For comparison, we also show the following parameterizations of Ri_f used in the literature:

- $Ri_f = 0.725\left[Ri_g + 0.186 - \left(Ri_g^2 - 0.316Ri_g + 0.0346\right)^{1/2}\right]$ (Mellor and Ya-

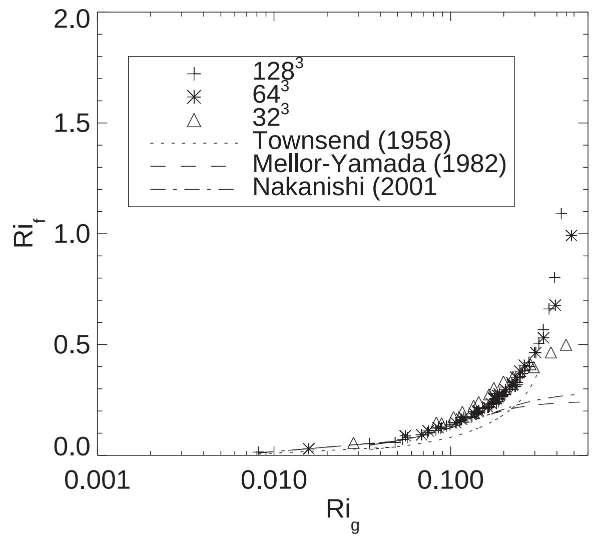

Figure 3.29. The flux Richardson number, Ri_f, as a function of the gradient Richardson number, Ri_g. Symbols represent values from LES runs averaged over the last hour of simulation. Lines represent commonly used parameterizations for Ri_f. A value of $Ri_{g,crit} = (1/3)$ has been used in Townsend's parameterization.

mada, 1982)

- $Ri_f = 0.774\left[Ri_g + 0.220 - \left(Ri_g^2 - 0.328Ri_g + 0.0484\right)^{1/2}\right]$ (Nakanishi, 2001)
- $Ri_f = 0.5\left[1 - (1 - Ri_g/Ri_{g,cr})^{1/2}\right]$ (Townsend, 1958).

Following Pardyjak et al. (2002), we use $Ri_{g,cr} = (1/3)$ in the parameterization of Townsend (1958). The parameterizations by Nakanishi (2001) and Mellor and Yamada (1982) are very similar for $Ri_g < 0.3$.

In Fig. (3.30), we reproduce a plot from Pardyjak et al. (2002) showing Ri_f (denoted as R_f in their figure) versus Ri_g using values obtained from field studies, laboratory measurements and a few parameterizations. The field studies include measurements taken in Salt Lake City, Utah, as part of the Vertical Transport and Mixing Experiment (VTMX), and in Los Alamos. The laboratory measurements of Ri_f and Ri_g were taken by Strang and Fernando (2001). The parameterizations shown in Fig. (3.30) are identical to those shown in Fig. (3.29), the only difference being that Fig. (3.30) shows Ri_f values using Townsend's parameterization for both $Ri_{g,crit} = (1/12)$ and $Ri_{g,crit} = (1/3)$. Pardyjak et al. (2002) found Ri_f

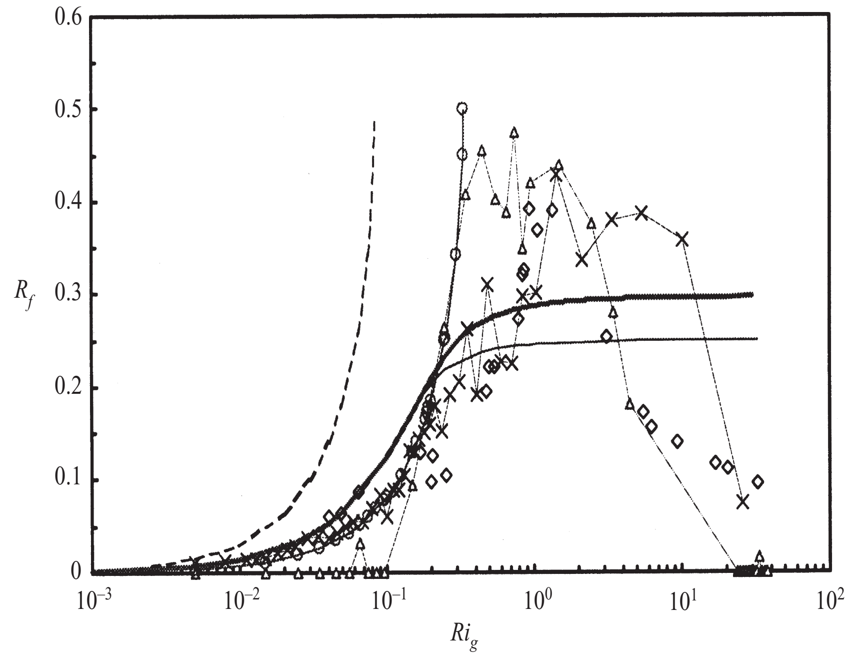

Figure 3.30. The flux Richardson number as a function of the gradient Richardson number, Ri_g (reproduced from Pardyjak et al. (2002)). Legend: $---$, Townsend (1958) with $Ri_{g,crit} = 1/12$; —, Mellor and Yamada (1982); ——, Nakanishi (2001); –△–, VTMX data; –x–, Los Alamos data; –◇–, Strang and Fernando (2001); –○–, Townsend with $Ri_{g,crit} = 1/3$.

from the field data to attain a maximum value of $0.4 - 0.5$ at $Ri_g \approx 1$ and to decrease for further increases in Ri_g. In general, they found the parameterizations to work satisfactorily only for $Ri_g < 0.1$. A comparison of Figs. (3.29)-(3.30) shows that for $0.01 < Ri_g < 0.06$, our LES results and two of the parameterizations (Mellor and Yamada, 1982; Nakanishi, 2001) agree well with observations. For $0.06 < Ri_g < 0.2$, they overpredict Ri_f while the parameterization by Townsend (1958) with $Ri_{g,crit} = 1/3$ yields better values of the same. For $Ri_g > 0.2$, the predictions by both LES and the various parameterizations are poor due to different reasons. The Townsend (1958) parameterization is defined only for Ri_g lesser than some maximum value by the nature of its definition while the other two parameterizations asymptote to non-zero values of Ri_f for high Ri_g which is inconsistent with observations. The LES results exhibit values of Ri_f that are unrealistically high for $Ri_g > 0.2$. As the critical value of Ri_g required to sustain continuous turbulence is ≈ 0.25 (Miles, 1961), values of Ri_g significantly greater than 0.25 correspond to very stable environments with highly intermittent turbulence wherein long periods of inactivity are punctuated by "bursting" phenomena with Ri_g alternating between sub-critical and super-critical values (Ohya et al., 2008; Pardyjak et al., 2002). Thus, the failure of our LES results and some of the parameterizations — which are sometimes tuned using LES — to predict Ri_f accurately at high Ri_g is a reflection of their inadequate performance in their current form, in very stable environments.

3.6.7 The "local" scaling hypothesis

The "local" scaling hypothesis (Nieuwstadt, 1984) posits that in the SBL, statistics scaled appropriately with variables at the same height (hence, "local") are functions solely of $\zeta = z/\Lambda$, where Λ is a local length scale given by,

$$\Lambda(z) = -\frac{\tau^{3/2}}{k(g/\theta_0)\langle w'\theta'\rangle}. \tag{3.5}$$

In Eq. (3.5), $\tau = [\langle u'w'\rangle(z) + \langle v'w'\rangle(z)]^{1/2}$ is the local stress magnitude, $\langle w'\theta'\rangle(z)$ is the local vertical potential temperature flux and k is the von Kármán constant. The length scale Λ tends to the Monin-Obukhov length, L, towards the surface. Nieuwstadt (1984) showed the set of scaling variables to be $(\Lambda, \tau, \langle w'\theta'\rangle)$. A corollary of the local scaling hypothesis is that variables scaled locally using the set $(\Lambda, \tau, \langle w'\theta'\rangle)$, tend to constant values in the limit $\zeta \to \infty$, also known as "z-less" scaling (Wyngaard, 1973). Physically, z-less scaling can be understood as arising due to stable stratification limiting the eddy size such that at large enough z, the flow is decoupled dynamically from the surface and z ceases to be a relevant length scale. Nieuwstadt (1984) demonstrated the validity of the local scaling hypothesis using both theoretical arguments and field studies carried out at Cabauw, Netherlands. While he observed z-less scaling for $\zeta < 4$, he found the locally scaled statistics at higher values of ζ to be "dubious because of large scatter." The local scaling hypothesis, by construction, is flux-based and hence might not be suitable for very large values of ζ which are associated with low levels of turbulence, and consequently, low magnitudes of turbulent fluxes. Using two data sets from the

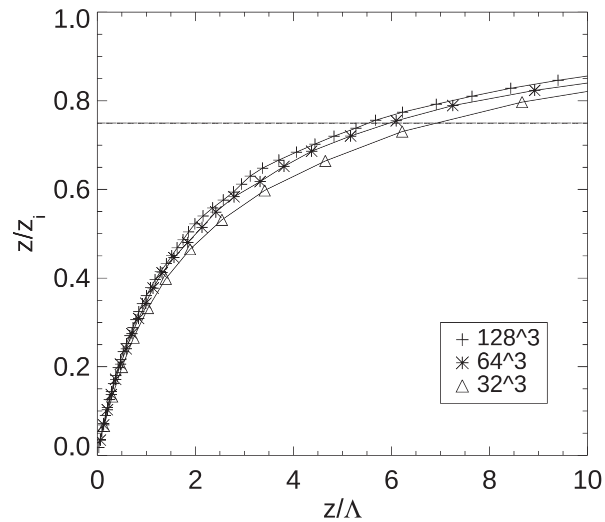

Figure 3.31. The variation of $\zeta = z/\Lambda$ versus z/z_i, where Λ is the local length scale. The horizontal dotted lined denotes $z/z_i = 0.75$.

CASES-99 experiment corresponding to continuous and weak turbulence, Sorbjan (2006) demonstrated that the flux-based local scaling arguments fail for the weakly turbulent case, which is characterized by weak winds and radiative cooling. He found a gradient-based scaling approach to work consistently in both the continuous and weakly turbulent cases.

Mahrt and Vickers (2003) have termed the functional dependence of turbulent statistics on ζ as "hybrid" similarity theory due to its consistency with both Monin-Obukhov scaling near the surface and z-less scaling away from the surface. Since Nieuwstadt's original study, both local scaling and z-less scaling have been validated in numerous field studies (Dias et al., 1995; Heinemann, 2004; Howell and Sun, 1999; Smedman, 1988), most recently in an elaborate study by Basu et al. (2006) combining field studies, wind-tunnel experiments and LES. Our focus in this study is the moderately stable boundary layers where local scaling is valid, as shown by the above studies. Thus, we do not explore the gradient-based scaling methodology outlined by Sorbjan (2006).

We consider only the lower 75% of the boundary layer while investigating our statistics for local scaling, in order to minimize the influence of the boundary layer top (Basu et al., 2006). Figure (3.31), a plot of ζ as a function of z/z_i, shows that

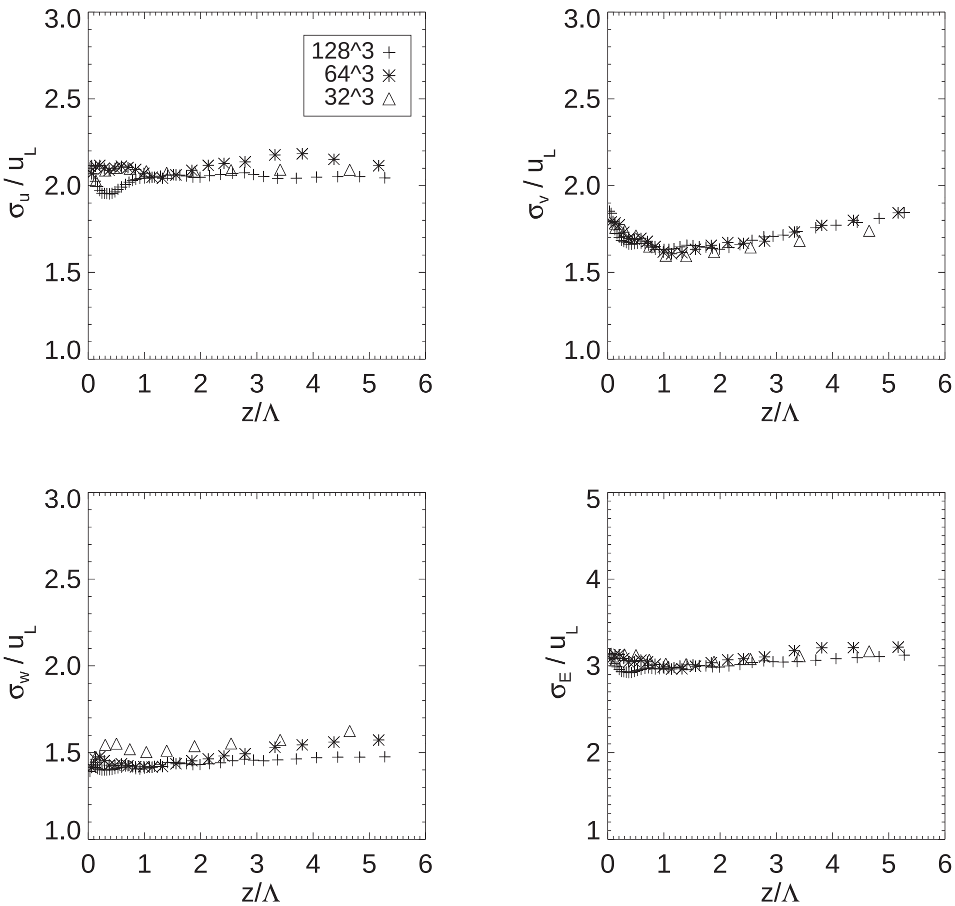

Figure 3.32. Variation of locally scaled $\sigma_u = \langle u'u' \rangle^{1/2}$, $\sigma_v = \langle v'v' \rangle^{1/2}$, $\sigma_w = \langle w'w' \rangle^{1/2}$ and $\sigma_E = \langle q'q' \rangle^{1/2}$ with $\zeta = z/\Lambda$, where $\langle q'q' \rangle = \langle u'u' \rangle + \langle v'v' \rangle + \langle w'w' \rangle$. The local variables have been scaled with $u_L = \sqrt{\tau}$.

$z/z_i = 0.75$ corresponds approximately to $\zeta = 6$–7.

3.6.7.1 Variances

In Fig. (3.32) we plot the locally scaled (resolved + SFS) standard deviations of the three velocity components and the turbulent kinetic energy. The evidence for z-less scaling is strongest in the results from the 128^3 run and in the case of σ_u, σ_w and σ_E. Locally scaled standard deviation of resolved-scale potential temperature is shown in Fig. (3.33). Both the 128^3 and 64^3 runs show σ_θ/θ_L leveling off at large ζ. We have shown here only the tendency of locally scaled statistics to

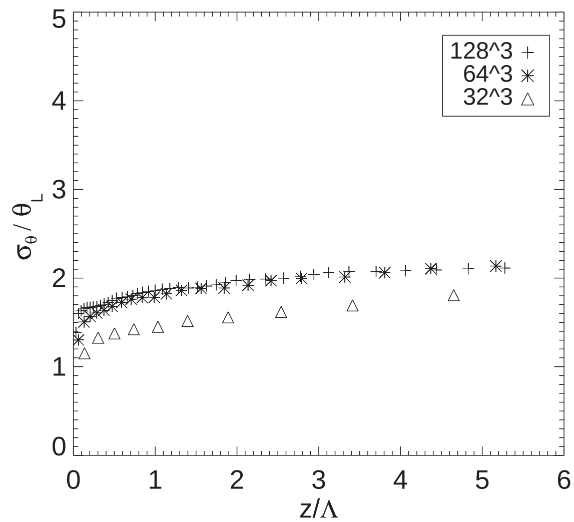

Figure 3.33. The variation of locally scaled standard deviation of resolved-scale potential temperature, σ_θ/θ_L, with $\zeta = z/\Lambda$. The local scale θ_L is given by $\theta_L = \langle w'\theta' \rangle/\tau^{0.5}$.

approach constant values at large ζ. A comparison of the actual z-less values with observations is undertaken in later sections.

3.6.7.2 Gradient-Richardson number

We plot in Fig. (3.34) the gradient-Richardson number as a function of ζ. The Cabauw data (Nieuwstadt, 1984) reveals Ri_g to increase steeply for $0 < \zeta < 1$ and at a much slower rate for $1 < \zeta < 4$, as it gradually tends towards a value of 0.2. Figure (3.34) shows that our LES results are consistent with the Cabauw data. The variation of the flux Richardson number (not shown) with ζ is very similar to that of Ri_g except that it has higher magnitudes, as discussed earlier in Sec. (3.6.6.1).

3.6.7.3 Eddy-diffusivities of momentum and heat

In Fig. (3.35), we plot the effective eddy-diffusivities of momentum and heat, denoted by K_m and K_h respectively, scaled locally using $\Lambda\tau^{0.5}$. The eddy-diffusivities,

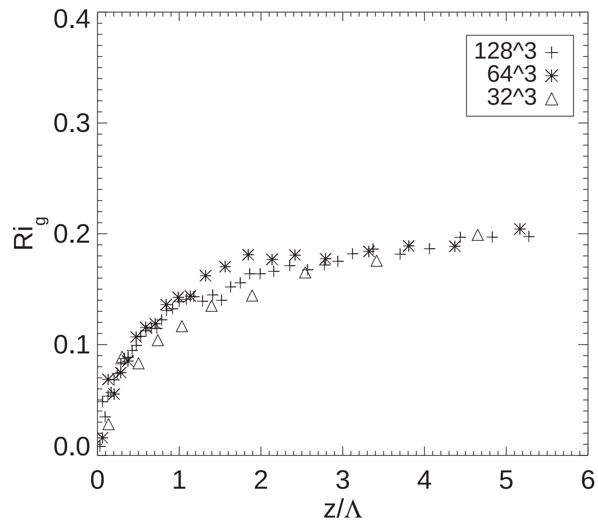

Figure 3.34. Variation of gradient-Richardson number, Ri_g, with $\zeta = z/\Lambda$.

K_m and K_h, are determined as follows:

$$K_m = \tau \left[\left(\frac{\partial \langle U \rangle}{\partial z} \right)^2 + \left(\frac{\partial \langle V \rangle}{\partial z} \right)^2 \right]^{-1/2} \quad ; \quad K_h = -\langle w'\theta' \rangle \left(\frac{\partial \langle \Theta \rangle}{\partial z} \right)^{-1} \tag{3.6}$$

For comparison, we have reproduced in Fig. (3.36), a similar plot from the GABLS experiment (Beare et al., 2006). The results shown in Fig. (3.36) are from LES runs at resolutions of 2 m (200^3) and 6.25 m (128^3). As the physical set-up of our runs is identical to that used in the GABLS experiment, a direct comparison between Fig. (3.35) and the right panel of Fig. (3.36) is possible. A visual comparison between the two plots shows that our LES predictions of scaled K_m and K_h are too high when compared to observations. The GABLS results show that most SFS models overpredict the locally scaled eddy-diffusivities considerably when compared to observations, especially at a resolution of 6.25 m. At this resolution, values of $K_m/(\Lambda\, \tau^{0.5})$ predicted by the modeled SFS conservation equations and about half of the SFS models tested by Beare et al. (2006) lie outside the observation range for low ζ, entering it at $3 < \zeta < 4$. Aircraft measurements under very stable conditions in Greenland as part of KABEG (Katabatic wind and Boundary-layer front Experiment around Greenland) (Heinemann, 2004) indicate

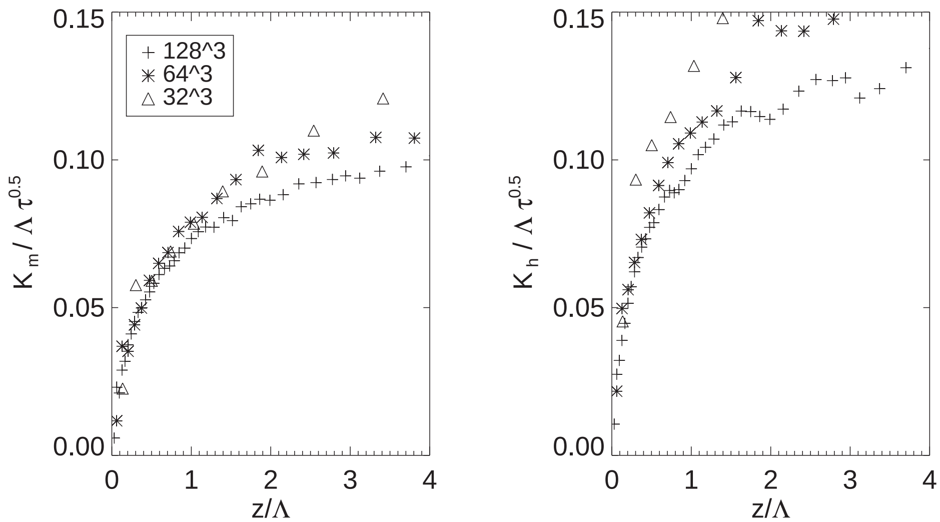

Figure 3.35. Locally scaled eddy-diffusivities of momentum (K_m) and heat (K_h), as a function of $\zeta = z/\Lambda$. The eddy-diffusivities have been scaled with $\Lambda\,\tau^{0.5}$.

a z-less value of 0.06 for $K_m/(\Lambda\tau^{0.5})$. The agreement between our LES results and observations is poorer for $K_h/(\Lambda\,\tau^{0.5})$ since its predicted values lie completely outside the observation range. This is also true of many of the SFS models tested in the GABLS experiment (Beare et al., 2006).

3.6.8 Nondimensional gradients of mean potential temperature and velocity

We plot first the nondimensional gradients as a function of gradient Richardson number and then as a function of ζ. Businger et al. (1971) derived the following empirical expressions for Ri_g, ϕ_m and ϕ_h as a function of $\zeta_s = z/L$:

$$Ri_g = \zeta_s \frac{0.74 + 4.7\,\zeta_s}{(1 + 4.7\,\zeta_s)^2}, \tag{3.7}$$

$$\phi_h = 0.74 + 4.7\,\zeta_s, \tag{3.8}$$

$$\phi_m = 1 + 4.7\,\zeta_s, \tag{3.9}$$

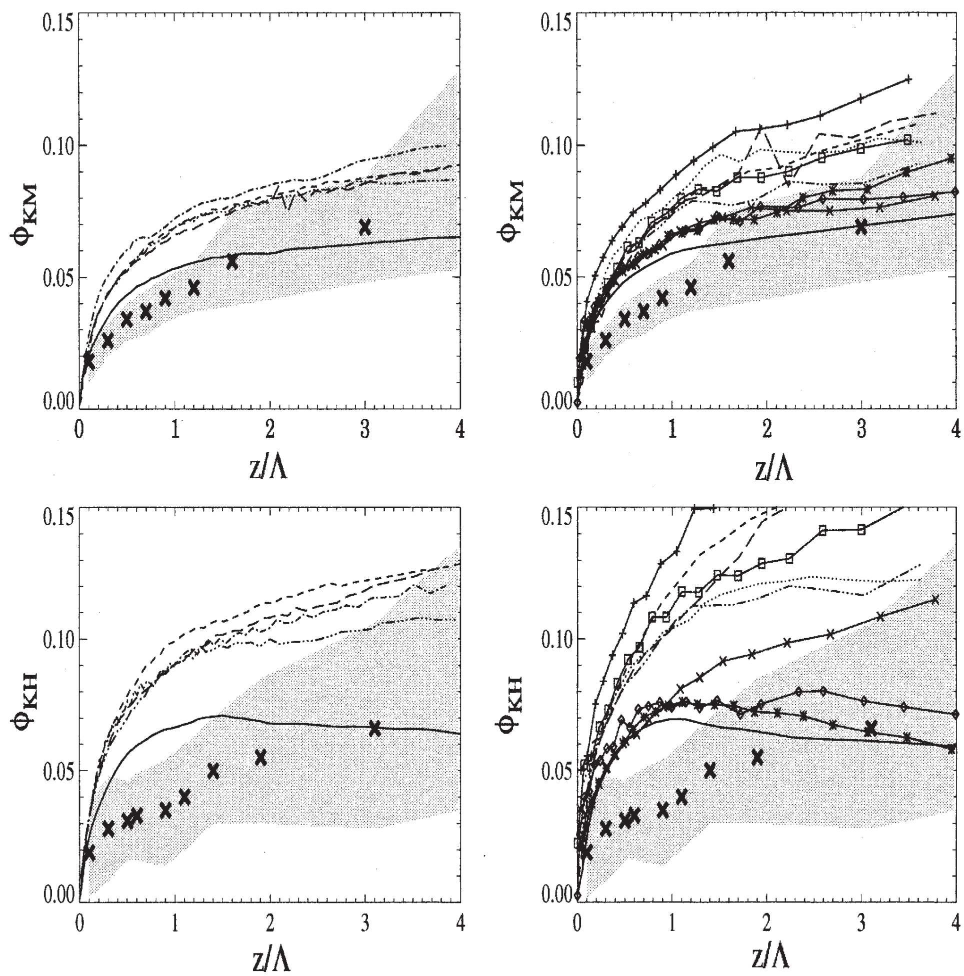

Figure 3.36. Reproduced from the GABLS LES-intercomparison study (Beare et al., 2006). The axes are the same as in Fig. (3.35). The nondimensional mean-gradients are given by $\Phi_{KM} = K_m/(\Lambda\,\tau^{0.5})$ and $\Phi_{KH} = K_h/(\Lambda\,\tau^{0.5})$. The left and right panels correspond to resolutions of 2 m (200^3) and 6.25 m (64^3), respectively. The crosses denote mean values obtained from the Cabauw data (Nieuwstadt, 1984) and the shaded area represents the associated spread in data. The different lines represent results from LES using 11 SFS models listed in Table 1 of Beare et al. (2006).

where ϕ_m is the nondimensional gradient of mean velocity and ϕ_h is the nondimensional gradient of mean potential temperature. In Eqs. (3.7)–(3.8), the functions are defined in terms of z/L and the scaling factors used to obtain the nondimensional gradients are kz/u_* or kz/θ_*, as appropriate. Eliminating ζ_s, we arrive at

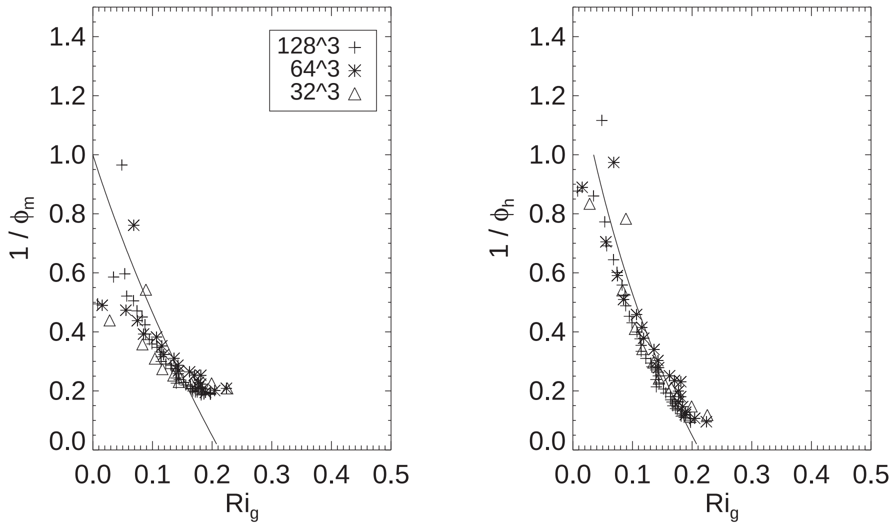

Figure 3.37. Plot of $1/\phi_m$ and $1/\phi_h$ versus gradient Richardson number, Ri_g.

the following expressions relating Ri_g to ϕ_m and ϕ_h:

$$Ri_g = \frac{(\phi_m - 1)}{4.7}\frac{(\phi_m - 0.26)}{\phi_m^2} \tag{3.10}$$

$$Ri_g = \frac{(\phi_h - 0.74)}{4.7}\frac{\phi_h}{(\phi_h + 0.26)^2} \tag{3.11}$$

We plot $1/\phi_m$ and $1/\phi_h$ as functions of Ri_g in Fig. (3.37) alongside the functions derived in Eqs. (3.10)–(3.11). Both $1/\phi_m$ and $1/\phi_h$ are underpredicted but the latter agrees slightly better with Businger's empirical fit.

To examine the presence of local scaling, we define new variables $\phi_{mL} = kz/u_L$ and $\phi_{hL} = kz/\theta_L$ ("L" stands for local) involving the local quantities $u_L = \sqrt{\tau}$ and $\theta_L = \langle w'\theta' \rangle / u_L$ (Howell and Sun, 1999; Sorbjan, 1986). In Fig. (3.38), we plot ϕ_{mL} and ϕ_{hL} as functions of ζ. For comparison, we also show the "local" versions (ζ_s is replaced by ζ) of empirical functions derived by: (i) Businger et al. (1971), shown in Eqs. (3.8)–(3.9): (ii) Mahrt and Vickers (2003), who recommend a slope of 3.7 instead of 4.7 in Eqs. (3.8)–(3.9); and (iii) Beljaars and Holtslag (1991), which are given below:

$$\phi_{mL} = 1 + \zeta\left[a + b\,e^{-d\zeta}\,(1 + c - d\,\zeta)\right], \tag{3.12}$$

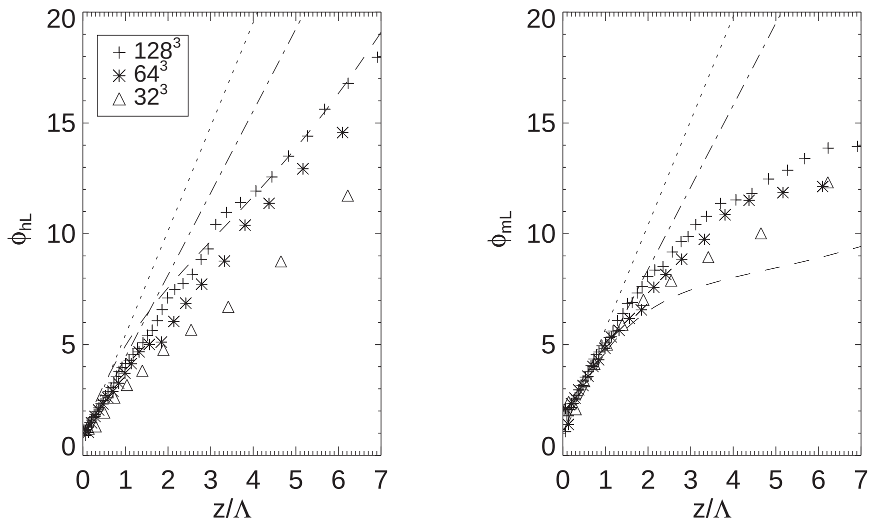

Figure 3.38. Plots of ϕ_{hL} (left) and ϕ_{mL} (right) versus $\zeta = z/\Lambda$, where ϕ_{mL} and ϕ_{hL} are the locally scaled nondimensional mean-gradients of velocity and potential temperature. The lines denote the following formulations – dotted : Businger et al. (1971), dash-dot : Mahrt and Vickers (2003), dashes : Beljaars and Holtslag (1991) .

$$\phi_{hL} \;\; = \;\; 1 + \zeta \left[a \left(1 + \frac{2}{3} a\, \zeta \right)^{1/2} + b\, e^{-d\,\zeta} \left(1 + c - d\,\zeta \right) \right] . \qquad (3.13)$$

The constants in Eqs. (3.12)–(3.13) are given by $(a, b, c, d) = (1, 2/3, 5, 0.35)$.

The predicted values of ϕ_{hL} are sensitive to resolution. At low Δ_w/Δ, the values of ϕ_{hL} at all three resolutions agree reasonably with the formulation by Mahrt and Vickers (2003). For higher ζ, ϕ_{hL} from the 128^3 run is better tracked by the functions derived by Beljaars and Holtslag (1991) while those from the other two coarser runs are not described satisfactorily by any of the three formulations. The LES predictions of ϕ_{mL} are also found to be sensitive to resolution, especially at higher ζ. At low ζ, the values of ϕ_{mL} from all three runs converge and show good agreement with the empirical fit suggested by Mahrt and Vickers (2003). As ζ increases, they start to diverge from each other and lie approximately between the formulations of Mahrt and Vickers (2003), and Beljaars and Holtslag (1991) in Fig. (3.38).

We re-plot in Figs. (3.39)–(3.40), ϕ_{mL} and ϕ_{hL} as functions of ζ using a log-log

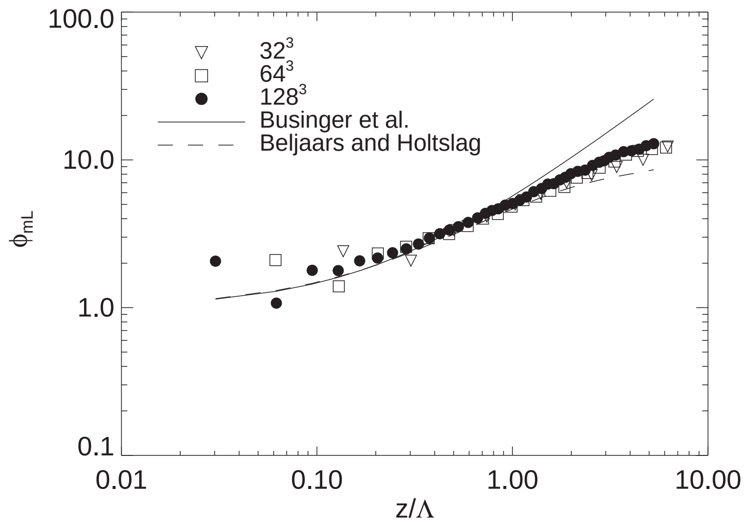

Figure 3.39. Plot of ϕ_{mL} versus $\zeta = z/\Lambda$ using a log-log scale, where ϕ_{mL} is the locally scaled nondimensional mean-gradient of velocity. The lines denote the following formulations – dotted : Businger et al. (1971), dash-dot : Mahrt and Vickers (2003), dashes : Beljaars and Holtslag (1991) .

scale and show similar plots in Fig. (3.41)–(3.42), obtained using the LASDD and PASDD models (Basu and Porté-Agel, 2006). At low ζ, predictions of ϕ_{mL} by both the LASDD and the modeled SFS conservation equations tend towards the Businger formulation, but the former exhibits better agreement with the empirical profile. At high ζ, the predictions of ϕ_{mL} by the LASDD model appear to agree better with the Businger formulation while those by the modeled SFS conservation equations follow more closely the profile obtained by Beljaars and Holtslag (1991). The predicted profiles of ϕ_{hL} by both closures don't differ significantly at large ζ. At low ζ, however, the LASDD model predicts ϕ_{hL} better than do the modeled SFS conservation equations as the latter overpredict ϕ_{hL} near the surface.

3.6.9 Steady-state profiles of τ and $\langle w'\theta' \rangle$

Local scaling, unlike Monin-Obukhov scaling, relates various turbulent statistics to local quantities which are themselves unknown. As a result, the local scaling hypothesis by itself is insufficient to obtain vertical profiles for quantities of interest. Thus, Nieuwstadt (1984) invoked a closure hypothesis wherein the z-less limits for

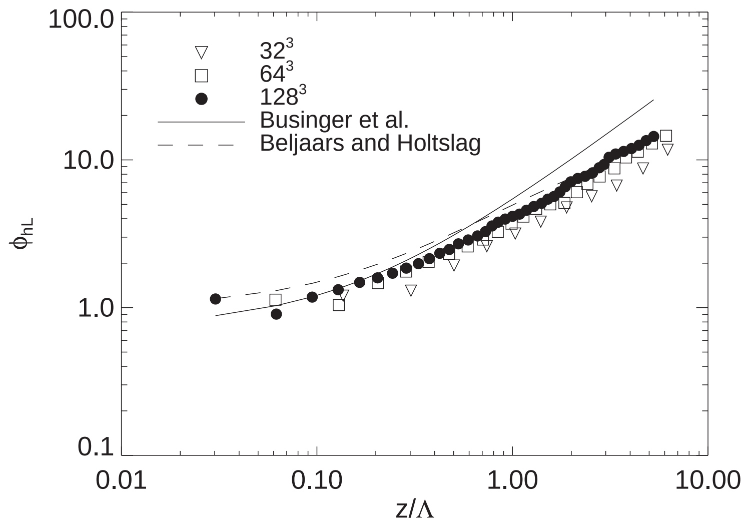

Figure 3.40. Plot of ϕ_{hL} versus $\zeta = z/\Lambda$ using a log-log scale, where ϕ_{hL} is the locally scaled nondimensional mean-gradient of potential temperature. The lines denote the following formulations – dotted : Businger et al. (1971), dash-dot : Mahrt and Vickers (2003), dashes : Beljaars and Holtslag (1991) .

Ri_g and Ri_f are assumed to be valid throughout the boundary layer. This is an approximation as Ri_g and Ri_f tend to zero towards the surface and thus, cannot be constant throughout the boundary layer. Using the new closure hypothesis, Nieuwstadt (1984) derived analytical profiles for τ and $\langle w'\theta'\rangle$ that are valid for an SBL in equilibrium. They are:

$$\frac{\tau}{u_*^2} = \left[1 - \left(\frac{z}{z_i}\right)\right]^{3/2} \quad (3.14)$$

$$\frac{\langle w'\theta'\rangle}{Q_0} = 1 - \frac{z}{z_i} \quad (3.15)$$

We plot in Fig. (3.43) the steady state profiles of τ/u_*^2 and $\langle w'\theta'\rangle/Q_0$ obtained from LES. They show good agreement with Nieuwstadt's analytical prediction for $z/z_i < 0.5$. They are also robust and show negligible sensitivity to resolution. The values of τ/u_*^2 at $z/z_i = 1$ are much smaller than those of $\langle w'\theta'\rangle/Q_0$ because the definition of inversion employed in this study involves momentum stresses, and

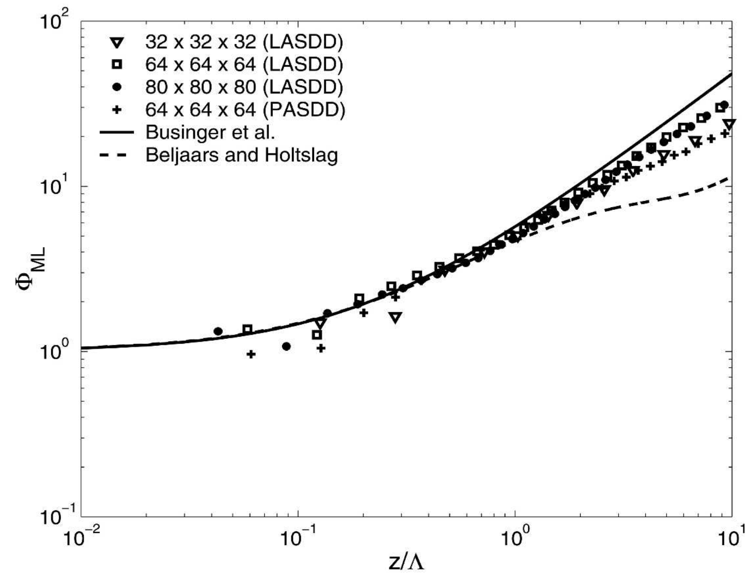

Figure 3.41. Reproduced from Basu and Porté-Agel (2006). Plot of Φ_{mL} versus $\zeta = z/\Lambda$ using a log-log scale, where Φ_{mL} (identical to ϕ_{mL} in Fig. (3.39)) is the locally scaled nondimensional mean-gradient of velocity. The lines denote the following formulations – dotted : Businger et al. (1971), dash-dot : Mahrt and Vickers (2003), dashes : Beljaars and Holtslag (1991) .

not the potential temperature fluxes (Kosović and Curry, 2000). The agreement between LES and theory is better in the lower regions of the ABL, a trend also witnessed in past LES studies (Basu and Porté-Agel, 2006; Beare et al., 2006; Stoll and Porté-Agel, 2008) as well. Since the assumption that Ri_g and Ri_f are constant isn't valid in the surface layer, we would expect poor agreement between LES and Nieuwstadt's predictions in that region. That we don't observe this in LES studies is counter-intuitive but we are unable to provide an explanation for it.

For comparison, we plot in Figs. (3.44)–(3.45), the steady state profiles of τ/u_*^2 and $\langle w'\theta'\rangle/Q_0$ obtained using the LASDD and the PASDD models (Basu and Porté-Agel, 2006). The LASDD model displays poorer agreement with theory and greater sensitivity to resolution when compared to the modeled SFS conservation equations.

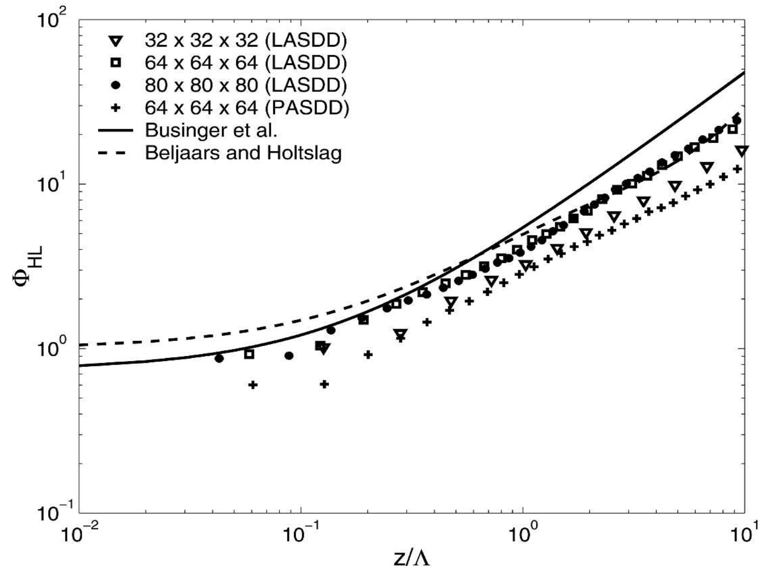

Figure 3.42. Reproduced from Basu and Porté-Agel (2006). Plot of Φ_{hL} versus $\zeta = z/\Lambda$ using a log-log scale, where Φ_{hL} (identical to ϕ_{hL} in Fig. (3.40)) is the locally scaled nondimensional mean-gradient of potential temperature. The lines denote the following formulations – dotted : Businger et al. (1971), dash-dot : Mahrt and Vickers (2003), dashes : Beljaars and Holtslag (1991) .

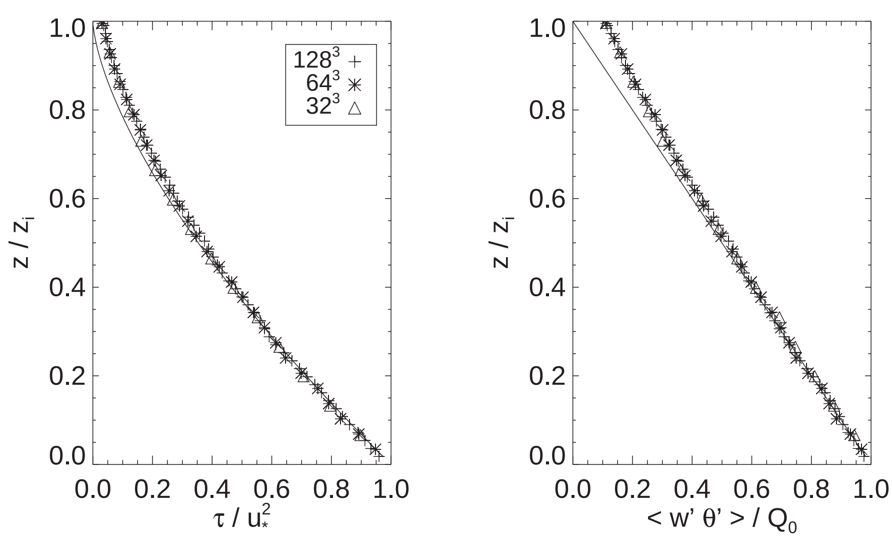

Figure 3.43. Steady-state profiles of τ/u_*^2 and $\langle w'\theta'\rangle/Q_0$, averaged over the last hour of simulation. The solid curves are theoretical profiles derived by Nieuwstadt (1984).

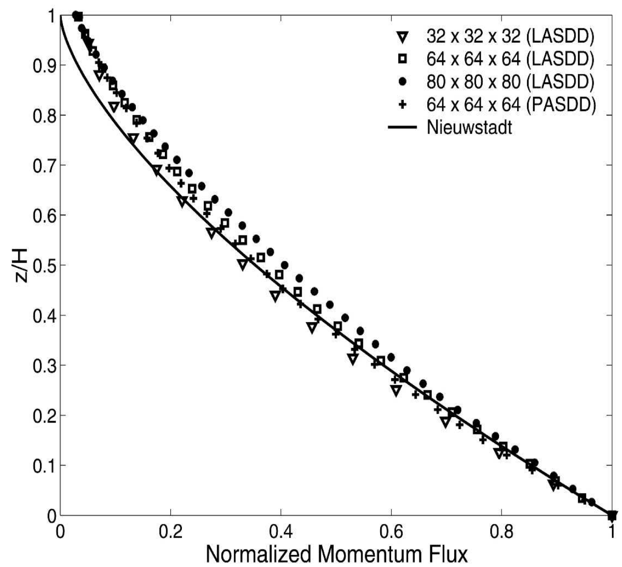

Figure 3.44. Reproduced from Basu and Porté-Agel (2006). Steady-state profile of τ/u_*^2 averaged over the last hour of simulation, using the locally-averaged (LASDD) and plane-averaged (PASDD) models. The solid curve is a theoretical profile derived by Nieuwstadt (1984).

3.6.10 Influence of surface cooling rate

In this section, we examine briefly the role of the surface cooling rate as an external parameter. We perform LES runs using a 128^3 grid ($\Delta = 3.125\,\mathrm{m}$) for the following cooling rates (in K/hr): (i) 0.1; (ii) 0.18; (iii) 0.5; and (iv) 0.7. Table (3.2) lists important bulk parameters for these runs. For the sake of completeness, we have also listed the values for the run corresponding to a surface cooling rate of 0.25 K/hr.

3.6.10.1 Evolution of the mean velocity

In Fig. (3.46) we plot the time evolution of ΔU and ΔV at the location of the jet maximum for the four cooling rates, where $\Delta U = \langle U \rangle - U_g$ and $\Delta V = \langle V \rangle - V_g$. We recall from our discussion of the inertial oscillation in Sec. (3.6.4.1) that the tip of the $(\Delta U, \Delta V)$ vector is supposed to trace out a circle (Blackadar, 1957). Fig. (3.46) shows that the circular arcs traced out by the $(\Delta U, \Delta V)$ vectors increase in length as the surface cooling rate is increased, which implies that the onset of the inertial

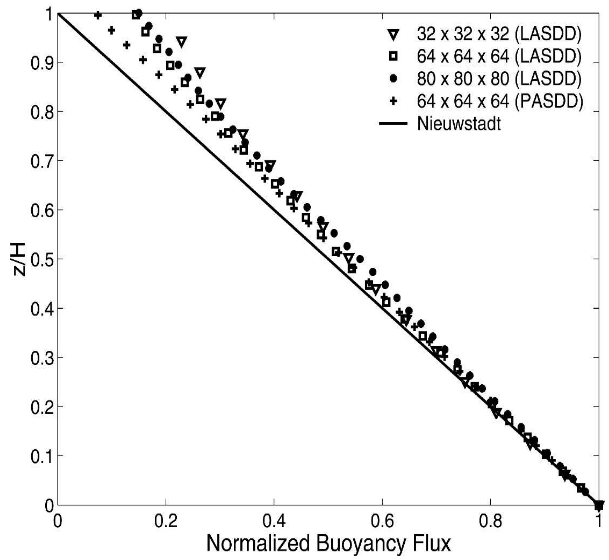

Figure 3.45. Reproduced from Basu and Porté-Agel (2006). Steady-state profile of $\langle w'\theta' \rangle / Q_0$ averaged over the last hour of simulation, using the locally-averaged (LASDD) and plane-averaged (PASDD) models. The solid straight line is a theoretical profile derived by Nieuwstadt (1984).

oscillation occurs quicker at higher surface cooling rates. For runs with weak surface cooling, the maximum value of ΔU hasn't been attained by the end of the simulation (9 hours). At cooling rates of 0.5 K/hr and 0.7 K/hr, the maximum value of ΔU is attained when $\Delta V \approx 0.5$ and not when $\Delta V = 0$. Thus ΔU and ΔV are not exactly 90^o out of phase, as implied by Blackadar's analysis. Saiki et al. (2000) found that increased surface cooling led to better agreement between LES predictions of the time-evolution of the jet maximum and Blackadar's analytical solution. They too found the phase difference between ΔU and ΔV to differ from 90^o. Thus, Fig. (3.46) agrees qualitatively with their findings. Closer observation of Fig. (3.46) reveals that the circular arcs are approximately concentric such that larger radii are associated with higher cooling rates, indicating that stronger surface cooling is associated with greater acceleration of the jet aloft.

3.6.10.2 Boundary layer height

In Fig. (3.47), we show the time-evolution of the boundary-layer height versus t/t_*, where $t_* = z_i/u_*$. Among the four runs, the simulation with the lowest cooling

Table 3.2. Boundary layer height (z_i), Monin-Obukhov (MO) length (L), Bulk Richardson number (Ri_b), surface flux (Q_0), MO scales u_* and θ_*, and the Zilitinkevich parameter, γ, where $\gamma = z_i/(u_* L/f)^{1/2}$. The statistics are averaged over the last hour of simulation.

Diagnosed physical parameters from LES runs with different surface cooling rates					
Surface cooling (K/hr)	**0.10**	**0.18**	**0.25**	**0.5**	**0.7**
z_i(m)	210	189	173	136	116
L(m)	231	145	107	53	36
Ri_b	0.12	0.14	0.16	0.21	0.25
Q_0(W m^{-2})	-8.9	-12.5	-14.6	-21.9	-25.7
u_*(ms^{-1})	0.284	0.273	0.262	0.235	0.219
θ_*(K)	0.023	0.034	0.043	0.070	0.088
γ	0.30	0.35	0.38	0.45	0.48

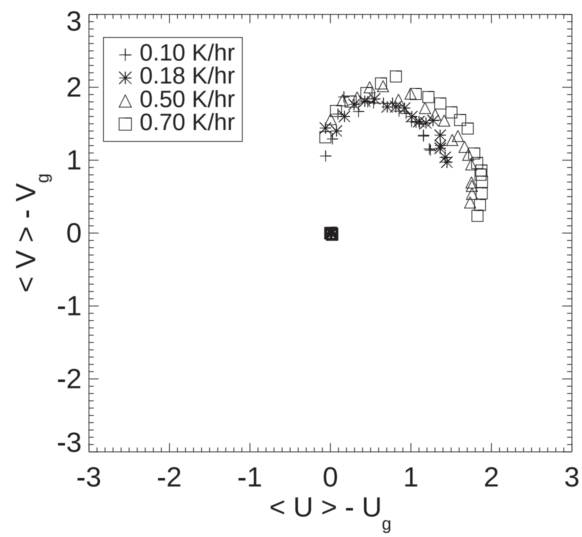

Figure 3.46. Time-evolution of the mean velocity components, ΔU and ΔV, where $\Delta U = \langle U \rangle - U_g$ and likewise for ΔV. Results shown are from simulations with four different cooling rates: 0.1 K/hr, 0.18 K/hr, 0.5 K/hr and 0.7 K/hr. The points correspond to samples collected every 1000 s over the entire course of the simulation.

rate (0.1 K/hr), takes the longest time — relative to t_* — for z_i to stabilize. For the other three cooling rates, z_i appears to stabilize at $t/t_* \approx 23$, which is close to the corresponding value for our earlier runs with the GABLS (Beare et al., 2006) cooling rate, i.e., 0.25 K/hr.

We list in Table (3.3) z_i obtained from LES and two commonly used parame-

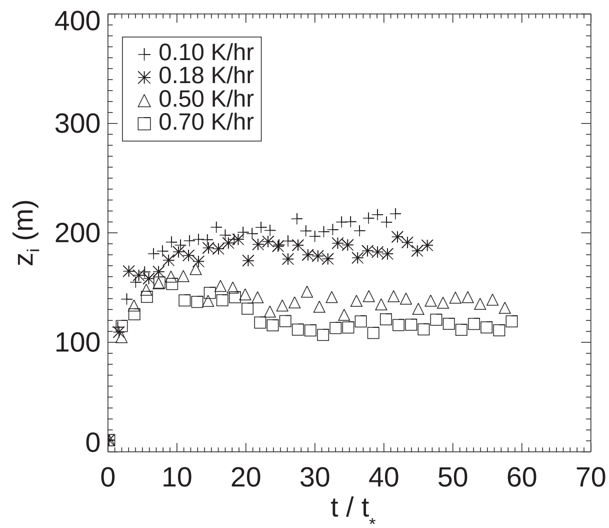

Figure 3.47. Time-evolution of the boundary layer height, z_i, versus t/t_*, where $t_* = z_i/u_*$. Results shown are from simulations with four different cooling rates: 0.1 K/hr, 0.18 K/hr, 0.5 K/hr and 0.7 K/hr. The points correspond to samples collected every 1000 s over the entire course of the simulation.

terizations, which are described below:

- $z_i = 0.4\,(u_*\,L/f)^{1/2}$ (Zilitinkevich, 1972)
- $\left(\dfrac{f\,z_i}{C_n\,u_*^2}\right)^2 + \dfrac{z_i}{C_s\,L} + \dfrac{N\,z_i}{C_i\,u_*} = 1$ (Zilitinkevich and Mironov, 1996)

We denote these parameterizations as Z72 and ZM96. The constants are given by $C_n = 0.1$, $C_s = 10$ and $C_i = 20$ (Zilitinkevich and Mironov, 1996). Nieuwstadt (1984) derived Z72 independently for a stably stratified boundary layer in equilibrium although he found the proportionality constant to be 0.35. The parameterization ZM96 is a more general form of Z72 as it also accounts for the effects of surface buoyancy and the free-flow stability through the introduction of the scales L and u_*/N, where N is the Brunt-Väisälä frequency in the layer above the boundary layer. In our LES studies, $N \approx 0.02$.

Table (3.3) shows that ZM96 predicts z_i well at weak stratifications but develops a systematic negative bias at stronger stratifications. Z72 overpredicts z_i at weak stratifications but like ZM96, underpredicts it as the stratification is increased.

Table 3.3. Table showing boundary-layer height obtained from LES and two commonly used parameterizations developed by Zilitinkevich (1972) and Zilitinkevich and Mironov (1996), referred to as Z72 and ZM96, respectively. The fractional error between LES and parameterized values are also indicated.

Comparison of boundary layer heights from LES and two parameterizations					
Surface cooling (K/hr)	**0.10**	**0.18**	**0.25**	**0.5**	**0.7**
z_i (m) (LES)	210	189	173	136	116
$z_{i,mod}$ (m) (Z72)	275	214	180	120	96
$z_{i,mod}$ (m) (ZM96)	208	179	158	110	86
$(z_{i,mod} - z_i)/z_i$ (Z72)	0.31	0.13	0.04	−0.12	−0.17
$(z_{i,mod} - z_i)/z_i$ (ZM96)	−0.01	−0.05	−0.09	−0.19	−0.26

Vickers and Mahrt (2004) have done a comprehensive study of various parameterizations — including Z72 and ZM96 — for the stable boundary-layer height using data from multiple experimental campaigns. Their findings also report a negative bias in predicted z_i by Z72 and ZM96 in strongly stratified environments.

3.6.10.3 Mean gradients of velocity and potential temperature

In Fig. (3.48) we plot the nondimensional gradients ϕ_h and ϕ_m as functions of ζ.

The slope of ϕ_h decreases with increasing surface cooling rate. For the cooling rates 0.1 K/hr and 0.18 K/hr, ϕ_h shows good agreement with the empirical profiles recommended by Mahrt and Vickers (2003) when $\zeta < 1$. For higher values of ζ, they are closer to the formulation by Beljaars and Holtslag (1991). In contrast, ϕ_h for the higher cooling rates agree poorly with all three empirical functions, as the LES predictions are lower than the empirically derived values at all ζ.

The ϕ_m profiles for the two lowest cooling rates agree well with the Businger (1971) formulation for $\zeta < 1$ but deviate considerably from it for higher ζ. At the higher cooling rates, ϕ_m follows closely the Mahrt and Vickers (2003) formulation for $\zeta < 1$ but yields relatively lesser values for higher ζ. For $\zeta < 3$, the spread in ϕ_m across different cooling rates is lesser than in ϕ_h. For further increases in ζ, ϕ_m increases with increasing surface cooling rate.

An alternative to plotting ϕ_{mL} and ϕ_{hL} versus ζ is to plot them as functions of z/l_b, as shown in Fig. (3.49). The variable $l_b = \sigma_w/N$ is the buoyancy length scale. The range of z/l_b considered in Fig. (3.49) corresponds to the bottom 75%

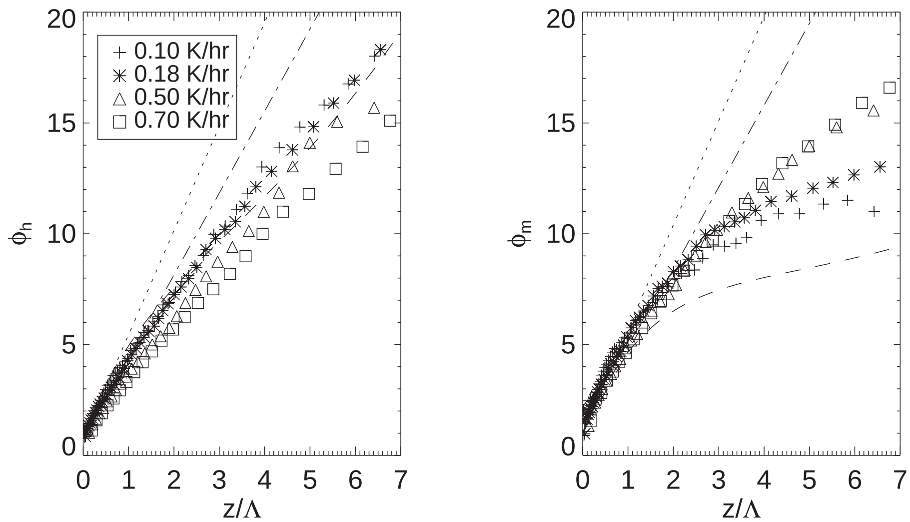

Figure 3.48. Plots of ϕ_{hL} (left) and ϕ_{mL} (right) versus $\zeta = z/\Lambda$ for different surface cooling rates, where ϕ_{mL} and ϕ_{hL} are the locally scaled nondimensional mean-gradients of velocity and potential temperature, respectively. The lines denote the following formulations – dotted : Businger et al. (1971), dash-dot : Mahrt and Vickers (2003), dashes : Beljaars and Holtslag (1991).

of the boundary layer. The nondimensional mean-gradients collapse significantly better compared to Fig. (3.48). Both ϕ_{mL} and ϕ_{hL} are nearly linear with slopes of 1.0 and 0.92, respectively. Aircraft measurements by Heinemann (2004) show that ϕ_{mL} and ϕ_{hL} are linear functions of z/l_b with slopes of 0.95 and 3.3, respectively. Field measurements in Antarctica by Forrer (1999) found both ϕ_{mL} and ϕ_{hL} to vary linearly versus z/l_b with a slope of 0.45. The experiments by Heinemann (2004) covered a wider range of z/Λ than did those by Forrer (1999). Our slope for ϕ_{mL} lies closer to observations compared to that for ϕ_{hL}. Nevertheless, Fig. (3.49) suggests that z/l_b is more consistent than z/Λ in describing the locally scaled nondimensional mean-gradients across a range of stabilities.

3.6.10.4 Equilibrium profiles of τ and $\langle w'\theta'\rangle$

In Fig. (3.50) we plot the profiles of τ/u_*^2 and $\langle w'\theta'\rangle/Q_0$ versus z/z_i. The solid lines denote profiles derived analytically by Nieuwstadt (1984). For all four cooling rates, the LES predictions of τ/u_*^2 are nearly coincident and exhibit good agreement with

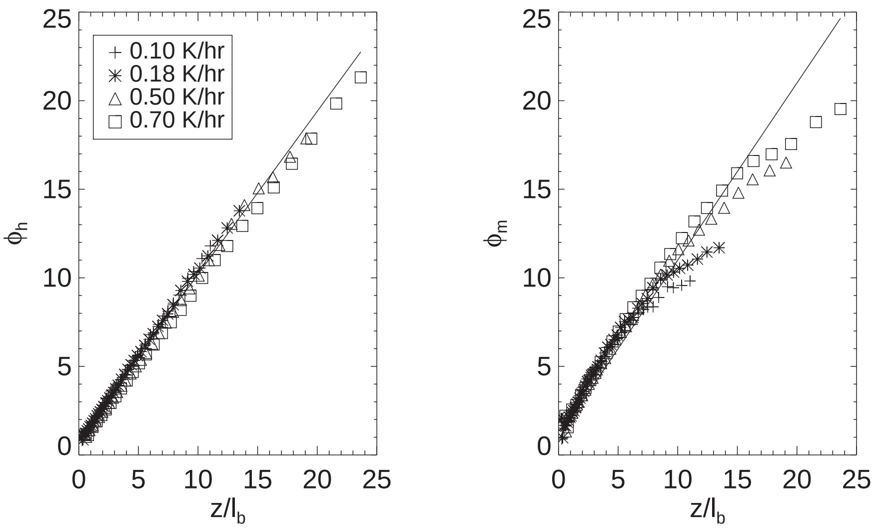

Figure 3.49. Plots of ϕ_{hL} (left) and ϕ_{mL} (right) versus z/l_b for different surface cooling rates, where ϕ_{mL} and ϕ_{hL} are the locally scaled nondimensional mean-gradients of velocity and potential temperature, respectively, and $l_b = \sigma_w/N$ is the buoyancy length scale. The solid lines in the left and right panels have slopes of 0.92 and 1.0, respectively.

the theoretical profile for $z/z_i < 0.4$. The profiles of $\langle w'\theta'\rangle/Q_0$ are approximately linear but differ markedly from Nieuwstadt's predictions for the two lowest cooling rates. As the cooling rate increases, they agree better with the theoretical profiles.

3.6.10.5 Potential temperature fluctuations

The resolved-scale standard deviation of potential temperature scaled with θ_* is shown in Fig. (3.51). The profiles converge approximately to a value of 1.7 for $z/z_i < 0.4$ but display markedly different behavior higher up in the boundary-layer. For the cooling rates 0.1 K/hr and 0.18 K/hr, the θ-fluctuations attain their maximum values slightly above the inversion. In contrast, for the cooling rates 0.5 K/hr and 0.7 K/hr, the θ-fluctuations attain their maximum values at $0.3 < z/z_i < 0.4$. The normalized θ-fluctuations for the two highest cooling rates are nearly identical.

We now attempt to explain the sharp decrease in the scaled potential temperature fluctuations near the inversion with increasing stratification. The generation of θ-fluctuations is primarily through the gradient-production term, $\langle w'\theta'\rangle\,(\partial\langle\Theta\rangle/\partial z)$.

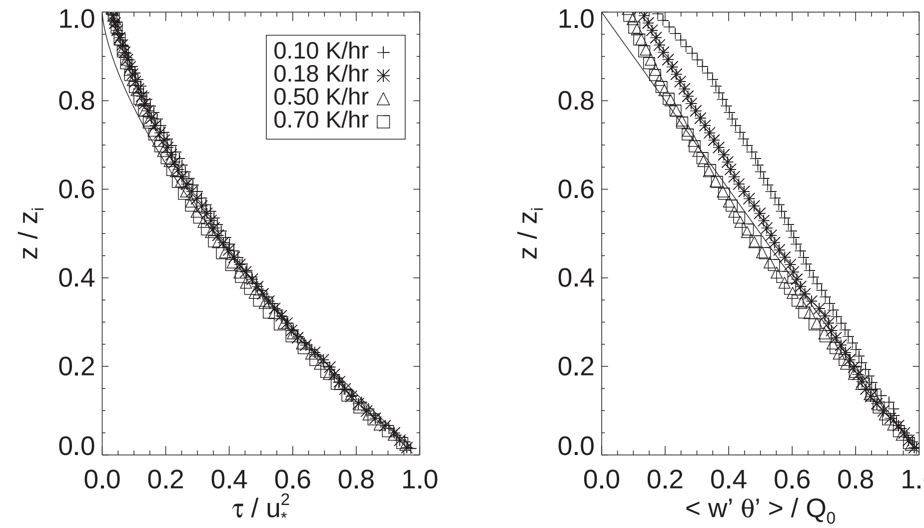

Figure 3.50. Equilibrium profiles of τ/u_*^2 and $\langle w'\theta'\rangle/Q_0$ averaged over the last hour of simulation, for different surface cooling rates. Solid lines denote theoretical profiles derived by Nieuwstadt (1984).

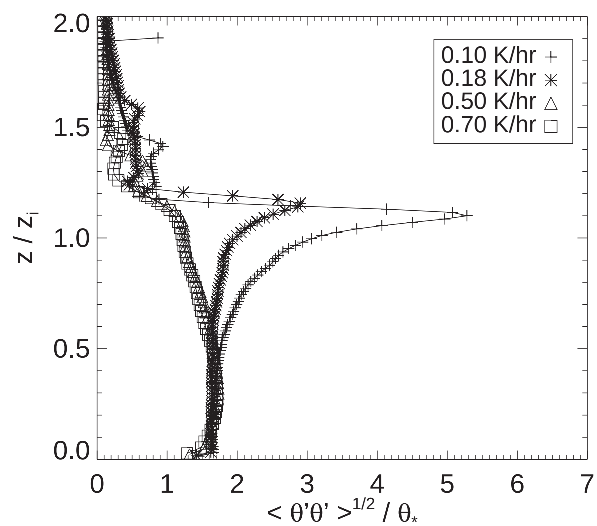

Figure 3.51. Resolved-scale standard deviation of potential temperature scaled with θ_*, for different surface cooling rates. Results are averaged over the last hour of simulation.

Thus, we expect high fluctuation levels in regions where both the gradients and turbulent fluxes of potential-temperature are significant. For a fixed surface cooling rate, the gradients are highest near the inversion (see Fig. (3.24). As the surface cooling rate increases in magnitude, the gradients of potential temperature steepen everywhere in the boundary layer. In contrast, the turbulent flux of potential temperature doesn't vary linearly with changes in the stratification but exhibits a so-called "dual" nature (Malhi, 1995). This is understood easily by considering two limiting cases: no stratification (neutral) and very high stratification. The potential temperature flux is negligible in both cases, due to zero buoyancy in the former and negligible levels of turbulence in the latter. It follows that $\langle w'\theta' \rangle$ peaks in magnitude at some intermediate level of stratification. Presumably, the potential temperature fluctuations also attain their maximum at the same stratification level. This is consistent qualitatively with DNS studies (Garciá-Villalba and del Álamo, 2008; Iida et al., 2002) of stably-stratified channel flow over a range of stratifications, which found that the normalized temperature fluctuations near the inversion peak at an intermediate stratification (as measured by Ri_b). From Fig. (3.51), the stratifications considered in our study appear to be greater than that corresponding to the maximum value of the heat flux. Thus, we speculate that simulations with weaker stratifications, i.e., with cooling rates lesser than 0.1 K/hr, would be necessary to observe a decrease in the potential temperature fluctuations near the inversion.

An interesting feature of the profiles at the two highest cooling rates is the evidence of limiting behavior and the presence of a maximum in the lower regions of the boundary-layer. We reproduce in Fig. (3.52) a plot from the study by Nieuwstadt (1984) showing the scaled potential temperature variances from four different sources: (i) unfiltered Cabauw data (contains signatures from mesoscale disturbances) denoted by circles (Nieuwstadt, 1984); (ii) filtered Cabauw data (no mesoscale fluctuations) denoted by triangles; (iii) Minnesota experiments (Caughey et al., 1979) denoted by crosses; and (iv) an analytical profile (Nieuwstadt, 1984), denoted by a solid line. Nieuwstadt (1984) found that filtering out the mesoscale content led to greatly improved agreement between theory and experiment. There is significant difference between the Cabauw (filtered) and Minnesota data. The scaled potential temperature fluctuations from the Minnesota experiments are greatest near the surface and decrease rapidly with height. Those obtained from the Cabauw data exhibit a maximum at $z/z_i \approx 0.4$ and decrease gradually with

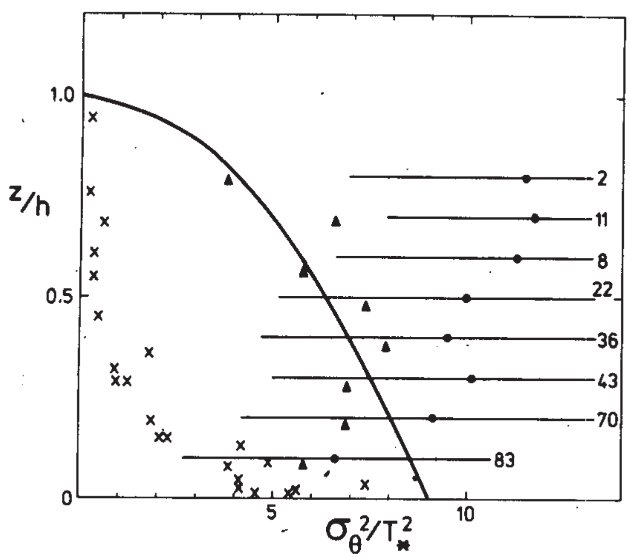

Figure 3.52. Reproduced from Nieuwstadt (1984). Plot showing variance of potential temperature scaled with T_*^2 (same as θ_*^2) versus z/h, where $h = z_i$ is the boundary layer depth. Legend — Unfiltered Cabauw data (contains mesoscale fluctuations) : circles, filtered Cabauw data (no mesoscale fluctuations) : triangles, Minnesota data (Caughey et al., 1979) : crosses, analytical profile (Nieuwstadt, 1984) : solid line.

height for $z/z_i > 0.4$. The profiles of temperature fluctuations in the studies by (Beare et al., 2006) and Basu and Porté-Agel (2006) — both of which used a cooling rate of 0.25 K/hr — are closer to the Cabauw data than to the Minnesota data. Even so, they tend to be approximately constant with height and don't exhibit a maximum in the lower boundary-layer. Our simulations with cooling rates of 0.18 K/hr and 0.25 K/hr yield similar results. The simulations with increased cooling rates, i.e., 0.5 K/hr and 0.7 K/hr, however, show better qualitative agreement with the Cabauw data in that the potential temperature fluctuations exhibit a maximum in the lower half of the ABL. The KABEG data (Heinemann, 2004), which covered a wide stability range ($0 < z/\Lambda < 25$), yielded maxima in potential temperature fluctuations both at $0.3 < z/z_i < 0.4$ and near the inversion. We conclude that the equilibrium profile of potential temperature fluctuations is quite sensitive to the level of stratification.

3.6.10.6 Z-less scaling

In this section, we tabulate the so-called z-less values for important turbulent statistics. Following convention, we split the data into five stability classes, as shown in Table (3.4).

Table 3.4. Table defining the stability classes and showing the number of samples in each stability class

Stability class	ζ	**Number of samples**
S1	$0.00 - 0.10$	5
S2	$0.10 - 0.25$	9
S3	$0.25 - 0.50$	13
S4	$0.50 - 1.00$	19
S5	> 1.00	82

Within each stability class, the values of a particular statistic are then averaged. We approximate the mean values in the S5 class to be the z-less values (Basu and Porté-Agel, 2006). As the values are averaged within each stability class, it is beneficial to have a large number of points in the classes corresponding to higher stabilities as the z-less values are realized at high ζ. Thus, we combine our results from multiple 128^3 simulations with different cooling rates in order to increase the number of samples in each stability class. Doing so enables us to create a large sample space without having to perform expensive runs at higher resolution. For the purposes of this section, we performed an additional LES for a cooling rate of 1.0 K/hr. We confirmed that the results from this run are qualitatively similar to those from our earlier runs with the higher cooling rates. Results from simulations with the following cooling rates (in K/hr) are grouped together: 0.25, 0.5, 0.7 and 1.0. For each simulation, we only consider heights such that $z/z_i < 0.75$. The final number of samples in each stability class is shown in Table (3.4).

We tabulate the z-less values in Table (3.5) alongside their corresponding values obtained from different studies. The variable r_{xy} in Table (3.5) denotes the correlation coefficient between x and y. Since the expressions in Table (3.5) have been computed using only the resolved-scale variance of θ (where applicable) we expect σ_θ/θ_L to be larger than the indicated value. By the same logic, the true correlations $r_{u\theta}$ and $r_{w\theta}$ will be lesser than their indicated values. The locally

Table 3.5. Z-less values for select statistics from LES (present study and the study by Basu and Porté-Agel (2006)) and various field experiments. The variable r_{xy} denotes the correlation coefficient between x and y. Numbers with a superscript, *, indicate use of resolved-scale θ-variance only. The values for Heinemann (2004) indicate the mid-points of the following ranges: $(1.2, 1.6)$, $(4.5, 7.3)$, $(-0.15, -0.30)$ and $(-0.1, -0.2)$.

	σ_u/u_L	σ_v/u_L	σ_w/u_L	σ_θ/θ_L	r_{uw}	$r_{u\theta}$	$r_{w\theta}$
LES	2.2	1.7	1.5	2.0^*	-0.3	0.6^*	-0.33^*
LES - LASDD model	2.3	1.7	1.4	2.4	-0.32	0.56	-0.3
Field observations	2.7	2.1	1.6	2.4	-0.21	0.51	-0.27
Nieuwstadt (1984)	2.0	1.7	1.4	3.0	–	–	-0.24
Sorbjan (1986)	2.4	1.8	1.6	2.4	–	0.5	–
Heinemann (2004)	–	–	1.4	5.9	-0.23	–	-0.15

scaled velocity variances are in reasonable agreement with observations while r_{uw} is at the higher end of the range of observations.

3.7 Summary

We have implemented a new SFS closure based on the conservation equations for the SFS stresses and fluxes, in LES of a stably-stratified atmospheric boundary layer. For our LES runs, we adopted the initial conditions and the physical set-up of the GABLS LES-intercomparison study (Beare et al., 2006), which describe an SBL with moderate stratification. We compared our LES results to past DNS studies, field experiments and other LES studies.

Following the GABLS experiment, we performed LES of a moderately stratified SBL with three resolutions, given by $\Delta = (3.125, 6.25, 12.5)$ m. One of the issues uncovered in the GABLS experiment was the tendency of some SFS models to yield laminar-like solutions at coarse resolutions, i.e., $\Delta = 12.5$ m. In our LES runs, the modeled SFS conservation equations produced turbulent solutions at all of the three resolutions listed above. The bulk parameters for the three resolutions were in reasonable agreement with each other and with their values in the GABLS experiment. The prediction of the boundary layer height, in particular, was more robust than most of the models tested in the GABLS experiment. The profiles of mean velocity and mean potential temperature showed low sensitivity to resolution. At coarse resolutions, the potential temperature profile did not smear out near the inversion, as observed for some SFS models in the GABLS experiment and for the LASDD model in the LES study by Basu and Porté-Agel (2006). The equilibrium profiles for the turbulent stresses and fluxes at all three resolutions displayed significantly better agreement with theory and robustness to resolution than those obtained using the LASDD model. Finally, we investigated the influence of the surface cooling rate as it varied from 0.1 K/hr to 1.0 K/hr. The locally scaled mean-gradients of velocity and potential temperature for different cooling rates collapsed significantly better when plotted versus z/l_b than versus z/Λ. The steady-state profile for the potential temperature fluctuations was found to be quite sensitive to the cooling rate. Our simulations at the higher cooling rates showed evidence of limiting behavior in the profiles for the potential temperature fluctuations after scaling them appropriately. These profiles were in better agreement with observations (Nieuwstadt, 1984) than were those observed in the GABLS experiment. The z-less values for the locally scaled velocity variances were found to be in reasonable agreement with observations while that for the correlation coefficient between u and w was closer to the high end of the observational range. The corresponding values obtained using the LASDD model yielded better agreement with observations and theory. The modeled SFS conservation equations yielded z-less values for the effective mixing coefficients that were unrealistically high compared to observations, a trend also seen in the GABLS numerical experiment.

Chapter 4

Large-eddy simulation of the neutral boundary layer

In the previous chapters, we explored the performance of a conservation-equation-based SFS model in LES of the convectively unstable and stable boundary layers. We also used HATS data to study the trends exhibited by important production terms in the SFS stress and flux budgets, when plotted versus the nondimensional parameter, Δ_w/Δ. In the current chapter, we apply the High Accuracy Zone (HAZ) framework developed by Brasseur and Wei (2010) to the modeled SFS conservation equations in LES of the shear-driven neutral boundary layer.

4.1 The overshoot problem

Inaccurate prediction of the mean velocity gradient has plagued LES of the ABL for a long time and was first brought to our attention by Mason and Thomson (1992). They showed that LES of the shear-driven neutral ABL tends to over-predict the nondimensional mean velocity gradient, ϕ_m, near the surface systematically, thereby causing it to overshoot its theoretical value of 1. This overshoot has also been observed in the nondimensional gradient of potential temperature, ϕ_h (Andren et al., 1994), in LES of the convective ABL. Subsequent research on the so-called overshoot problem has focused primarily on improving the underlying SFS model with the understanding that better SFS models should lead to better predictions of ϕ_m. Brasseur and Wei (2010) provide a comprehensive survey of the various studies that have addressed the overshoot problem, a few of which we now mention.

Sullivan et al. (1994) developed a two-part eddy viscosity model that improved the ϕ_m and ϕ_h profiles significantly. Their SFS model behaved like a traditional eddy-viscosity model in regions of well-resolved turbulence but transitioned to a RANS-like model towards the surface, where the turbulence is under-resolved. Using LES with two different SFS models, Khanna and Brasseur (1998) showed that the one with the more prominent overshoot was also associated with stronger and more coherent thermals that were over-aligned with the mean wind. They found that in moderately convective ABLs, the presence of buoyancy strengthened the dynamical coupling between the surface layer and the overlying region, thereby causing errors in the surface layer to propagate upwards into the ABL. Kosović (1997) designed an SFS model that related the SFS stresses and the resolved-scale strain rate nonlinearly, and yielded good improvement in the ϕ_m profile in LES of the neutral ABL. Porté-Agel et al. (2000) used a scale-dependent dynamic model which reduced the overshoot in ϕ_m. More recent work focused on the overshoot problem includes research by Chow et al. (2005), Esau (2004) and Drobinski et al. (2007). While the above studies have all contributed to our understanding of the issues underlying the overshoot problem, they fail to provide a systematic approach to reduce or eliminate the overshoot, that in principle is valid for any SFS model. This is partly because these studies were unsuccessful in isolating the fundamental reasons for the presence of the overshoot in ϕ_m. We now review briefly the main findings of Brasseur and Wei (2010).

4.2 The 'High Accuracy Zone' framework

Using DNS data corresponding to a smooth walled neutral channel flow, Brasseur and Wei (2010) observed an overshoot in the ϕ_m profile that occurs inside the viscous layer. The observed overshoot in ϕ_m within the viscous layer reflects the incorrect use of the inertial surface layer length scale, z, in a region where the appropriate length scale is $l_\nu = \nu/u_*$. In LES of high Reynolds number flows, however, we don't resolve the viscous layer as the first grid level is well into the inertial surface layer. In principle, therefore, z should be the only relevant length scale in the resolved surface layer. Brasseur and Wei (2010) showed that the overshoot in LES results from a competition between the correct inertial surface layer scale, z, and a spurious length scale that arises due to "numerical friction." In DNS, they found the overshoot to peak within the viscous layer at a height where the turbulent and viscous components of the shear stress ((1,3) component) cross over. In LES, the overshoot was found to peak at a height where the resolved and SFS components of the shear stress cross over. Thus, the overshoot observed in DNS has a physical basis but that seen in LES is purely a numerical artifact. The source of numerical friction lies in a combination of factors involving the SFS model and the computational grid, which Brasseur and Wei (2010) found can be understood in terms of the following three nondimensional parameters:

1. $R = T_r/T_s$, where T_r and T_s are the resolved-scale and SFS components of the (1,3) component of τ_{ij}, at the first grid point.

2. N_δ, the number of grid points in the vertical direction within the boundary layer.

3. $Re_{LES} = N_\delta(R+1)/(\xi_2\,\tilde{\kappa}_1)$; ξ_2 is the ratio of (T_r+T_s) at the second grid point to that at the first grid point and is ≈ 1, $\tilde{\kappa}_1$ is the predicted von Kármán constant assuming law-of-the-wall holds at the first grid point above the wall.

In LES of the neutral ABL, typically, $N_\delta \approx N_z/2$, where N_z is the total number of grid points in the vertical direction. This ensures that the top of the boundary layer in the fully developed turbulent flow is well below the top of the domain, thereby minimizing any possible influence of the upper boundary condition. The parameters (R, Re_{LES}, N_δ) describe a two-dimensional R-Re_{LES} space with constant values of N_δ corresponding to straight lines that sweep across this space, as shown in Fig. (4.1), which has been reproduced from Brasseur and Wei (2010). Any particular simulation has (R, Re_{LES}, N_δ) fixed and hence, corresponds to a unique point in R-Re_{LES} space, although two different simulations could correspond to the same point in R-Re_{LES} space. Brasseur and Wei (2010) identify an optimal region in R-Re_{LES} space called the 'High Accuracy Zone' (HAZ) within which LES captures law-of-the-wall scaling without exhibiting an overshoot in ϕ_m. The boundaries of the HAZ are defined in terms of constraints on (R, Re_{LES}, N_δ)

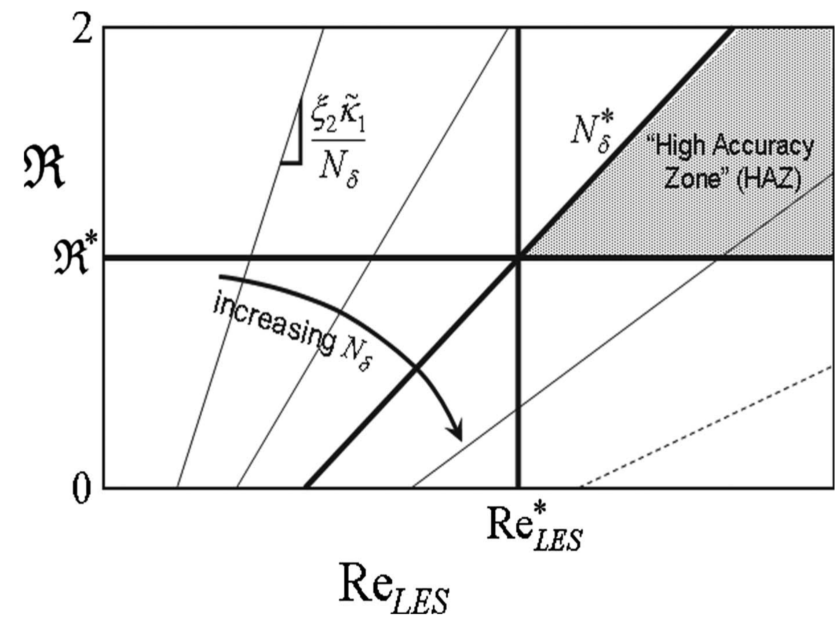

Figure 4.1. A schematic of the $R - Re_{LES}$ space with lines of constant N_δ showing conceptually the High Accuracy Zone. Reproduced from Brasseur and Wei (2010).

given by: (i) $R > R^*$; (ii) $Re_{LES} > Re^*_{LES}$; and (iii) $N_\delta > N^*_\delta$. The parameters $(R^*, Re^*_{LES}, N^*_\delta)$ represent critical values that must be exceeded for the LES to reside in the HAZ. Brasseur and Wei (2010) estimate $(R^*, Re^*_{LES}, N^*_\delta)$ to be $\approx (1, 350, 50)$. The constraint on N_δ can be shown to follow from the first two. Satisfying the three constraints, in effect, suppresses the frictional content in the LES sufficiently, thereby preventing it from interfering with law-of-the-wall scaling in the surface layer.

Using the parameters (R, Re_{LES}, N_δ), Brasseur and Wei (2010) prescribe the following simple algorithm to move the simulation systematically into the HAZ:

1. Increase N_z holding other parameters fixed, such that N_δ in the fully developed flow exceeds N^*_δ.

2. Decrease the SFS model constant and aspect ratio, AR, systematically such that the simulation moves along a constant N_δ line into the HAZ. Equivalently, the simulation can be considered to shift from a "subcritical" region in R-Re_{LES} space that is outside the HAZ into the HAZ.

For the Smagorinsky closure, they showed that the expressions for R and Re_{LES} can be rewritten as:

$$R = \frac{\xi \tilde{\kappa}_1^2}{C_s^2\, AR^{4/3}} - 1 \quad ; \quad Re_{LES} = \frac{\tilde{\kappa}_1}{\xi_1} \frac{N_\delta}{(C_s^2\, AR^{4/3})}, \tag{4.1}$$

where C_s is the SFS model constant in the Smagorinsky closure, AR is the grid aspect ratio and ξ_1 is a constant found to be ≈ 1 for LES of the neutral ABL. The benefit of Eq. (4.1) is that it relates R and Re_{LES} explicitly to the SFS model constant and the grid aspect ratio, both of which are known prior to performing the simulation. Using Eq. (4.1) and the estimates for $(R^*, Re^*_{LES}, N^*_\delta)$ as guidelines, Brasseur and Wei (2010) demonstrated the validity of their two-step algorithm described above, for the Smagorinsky closure. Their simulations inside the HAZ yielded ϕ_m profiles that exhibited: (i) correct law-of-the-wall scaling without any overshoot; and (ii) grid convergence. Recent work (Brasseur et al., 2009) has confirmed the validity of the HAZ framework for another commonly used eddy-diffusivity closure, namely, the one-equation model (Moeng, 1984). It turns out that the one-equation eddy-viscosity model yields expressions similar in form to Eq. (4.1) but with different exponents on the SFS model constant and the aspect ratio (Brasseur et al., 2009). As both the Smagorinsky closure and the one-equation model are eddy-viscosity closures, a natural question arises: does the HAZ framework hold for non-eddy-viscosity closures as well? We address this question in the present chapter by showing that the HAZ formulation is also applicable to the modeled SFS conservation equations, an example of a non-eddy-viscosity closure.

4.3 Set-up of LES runs

The details of the pseudospectral LES code and the numerical algorithm have already been described in Ch. (2). We list in Table (4.1) the important physical parameters that are prescribed in our LES runs. Their values are identical to those used by Brasseur and Wei (2010). The surface flux is set to zero in order to ensure zero buoyant forcing. We do impose a capping inversion which results in weak negative fluxes at the boundary layer top. The influence of the capping inversion, however, is minimal over the bulk of the boundary layer where the

Table 4.1. A list of important prescribed physical parameters. L_x, L_y and L_z are the physical dimensions of the computational domain in the x, y and z directions, respectively. N_x is the number of grid points in the x-direction and, similarly for N_y and N_z. Q_0 is the prescribed kinematic surface potential temperature flux, z_0 is the roughness length, U_g and V_g are the geostrophic wind velocity components in the x and y directions, and Γ is the lapse rate above the capping inversion.

Prescribed physical parameters of LES	
L_x (m)	3000
L_y (m)	3000
L_z (m)	1000
Q_0 (Kms^{-1})	0.0
z_0 (m)	0.16
U_g (ms^{-1})	15
V_g (ms^{-1})	0
Γ (Km^{-1})	0.003

heat fluxes are negligible. We collect statistics after 15–20 eddy turnover times which is approximately the duration of the transient phase in the evolution of the flow. Note that the inclusion of Coriolis forcing implies that even after equilibrium is achieved, the mean velocity continues to exhibit oscillatory behavior over a timescale $\sim (1/f)$.

4.4 Results

Let (N_x, N_y, N_z) denote the number of grid points in the x-, y- and z-directions, respectively. We present results for three different values of N_z, given by $N_z = (32, 64, 96)$. Based on the estimates by Brasseur and Wei (2010), $N_z = 32$ and $N_z = 64$ correspond to $N_\delta < N_\delta^*$, while $N_z = 96$ corresponds to the lowest vertical resolution that meets the criterion $N_\delta > N_\delta^*$.

4.4.1 ϕ_m profiles for $N_z = 32$ and $N_z = 64$

In Fig. (4.2), we plot ϕ_m corresponding to $N_z = 32$ and $N_z = 64$ with different grid aspect ratios. In all our simulations, $N_x = N_y$ so that there is no grid-induced anisotropy in the horizontal plane. For $N_z = 32$, the symbols correspond to increasing values of N_x in the following sequence: $+$ (32), $*$ (64) and $\diamond$ (128).

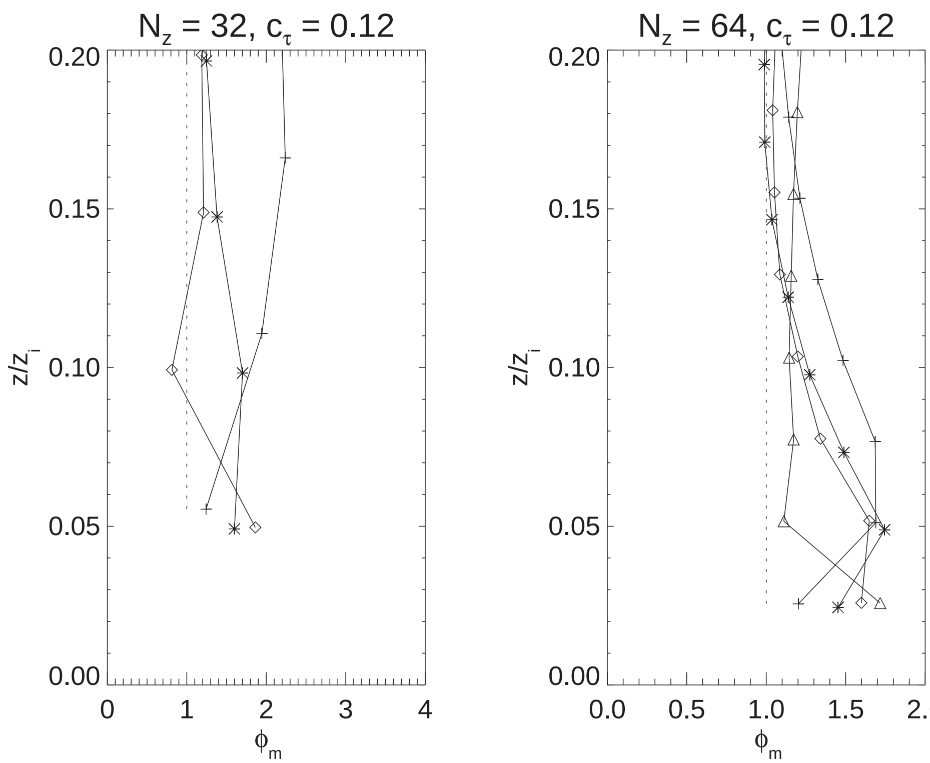

Figure 4.2. ϕ_m for $c_\tau = 0.12$. Left panel: $N_z = 32, N_x = 32\,(+), 64\,(*), 128\,(\diamond)$. Right panel: $N_z = 64, N_x = 64\,(+), 96\,(*), 128\,(\diamond), 192\,(\triangle)$. The dotted line denotes the theoretical value of ϕ_m for the neutral boundary layer, assuming $\kappa = 0.4$.

The corresponding sequence for $N_z = 64$ is given by: $+$ (64), $*$ (96), $\diamond$ (128) and $\triangle$ (192). The value of c_τ is held fixed at 0.12. Recall that c_τ is the SFS model constant in the modeled conservation equations for τ^d_{ij}. We found that the results were insensitive to the choice of c_θ, the SFS model constant in the conservation equations for the SFS potential temperature flux, f_i. This is consistent with the fact we are simulating a neutral ABL with negligible heat flux within the boundary layer. We discuss first the ϕ_m profiles for $N_z = 32$ followed by those for $N_z = 64$.

The ϕ_m profile for $N_z = 32$ and $N_x = 32$ is similar to what we would observe in low Reynolds number laminar flow, which suggests that the grid is barely able to sustain turbulence. Brasseur and Wei (2010) obtained similar results for $N_z = 32$ and high grid aspect ratios (low N_x) with the Smagorinsky closure (see their Fig. 5c). As N_x increases, there is marginal improvement in the ϕ_m profiles as the grid begins to resolve some of the turbulence. At the highest value of N_x,

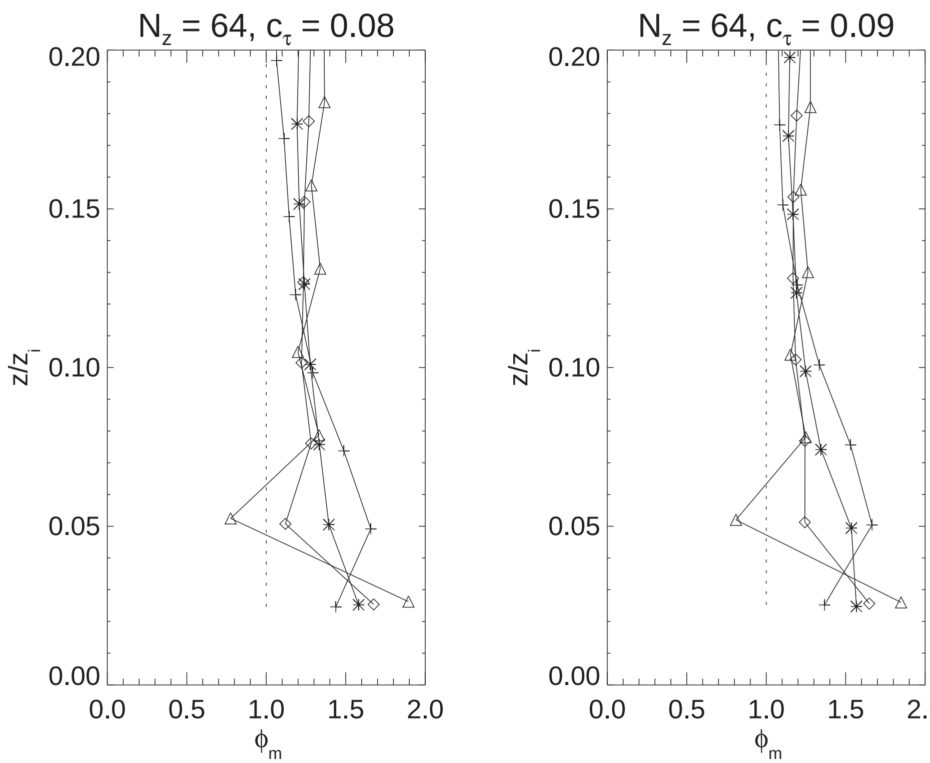

Figure 4.3. ϕ_m for $N_z = 64$. Left panel: $c_\tau = 0.08, N_x = 64\,(+), 96\,(*), 128\,(\diamond), 192\,(\triangle)$. Right panel: $c_\tau = 0.09, N_x = 64\,(+), 96\,(*), 128\,(\diamond), 192\,(\triangle)$. The dotted line denotes the theoretical value of ϕ_m for the neutral boundary layer, assuming $\kappa = 0.4$.

i.e, $N_x = 128$, ϕ_m still fails to exhibit law-of-the-wall scaling even as it starts to develop oscillations at the surface.

For $N_z = 64$, we see the presence of a well-defined overshoot in ϕ_m at the higher aspect ratios. As N_x is increased to 192 ($\triangle$), the overshoot disappears gradually although we have still not recovered law-of-the-wall scaling. In Fig. (4.3), we plot ϕ_m for $N_z = 64$ and two lower values of c_τ, 0.08 and 0.09. The symbols in Fig. (4.3) have the same meaning as in Fig. (4.2) for $N_z = 64$. We note trends similar to that in Fig. (4.2): vanishing of the overshoot and the development of oscillations at the surface, with decreasing aspect ratio. Comparing Fig. (4.2) and Fig. (4.3), we also observe that for a fixed aspect ratio, lower values of c_τ are associated with a reduced overshoot.

To understand better the significance of the trends in Fig. (4.2) and Fig. (4.3), we compute R and Re_{LES} for the above simulations and plot their values in R–

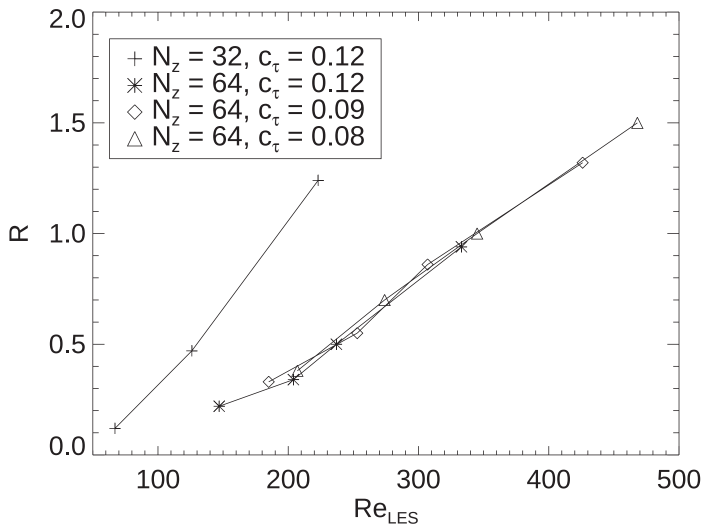

Figure 4.4. Values of R and Re_{LES} associated with the simulations in Fig. (4.2) and Fig. (4.3). Lines correspond to constant N_z while increasing values of N_x (for fixed N_z) correspond to upward movement along the lines.

Re_{LES} space in Fig. (4.4). Note that we use the general definitions of R and Re_{LES} and not the forms given by Eq. (4.1) which are valid only for the Smagorinsky closure. A couple of important trends emerge in Fig. (4.4). Firstly, the slope of the lines in R-Re_{LES} space vary inversely with N_z. Secondly, for fixed N_z, decreasing the aspect ratio (AR) and SFS model constant (c_τ) yields higher values of R and Re_{LES}. Both these trends are identical to those observed with eddy-viscosity closures (Brasseur and Wei, 2010; Brasseur et al., 2009). Hence, although the exact functional forms in Eq. (4.1) are valid only for the Smagorinsky closure, their predicted qualitative dependence of (R, Re_{LES}) on the SFS model constant and aspect ratio appears to be general in nature.

For some of these simulations, R and Re_{LES} exceed their critical values, R^* and Re^*_{LES}, as estimated by Brasseur and Wei (2010). Their ϕ_m profiles, however, fail to display grid convergence and law-of-the-wall scaling. This is because we haven't yet satisfied the third requirement to move a simulation into the HAZ, namely, $N_\delta > N^*_\delta$. We now proceed to discuss results for $N_z = 96$.

4.4.2 ϕ_m profiles for $N_z = 96$

Simulations of the neutral ABL can be computationally expensive due to the long transient phase whose duration $\sim 1/f$. Thus, a higher value of f shortens the transient phase. In our simulations with $N_z = 32$ and $N_z = 64$ we used $f = 0.000146$, which corresponds to a latitude of 90°, i.e., the poles. Brasseur and Wei (2010) use a still higher value, $f = 0.0004$, in their simulations. We use the same value of f for our LES runs with $N_z = 96$, in order to reduce the computational time.

Figure (4.5) shows profiles of τ_{13}^d over the surface layer for a series of simulations, where $c_\tau = 0.07$ and N_x increases from 64 to 216. The corresponding ϕ_m profiles are shown in Fig. (4.6). From Fig. (4.5), a decrease in the aspect ratio, $\mathcal{AR}$, is accompanied by an increase in $\mathcal{R}$, which we recall is the ratio of the resolved to the SFS component of τ_{13}^d at the first grid point. This relationship between $\mathcal{AR}$ and $\mathcal{R}$ is consistent qualitatively with the expressions in Eq. (4.1) and our results for $N_z = (32, 64)$. Figure (4.6) shows that increasing values of $\mathcal{R}$ are associated with a reduction in the overshoot in ϕ_m. For $N_x = 144$ and $N_x = 192$, the ϕ_m profiles are free of the overshoot and relatively vertical over bulk of the surface layer indicating that law-of-the-wall scaling has been achieved. In other words, the simulations with $N_x = 144$ and $N_x = 192$ are in the HAZ. As N_x increases further to 216, ϕ_m develops oscillations near the surface. The progression in the evolution of ϕ_m shown in Fig. (4.6) is strikingly similar to that obtained by Brasseur and Wei (2010) with the Smagorinsky closure (see their Fig. 10). In more recent work, Wei and Brasseur show that the oscillations in ϕ_m near the ground are caused due to deficiencies in the surface stress model. They were able to reduce the oscillations substantially by using an improved formulation of the surface stress model.

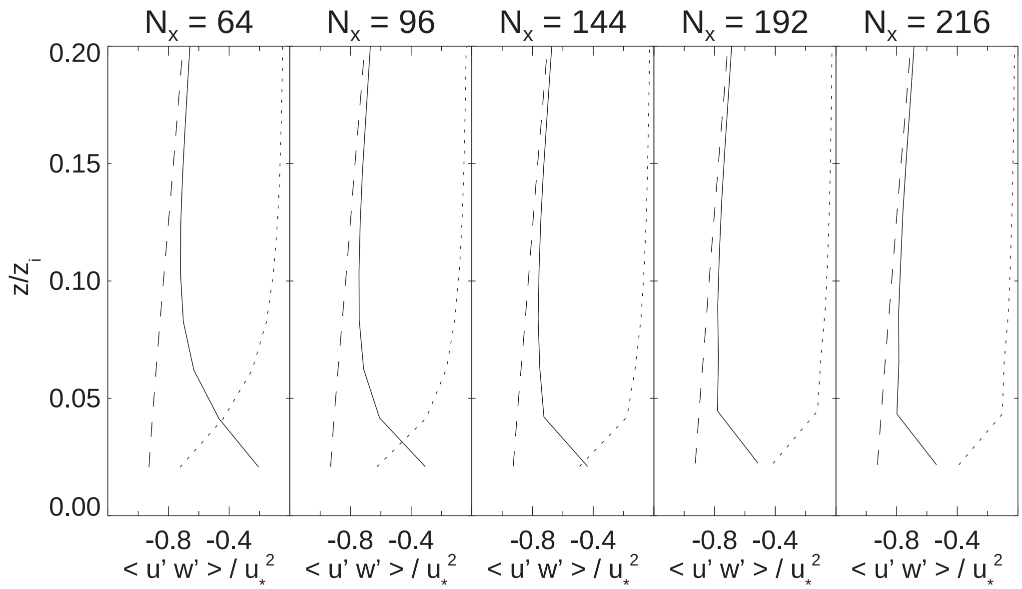

Figure 4.5. (1,3) component of τ_{ij}^d for $c_\tau = 0.07$ and $N_z = 96$. Legend: resolved (—), SFS ($\cdots$) and total (−−). Corresponding ϕ_m is shown below.

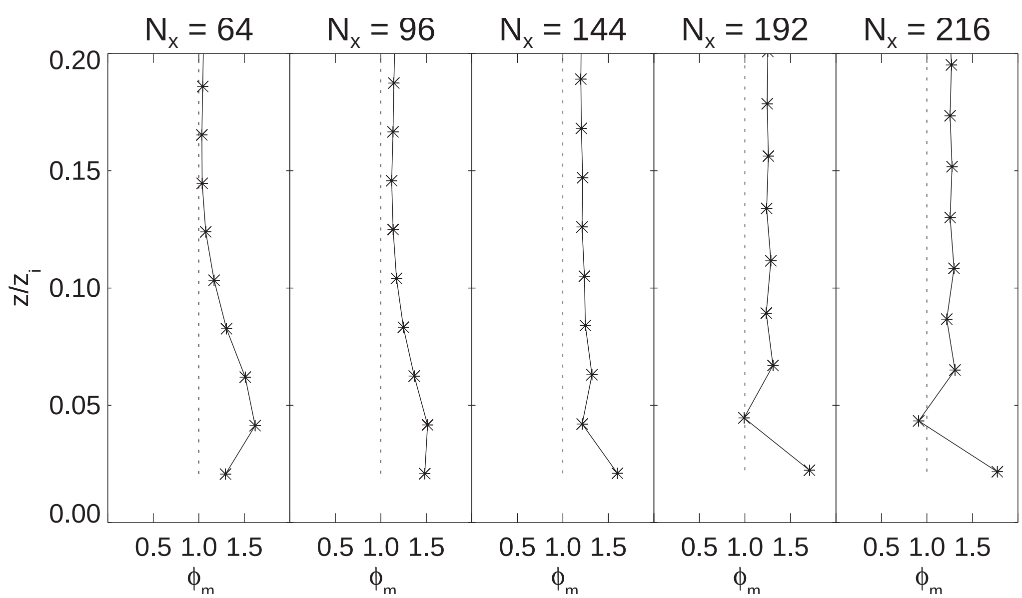

Figure 4.6. ϕ_m profiles for the simulations in Fig. (4.5).

To understand better the interplay between the SFS model constant, c_τ, and AR, we plot in Fig. (4.7), ϕ_m for $c_\tau = (0.06, 0.08, 0.12)$. For each of these c_τ values, we consider three values of N_x, given by $N_x = (64, 144, 192)$. Thus, Fig. (4.7) shows

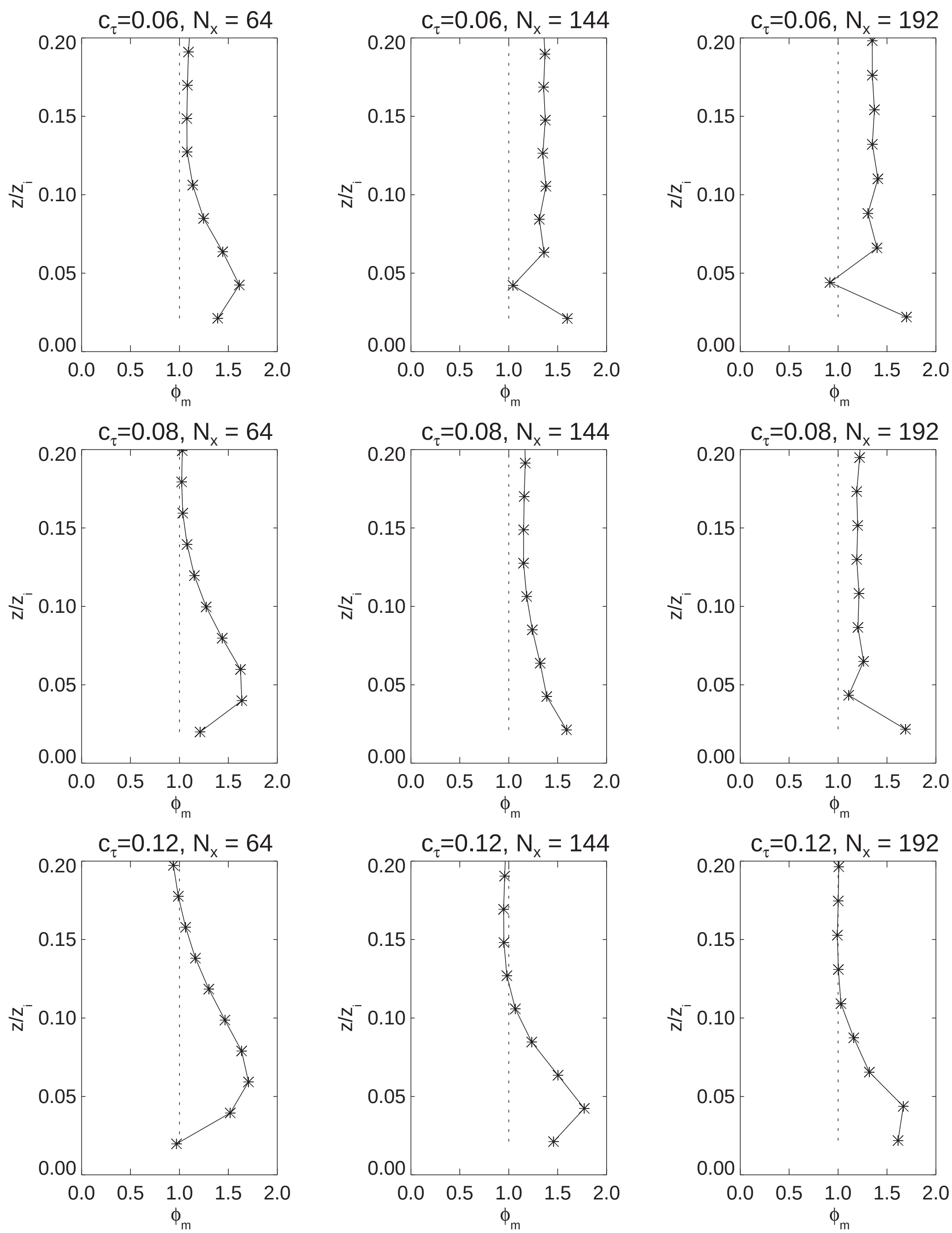

Figure 4.7. ϕ_m profiles for 9 simulations corresponding to three different $N_x = (64, 144, 192)$ for each of three different $c_\tau = (0.06, 0.08, 0.12)$.

ϕ_m profiles obtained from 9 simulations. Moving from left to right along a row of plots in Fig. (4.7) corresponds to constant c_τ and decreasing AR. Moving from top to bottom along a column of plots corresponds to constant AR and increasing c_τ.

Let us begin with the bottom row, which corresponds to $c_\tau = 0.12$. For this value of c_τ, none of the three N_x values manage to get rid of the overshoot and recover law-of-the-wall scaling. For $c_\tau = 0.08$, there is a pronounced overshoot when $N_x = 64$. When N_x is increased to 192, however, the overshoot disappears yielding better ϕ_m profiles. In simulations with $c_\tau = 0.06$, the overshoot vanishes even earlier for $N_x = 144$. This is accompanied, however, by a quicker intensification of oscillations, as evidenced by a comparison of the ϕ_m profiles for $N_x = 192$ among the three values of c_τ. Note also that the ϕ_m profile for $c_\tau = 0.06$ and $N_x = 192$ is further away from the theoretical profile when compared to that for $c_\tau = 0.08$ and $N_x = 192$. We now interpret these observations in terms of the HAZ framework.

Analysis for eddy-viscosity closures (Brasseur and Wei, 2010; Brasseur et al., 2009) reveals that the SFS model constant, C_s, and AR combine in the form $D_s = C_s^a AR^b$ to determine R and Re_{LES}. In particular, for the Smagorinsky closure, Eq. (4.1) shows that R and Re_{LES} vary inversely with D_s. A similar relationship holds for the one-equation model as well. It follows that D_s must be less than some critical value D_s^* for R and Re_{LES} to exceed their critical values. Thus, in order to place a simulation inside the HAZ, high SFS dissipation, i.e., high values of C_s, must be complemented by low AR and vice versa. This is precisely the message conveyed by Fig. (4.7), even though for the modeled SFS conservation equations we don't know the exact combination of c_τ and AR that determines R and Re_{LES}. The simulations with $c_\tau = 0.12$ can now be interpreted as having too much model dissipation which require aspect ratios lower than that corresponding to $N_x = 192$, if the overshoot is to be removed. By the same logic, simulations with $c_\tau = 0.06$ have low model dissipation so that aspect ratios corresponding to $N_x = 144$ are sufficient to eliminate the overshoot. Fig. (4.6) and Fig. (4.7) show that R and Re_{LES} need to exceed their critical values, but must stay within bounds to prevent severe oscillations in ϕ_m. Equivalently, the amount of friction in the simulation needs to be sufficiently low to eliminate the overshoot and at the same time above some threshold. These observations parallel findings for eddy-viscosity closures by Brasseur and Wei (2010).

Apart from the cases shown in Fig. (4.6) and Fig. (4.7), we performed additional simulations for $N_z = 96$ while varying c_τ and N_x according to Table (4.2).

Table 4.2. Values of $c_\mathcal{T}$ and N_x used in simulations where $N_z = 96$ was held fixed.

$\mathbf{c}_\mathcal{T}$	$\mathbf{N_z}$	$\mathbf{N_x}$
0.05	96	96, 144, 192
0.06	96	64, 96, 144, 160, 192, 216
0.07	96	64, 96, 144, 160, 192, 216
0.08	96	64, 96, 144, 160, 192, 216
0.09	96	64, 96, 144, 160, 192, 216
0.12	96	64, 144, 160, 192

In Fig. (4.8), we plot the R and Re_{LES} values for all the simulations listed in Table (4.2). The trends in Fig. (4.8) are consistent with the ϕ_m profiles shown in Fig. (4.6) and Fig. (4.7). For instance, the simulations with $c_\mathcal{T} = 0.12$ which yielded a severe overshoot, occupy a subcritical region in R-Re_{LES} space. The simulations with lower values of $c_\mathcal{T}$ which yield improved ϕ_m profiles tend to be associated with values of R and Re_{LES} that are higher than their critical values. Simulations with excessively low values of $c_\mathcal{T}$ that yield severe oscillations in ϕ_m near the surface, tend towards the upper right corner of Fig. (4.8).

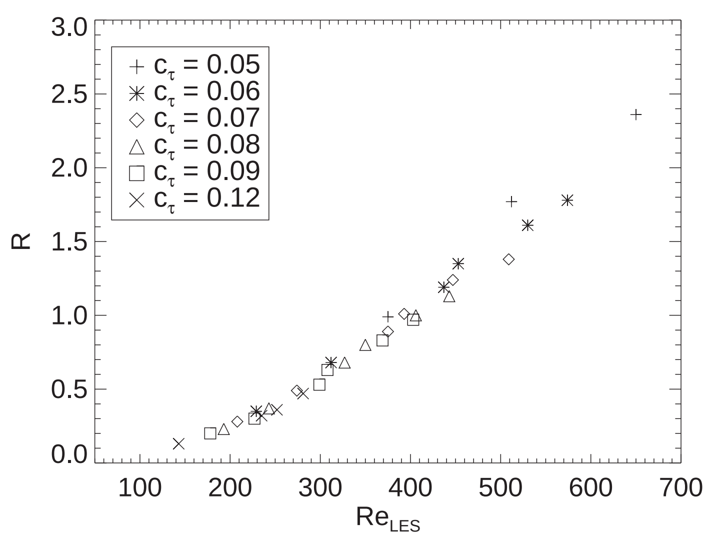

Figure 4.8. Values of R and Re_{LES} for the simulations listed in Table (4.2).

In Fig. (4.9), we plot ϕ_m profiles for those simulations which are inside the HAZ. Above the first couple of grid points, there is reasonable grid convergence

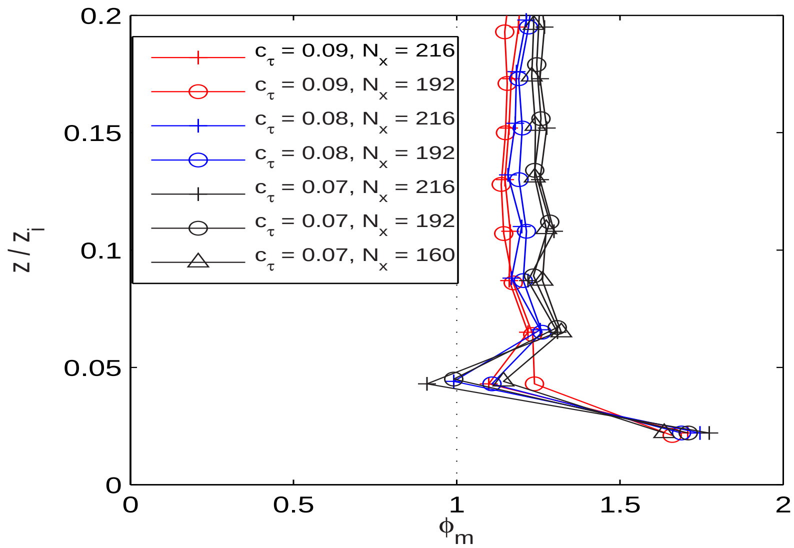

Figure 4.9. ϕ_m for simulations inside the HAZ. The values of c_τ range from 0.07 (black) to 0.09 (red) while those of N_x range from 160 to 216. The dotted line denotes the theoretical value of ϕ_m for the neutral ABL.

between the profiles for a given value of c_τ. As c_τ increases, there is a clear tendency for the profiles to shift horizontally towards the dotted line, which is the theoretical ϕ_m value for a neutral ABL. A ϕ_m profile that coincides with the dotted line would yield a κ value of 0.4 which implies that all the profiles shown in Fig. (4.9) correspond to $\kappa < 0.4$. Averaging the κ values in Fig. (4.9) over simulations corresponding to a constant c_τ, we obtain $\kappa = (0.317, 0.332, 0.342)$ for $c_\tau = (0.07, 0.08, 0.09)$, respectively. Brasseur and Wei (2010) note that the value of κ is not universal but appears to vary with the outer scale flow characteristics. Nagib and Chauhan (2008) estimate κ to be 0.37 in channel flow and 0.41 in pipe flow. Andreas et al. (2006) estimate κ to be 0.387 in the atmospheric surface layer. Field measurements under near-neutral conditions yield $\kappa \approx 0.365$ (Oncley et al., 1996). An alternate formulation for the surface stress model developed by Wei and Brasseur (2010) yields ϕ_m profiles that are closer to unity in the surface layer and consequently, higher values of κ. In later sections, we show results from a couple of simulations that employ the new surface stress model.

4.4.3 Dependence of $(R,\, Re_{LES})$ on $(c_\tau,\, AR)$

It is straightforward to determine the exact functional form of the relationship between (R, Re_{LES}) and (C_s, AR) for eddy-viscosity closures due to their simplicity. Such a feat is considerably harder with the modeled SFS conservations or other closures which don't use an eddy-viscosity explicitly. It might be be possible, however, to deduce such relationships numerically using LES results. Let us assume that the relevant combination of c_τ and AR for the modeled conservation equations is $c_\tau^{s_1}\, AR^{s_2}$. Eq. (4.1) shows that the Smagorinsky closure yields $Re_{LES} \propto 1/(C_s^2\, AR^{4/3})$. If a similar relationship were to hold for Re_{LES} in the conservation-equation-based closure, then plotting Re_{LES} versus c_τ for fixed AR using a log-log scale would yield straight lines with a slope s_1. A similar procedure could be used to determine s_2.

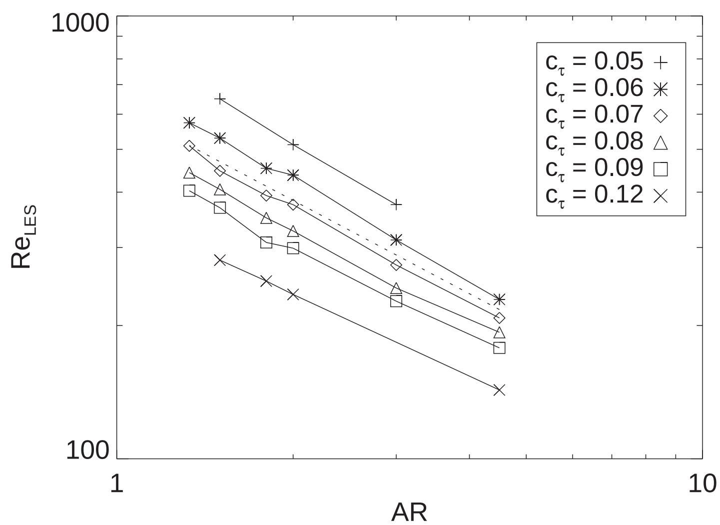

Figure 4.10. Re_{LES} as a function of AR, for $N_z = 96$ and different values of c_τ. The dotted line has a slope of -0.7.

In Fig. (4.10), we plot Re_{LES} versus AR with c_τ as a parameter using a logarithmic scale on both axes. Only simulations with $N_z = 96$ have been considered. The plotted curves are approximately linear which suggests an inverse power relationship between Re_{LES} and AR. The curve for $c_\tau = 0.12$ has a noticeably lesser slope than the others. Recall that $c_\tau = 0.12$ corresponds to highly dissipative

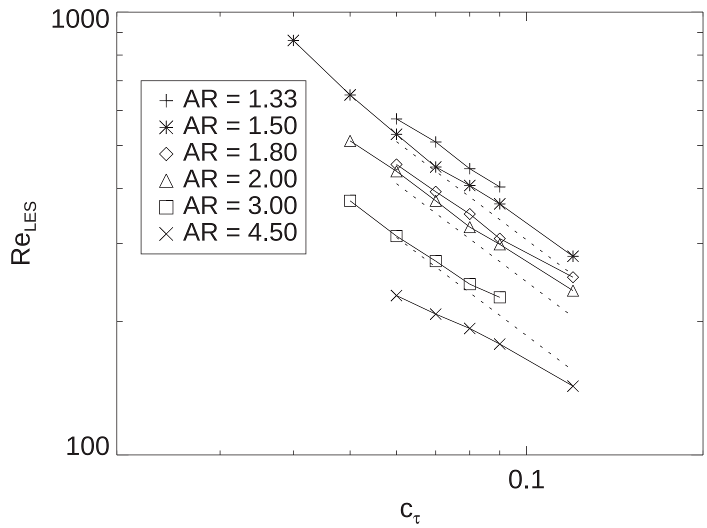

Figure 4.11. Re_{LES} as a function of c_τ for $N_z = 96$ and different values of AR. The dotted lines have a slope of -1.0.

simulations with a strong overshoot in ϕ_m. The curves for the other c_τ values have an approximate slope of -0.7, indicated by a dotted line in the figure.

Figure (4.11) shows Re_{LES} as a function of c_τ for different values of AR. The curves are not strictly linear but are instead piecewise linear. For each curve, the portion connecting points representing simulations inside the HAZ, i.e, those typically with low c_τ and high Re_{LES}, is nearly linear with a slope ≈ -1, indicated by dotted lines in the figure. Towards higher values of c_τ, the slopes of the curves deviate systematically from unity to assume lesser values (in magnitude). Once again, the curve for $c_\tau = 0.12$ is considerably different from the other curves.

Based on Fig. (4.10) and Fig. (4.11), Re_{LES} is approximately proportional to $(c_\tau \, AR^{0.7})^{-1}$. We can contrast this result with the corresponding expressions for the Smagorinsky closure and the one-equation eddy-viscosity model, given by $(C_s^2 \, AR^{1.33})^{-1}$ and $(C_K \, AR^{-0.89})^{-1}$, respectively. The exponents on the SFS model constants are consistent with the nature of the respective closures. The eddy-viscosities in the Smagorinsky closure and the one-equation model are proportional to C_s^2 and C_k, respectively. For the modeled conservation equations, we can show (Hatlee and Wyngaard, 2007) by retaining one production and one destruction term that an effective eddy-viscosity is proportional to c_τ. Thus, the exponent on the SFS model constant in its combination with AR is determined by how it relates to the eddy-viscosity, either explicitly or implicitly. We are unable to provide a physical explanation for the -0.7 exponent on AR beyond inferring its approximate value from Fig. (4.10).

4.4.4 Influence of surface stress model

In this section, we use a new formulation for the surface stress model (Wei and Brasseur, 2010) and examine its effect on ϕ_m and the streamwise velocity variance near the ground. Wei and Brasseur (2010) implemented the new formulation in LES with the Smagorinsky closure and found that it led to more realistic predictions of κ, and the scaled streamwise velocity variance near the ground. Thus, it is of interest to see if their surface stress model yields similar improvements for the conservation-equation-based closure. We review briefly the new surface stress model developed by Wei and Brasseur (2010) before presenting our LES results.

We denote the modeled instantaneous wall shear stress by $\tilde{\tau}_{13}^{tot}(x, y, 0; t)$. The subscript 'tot' refers to the fact that the modeled wall stress has resolved-scale, SFS and viscous components (Wei and Brasseur, 2010) but it is their sum that is modeled. Decomposing $\tilde{\tau}_{13}^{tot}(x, y, 0; t)$ into mean and fluctuating parts,

$$\tilde{\tau}_{13}^{tot}(x, y, 0; t) = \langle \tau_{13}^{tot} \rangle_0 + \tau_{13}^{tot}(x, y, 0; t). \tag{4.2}$$

Wei and Brasseur (2010) showed that $\langle \tau_{13}^{tot} \rangle_0$ is dictated by global momentum balance and is equal to $(\delta/\rho)\,(\partial \langle \bar{p} \rangle / \partial x_1)$ for a channel flow, where δ is the half-channel width and $\bar{p}$ is the filtered pressure field. Thus, it is the fluctuating part, $\tau_{13}^{tot}(x, y, 0; t)$, that differs from one wall stress model to another. In LES of the ABL, the mean pressure gradient is specified through the geostrophic velocities but the modeling of the wall stress model is similar to that for a channel flow to the extent that $\langle \tau_{13}^{tot} \rangle_0$ is determined by the global flow balance in both flows. The fluctuating wall stress is further rewritten as (Wei and Brasseur, 2010):

$$\frac{\tau_{i3}(x, y, 0; t)}{u_*^2} = \beta_{i3}\, g_{i3}(x, y; t), \tag{4.3}$$

where $i = (1, 2)$ denotes the streamwise and spanwise directions, respectively.

From Eq. (4.3), it is clear that $g_{i3}(x, y; t)$ has to meet the following constraints:

$$\langle g_{i3}(x, y; t)\rangle = 0 \quad ; \quad \sqrt{\langle g_{i3}(x, y; t)\, g_{i3}(x, y; t)\rangle} = 1 \tag{4.4}$$

Equations (4.3)–(4.4) show that the fluctuation level of $\tau_{i3}(x, y, 0; t)$ is set by β_{i3} and the structure of the fluctuations themselves are determined by $g_{i3}(x, y; t)$. In our LES code, we use the wall stress model developed originally by Moeng (1984) (hereafter referred to as M84), for which $\tilde{\tau}_{i3}(x, y, 0)$, β_{i3} and $g_{i3}(x, y; t)$ are given by (Wei and Brasseur, 2010):

$$\begin{aligned}
\tilde{\tau}_{i3}(x, y, 0) &= -u_*^2 \frac{\left[\langle \bar{s}\rangle \left(\bar{u}_i - \langle \bar{u}_i\rangle\right) + \bar{s}\,\langle \bar{u}_i\rangle\right]_{\Delta z/2}}{\langle \bar{s}\rangle^2_{\Delta z/2}} && (4.5)\\
\beta_{i3} &= -\frac{\sqrt{\left[\langle \bar{s}\rangle \left(\bar{u}_i - \langle \bar{u}_i\rangle\right) + \langle \bar{u}_i\rangle \left(\bar{s} - \langle \bar{s}\rangle\right)\right]^2_{\Delta z/2}}}{\langle \bar{s}\rangle^2_{\Delta z/2}} && (4.6)\\
g_{i3}(x, y) &= \frac{\left[\langle \bar{s}\rangle \left(\bar{u}_i - \langle \bar{u}_i\rangle\right) + \langle \bar{u}_i\rangle \left(\bar{s} - \langle \bar{s}\rangle\right)\right]_{\Delta z/2}}{\sqrt{\left[\langle \bar{s}\rangle \left(\bar{u}_i - \langle \bar{u}_i\rangle\right) + \langle \bar{u}_i\rangle \left(\bar{s} - \langle \bar{s}\rangle\right)\right]^2_{\Delta z/2}}}. && (4.7)
\end{aligned}$$

In Eqs. (4.5)–(4.7), $\bar{u}_i$ is the filtered velocity and $\bar{s}$ is the filtered resultant horizontal velocity. The $\Delta z/2$ subscript reminds us that these variables are computed at the first model grid level for u and v, which is located physically at $z = \Delta z/2$. Wei and Brasseur (2010) showed that β_{i3} is negative and has a magnitude close to 0.2 for the M84 wall stress model.

We present in Fig. (4.12) plots of streamwise velocity variances for two simulations, one inside the HAZ and another outside it. The ϕ_m profiles for these two simulations are shown in Fig. (4.6). In both cases, the variance profiles (total and resolved) don't increase smoothly towards the ground but exhibit a kink such that there is a decrease in their magnitude at the first grid level. In smooth wall boundary layer flows, the streamwise velocity variance peaks deep inside the viscous layer at $zu_*/\nu \approx 15$ and decreases sharply to zero towards the wall. Since we don't resolve the viscous layer in LES, the peak at $zu_*/\nu \approx 15$ lies well below the first grid level. Thus, the kink seen in Fig. (4.12) is unphysical and doesn't conform to observations (Grant, 1986). Wei and Brasseur (2010) were successful in removing the kink by changing the sign of β_{i3} from negative to positive in Eq. (4.3).

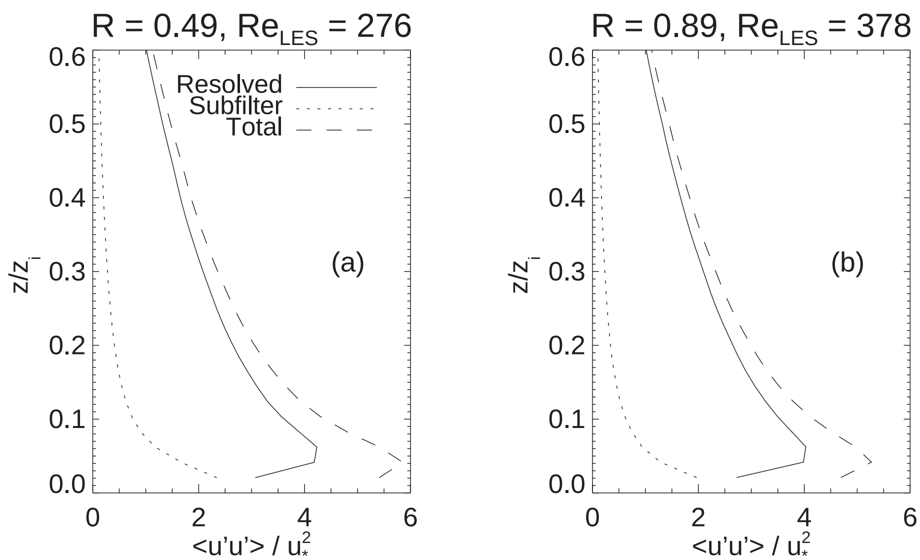

Figure 4.12. Scaled streamwise variances, $\langle u'u' \rangle / u_*^2$, versus z/z_i for two simulations, one outside the HAZ (panel (a)) and one within the HAZ (panel (b)). $N_x (= N_y)$ for (a) and (b) is 96 and 192, respectively, while $N_z = 96$ for both cases. For both simulations, $c_\tau = 0.07$.

They further showed that a negative value of β_{i3} results in a sink-like term in the prognostic equation for the streamwise velocity variance. In Fig. (4.13) we contrast $\langle u'_r u'_r \rangle / u_*^2$ ('r' denotes resolved-scale) and ϕ_m obtained with two wall stress models: M84 and that developed by Wei and Brasseur (2010) (referred to as WB10 in the figure) in which $g_{i3}(x, y)$ is given by Eq. (4.7) and $\beta_{i3} = 0.15$. The M84 model yields $(R, Re_{LES}) = (0.89, 378)$ and the WB10 model yields $(R, RE_{LES}) = (1.58, 391)$. Both simulations lie inside the HAZ and have similar Re_{LES} values although the WB10 model yields a sharp increase in R, which is solely due to the effect of the wall stress model as all other factors such as SFS model constant, grid size, etc. are held fixed. With the WB10 model, the streamwise variance profile increases smoothly without exhibiting a kink. In contrast, the LES with the M84 wall model yields a kink in the streamwise variance profile although the simulation parameters are inside the HAZ. The corresponding ϕ_m profiles show that the WB10 wall stress model reduces the oscillation at the first grid level and yields ϕ_m values slightly closer to 1, thereby implying a higher value of κ. The trends seen in Fig. (4.13) mirror those observed for eddy-viscosity closures (Brasseur et al., 2009).

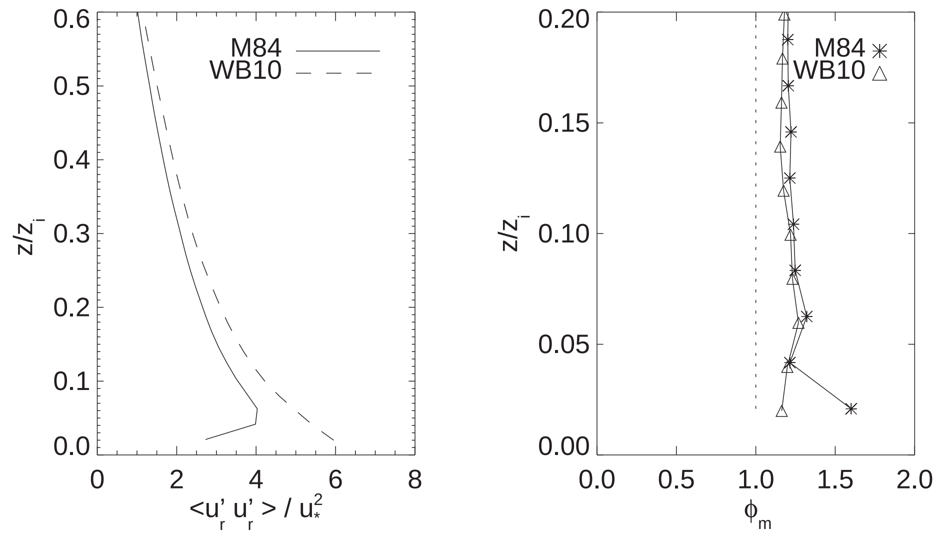

Figure 4.13. (a) Nondimensional resolved-scale streamwise variances, $\langle u'u' \rangle / u_*^2$, versus z/z_i. (b) ϕ_m profiles. M84 refers to the wall stress model developed by Moeng (1984) and WB10 to that developed by Wei and Brasseur (2010). $N_x (= N_y)$ and N_z for (a) and (b) are 144 and 96, respectively. For the simulation using M84, $(R, Re_{LES}) = (0.89, 378)$, while for that using WB10, $(R, Re_{LES}) = (1.58, 391)$. For both cases, $c_\tau = 0.07$.

4.5 Summary

In this chapter, we explored the applicability of the 'High Accuracy Zone' (HAZ) framework (Brasseur and Wei, 2010) to a closure based on the SFS conservation equations. The HAZ framework is a systematic approach to recovering law-of-the-wall scaling and obtaining accurate predictions of ϕ_m in LES of high Reynolds number flows. Past work (Brasseur and Wei, 2010; Brasseur et al., 2009) has demonstrated the validity of the HAZ framework for commonly used eddy-viscosity closures. Our results show that the arguments put forth by Brasseur and Wei (2010) are equally valid for the conservation-equation-based closure. We found significant improvement in the accuracy of ϕ_m predictions upon following the algorithm outlined by Brasseur and Wei (2010) delineating the HAZ framework. As the modeled SFS conservation equations bear little resemblance to standard eddy-viscosity closures, our findings support the conclusion of Brasseur and Wei (2010) that the HAZ framework is relevant to accurate predictions in LES irrespective of the underlying SFS model.

We also examined the effects of a new wall stress model (Wei and Brasseur, 2010) on the predictions of streamwise velocity variance and ϕ_m, using the modeled SFS conservation equations. We found that it significantly reduced the oscillations in ϕ_m at the first grid level and led to better representation of the streamwise velocity fluctuations, similar to earlier findings by Wei and Brasseur (2010) for eddy-viscosity closures.

Chapter 5

Conclusions

When the filter width, Δ, is much smaller than the energy-containing length scales, l, the subfilter scales account for a small fraction of the turbulent fluxes and it is sufficient that the SFS model accomplish the downscale transfer of energy at the correct rate. When $l \sim \Delta$, however, a significant fraction of the turbulent fluxes resides in the subfilter scales. Thus, it is essential that the SFS model not only drain energy from the large eddies but also represent the SFS motions accurately. While there have been attempts to address some of the limitations of standard eddy-diffusivity closures by making the SFS model constant depend on local flow parameters of the atmospheric boundary layer (ABL), "the best one can hope for is to improve the model's accuracy in representing the energy transfer to smaller scales" (Chamecki et al., 2007). A better parameterization of the subfilter scales themselves will require incorporating essential SFS physics into the SFS model. This dissertation is an attempt towards achieving that objective. We have focused on studying the performance of an SFS model that solves for the SFS fluxes using a truncated version of their conservation equations, one similar to that used by Hatlee and Wyngaard (2007). In the modeled SFS conservation equations, we neglect the transport terms and model the slow pressure strain-rate covariance using a linear return-to-isotropy model (Rotta, 1951) while retaining advection and dominant production terms in their exact analytical form. We studied the performance of the modeled SFS conservation equations in LES of convective, stably stratified and neutral ABLs. Our LES studies for the convective and stably stratified ABLs were supplemented by analysis of the SFS conservation equations using surface layer data from the Horizontal Array Turbulence Study (HATS) experiment (Horst et al., 2003).

5.1 Studies of the convective ABL

As part of our analysis of the convective ABL, we studied the nature of balance in the modeled SFS conservation equations and trends exhibited by the low-order moments of the SFS fluxes (means and fluctuations), when plotted against the nondimensional parameter Δ_w/Δ (Sullivan et al., 2003), where Δ_w is the wavelength corresponding to the peak in the vertical velocity spectrum. The modeled conservation equations for the SFS deviatoric stresses, τ_{ij}^d, predicted the dominance of anisotropic production in the $\tau_{\alpha\alpha}^d$ budgets and that of isotropic production in the τ_{13}^d budget with decreasing Δ_w/Δ, in agreement with observations. They, however, underpredicted the magnitude of anisotropic production in the τ_{13}^d budget at low Δ_w/Δ, when compared to observations. The advection terms were found to be negligible in the mean, but were required to prevent a spurious build up of resolved-scale energy close to the filter cutoff. One of the interesting features of the modeled conservation equations was the tendency of the scaled, principal production terms in the $\tau_{\alpha\alpha}^d$ and τ_{13}^d budgets to yield asymptotes at low Δ_w/Δ, some of which were in good agreement with theoretically derived values in the limit $\Delta_w/\Delta \to 0$, i.e., the "RANS limit." This shows the ability of the transport-equation-based SFS model to predict the dominant SFS production terms consistently across a range of Δ_w/Δ without any ad hoc modifications to it in regions where $\Delta_w \sim \Delta$, such as the near-wall region. Thus, this SFS model can be viewed as an alternative to "hybrid" methods which try to unify LES and RANS formulations into one model.

The modeled conservation equations for the SFS scalar fluxes, f_i, reproduced successfully the major trends observed in the HATS data, namely, the dominance of flux tilting and anisotropic gradient-production in the f_1 budget, and that of isotropic gradient-production in the f_3 budget. As in the modeled τ_{ij}^d budgets, the advection terms while insignificant in the mean were essential to ensure proper downscale transfer of resolved-scale variance. Our LES results showed that an eddy-viscosity closure yields near-zero values of f_1 while observations (Hatlee and Wyngaard, 2007) reveal it to be significant in regions of high mean shear within the

ABL. In general, the eddy-viscosity closure predicted well only those components of τ_{ij}^d and f_i which are produced primarily through isotropic production, namely, τ_{13}^d and f_3.

Apart from studying the trends exhibited by different SFS statistics as a function of Δ_w/Δ, we also examined the conditional means of the two terms in the resolved-scale velocity jpdf equation that involve a direct contribution from the SFS model (Chen et al., 2009; Chen and Tong, 2006): (i) SFS deviatoric stress, τ_{ij}^d; and (ii) SFS production rate, P_{ij}^d. Overall, the modeled SFS conservation equations predicted trends in the conditional means of τ_{ij}^d and P_{ij}^d better than did an eddy-diffusivity closure due to two factors: (i) they include the dominant production terms for all the τ_{ij}^d components; and (ii) they include SFS advection. Thus, apart from its direct impact on the downscale transfer of energy, SFS advection also influences resolved-scale statistics indirectly through its beneficial role in the prediction of the conditional means of τ_{ij}^d and P_{ij}^d.

5.2 Studies of the stably stratified ABL

The stably stratified ABL is associated typically with low Δ_w/Δ as stratification confines the energy carrying eddies to scales smaller than in the convective ABL. Accordingly, our analysis of the SFS budgets in the stably stratified surface layer, using HATS data, found that terms typically ignored in eddy-viscosity closures play an even greater role than in the convective ABL. In the τ_{ij}^d budgets, we found that anisotropic production and buoyant production contribute significantly to both the mean values and fluctuation levels of τ_{ij}^d. The dominant production terms, scaled appropriately, yielded asymptotes at low Δ_w/Δ that agreed well with our analytically derived values in the limit $\Delta_w/\Delta \to 0$.

In the f_1 budget, we found the tilting and anisotropic gradient production contribute significantly to the mean and fluctuation level of f_1. While isotropic gradient-production remained the principal contributor to the mean and fluctuation level of f_3 across the entire range of Δ_w/Δ considered in our study, anisotropic gradient-production and buoyant destruction played an increasingly important role as Δ_w/Δ decreased.

Following our analysis of the stable surface layer using HATS data, we performed LES of the moderately stable boundary layer using an SFS model identical to that used in our LES of the convective ABL. The LES runs employed physical conditions identical to that prescribed in the GABLS LES-intercomparison study (Beare et al., 2006) and were performed at three resolutions:$(3.125, 6.25, 12.5)$m with a prescribed surface cooling rate of 0.25K/hr. One of the findings of the GABLS study was that convergence in various resolved-scale statistics occurred only at resolutions finer than 3.125m. In particular, the prediction of the boundary layer depth was found to be quite sensitive to the grid resolution. For instance, at the coarsest resolution of 12.5m, some of the SFS models tested exhibited a smearing out of the inversion base and yielded boundary layers significantly deeper than those observed in LES runs at finer resolutions. In contrast, the predicted boundary layer depth by the modeled SFS conservation equations was more robust to changes in resolution. The equilibrium profiles of turbulent momentum flux and turbulent heat flux showed good agreement with theory (Nieuwstadt, 1984). The steady-state profiles of potential temperature, velocity and Richardson numbers converged well for all three resolutions. One important limitation of the modeled SFS conservation equations was their overprediction of locally scaled turbulent mixing — as quantified through effective eddy-viscosities for heat and momentum — compared to observations. Finally, we observed evidence of limiting behavior in the profile of normalized potential temperature fluctuations with increasing surface cooling rate. This limiting profile exhibited a maximum at mid-ABL heights, in agreement with observations (Nieuwstadt, 1984).

5.3 LES studies of the neutral ABL

Our final set of LES studies with the modeled SFS conservation equations involved simulation of a shear-driven neutral ABL. in order to test the applicability of the High Accuracy Zone (HAZ) framework (Brasseur and Wei, 2010) to non-eddy-viscosity closures. The HAZ refers to a region in parameter space in which LES recovers law-of-the-wall scaling in the inertial surface layer without an overshoot in the profile of ϕ_m, where ϕ_m is the nondimensional mean-gradient of velocity. We found that without satisfying the criteria specified by Brasseur and Wei (2010), the modeled SFS conservations failed to eliminate the overshoot in ϕ_m. We were able to remove the overshoot and recover law-of-the-wall scaling only after following systematically the algorithm prescribed by Brasseur and Wei (2010). As the modeled SFS conservations are fundamentally different from eddy-viscosity closures, our results provide evidence for the generality of the HAZ framework. We also tested a new formulation for the surface stress model (Wei and Brasseur, 2010) and found that it led to reduced oscillations in ϕ_m near the surface. Brasseur et al. (2009) observed similar effects with the new surface stress model for two commonly used eddy-viscosity closures.

5.4 Future Work

We list some potential topics for future research:

1. In the modeled SFS conservation equations, we considered only the slow part of the pressure strain-rate covariance but neglected the rapid and buoyant contributions, both of which are important in the ABL (Moeng and Wyngaard, 1986). The difficulty of measuring turbulent pressure fluctuations (Wyngaard et al., 1994) accurately has been an obstacle to evaluating models for the pressure strain-rate covariance although LES studies (Moeng and Wyngaard, 1986) have been used in the past for this purpose. The recently concluded AHATS (Advection HATS) experiments by a team of researchers from Clemson University, Pennsylvania State University and National Center for Atmospheric Research have succeeded in measuring turbulent pressure fluctuations reliably over a wide range of atmospheric stabilities. Data from this experiment can be used to gain insight into the role played by the pressure terms in the conservation equations and develop better models for the pressure strain-rate covariance.

2. The AHATS experiments also facilitate the evaluation of the streamwise advection terms in the SFS conservation equations. While our LES studies showed that the advection terms are negligible in the mean, they can be a significant contributor to the fluctuation levels of the SFS stresses (Wyngaard, 2004). Thus, their study enables a fuller understanding of the SFS conservation equations.

3. The Kansas experiments provided the first detailed surface-layer measurements of the Reynolds stress and flux budgets, and have significantly shaped our understanding of turbulence in the atmospheric boundary layer (Wyngaard, 1992). It would be desirable to gain insight into the more general SFS stress and flux budgets, which tend to their Reynolds-averaged counterparts as $\Delta_w/\Delta \to 0$. Toward that end, experiments based on the array technique (Tong et al., 1998), such as HATS and AHATS, play a unique role in that they enable the measurement of filtered fields which can be compared directly to LES results. Using data from these experiments it would be useful to construct the SFS budgets as a function of suitable nondimensional parameters (like Δ_w/Δ). Such SFS budgets can be used, in principle, to develop closures that perform seamlessly across scale and stability.

Appendix A

Derivation of asymptotic values for the dominant production terms in the $\tau^d_{\alpha\alpha}$ and τ^d_{13} budgets, as $\Delta_w/\Delta \rightarrow 0$ ("RANS limit")

In this section, we provide further explanation for the asymptotic limits at low values of Δ_w/Δ, as observed in Figs. (2.21)-(2.22) in Sec. (2.5.3.3). In particular, we are interested in the limits of the anisotropic production term in the $\tau^d_{\alpha\alpha}$ budgets and that of the isotropic production term in the τ^d_{13} budget. We first discuss the anisotropic production terms followed by the isotropic production terms. For notational ease, we denote the anisotropic production term in the τ^d_{ij} budget as Aniso(i,j) and the isotropic production term as Iso(i,j).

A.1 $\tau^d_{\alpha\alpha}$ budgets

In the following derivation, we consider a horizontally homogeneous ABL with a mean geostrophic wind in the x-direction. This induces a non-zero mean wind in the y-direction due to the Coriolis force but because it is much smaller than the x-component, we will treat the mean vertical wind shear as arising solely due to the mean wind in the x-direction.

As $\Delta_w/\Delta \to 0$, the filtering operation tends towards Reynolds averaging (Sullivan et al., 2003). Thus, in this limit, filtering a variable yields its ensemble mean. For instance, if u denotes the unfiltered streamwise velocity component, it follows that $u = U + u'$ where $U = \langle u \rangle = \bar{u}$ is the ensemble mean and u' is the fluctuation about the ensemble mean. A similar decomposition holds for other variables, in the RANS limit. Invoking horizontal homogeneity,

$$\frac{\partial U}{\partial x} = \frac{\partial U}{\partial y} = \frac{\partial V}{\partial x} = \frac{\partial V}{\partial y} = \frac{\partial W}{\partial x} = \frac{\partial W}{\partial y} = 0 \tag{A.1}$$

Incompressibility implies that both the ensemble-mean and the fluctuating parts of the velocity field are divergence free (Wyngaard, 2010). Hence,

$$\frac{\partial U}{\partial x} + \frac{\partial V}{\partial y} + \frac{\partial W}{\partial z} = 0 \tag{A.2}$$

Combining Eqns. (A.1)-(A.2), we get $\partial W/\partial z = 0$. Using the lower boundary condition at the wall, $W|_{z=0} = 0$, in conjunction with Eq. (A.1) yields $W \equiv 0$. Expanding out Aniso(i,j),

$$\mathrm{Aniso(i,j)} = -\left[\tau^d_{ik}\frac{\partial \bar{u}_j}{\partial x_k} + \tau^d_{jk}\frac{\partial \bar{u}_i}{\partial x_i}\right] + \left(\frac{2}{3}\right)\tau^d_{kl}\bar{S}_{kl} \;\; ; \;\; \bar{S}_{kl} = \frac{1}{2}\left(\frac{\partial \bar{u}_k}{\partial x_l} + \frac{\partial \bar{u}_l}{\partial x_k}\right) \tag{A.3}$$

Taking the ensemble average of Eq. (A.3),

$$\langle \mathrm{Aniso(i,j)} \rangle = \left\langle -\left[\tau^d_{ik}\frac{\partial \bar{u}_j}{\partial x_k} + \tau^d_{jk}\frac{\partial \bar{u}_i}{\partial x_i}\right]\right\rangle + \left(\frac{2}{3}\right)\left\langle \tau^d_{kl}\bar{S}_{kl}\right\rangle \tag{A.4}$$

We recognize $\left\langle \tau^d_{kl}\bar{S}_{kl}\right\rangle$ as the ensemble mean rate of energy transfer from the resolved to the subfilter scales. At steady state, $\left\langle -\tau^d_{kl}\bar{S}_{kl}\right\rangle$ is the principal mean production term in the conservation equation for e, the SFS kinetic energy, and is balanced primarily by $\langle \epsilon \rangle$, the mean rate of molecular destruction. Hence $\left\langle -\tau^d_{kl}\bar{S}_{kl}\right\rangle = \langle \epsilon \rangle$. In Eqs. (A.3)-(A.4), we have not yet invoked the limit $\Delta_w/\Delta \to 0$, which we recall is equivalent to replacing the overbar by the ensemble averaging operator.

For $i = j = 1$, Eq. (A.4) in the limit $\Delta_w/\Delta \to 0$, yields,

$$\langle \text{Aniso}(1,1) \rangle \xrightarrow{\Delta_w/\Delta \to 0} \left\langle -2 \left[\tau_{11}^d \cancelto{0}{\frac{\partial U}{\partial x}} + \tau_{12}^d \cancelto{0}{\frac{\partial U}{\partial y}} + \tau_{13}^d \frac{\partial U}{\partial z} \right] \right\rangle - \left(\frac{2}{3} \right) \langle \epsilon \rangle \tag{A.5}$$

We can also further simplify $\langle \epsilon \rangle = \left\langle -\tau_{kl}^d \bar{S}_{kl} \right\rangle$ in the limit $\Delta_w/\Delta \to 0$ as follows:

$$\langle \epsilon \rangle = \left\langle -\tau_{kl}^d \bar{S}_{kl} \right\rangle \xrightarrow{\Delta_w/\Delta \to 0} \left\langle -\tau_{kl}^d \langle S_{kl} \rangle \right\rangle = \left\langle -\tau_{13}^d \frac{\partial U}{\partial z} \right\rangle, \tag{A.6}$$

The other five components of $\langle S_{ij} \rangle$ are all zero, which follows from Eq. (A.1), $W \equiv 0$ and our approximation regarding the vertical wind shear (explained earlier). Equation (A.5) simplifies to,

$$\begin{aligned} &\langle \text{Aniso}(1,1) \rangle \xrightarrow{\Delta_w/\Delta \to 0} 2 \langle \epsilon \rangle - \left(\frac{2}{3} \right) \langle \epsilon \rangle = \left(\frac{4}{3} \right) \langle \epsilon \rangle \\ \implies \quad & \boxed{\frac{\langle \text{Aniso}(1,1) \rangle}{\langle \epsilon \rangle} \xrightarrow{\Delta_w/\Delta \to 0} \left(\frac{4}{3} \right)} \end{aligned} \tag{A.7}$$

Repeating the above analysis for the (2,2) component,

$$\langle \text{Aniso}(2,2) \rangle \xrightarrow{\Delta_w/\Delta \to 0} \left\langle -2 \left[\tau_{12}^d \cancelto{0}{\frac{\partial V}{\partial x}} + \tau_{22}^d \cancelto{0}{\frac{\partial V}{\partial y}} + \tau_{23}^d \cancelto{0}{\frac{\partial V}{\partial z}} \right] \right\rangle - \left(\frac{2}{3} \right) \langle \epsilon \rangle . \tag{A.8}$$

It follows that,

$$\boxed{\frac{\langle \text{Aniso}(2,2) \rangle}{\langle \epsilon \rangle} \xrightarrow{\Delta_w/\Delta \to 0} \left(-\frac{2}{3} \right)} \tag{A.9}$$

Since $\text{Aniso}(1,1) + \text{Aniso}(2,2) + \text{Aniso}(3,3) = 0$, it follows trivially that,

$$\boxed{\frac{\langle \text{Aniso}(3,3) \rangle}{\langle \epsilon \rangle} \xrightarrow{\Delta_w/\Delta \to 0} \left(-\frac{2}{3} \right)} \tag{A.10}$$

A.2 τ_{13}^d budget

We recall that the dominant production term in the τ_{13}^d budget is isotropic production. Expanding out Iso(1,3) in the limit $\Delta_w/\Delta \to 0$,

$$\langle \mathrm{Iso}(1,3)\rangle \xrightarrow{\Delta_w/\Delta\to 0} -\left(\frac{2}{3}\right)\langle e\rangle\left\langle\frac{\partial U}{\partial z}\right\rangle$$

$$\Longrightarrow \quad \frac{\langle \mathrm{Iso}(1,3)\rangle}{\langle \epsilon\rangle} \xrightarrow{\Delta_w/\Delta\to 0} \left(\frac{2}{3}\right)\left.\frac{-\langle e\rangle\left\langle\frac{\partial U}{\partial z}\right\rangle}{-\left\langle\tau_{13}^d\right\rangle\left\langle\frac{\partial U}{\partial z}\right\rangle}\right|_{\Delta_w/\Delta\to 0} = \frac{1}{3}\left.\left(\frac{\tau_{13}^d}{2\,e}\right)^{-1}\right|_{\Delta_w/\Delta\to 0} \tag{A.11}$$

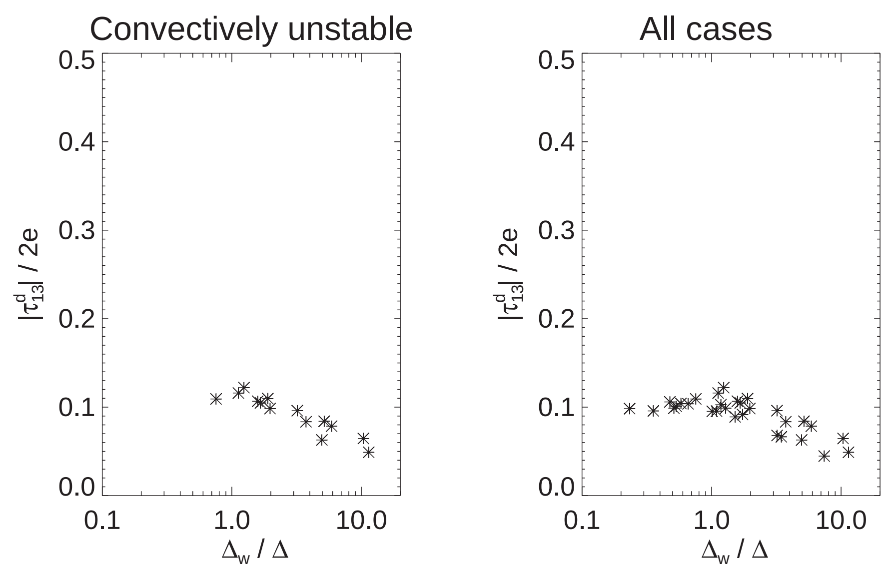

Figure A.1. HATS: Magnitude of (1,3) component of normalized anisotropy tensor, $b_{13} = |\tau_{13}^d|/2e$, for convectively unstable cases only (left) and the entire range of stabilities in the HATS data set (right).

To deduce the limit on the right side of Eq. (A.11), we plot in Fig. (A.1) the mean magnitude of $\tau_{13}^d/2e$ as a function of Δ_w/Δ for the unstable cases and for the entire range of stabilities. Corresponding plots from LES for the SFS conservation equations and the eddy-diffusivity closure are shown in Fig. (A.2). From Fig. (A.1), the mean value of $|\tau_{13}^d/2e|$ appears to asymptote approximately to 0.1, at lower values of Δ_w/Δ. This trend is weakly visible for the convectively unstable cases but

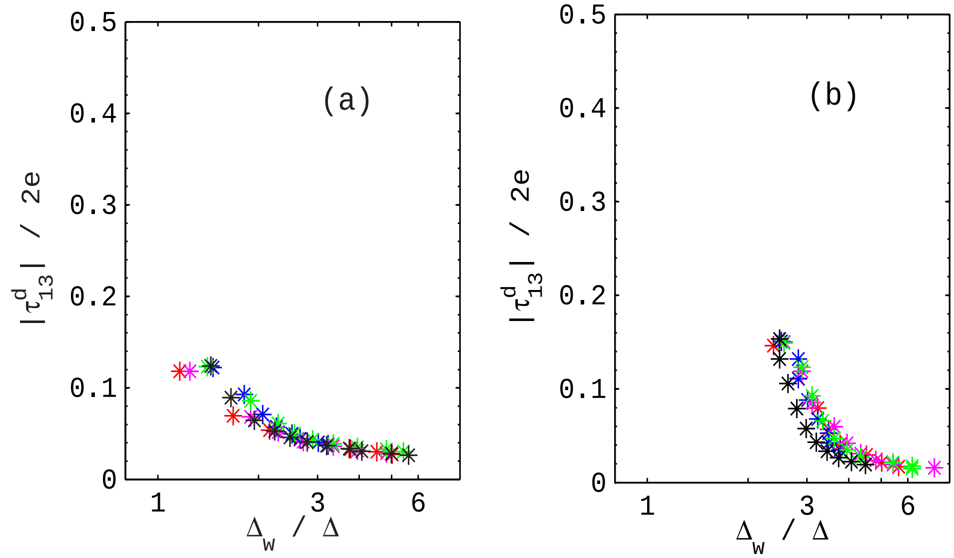

Figure A.2. LES: Magnitude of (1,3) component of normalized anisotropy tensor, $b_{13} = |\tau^d_{13}|/2e$, using (a) SFS conservation equations; and (b) eddy-diffusivity closure. Color legend: —— : $-z_i/L = 1.21$, —— : $-z_i/L = 3.78$, —— : $-z_i/L = 3.82$, —— : $-z_i/L = 5.47$,—— : $-z_i/L = 7.2$

is clearer for the whole HATS data set covering both stable and unstable regimes. While we are unable to provide an analytical proof, we infer from Figs. (A.1) that $\tau^d_{13}/2e$ tends approximately to -0.1 in the mean as $\Delta_w/\Delta \to 0$, using the fact that τ^d_{13} is negative in the ABL. Using this inferred limit for $\tau^d_{13}/2e$ as $\Delta_w/\Delta \to 0$,

$$\boxed{\frac{\langle \mathrm{Iso}(1,3)\rangle}{\langle \epsilon \rangle} \xrightarrow{\Delta_w/\Delta \to 0} -\left(\frac{1}{3}\right)\left(\frac{1}{0.1}\right) = -3.33} \tag{A.12}$$

Finally, we note that our LES results correspond to spatial averaging whereas in the above derivation we have used ensemble averaging. We can equate the two kinds of averages by invoking ergodicity.

Bibliography

André, J. C. and L. Mahrt, 1982: The nocturnal surface inversion and influence of clear-air radiative cooling. *J. Atmos. Sci.*, **39**, 864–878.

Andreas, E. L., K. J. Claffey, R. E. Jordan, C. W. Fairall, P. S. Guest, P. O. G. Perrson, and A. A. Grachev, 2006: Evaluations of the von Kármán constant in the atmospheric surface layer. *J. Fluid. Mech.*, **559**, 117–149.

Andreas, E. L., K. J. Claffey, and A. P. Makshtas, 2000: Low-level atmospheric jets and inversions over the western Weddell Sea. *Bound. Layer Meteo.*, **97**, 459–486.

Andren, A., A. R. Brown, J. Graf, P. J. Mason, C.-H. Moeng, F. T. M. Nieuwstadt, and U. Schumann, 1994: Large-eddy simulation of a neutrally stratified boundary layer. *Quart. J. Roy. Met. Soc.*, **120**, 1457–1484.

Banta, R. M., R. K. Newsom, J. K. Lundquist, Y. L. Pichugina, R. L. Coulter, and L. Mahrt, 2002: Nocturnal low-level jet characteristics over Kansas during CASES-99. *Bound. Layer Meteo.*, **105**, 221–252.

Banta, R. M., Y. L. Pichugina, and W. A. Brewer, 2006: Turbulence velocity-variance profiles in the stable boundary layer generated by a nocturnal low-level jet. *J. Atmos. Sci.*, **63**, 2700–2719.

Banta, R. M., Y. L. Pichugina, N. D. Kelley, B. L. Jonkman, and W. A. Brewer, 2008: Doppler Lidar measurements of the Great Plains low-level jet: Applications to wind energy. *14th International symposium for the advancement of boundary layer remote sensing*, Risø National Laboratory, DTU, Roskilde, Denmark.

Banta, R. M., Y. L. Pichugina, and R. K. Newsom, 2003: Relationship between low-level jet properties and turbulence kinetic energy in the nocturnal stable boundary layer. *J. Atmos. Sci.*, **60**, 2549–2555.

Banta, R. M., J. C. Senff, A. B. White, M. Trainer, R. T. Mcnider, R. J. Valente, S. D. Mayor, R. J. Alvarez, R. M. Hardesty, D. D. Parish, and F. C. Fehsenfeld, 1998: Daytime buildup and nighttime transport of urban ozone in the boundary layer during a stagnation episode. *J. Geophy. Res.*, **103**, 22519–22544.

Basu, S., A. A. M. Holtslag, B. J. H. V. D. Wiel, A. F. Moene, and G.-J. Steeneveld, 2008: An inconvenient "truth" about using sensible heat flux as a surface boundary condition in models under stably stratified regimes. *Acta Geo.*, **56**, 88–99.

Basu, S. and F. Porté-Agel, 2006: Large-eddy simulation of stably stratified atmospheric boundary layer turbulence: A scale-dependent dynamic modeling approach. *J. Atmos. Sci.*, **63**, 2074–2091.

Basu, S., F. Porté-Agel, E. Foufoula-Georgiou, J. F. Vinuesa, and M. Pahlow, 2006: Revisiting the local scaling hypothesis in stably stratified atmospheric boundary layer turbulence: an integration of field and laboratory measurements with large-eddy simulations. *Bound. Layer Meteo.*, **119**, 473–500.

Beare, R. J., M. K. Macvean, A. A. M. Holtslag, J. Cuxart, I. Esau, J.-C. Golaz, M. A. Jimenez, M. Khairoutdinov, B. Kosović, D. Lewellen, T. S. Lund, J. K. Lundquist, A. Mccabe, A. F. Moene, Y. Noh, and P. P. Sullivan, 2006: An intercomparison of large-eddy simulations of the stable boundary layer. *Bound. Layer. Meteo.*, **118**, 247–272.

Beljaars, A. C. M. and A. A. M. Holtslag, 1991: Flux-parameterization over land surfaces for atmospheric models. *J. Appl. Meteo.*, **30**, 327–341.

Blackadar, A. K., 1957: Boundary layer wind maxima and their significance for the growth of nocturnal inversions. *Bull. Amer. Met. Soc.*, **38**, 283–290.

Brasseur, J. G. and T. Wei, 2010: Designing large-eddy simulation of the turbulent boundary layer to capture law-of-the-wall scaling. *Phys. Fluids.*, **22**, 1–21.

Brasseur, J. G., T. Wei, and S. Ramachandran, 2009: Predicting law-of-the-wall with LES: Role of SFS and surface stress models. *Bull. Amer. Phys. Soc.*, **54**, 228.

Brost, R. A. and J. C. Wyngaard, 1978: A model study of the stably-stratified planetary boundary layer. *J. Atmos. Sci.*, **35**, 1427–1440.

Brown, A. R., J. M. Hobson, and N. Wood, 2001: Large-eddy simulation of neutral turbulent flow over rough sinusoidal ridges. *Bound. Layer. Meteo.*, **98**, 411–441.

Businger, J. A., J. C. Wyngaard, Y. Izumi, and E. F. Bradley, 1971: Flux-profile relationships in the atmospheric surface layer. *J. Atmos. Sci.*, **28**, 181–189.

Canuto, V. M., F. Minotti, C. Ronchi, R. M. Ypma, and O. Zeman, 1993: Second-order closure PBL model with new third-order moments: Comparison with LES data. *J. Atmos. Sci.*, **51**, 1605–1618.

Caughey, S. J., J. C. Wyngaard, and J. C. Kaimal, 1979: Turbulence in the evolving stable boundary layer. *J. Atmos. Sci.*, **36**, 1041–1052.

Chamecki, M., C. Meneveau, and M. B. Parlange, 2007: The local structure of atmospheric turbulence and its effect on the Smagorinsky model for large eddy simulation. *J. Atmos. Sci.*, **64**, 1941–1958.

Chen, Q., M. Otte, P. Sullivan, and C. Tong, 2009: *Aposteriori* subgrid-scale models tests based on the conditional means of subgrid-scale stress and its production rate. *J. Fluid. Mech.*, **626**, 149–181.

Chen, Q. and C. Tong, 2006: Investigation of the subgrid-scale stress and its production rate in a convective atmospheric boundary layer using measurement data. *J. Fluid. Mech.*, **547**, 65–104.

Chen, Q., D. Wang, H. Zhang, and C. Tong, 2005: Effects of subgrid-scale turbulence on resolvable-scale velocity-scalar statistics. *J. Turb.*, **6**, 1–31.

Cheng, Y., V. M. Canuto, and A. M. Howard, 2001: An improved model for the turbulent PBL. *J. Atmos. Sci.*, **59**, 1550–1565.

Chow, F. K., R. Street, M. Xue, and J. H. Ferziger, 2005: Explicit filtering and reconstruction turbulence modeling for large-eddy simulation of neutral boundary layer flow. *J. Atmos. Sci.*, **62**, 2058–2077.

Davies, P. A., 2000: Development and mechanisms of the nocturnal jet. *Meteo. Appl.*, **7**, 239–246.

Deardorff, J. W., 1973: The use of subgrid transport equations in a three-dimensional model of atmospheric turbulence. *J. Fluids. Eng.*, **95**, 429–438.

— 1980: Stratocumulus-capped mixed layers derived from a three-dimensional model. *Bound. Layer. Meteo.*, **18**, 495–527.

Derbyshire, S. H., 1990: Nieuwstadt's stable boundary layer revisited. *Quart. J. Roy. Met. Soc.*, **116**, 127–158.

Dias, N. L., W. Brutsaert, and M. L. Wesely, 1995: Z-less stratification under stable conditions. *Bound. Layer Meteo.*, **75**, 175–187.

Drobinski, P., P. Carlotti, J.-L. Redelsperger, R. M. Banta, V. Masson, and R. K. Newsom, 2007: Numerical and experimental investigation of the neutral atmospheric surface layer. *J. Atmos. Sci.*, **64**, 137–156.

Duynkerke, P. G., 1999: Turbulence, radiation and fog in dutch stable boundary layers. *Bound. Layer Meteo.*, **90**, 447–477.

Esau, I., 2004: Simulation of Ekman boundary layers by large-eddy model with dynamic mixed subfilter closure. *Env. Flu. Mech.*, **4**, 273–303.

Forrer, J., 1999: *The structure and turbulence characteristics of the stable boundary layer over the Greenland ice sheet*. ETH Zurich, Züricher Klimaschriften 75 edition, 132 pp.

Galmarini, S., C. Beets, P. G. Duynkerke, and J. V.-G. D. Arellano, 1998: Stable nocturnal boundary layers: a comparison of one-dimensional and large-eddy simulation models. *Bound. Layer Meteo.*, **88**, 181–210.

Garciá-Villalba, M. and J. C. del Álamo, 2008: Turbulence and internal waves in a stably-stratified channel flow. *High performance computing in science and engineering*, W. E. Nagel, D. Kröner, and M. Resch, eds., Springer-Verlag, 217–228.

Garratt, J. R., 1982: Observations in the nocturnal boundary layer. *Bound. Layer. Meteo.*, **22**, 21–48.

Germano, M., U. Piomelli, P. Moin, and W. H. Cabot, 1991: A dynamic subgrid-scale eddy viscosity model. *Phys. Fluids.*, **3**, 1760–1765.

Ghosal, S. and P. Moin, 1995: The basic equations for the large-eddy simulation of turbulent flows in complex geometry. *J. Comp. Phy.*, **118**, 24–37.

Grant, A. L. M., 1986: Observations of boundary layer structure made during the 1981 KONTUR experiment. *Quart. J. Roy. Met. Soc.*, **112**, 825–841.

Ha, K. J., Y. K. Hyun, H. M. Oh, K. E. Kim, and L. Mahrt, 2007: Evaluation of boundary layer similarity theory for stable conditions in CASES-99. *Mon. Wea. Rev.*, **135**, 3474–3483.

Hatlee, S. C. and J. C. Wyngaard, 2007: Improved subfilter-scale models from the HATS field data. *J. Atmos. Sci.*, **64**, 1694–1705.

Haugen, D. A., J. C. Kaimal, and E. F. Bradley, 1971: An experimental study of reynolds stress and heat flux in the atmospheric surface layer. *Quart. J. Roy. Met. Soc.*, **97**, 168–180.

Heinemann, G., 2004: Local similarity properties of the continuously turbulent stable boundary layer over Greenland. *Bound. Layer Meteo.*, **112**, 283–305.

Higgins, C. W., C. Meneveau, and M. B. Parlange, 2007: The effect of filter dimension on the subgrid-scale stress, heat flux and tensor alignments in the atmospheric surface layer. *J. Atmos. & Ocean. Tech.*, **24**, 360–375.

Hogan, R. J., A. L. M. Grant, A. J. Illingworth, G. N. Pearson, and E. J. O'Connor, 2009: Vertical velocity variance and skewness in clear and cloud-topped boundary layers as revealed by Doppler lidar. *Quart. J. Roy. Met. Soc.*, **135**, 635–643.

Horst, T. W., J. Kleissl, D. H. Lenschow, C. Meneveau, C.-H. Moeng, M. B. Parlange, P. P. Sullivan, and J. C. Weil, 2003: HATS: Field observations to obtain spatially filtered turbulence fields from crosswind arrays of sonic anemometers in the atmospheric surface layer. *J. Atmos. Sci.*, **61**, 1566–1581.

Howell, J. F. and J. Sun, 1999: Surface-layer fluxes in stable conditions. *Bound. Layer Meteo.*, **90**, 495–520.

Hunt, J. C. R., J. C. Kaimal, and J. E. Gaynor, 1985: Some observations of turbulence structure in stable layers. *Quart. J. Roy. Met. Soc.*, **111**, 793–815.

Hyun, Y. K., K. E. Kim, and K. J. Ha, 2005: A comparison of methods to estimate the height of stable boundary layer over a template grassland. *Agr. For. Meteo.*, **132**, 132–142.

Iida, O., N. Kasagi, and Y. Nagano, 2002: Direct numerical simulation of turbulent channel flow under stable density stratification. *Int. J. Heat & Mass Trans.*, **45**, 1693–1703.

Jimenez, M. A. and J. Cuxart, 2005: Large-eddy simulations of the stable boundary layer using the standard Kolmogorov theory: range of applicability. *Bound. Layer Meteo.*, **115**, 241–261.

Juneja, A. and J. G. Brasseur, 1999: Characteristics of subgrid-resolved-scale dynamics in anisotropic turbulence, with application to rough-wall boundary layers. *Phys. Fluids.*, **11**, 3054–3068.

Kaimal, J. C. and J. J. Finnigan, 1994: *Atmospheric boundary layer flows*. Oxford University Press, 1st edition, 289 pp.

Kaimal, J. C., J. C. Wyngaard, Y. Izumi, and O. R. Coté, 1972: Spectral characteristics of surface-layer turbulence. *Quart. J. Roy. Met. Soc.*, **98**, 563–589.

Katul, G. G., M. B. Parlange, J. D. Albertson, and C. R. Chu, 1995: Local isotropy and anisotropy in the sheared and heated atmospheric surface layer. *Bound. Layer. Meteo.*, **72**, 123–148.

Khanna, S., 1995: *Structure of the atmospheric boundary layer from large eddy simulation, Ph.D dissertation*. Pennsylvania State University, 195 pp.

Khanna, S. and J. G. Brasseur, 1997: Analysis of Monin-Obukhov similarity from large-eddy simulation. *J. Fluid. Mech.*, **345**, 251–286.

— 1998: Three-dimensional buoyancy- and shear-induced local structure of the atmospheric boundary layer. *J. Atmos. Sci.*, **55**, 710–743.

King, J. C., W. M. Connolley, and S. H. Derbyshire, 2001: Sensitivity of modeled Antarctic climate to surface and boundary-layer flux parameterizations. *Quart. J. Roy. Met. Soc.*, **127**, 779–794.

Kleissl, J., C. Meneveau, and M. Parlange, 2003: On the magnitude and variability of subgrid-scale eddy-diffusion coefficients in the atmospheric surface layer. *J. Atmos. Sci.*, **60**, 2372–2388.

Klemp, J. and D. Durran, 1983: An upper boundary condition permitting internal gravity wave radiation in numerical mesoscale models. *Mon. Wea. Rev.*, **11**, 430–444.

Kosović, B., 1997: Subgrid-scale modeling for the large-eddy simulation of high-reynolds-number boundary layer. *J. Fluid. Mech.*, **336**, 151–182.

Kosović, B. and J. A. Curry, 2000: A large-eddy simulation study of a quasi-steady, stably stratified atmospheric boundary layer. *J. Atmos. Sci.*, **57**, 1052–1068.

Lenschow, D. H., X. S. Li, C. J. Zhu, and B. B. Stankov, 1988: The stably stratified boundary layer over the great plains. i: Mean turbulence and structure. *Bound. Layer Meteo.*, **42**, 95–121.

Lenschow, D. H., J. C. Wyngaard, and W. T. Pennell, 1980: Mean-field and second-moment budgets in a baroclinic, convective boundary layer. *J. Atmos. Sci.*, **37**, 1313–1326.

Lilly, D. K., 1967: The representation of small-scale turbulence in numerical experiments. *Proc. IBM Scientific Computing Symp. on Environmental Sciences*, Thomas J. Watson Research Center, IBM, Yorktown Heights, NY, 195–210.

Lumley, J. L. and H. A. Panofsky, 1964: *Structure of atmospheric turbulence*. Interscience Publishers, 1st edition, 239 pp.

Mahrt, L., 1981: The early evening boundary-layer transition. *Quart. J. Roy. Met. Soc.*, **107**, 329–344.

— 1989: Intermittency of atmospheric turbulence. *J. Atmos. Sci.*, **46**, 79–95.

— 1998: Stratified atmospheric boundary layers and breakdown of models. *J. Theo. Comp. Fluid Dyn.*, **11**, 263–279.

— 1999: Stratified atmospheric boundary layers. *Bound. Layer Meteo.*, **90**, 375–396.

Mahrt, L. and D. Vickers, 2002: Contrasting vertical structures of nocturnal boundary layers. *Bound. Layer Meteo.*, **105**, 351–363.

— 2003: Formulation of turbulent fluxes in the stable boundary layer. *J. Atmos. Sci.*, **60**, 2538–2548.

Malhi, Y. S., 1995: The significance of the dual solutions for the heat fluxes measured by the temperature fluctuations method in stable conditions. *Bound. Layer Meteo.*, **74**, 389–396.

Mason, P. J. and S. H. Derbyshire, 1990: Large-eddy simulation of the stably-stratified atmospheric boundary layer. *Bound. Layer Meteo.*, **53**, 117–162.

Mason, P. J. and D. J. Thomson, 1992: Stochastic backscatter in large-eddy simulation of boundary layers. *J. Fluid. Mech.*, **242**, 51–78.

Mathieu, J. and J. Scott, 2000: *An introduction to turbulent flow*. Cambridge University Press, 1st edition, 374 pp.

Mellor, G. L. and T. Yamada, 1974: A hierarchy of turbulence closure models for planetary boundary layers. *J. Atmos. Sci.*, **31**, 1791–1806.

— 1982: Development of a turbulence closure model for geophysical fluid problems. *Rev. Geophys. Space Phys.*, **20**, 851–875.

Meneveau, C., 1994: Statistics of turbulence subgrid-scale stresses: Necessary conditions and experimental tests. *Phys. Fluids*, **6**, 815–833.

Miles, J. W., 1961: On the stability of heterogeneous shear flows. *J. Fluid. Mech.*, **10**, 496–508.

Moeng, C.-H., 1984: A large-eddy simulation model for the study of planetary boundary-layer turbulence. *J. Atmos. Sci.*, **41**, 2052–2062.

Moeng, C.-H. and J. C. Wyngaard, 1986: An analysis of closures for pressure-scalar covariances in the convective boundary layer. *J. Atmos. Sci.*, **43**, 2499–2513.

— 1988: Spectral analysis of large eddy simulations of the convective boundary layer. *J. Atmos. Sci.*, **45**, 3573–3587.

Mydlarski, L., 2003: Mixed velocity-passive scalar statistics in high-Reynolds-number turbulence. *J. Fluid. Mech.*, **475**, 173–203.

Nagib, H. M. and K. A. Chauhan, 2008: Variations of von Kármán coefficient in canonical flows. *Phys. Fluids*, **20**, 101518–101527.

Nakanishi, M., 2001: Improvement of the Mellor-Yamada turbulence closure model based on large-eddy simulation data. *Bound. Layer Meteo.*, **99**, 349–378.

Newsom, R. K. and R. M. Banta, 2003: Shear-flow instability in the stable nocturnal boundary layer as observed by Doppler Lidar during CASES-99. *J. Atmos. Sci.*, **60**, 16–33.

Nieuwstadt, F. T. M., 1984: The turbulent structure of the stable, nocturnal boundary layer. *J. Atmos. Sci.*, **41**, 2202–2216.

— 1985: A model for the stationary, stable boundary layer. *Turbulence and diffusion in stable environments*, J. C. R. Hunt, ed., Clarendon Press, 149–179.

— 2005: Direct numerical simulation of stable channel flow at large stability. *Bound. Layer Meteo.*, **116**, 277–299.

Ohya, Y., 2001: Wind-tunnel study of atmospheric stable boundary layers over a rough surface. *Bound. Layer Meteo.*, **98**, 57–82.

Ohya, Y., R. Nakamura, and T. Uchida, 2008: Intermittent bursting of turbulence in a stable boundary layer with low-level jet. *Bound. Layer Meteo.*, **126**, 349–363.

Ohya, Y., D. E. Neff, and R. N. Meroney, 1997: Turbulence structure in a stratified boundary layer under stable conditions. *Bound. Layer Meteo.*, **83**, 139–161.

Oncley, S. P., C. A. Friehe, J. C. Larue, J. A. Businger, E. C. Itsweire, and S. S. Chang, 1996: Surface-layer fluxes, profiles and turbulence measurements over uniform terrain under near-neutral conditions. *J. Atmos. Sci.*, **53**, 1029–1044.

Otte, M. J. and J. C. Wyngaard, 2001: Stably stratified interfacial-layer turbulence from large-eddy simulation. *J. Atmos. Sci.*, **58**, 3424–3442.

Pardyjak, E. R., P. Monti, and H. J. S. Fernando, 2002: Flux richardson number measurements in stable atmospheric shear flows. *J. Fluid. Mech.*, **459**, 307–316.

Paulson, C. A., 1970: The mathematical representation of wind speed and temperature profiles in the unstable atmospheric surface layer. *J. Appl. Meteo.*, **9**, 857–861.

Peltier, L. J., J. C. Wyngaard, S. Khanna, and J. G. Brasseur, 1996: Spectra in the unstable surface layer. *J. Atmos. Sci.*, **53**, 49–61.

Pichugina, Y. L., R. M. Banta, N. D. Kelley, W. A. Brewer, S. P. Sandburg, J. L. Machol, and B. L. Jonkman, 2008: Remote sensing of the nocturnal boundary layer for wind energy applications. *14th International symposium for the advancement of boundary layer remote sensing*, Risø National Laboratory, DTU, Roskilde, Denmark.

Piomelli, U., W. H. Cabot, P. Moin, and S. Lee, 1991: Subgrid-scale backscatter in turbulent and transitional flows. *Phys. Fluids.*, **3**, 1766–1771.

Porté-Agel, F., 2004: A scale-dependent dynamic model for scalar transport in les of the atmospheric boundary layer. *Bound. Layer Meteo.*, **112**, 81–105.

Porté-Agel, F., C. Meneveau, and M. B. Parlange, 1998: Some basic properties of the surrogate subgrid-scale heat flux in the atmospheric boundary layer. *Bound. Layer Meteo.*, **88**, 425–444.

— 2000: A scale-dependent dynamic model for large-eddy simulation: application to a neutral atmospheric boundary layer. *J. Fluid. Mech.*, **415**, 261–284.

Porté-Agel, F., M. B. Parlange, C. Meneveau, and W. E. Eichinger, 2001: A priori field study of the subgrid-scale heat fluxes and dissipation in the atmospheric surface layer. *J. Atmos. Sci.*, **58**, 2673–2698.

Poulos, G. S., W. Blumen, J. C. L. D. C. Fritts, J. Sun, S. P. Burns, C. Nappo, R. Banta, R. Newsom, J. Cuxart, E. Terradellas, B. Balsley, and M. Jensen, 2003: CASES-99: A comprehensive investigation of the stable nocturnal boundary layer. *Bull. Amer. Met. Soc.*, **83**, 555–581.

Rotta, J. C., 1951: Statistiche theorie nichthomogener turbulenz. *Z. Phys.*, **129**, 547–572.

Saiki, E. M., C.-H. Moeng, and P. P. Sullivan, 2000: Large-eddy simulation of the stably-stratified planetary boundary layer. *Bound. Layer Meteo.*, **95**, 1–30.

Schumann, U., 1975: Subgrid scales model for finite difference simulation of turbulent flows in plane channels and annuli. *J. Comput. Phys.*, **18**, 376–404.

Schumann, U. and T. Gerz, 1995: Turbulent mixing in stably stratified shear flows. *J. Appl. Meteo.*, **34**, 33–48.

Sim, C., S. Basu, and L. Manuel, 2009: The influence of stable boundary layer flows on wind turbine fatigue loads. *47th AIAA Aerospace Sciences Meeting*, Orlando, Florida.

Skamarock, W. C. and J. B. Klemp, 2008: A time-split nonhydrostatic atmospheric model for weather research and forecasting applications. *J. Comp. Phy.*, **227**, 3465–3485.

Smagorinsky, J., 1963: General Circulation experiments with the primitive equations I. The basic experiment. *Mon. Wea. Rev.*, **91**, 99–164.

Smedman, A. S., 1988: Observations of a multi-level turbulence structure in a very stable atmospheric boundary layer. *Bound. Layer. Meteo.*, **44**, 231–253.

Sorbjan, Z., 1986: Local similarity of spectral and cospectral characteristics in the stable-continuous boundary layer. *Bound. Layer Meteo.*, **35**, 257–275.

— 2006: Local structure of turbulence in stably stratified boundary layers. *J. Atmos. Sci.*, **63**, 1526–1537.

Speziale, C. J., 1991: Analytical methods for the development of reynolds-stress closures in turbulence. *Ann. Rev. Fluid. Mech.*, **23**, 107–157.

Sreenivasan, K. R., 1995: On the universality of the Kolmogorov constant. *Phys. Fluids.*, **7**, 2778–2784.

— 1996: The passive scalar spectrum and the Obukhov-Corrsin constant. *Phys. Fluids.*, **8**, 189–196.

Stoll, R. and F. Porté-Agel, 2008: Large-eddy simulation of the stable atmospheric boundary layer using dynamic models with different averaging schemes. *Bound. Layer Meteo.*, **126**, 1–28.

Strang, E. J. and H. J. S. Fernando, 2001: Vertical mixing and transports through a stratified shear layer. *J. Phys. Ocean.*, **31**, 2026–2048.

Sullivan, P. P., 2010: On the isotropic and anisotropic production of subfilter scale momentum and scalar fluxes across scale and stability. *to be submitted, J. Atmos. Sci.*.

Sullivan, P. P., T. W. Horst, D. H. Lenschow, C. Moeng, and J. C. Weil, 2003: Structure of subfilter-scale fluxes in the atmospheric surface layer with application to large-eddy simulation modeling. *J. Fluid. Mech.*, **482**, 101–139.

Sullivan, P. P., J. C. McWilliams, and C. Moeng, 1994: A subgrid-scale model for large-eddy simulation of planetary boundary-layer flows. *Bound. Layer Meteo.*, **71**, 247–276.

— 1996: A grid nesting method for large-eddy simulation of planetary boundary layer flows. *Bound. Layer Meteo.*, **80**, 167–202.

Sullivan, P. P. and C. Moeng, 1994: A comparison of shear- and buoyancy-driven planetary boundary layer flows. *J. Atmos. Sci.*, **51**, 999–1022.

Tao, B., J. Katz, and C. Meneveau, 2002: Statistical geometry of subgrid-scale stresses determined from holographic particle image velocimetry measurements. *J. Fluid. Mech.*, **457**, 35–78.

Tennekes, H. and J. L. Lumley, 1972: *A First Course in Turbulence*. The MIT Press, 300 pp.

Tong, C., J. Wyngaard, S. Khanna, and J. G. Brasseur, 1998: Resolvable- and subgrid-scale measurement in the atmospheric surface layer: technique and issues. *J. Atmos. Sci.*, **55**, 3114–3126.

Townsend, A. A., 1958: The effects of radiative transfer on turbulent flow of a stratified fluid. *J. Fluid. Mech.*, **3**, 361–372.

— 1976: *The structure of turbulent shear flow*. Cambridge University Press, 1st edition, 429 pp.

Van de Wiel, B. J. H., A. F. Moene, O. K. Hartogensis, H. A. R. de Bruin, and A. A. M. Holtslag, 2003: Intermittent turbulence in the stable boundary layer over land. part iii: A classification for observations during CASES-99. *J. Atmos. Sci.*, **60**, 2509–2522.

Van de Wiel, B. J. H., A. F. Moene, G. J. Steeneveld, O. K. Hartogensis, and A. A. M. Holtslag, 2007: Predicting the collapse of turbulence in stably stratified boundary layers. *Flow. Turb. & Comb.*, **79**, 251–274.

Vickers, D. and L. Mahrt, 2004: Evaluating formulations of stable boundary layer height. *J. Appl. Meteo.*, **43**, 1736–1749.

Vreman, B., B. Geurts, and H. Kuerten, 1994: Realizability conditions for the turbulent stress tensor in large-eddy simulation. *J. Fluid. Mech.*, **278**, 351–362.

Wei, T. and J. G. Brasseur, 2010: The surface stress boundary condition in large-eddy simulation of high reynolds number turbulent boundary layer flows. *To be submitted to Bound. Layer. Meteo.*.

Wong, V. C. and D. K. Lilly, 1994: A comparison of two dynamic subgrid closure methods for turbulent thermal-convection. *Phys. Fluids.*, **6**, 1016–1023.

Wyngaard, J. C., 1973: On surface layer turbulence. *Workshop on micrometeorology*, D. A. Haugen, ed., American Meteorological Society, Boston, 109–149.

— 1992: Atmospheric turbulence. *Ann. Rev. Fluid. Mech.*, **24**, 205–233.

— 2004: Towards numerical modeling in the "terra incognita". *J. Atmos. Sci.*, **61**, 1816–1826.

— 2010: *Turbulence in the atmosphere*. Cambridge University Press, 1st edition, 408 pp.

Wyngaard, J. C. and O. R. Coté, 1971: The budgets of turbulent kinetic energy and temperature variance in the atmospheric surface layer. *J. Atmos. Sci.*, **28**, 190–201.

Wyngaard, J. C., O. R. Coté, and Y. Izumi, 1971: Local free convection, similarity, and the budgets of shear stress and heat flux. *J. Atmos. Sci.*, **28**, 1171–1182.

Wyngaard, J. C., A. Siegel, and J. M. Wilczak, 1994: On the response of a turbulent-pressure probe and the measurement of pressure transport. *Bound. Layer. Meteo.*, **69**, 379–396.

Xue, M., K. K. Droegemeier, and V. Wong, 2000: The advanced regional prediction system (ARPS) - a multi-scale nonhydrostatic atmospheric simulation and prediction model. Part I: Model dynamics and verification. *Meteo. Atmos. Phy.*, **75**, 161–193.

Yakhot, V. and S. A. Orszag, 1986: Renormalization group analysis of turbulence I: Basic theory. *J. Sci. Comp.*, **1**, 3–51.

Zeman, O., 1981: Progress in the modeling of planetary boundary layers. *Ann. Rev. Fluid. Mech.*, **13**, 253–272.

Zhou, Y., J. G. Brasseur, and A. Juneja, 2001: A resolvable subfilter-scale model specific to large-eddy simulation of under-resolved turbulence. *Phys. Fluids.*, **13**, 2602–2610.

Zilitinkevich, S. S., 1972: On the determination of the height of the Ekman boundary layer. *Bound. Layer Meteo.*, **3**, 141–145.

Zilitinkevich, S. S. and D. V. Mironov, 1996: A multi-limit formulation for the equilibrium depth of a stably stratified boundary layer. *Bound. Layer Meteo.*, **81**, 325–351.

Vita

Sanjiv Ramachandran

Sanjiv Ramachandran was born in Chennai, India on November 7, 1978, but moved to Bangalore soon after where he spent nearly two decades. He received his B.S. degree in Aerospace Engineering from the Indian Institute of Technology, Mumbai, in 2002 and his M.S. degree, also in Aerospace Engineering, from Pennsylvania State University in 2004. Since September of 2004, he has been enrolled as a Ph.D. student in the Department of Meteorology at Pennsylvania State University.